QEPAS gas sensors for air quality monitoring

Roman Rousseau

THÈSE POUR OBTENIR LE GRADE DE DOCTEUR DE L'UNIVERSITÉ DE MONTPELLIER

En Electronique

École doctorale : Information, Structures, Systèmes

Unité de recherche : Institut d'Electronique et des systèmes

QEPAS GAS SENSORS FOR AIR QUALITY MONITORING

~

CAPTEURS QEPAS POUR LA SURVEILLANCE DE LA QUALITE DE L'AIR

Présentée par Roman ROUSSEAU

Le 15 Octobre 2020

Sous la direction de Aurore VICET

Devant le jury composé de

Georges DURRY, Professeur, Université Reims Champagne-Ardenne	Rapporteur
Antoine GODARD, Chercheur, ONERA Palaiseau	Rapporteur
Weidong CHEN, Professeur, Université Côte d'Opale	Examinateur
Guillaume AOUST, Ingénieur, Société mirSense	Examinateur
Philippe COMBETTE, Professeur, IES - Université Montpellier	Président
Aurore VICET, Maître de conférences, IES - Université Montpellier	Directrice de thèse
Roland TEISSIER, Directeur de recherche, IES - CNRS	Examinateur
Michael BAHRIZ, Maître de conférences, IES - Université Montpellier	Invité

UNIVERSITÉ DE MONTPELLIER

Contents

Introduction

Gas sensing consists in determining the concentration of a given set of molecular species in a gas sample. Those 'target' species are often found in minute quantities in the sample. The diversity of target molecules and their concentration depend on the application. One the main application is the monitoring of air pollutants. Pollutants represents only a fraction of the ambient air, approximately 0.01%. Their emission can be attributed to natural processes as well as human activities. Recent concerns have brought attention onto the CO_2, as a greenhouse gas, which is the main contributor to the climate change. Many other molecules have to be considered, which are classified by the Environmental Protection Agency (EPA) in three main categories: Criteria air pollutants, toxic pollutants and greenhouses gases. Criteria air pollutants are the six most common pollutants including particulate matter (PM), carbon monoxide, sulfur oxide, nitrogen oxide, ozone and lead. Other common pollutants include methane, ammonia, Volatile Organic Compounds (VOCs), BTEX[1]…

Most of the energy produced by human is generated by burning fuels, i.e. oxidizing, the hydrocarbons compounds. The incomplete combustion results in the formation in toxic oxide (CO, NO_x, SO_2, etc.), which can also subsequently agglomerate to form micrometric Particle Matter. In cities, the main source of emissions is related to road transport while outside the cities, fabrication industries, energy production and agriculture contribute to air pollution. Exposure to criteria pollutants can cause adverse effect to public health and welfare. A sudden pollution peak (Figure 1(a)) can results in acute effects such as respiratory discomfort and headaches. Long term exposure is also a serious threat, because chronic effects can appear several years after repeated exposure, even at low concentrations. It can lead to severe diseases such as asthma and lung cancers.

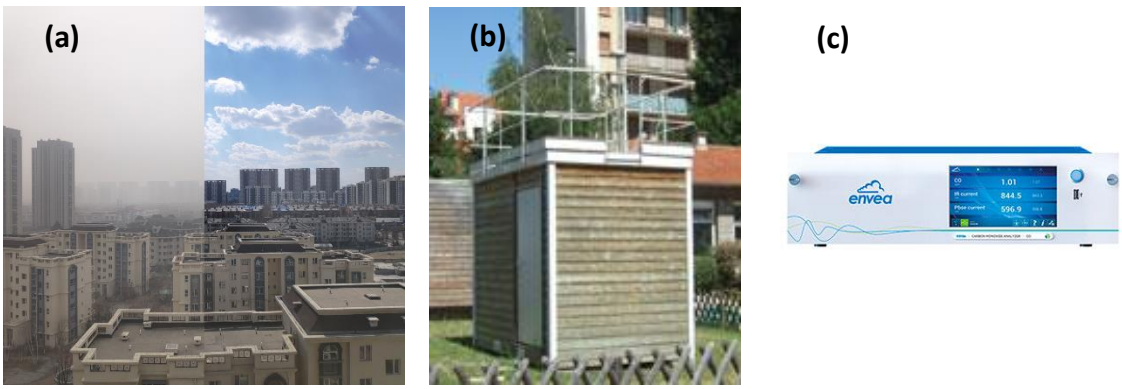

Figure 1: (a) A city with smog (left) and without (right). (b) A measurement stations in the suburbs of Paris (Nogent-sur-Marne)[2]. (c) A certified gas analyzer from ENVEA, for monitoring the concentration of carbon monoxide.

[1] BTEX : Benzene, Toluene, Ethylbenzene, Xylene.
[2] https://www.airparif.asso.fr/stations/index#NOGENT

Criteria pollutants are a serious issue of the modern society, therefore their concentration in ambient air is closely monitored. For instance, in France, the AASQA[3] associations are in charge of the air quality monitoring at a regional level. Their main missions are to monitor the air quality, inform the population, advise the decision-makers on environmental regulations. In particular, the air quality can be visualized in real time on the AASQA websites[4] and is quantified using the atmo index[5] which is based on the measurement of some criteria pollutants . The air quality can be considered good (atmo index < 5) for instance in terms of nitrogen oxide if its concentration in the air is under 54 pbbv (part per billion volume) (equivalent to 0.000 0054% or 110µg/m^3). The measurement of such low concentrations is delicate, requiring accurate gas analyzers and thorough calibration procedures. 1900 gas analyzers are deployed in France over 670 measurement stations. In order to ensure the consistency of the measurement, gas analyzers are certified. In France, the certification is edited by the AFNOR, which specifies the physical principle for each gas species[6]: chemiluminescence for NO_x, ultraviolet absorption for ozone, infrared absorption for carbon monoxide. Only a few gas analyzers on the market are certified (Figure 1(c)). They are expensive and cumbersome which limits their number and their use to non-mobile applications (Figure 1(b)). They often measure only one gas specie. Affordable, compact and multi-species gas analyzers are therefore awaited on the market of air quality monitoring.

The market of gas sensors is rapidly growing. Apart of air quality monitoring, gas sensors are also employed in a variety of applications:

- Preservation of fresh products (C_2H_4) in the food industry:
- Detection of methane leaks (CH_4) in pipelines
- Early detection of pathologies (CO, NO, acetone)
- Reduction of industrial emissions (SO_2, PM)
- Industrial process control such as production of biogas (CH_4, NH_3, H_2S)
- Scientific atmospheric measurements (O_3, CH_4)
- Defense: detection of neurotoxic gases such as Sarin

Depending on the application, gas sensors must fulfill various features. Most likely, they should be able to detect very little quantity of molecules (*sensitivity*), should respond only to the target molecule and not to interferent species (*selectivity*), have moderate footprint (*compactness*) and effective *cost*. Moreover, detecting multiple species is often required. Today, gas sensors on the market can be classified into two categories. On the one hand, electrochemical sensors and semiconductor sensors are portable low-cost devices which suffer from low sensitivity, low selectivity, background drift and humidity variation. On the other hand, sensitive gas analyzers, for instance used today for air quality monitoring, are expensive and massive, which prevents their integration into smart system such as drones, smartphones, vehicles. There is a need for a sensitive, selective, compact, low-cost and multi-species gas sensor. A promising technology is based on laser spectroscopy.

[3] Association Agrée pour la Surveillance de la Qualité de l'Air (AASQA)
[4] https://atmo-france.org/les-donnees/
[5] https://atmo-france.org/lindice-atmo/
[6] https://atmo-reunion.net/les-techniques-de-mesures

Most molecular species possess a well-defined absorption spectrum or 'fingerprint', which can be efficiently sensed using a laser at a given wavelength, leading to an excellent selectivity. Moreover, the high optical power of the laser combined with a strong molecular absorption yields a very good sensitivity. Laser spectroscopy have been realized in the near-InfraRed (IR) (1-2μm) with telecom lasers. However, stronger molecular absorption lines are found in the mid-IR (2-20μm), where there has long been a lack of reliable laser sources. The situation changed with the invention of the antimonide and arsenide quantum wells laser, then Quantum Cascade Laser (QCL) and Interband Cascade Lasers (ICL) which can cover the whole mid-IR. As other semiconductor lasers, the emission of cascade lasers can be adjusted in wavelength in order to target a given specie. Moreover, they are very compact, low-consumption (compared to other mid-IR lasers) and can be fabricated with great reproducibility. Following the developments of silicon photonics, multiple laser sources could be integrated on silicon with electro-optical components to form a compact multi-gas sensor platform.

Another critical part of the sensor is the measurement of the absorbed energy. It can be measured with a photodetector, but this configuration has several drawbacks. The size of the sensor is limited by the absorption path length, which should be as long as possible. Photodetectors tend to have decreased performances with increasing wavelength and operate at low temperature. These limitations can be overcome by using photoacoustic spectroscopy, in which the absorbed light is converted to an acoustic wave. Photoacoustics is based on a localized effect and therefore combines compactness and high sensitivity. The generated acoustic wave can be detected with an electromechanical transducer. The collection of the acoustic energy and the transduction mechanism are crucial for the sensitivity of the sensor. The transducer can be an audio microphone in conventional photoacoustics, a quartz tuning fork (QTF) in Quartz-Enhanced Photoacoustic Spectroscopy (QEPAS) or a cantilever in Cantilever-Enhanced Photoacoustic Spectroscopy (CEPAS). QEPAS and CEPAS have emerged more recently than the conventional photoacoustics but all three techniques have shown very similar performances and are still active research topics.

The objective of the ANR MULTIPAS[7] project was to develop a multi-gas sensor for monitoring the air quality based on the QEPAS technique. 3 industrial companies (mirSense, Valotec, ENVEA) et 2 academic laboratories (IES, LPCA) were involved in the project. At the IES, our group NanoMIR was in charge of the QEPAS sensor design, using different lasers sources (IES, mirSense) and a dedicated electronics (Valotec). At the same time, we explored various configurations which lead to improvements of the QEPAS technique.

The manuscript is composed of 3 chapters.

Chapter 1:

The first chapter describes the theoretical foundations of a QEPAS sensor. QEPAS is a complex technique involving multiple stages, i.e. multiple physical processes, which are progressively introduced along the chapter by visiting the different spectroscopic techniques. First, we present the absorption spectroscopy and the motivation for using mid IR lasers. Then, we develop the photoacoustic spectroscopy which has many similarities with QEPAS. Finally, QEPAS is detailed with a specific focus on the transducer: the Quartz Tuning Fork.

[7] ANR MULTIPAS project (ANR-16-CE04-0012)

Chapter 2:
In the first section, we present a preliminary study of the MULTIPAS project: we select the ideal laser wavelengths for the different target species and assess the feasibility of the gas sensor.
Then, we focus on the optimization of the QEPAS detector (or spectrophone), most specifically we realize a complete study of the acoustic microresonators. We simulate their acoustic response using finite elements, fabricate them using 3D printing, measure their resonance using a specific characterization setup, and propose novel designs. We employ the optimized microresonators in the QEPAS sensor and demonstrate the detection of C_2H_4 using a 11μm quantum cascade laser with a specific laser modulation. Then, we employ a 4.7μm QCL for the detection of carbon monoxide and apply it for a biomedical application.

Chapter 3:
In this last chapter we develop a technique for measuring the resonance of the Quartz Tuning Fork in real time in order to prevent unwanted drifts of the QEPAS sensor due to environmental variabilities. We present a literature review and a theoretical study of the techniques to measure the QTF resonance with 2 different approaches: based on the frequency response and based on the transient response. Next, we describe our setup based on the transient response and validate the accuracy of the technique by monitoring the influence of the temperature and the humidity onto the QTF resonance. Then, we implement our new technique, the Resonance Tracking (RT) QEPAS, in a gas experiment as a proof of concept. Finally, we develop a damping circuit in order to optimize the time spent for characterizing the QTF.

List of abbreviations

BF	Beat Frequency
BVD	Butterworth-Von Dyke
DAQ	Data Acquisition
FFT	Fast Fourier Transform
FM	Frequency Modulation
FTIR	Fourier Transform Infrared
ICL	Interband Cascade Laser
IM	Intensity Modulation
IR	Infrared
LIA	Lock-in amplifier
LOD	Limit of detection
MEMS	Micro Electromechanical System
mR	microresonator
NDIR	Non Dispersive Infrared
NNEA	Normalized Noise Equivalent Absorption
PAS	Photoacoustic Spectroscopy
ppbv	part per billion volume
ppmv	part per million volume
QCL	Quantum Cascade Laser
QEPAS	Quartz-Enhanced Photoacoustic Spectroscopy
QTF	Quartz Tuning Fork
RH	Relative Humidity
TA	Transimpedance Amplifier
TDLAS	Tunable Diode Laser Spectroscopy
WMS	Wavelength Modulation Spectroscopy

Chapter 1

Theoretical background

1.1. Laser spectroscopy

1.1.1. Direct Absorption Spectroscopy

When the bright rays emitted by the sun are passed through a prism, the spectral components of light are spatially separated. When passing the different colors through a given sample, certain colors are kept within the sample. This phenomena, named absorption, is the pillar of Spectroscopy.

Spectroscopy concerns the interaction between light and matter. Since the XXth century, light is modeled as an electromagnetic wave, i.e. the combination of an electric and a magnetic field oscillating at a given frequency ν. Besides, there is matter, represented by the atoms and molecules, which, depending on their molecular weight, the conditions of pressure and temperature, can occur in 3 different states: solid, liquid or gas. The 3 states of matter are presented in a decreasing molecular density. When the average distance between each individual increases, the inter-molecular interactions become weaker. In a gas, molecules can be considered almost isolated. Therefore, the spectroscopy of a gas sample is a straightforward access to study light-matter interactions.

As expressed by the quantum physics, the energetic states in a molecule are quantized, i.e. they correspond to finite levels of energy (rotational, vibrational an electronic). The transitions between those discrete energy levels correspond to a well-defined molecular absorption spectrum. For the transition between a state i and a state j, the absorbed photon energy correspond to the difference of the energy levels E_i and E_j :

$$E_{ij} = E_j - E_i = h\,\nu_{ij} \tag{1.1}$$

With h the Planck's constant. The frequency ν is proportional to the wavenumber $\sigma = \nu/c$ with c the speed of light. The wavenumber is commonly employed in spectroscopy. In a typical experiment of spectroscopy, a monochromatic light source of wavenumber σ (=1/λ) [cm^{-1}] and intensity I_0 is used to illuminate a gas sample of length L [cm]. The transmittance is defined as the ratio of the measured intensity after the gas sample to the initial intensity, as described by the Beer Lambert Law :

$$T(\sigma) = \frac{I_t(\sigma)}{I_0(\sigma)} = e^{-\alpha(\sigma)L} \tag{1.2}$$

where α is the linear absorption coefficient and describes the strength of the absorption.

Trace gas analysis usually deals with very low concentrations, the term αL is relatively small (αL<<1), therefore the Beer Lambert L can be directly linearized:

$$T(\sigma) \approx 1 - \alpha(\sigma)L = 1 - A(\sigma) \tag{1.3}$$

$A(\sigma)$ is known as the absorbance and corresponds to the amount of energy absorbed by the sample. Another definition of the absorbance, often used in chemistry, is based on the logarithm base 10, differing by a factor 1/ln10 from equation (1.2):

$$A^*(\sigma) = -\log T(\sigma) = \frac{\alpha(\sigma)L}{ln10} \tag{1.4}$$

Using HITRAN's terminology [1], the absorption cross section k_v [cm^2.$molecule^{-1}$] is defined as:

$$k_v(\sigma) = \frac{\alpha(\sigma)}{\rho} \tag{1.5}$$

where ρ is the volumetric number density of the target species [$molecule.cm^{-3}$].

For a given molecular transition ij, the absorption cross section is a function of the wavenumber, the temperature and the pressure. It can be written as the product of a the linestrength S and a line shape function *f*.

$$k_{v,ij}(\sigma, p, T) = S_{ij}(T)\, f(\sigma - \sigma_{ij}, p, T) \tag{1.6}$$

$f(\sigma)$ describes the shape of the peak and accounts for the broadening effects, i.e. the physical processes causing the dirac delta function located in σ_{ij} to broaden, giving the peak a linewidth γ, at a given pressure P and temperature T. S_{ij} [cm^{-1}/(molecule·cm^{-2})], called the linestrength, is the area under the curve of the cross section and is constant with the pressure.

The total absorption cross section can be obtained by summing the monochromatic absorption cross section of every lines ij:

$$k_v(\sigma, p, T) = \sum_{ij} k_{v,ij}(\sigma, p, T) \tag{1.7}$$

1.1.1.1. Concentration of the target specie

A gas sample is a generally a mixture of many molecular species. The target specie, i.e. the molecules which undergoes the absorption, constitutes only a fraction of the gas sample. The volume mixing ratio (concentration) corresponds to the ratio of the number of target molecules ρ to the total number of molecules per unit volume ρ_0:

$$C = \frac{\rho}{\rho_0} \tag{1.8}$$

The total number of molecules per unit volume ρ_0 can be obtained from the ideal gas law :

$$\rho_0(p, T) = \frac{p}{p_0}\frac{T_0}{T}\frac{N_A}{V_0} \tag{1.9}$$

with p_0 and T_0 the standard pressure and temperature, V_0 the molar volume of an ideal gas, N_A the Avogadro constant.

The volume mixing ratio is often expressed in ppmv (part per million volume) or in ppbv (part per billion volume):

$$C_{ppmv} = \frac{\rho}{\rho_0} 10^6 \quad C_{ppbv} = \frac{\rho}{\rho_0} 10^9 \tag{1.10}$$

1.1.1.2. Line broadening

The main broadening effects are the natural broadening, due to the lifetime of excited states, the Doppler broadening, due to the distribution of the molecular velocity, and the collision broadening, due to the uncertainty in the collisional lifetime. The natural and collision broadening are considered homogenous; they have the same effect on every molecule. In the infrared spectrum, the natural broadening is negligible in front of the collision broadening. The latter can be described with a Lorentzian line shape:

$$f_L(\sigma - \sigma_{ij}, P, T) = \frac{1}{\pi} \frac{\gamma_L(p,T)}{\gamma_L^2(p,T) + (\sigma - \sigma_{ij})^2} \tag{1.11}$$

The Lorentzian linewidth γ_L is the half width at half maximum and is calculated by considering the effects of every species s present in the gas sample:

$$\gamma_L(p,T) = \sum_s \gamma_{L,s}^0 \frac{p_s}{p_0} \left(\frac{T_{ref}}{T}\right)^{n_s} \tag{1.12}$$

with $\gamma_{L,s}^0$ the broadening due to the specie s at p_0 and T_0, p_s the partial pressure of the specie s and n_s a temperature-dependent coefficient.

The Doppler effect causes the frequency of a moving object to shift depending on the direction of the movement. Thermal excitation (Brownian motion) causes a random molecular motion, and therefore a random frequency shift. Oppositely to the natural and the collision broadening, the Doppler broadening is inhomogeneous and follows a Gaussian Line shape:

$$f_G(\sigma - \sigma_{ij}, P, T) = \frac{1}{\gamma_G(p,T)} \sqrt{\frac{\ln 2}{\pi}} \exp\left(-\ln 2 \left(\frac{\sigma - \sigma_{ij}}{\gamma_G(p,T)}\right)^2\right) \tag{1.13}$$

The linewidth of the Doppler broadening is given by:

$$\gamma_D = \frac{\sigma_{ij}}{c} \left(2 \ln 2 \frac{kT}{m}\right)^{\frac{1}{2}} \tag{1.14}$$

Where c is the speed of light, k the Boltzmann constant and m the mass of the target specie.

Collision broadening, is also called pressure broadening, as it increases with the pressure. At low pressure (p<10Torr), the broadening is attributed to the Doppler effect while at atmospheric pressure, collision broadening dominates. In between, the absorption line shape can be described by the convolution of the Lorentzian and Gaussian function called the Voigt function f_v:

$$f_V(\sigma - \sigma_{ij}, P, T) = f_L(\sigma - \sigma_{ij}, P, T) \otimes f_G(\sigma - \sigma_{ij}, P, T) \tag{1.15}$$

1.1.2. Measuring the concentration of a specie from the IR spectrum

Absorption spectroscopy can be employed mainly to two ends: composition and concentration measurement (gas sensors) of a target molecule. Composition measurement requires to record the absorption over a broad spectrum, if possible covering the whole mid-infrared region. The Fourier Transform InfraRed spectrometer (FTIR) (Figure 1.1(a)), which is an extensively employed instrument, for instance in analytical chemistry, makes use of a thermal emitter as a broadband optical infrared source [2]. It allows to observe a large IR (InfraRed) spectrum, with numerous absorption features, corresponding to various molecular resonances, which can be processed to determine the molecular composition of the sample. FTIR is a versatile tool for molecular identification, but the complex optical setup and the electronics makes it expensive and a table-top size instrument.

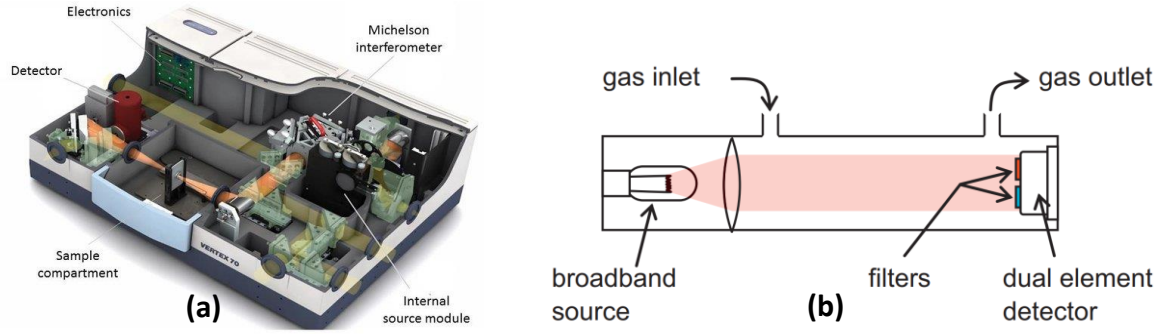

Figure 1.1: (a) Internal structure of a FTIR spectrometer [3]. (b) Schematic of a NDIR sensor, composed of a broadband source whose light is collimated to cross the gas cell and a detector with selective spectral filters [4].

At the extreme opposite, cheap portable sensors can also be built with broadband emitters: Non Dispersive InfraRed (NDIR) sensors (Figure 1.1(b)) [5]. The optical source is typically a thermal emitter [6] or a mid-infrared LED [7,8], which are small, affordable and have low power consumption. The optical setup can be as simple as a single parabolic reflector [4]. The selectivity is obtained by applying different color filters, to select different spectral ranges of the broadband spectrum. NDIR sensors yield good results if the absorbing molecules in the sample have largely separated absorption spectrum. In other cases, the selectivity of the sensor is very limited.

In order to circumvent the high cost and complex setup of a FTIR spectrometer and the poor selectivity of a NDIR sensor, the broadband emitter can be conveniently replaced by a narrowband laser. The narrow spectrum of a laser, which is around a few MHz [9], allows to specifically target a molecular line, whose linewidth is in the range of GHz at atmospheric pressure, hence obtaining a very good selectivity without the need for spectral filtering. The other advantage of the narrow emission compared to a broadband emission, is that the whole optical power contributes to the absorption. This efficient optical-to-molecular-excitation energy conversion gives laser based gas sensors their low limit of detection.

Semiconductor lasers are widespread, notably in the telecommunication industry in the near-IR. Going toward longer wavelengths (λ>2μm) requires to use different families of semiconductor materials and different laser structures, that are still a hot topic of research. Gas

sensing applications is one of the main motivations for the development of efficient, low consumption and compact mid-IR lasers.

1.1.3. Mid-InfraRed semiconductor lasers

In the mid-IR (2-20μm), three semiconductor materials families with direct bandgaps are available [10] (HgCdTe II-VI, Lead-salt IV-VI and Antimonides III-V[8]) and can be used for making mid-IR lasers based on quantum wells. The first family is well known for making mid-IR photodetectors but exhibits poor performances for lasers. The second family was used for fabricating the first mid-IR laser diodes. However, they suffered from thermal issues and could only be operated in pulsed regime at room temperature [11]. With the third family, the Antimonides III-V compounds, lasers have shown good performances. They can be operated in continuous wave regime at room temperature and emit from 2 μm to 3.3 μm [12]. In order to go further in wavelength, other types of laser structures can be used such as Quantum Cascade Lasers (QCL) and Interband Cascade Lasers (ICL).

The quantum cascade laser structure is fundamentally different from the quantum wells. In a quantum well laser, interband transitions are exploited, that is transitions between the conduction band and the valence band. In a QCL, the photon emission is based on intersubband transitions, i.e. transitions between discrete energy levels within the conduction band. Since the electron stays on the conduction band after the energy transition, it can subsequently undergo another intersubband transition. Multiple periods, i.e. stacks of materials which enables intersubband transitions, can be added in series, or 'cascaded', in order to increase the emitted optical power. By playing on the thickness of the quantum wells, the sub bands can be adjusted to reach a given laser emission wavelength. Compared to conventional quantum well lasers, the emitted wavelength of cascade lasers does not depend on the material bandgap. Usual semiconductor materials, such as the InP family normally used for making near-IR laser, can be employed to fabricate QCLs emitting in the mid-IR above 5 μm [13]. The Antimonides III-V materials have also been successfully utilized for making QCLs and ICLs [12].

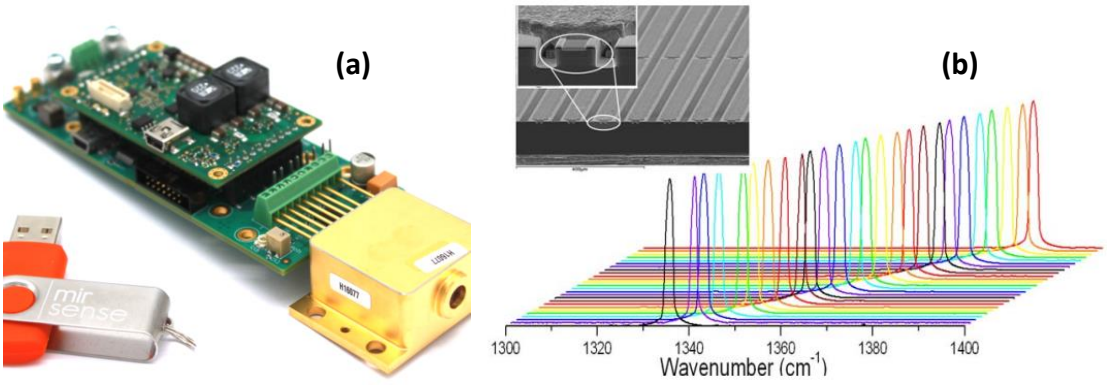

Figure 1.2: (a) A mirSense QCL product in a HHL package, and its dedicated OEM electronics [14]. (b) Spectra of an array of 30 lasers. Inset: Micrograph of the QCL array [15].

QCLs operate at high current, which generates an important amount of heat. Heat dissipation is therefore a critical technical issue in QCLs, which can be tackled by minimizing

[8] Antimonides III-V materials are made of atoms from the column III of the periodic table (e.g. Al, Ga, In) and from the column V, the Antimony (Sb) and possibly the Arsenic (As).

the thermal resistance between the laser and the cooling element. A typical package used for heat dissipation is called High Heat Load (HHL) (Figure 1.2(a)).

QCLs and ICLs cover the whole mid-IR spectral range from below 3µm up to close to the THz. Therefore, they are complementary to the quantum well laser diodes which perform efficiently until 2.7 µm. A major challenge is to combine the different laser sources on the same chip. The building blocks of photonics circuits, such as optical modulators [16], multiplexors, waveguides [15] and photodetectors [17] have already been realized on silicon substrates. One major effort remains in the integration of the laser sources made of the III-V materials on silicon. This opens the way to a multi-wavelength laser platform where QCLs, ICLs and laser diodes can cover both near and mid IR and therefore target multiple gases. One example of such multi-wavelength laser sources are the QCL arrays (Figure 1.2(b)) where each QCL has its own wavelength tuning range, allowing the QCL array to cover up to tens of cm^{-1}.

Other types of coherent sources based on semiconductor lasers have also attracted some interest for spectroscopic purposes: Optical Parametric Oscillator, External-Cavity (EC) QCL [18], optical comb frequency [19], supercontinuum [20]. However, they might not be as mature as single-frequency lasers chips for the realization of compact gas sensors.

With the development of Quantum Cascade Lasers, lasers sources are now available in the mid-IR (2-20µm) where strong molecular absorption occurs. Moreover, they offer high power and single frequency emission, making them good candidates for the realization of a selective, sensitive and compact gas sensor.

1.1.4. Wavelength Modulation Spectroscopy

1.1.4.1. The motivation for laser modulation

When measuring traces of gas with a short optical path length (<1m), the absorbance is small, and consequently the transmittance is large. It means that the photodetector signal has a large level offset; which complicates the analog-to-digital conversion. Another limitation comes from the noise at low frequency. Indeed, it is well-known that the noise spectral density behaves as a 1/f law at low frequency. It is true both for the laser (Figure 1.3(a)) and the photodetector electronics (Figure 1.3 (b)).

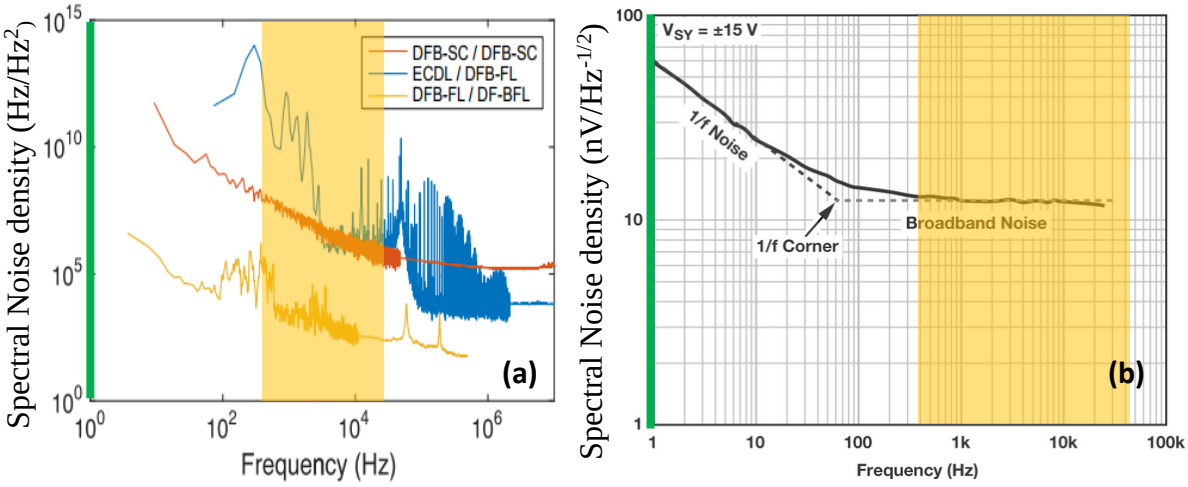

Figure 1.3: Typical noise spectral density for semiconductor lasers [9] (a) and for an operational amplifier (ADA4622-2) [21] (b). The noise domains for a direct absorption and for a modulated

absorption are represented by the green line and the yellow area, resp. The lasers are of different technology: a diode laser (DFB-SC, 894nm), a fiber laser (DFB-FL, 1553nm) and an external cavity diode laser (ECDL, 1530nm).

Direct absorption spectroscopy signal operates in continuous regime, meaning the frequency is 0 Hz (green line). In order to avoid the low frequency noise, a modulation can be applied to the laser in order to work in the kHz range (yellow rectangle). The modulated signal measured by the photodiode is then demodulated in order to obtain the amplitude of the signal. The signal carrier is translated in frequency where the noise density is lower, thus increasing of the SNR of the whole setup. When using a broadband light source, the modulation technique is often applied using a mechanical chopper. However, the chopper has limited frequency, can be a source of noise and has a heavy footprint. In semiconductor lasers, the emitted wavelength can be tuned with the injection current: this is the heart of Tunable Diode Laser Spectroscopy (TDLAS). The current modulation is achieved with simple electronics, can be tailored precisely and significantly reduces the sensor's noise.

Frequency modulation techniques can be separated in two different methods: Frequency Modulation Spectroscopy (FMS) and Wavelength Modulation Spectroscopy (WMS). They differ by the frequency value of the modulation. Indeed, the frequency modulated laser beam will interact with the gas absorption line, whose linewidth is typically in the range of GHz at atmospheric pressure. In FMS, the modulation frequency has the same order of magnitude as the absorption linewidth ($f_m > \Delta\nu_{line}$) whereas in WMS, the modulation frequency (few kHz to MHz) is much smaller than the absorption linewidth ($f_m << \Delta\nu_{line}$). As we will be working at tens of kHz with photoacoustics, we focus on the description of WMS. **It is important to note that even in the frame of WMS, the term frequency modulation (FM) is employed** to describe the effect of the modulation onto the laser instantaneous wavelength.

1.1.4.2. The typical WMS setup

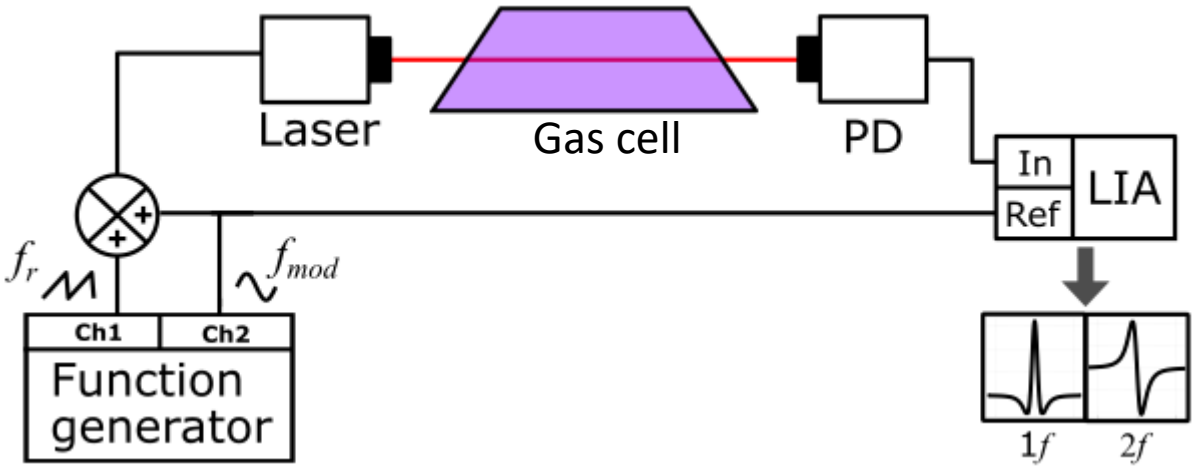

Figure 1.4: Schematic of a typical WMS setup, including a laser, a gas cell and a photodetector (PD). The laser current is modulated with a slow ramp of frequency f_r and a fast sine wave of frequency f_{mod}. The signal photodetector is amplified and demodulated by the lock-in amplifier (LIA), giving the typical 1f or 2f signal.

A typical WMS setup is represented on Figure 1.4. The laser beam propagates through the gas cell and is partially absorbed. The transmitted optical power is measured through a photodiode (PD). So far the system is similar to the one of direct absorption spectroscopy. Then, the modulation is added. In semiconductor lasers, the emission wavelength is proportional to the injection current. This property is mostly due to thermal effects and is called the tunability (expressed in GHz/mA, nm/mA or cm^{-1}/mA). Tunability gives the opportunity to drive the optical modulation electrically. A function generator provides a sawtooth and a sinewave signal which serve different purposes. The sawtooth is used to scan across the absorption features. It has a slow frequency f_{ramp} (typ. 0.1-10Hz) and a large amplitude to cover one or more absorption lines (typ. 5-100mA). The sinewave is used for the modulation/demodulation at a frequency f_{mod} ranging from kHz to MHz. This high-frequency component is what distinguishes WMS from direct absorption spectroscopy and transforms the absorption profile into a FM modulated signal. The transmitted signal measured by the photodiode is composed of the harmonics of the modulation frequency. The demodulation, realized by a lock-in amplifier (LIA), allows to select one of the *n-th* harmonics ($n \times f_{mod}$). In WMS, the detection is often realized with the second harmonic (the 2*f* mode) and sometimes the first harmonic (the 1*f* mode). The 1*f* signal has a higher amplitude than the 2 *f* signal, but the latter is often preferred because it is offset free and exhibits lower noise levels. The 3rd harmonics is frequently used for locking the laser wavelength and avoid its spectral drift [22]. Higher harmonics are rarely employed because of their lower amplitude. Harmonics have different shapes that can be theoretically described. The maximum of each harmonics is reached for different conditions of current, modulation amplitude and LIA detection phase.

1.1.5. Theoretical description of the WMS signal

Some analytical models were proposed in FMS based on the description of the electric field of the laser. The modulated electric field gives rise to multiple spectral components that interact with the absorption lines. For low modulation frequencies, the number of spectral components increases considerably, therefore the model is complex and inappropriate. In WMS, we prefer to focus on the description of the laser intensity rather than the electric field. Also, only the absorption is considered, because the dispersion is about 5 orders of magnitude smaller [23].

First, we describe the WM signal in the case of a pure frequency modulation, i.e. only considering the effect of the modulation onto the laser emission wavelength. A solution is obtained for small signal, offering a simple derivative expression. Then, the second model describes the complex expression for higher modulation amplitude. Eventually, the intensity modulation, i.e. the effect of the modulation onto the laser power is added to the FM contribution, giving the solution that best fit to the WMS experimental conditions using tunable lasers.

1.1.5.1. Small signals pure frequency modulation

The description of the frequency modulated signal was pioneered by Arndt [24]. Arndt's model considers the effect of the modulation onto the laser wavelength:

$$\nu(t) = \nu_0 - \Delta\nu \cos(\omega_m t) \tag{1.16}$$

with ν(t) the instantaneous frequency, ν_0 the carrier frequency, Δν the maximum deviation and $\omega_m=2\pi f_m$ the angular modulation frequency. As defined in signal processing, the frequency modulation index β is the ratio of the maximum deviation to the modulation frequency:

$$\beta = \frac{\Delta\nu}{f_m} \tag{1.17}$$

β describes the relative frequency variations of the signal around the carrier frequency, i.e. how widespread is the FM spectra around its central frequency f_m. The higher the β, the more spectral components are needed to properly represent the FM modulated signal [23]. Here, the optimum value of β depends on the gas absorption linewidth. The larger is the absorption linewidth, the larger the modulation amplitude required to efficiently modulate the absorption. Arndt suggest a convenient normalization, by re-writing (1.16) as the normalized instantaneous frequency x(t):

$$x(t) = \ x_0 - m\cos(\omega_m t) \tag{1.18}$$

with $x(t) = (\nu(t) - \nu_{line})/\Delta\nu_{line}$.
The modulation index β is replaced by a normalized modulation index $m = \Delta\nu/\Delta\nu_{line}$.
As shown on Figure 1.5, the WM signal depends both on the modulation frequency f_m and the frequency modulation index β. The diagonal corresponds to the modulation index m, that can be expressed as the product of the two axis of Figure 1.5:

$$m = \beta x_m \ with \ x_m = \frac{f_m}{\Delta\nu_{line}} \tag{1.19}$$

It can be noticed that the signal shape is constant diagonally, that is constant with m. Therefore, the optimization of the WM signal is based on the value of the modulation index m instead of the modulation index β or the modulation frequency f_m.

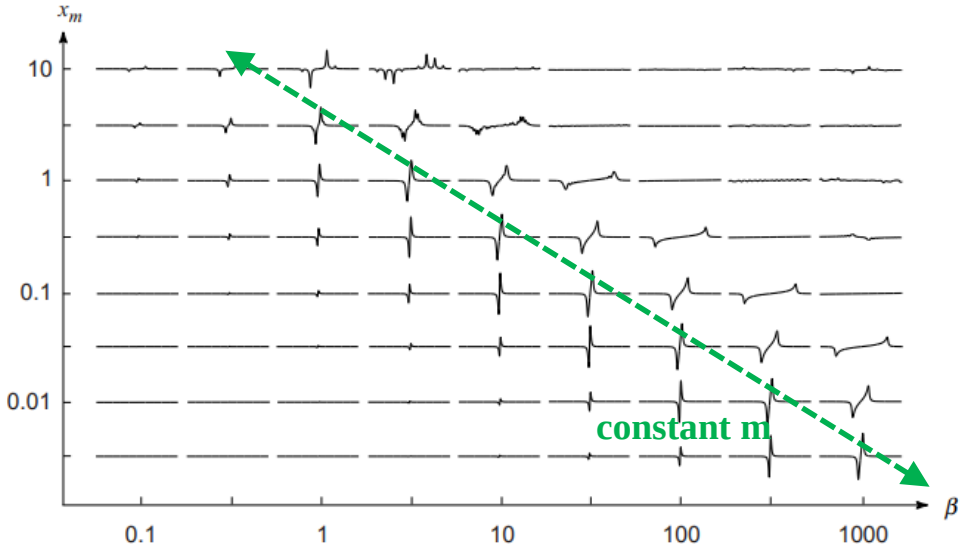

Figure 1.5: Effect of the modulation index β and the normalized modulation frequency x_m onto the WM signal. The dotted line corresponds to a constant value of the modulation index m. [23]

The WM signal corresponds to the intensity transmitted after the sample given by equation (1.3), and after the normalization gives:

$$s(x) = I_t(x) = I_0(1 - \alpha(x)L) \tag{1.20}$$

Inserting (1.18) into (1.20) :

$$s(x) = I_0(1 - \alpha(x_0 - m\cos(\omega_m t))L) \tag{1.21}$$

The signal can be developed as a sum of the harmonics using Taylor's series [23]:

$$s(x) = I_0 + \sum_{i=1}^{\infty} s_n(x)\cos(n\omega_m t) \tag{1.22}$$

with s_n corresponding to the shape of the WM signal at the *n-th* harmonics. The first three harmonics are expressed as:

$$s_1(x) = -I_0 L \frac{d\alpha}{dx}\Big|_{x_0} (-m) \quad s_2(x) = -I_0 L \frac{d^2\alpha}{dx^2}\Big|_{x_0} \frac{m^2}{4} \quad s_3(x) = -I_0 L \frac{d^3\alpha}{dx^3}\Big|_{x_0} \frac{-m^3}{4} \tag{1.23}$$

The harmonics are proportional to the *n-th* derivative of the absorption line and can very easily be simulated (Figure 1.6).

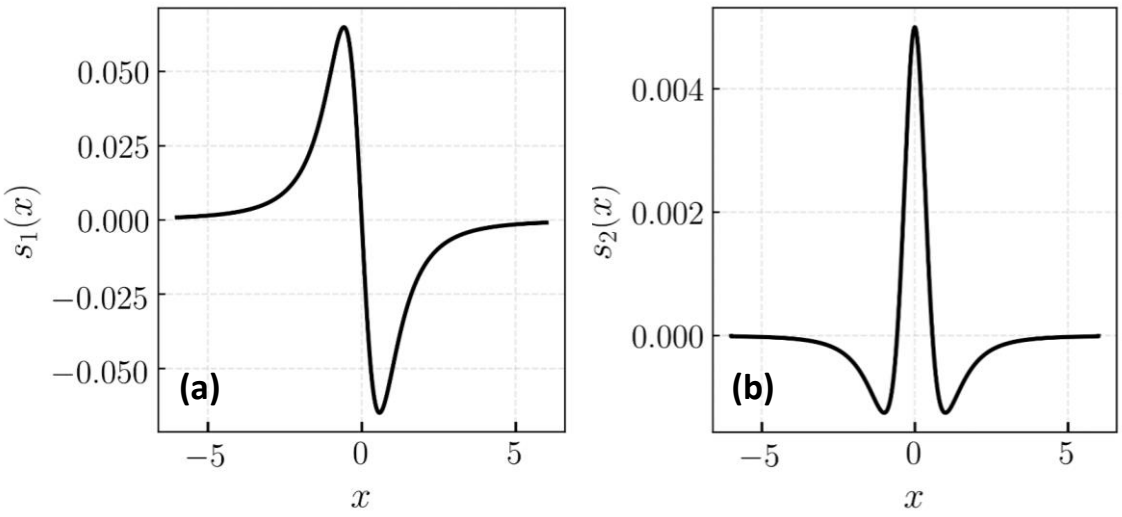

Figure 1.6: WM signal for the 1st and 2nd harmonics, proportional to the 1st and 2nd derivative of a normalized Lorentzian profile ($\alpha = 1/(1 + x^2)$), respectively. The modulation index m is chosen equal to 0.1 ($m \ll 1$).

Nonetheless, these expressions (1.23) are valid under the assumption of small modulation index ($m \ll 1$). In spectroscopy, higher modulation indexes are often employed because the WM signal is greater. For higher values of m, the expression becomes more complex. There are distortions of the signal, i.e. the WM signal at the *n-th* harmonic will include some contribution from other harmonics.

1.1.5.2. Generalized expression for pure FM

The general expression of the WM signal can be obtained by following Arndt's procedure [24]. As before, the signal equals to the intensity transmitted after the sample:

$$s(x) = I_0(1 - \alpha(x_0 - m\cos(\omega_m t))L) \tag{1.24}$$

Instead of expressing the signal directly in terms of Taylor's series, the Fourier transform of s(x) is taken, expressed as a series of harmonics and finally the inverse Fourier transform is applied. The calculations are not straightforward and are detailed in Schilt's thesis [23]. The major assumption is to consider the absorption as a pure Lorentzian function. For optical gas sensors operating at standard conditions of temperature and pressure, this assumption is fulfilled. The Lorentzian function can be written as in equation (1.11) for the normalized frequency :

$$f_L(x,P,T) = \frac{1}{\pi\gamma_L(p,T)}\frac{1}{1+x^2} \tag{1.25}$$

The solution for the first harmonics are obtained as:

$$s_0(x) = I_0\left[1 - a_0\frac{\sqrt{2}}{2}\frac{\sqrt{r+X}}{r}\right]$$

$$s_1(x) = I_0 a_0\left[-\text{sign}(x)\ \frac{\sqrt{2}}{m}\cdot\frac{|x|\sqrt{r+X}-\sqrt{r-X}}{r}\right] \tag{1.26}$$

$$s_2(x) = I_0 a_0\left[-\frac{4}{m^2}+\frac{\sqrt{2}}{m^2}\cdot\frac{(r+1-x^2)\sqrt{r+X}+2|x|\sqrt{r-X}}{r}\right]$$

$$\text{with } X = 1-x^2+m^2 \text{ and } r = \sqrt{X^2+4x^2} \tag{1.27}$$

They are represented on Figure 1.7, and compared with the derivative expressions from the previous section.

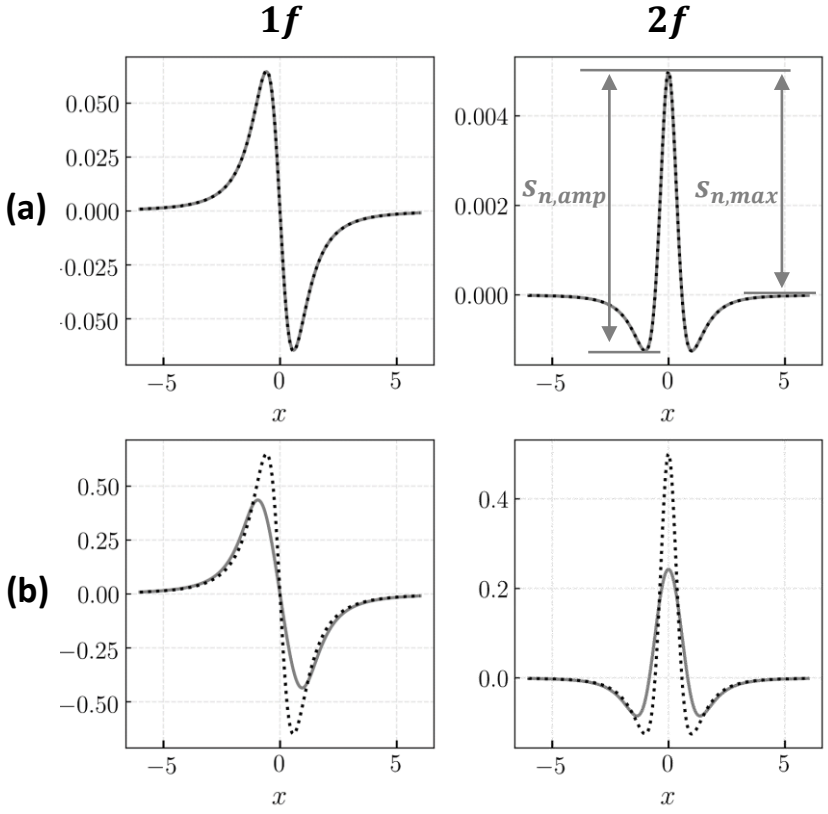

Figure 1.7: The WM signal (grey) is compared to the derivative expression (dashed line black), for the 1st (1*f*) and 2nd (2*f*) harmonics , and for m=0.1 (a) and m=1 (b). The absorption is a normalized Lorentzian (equation (1.25) with $\gamma_L = 1/\pi$).

The odd (resp even) harmonics show an anti-symmetry (resp mirror symmetry) with respect to the origin (resp linecenter). For low modulation amplitudes they correspond well to the derivative expression, while they differ for higher modulation amplitudes. Indeed, the WM signal becomes distorted, broader than the derivative and with a reduced amplitude. For the optimization of the modulation amplitude, the amplitude $s_{n,amp}$ and maximum $s_{n,max}$ of each harmonic n are represented as a function of m (Figure 1.8). Generally, the amplitude is measured for odd harmonics while it is the maximum is taken for even harmonics (see justification in 1.1.5.4).

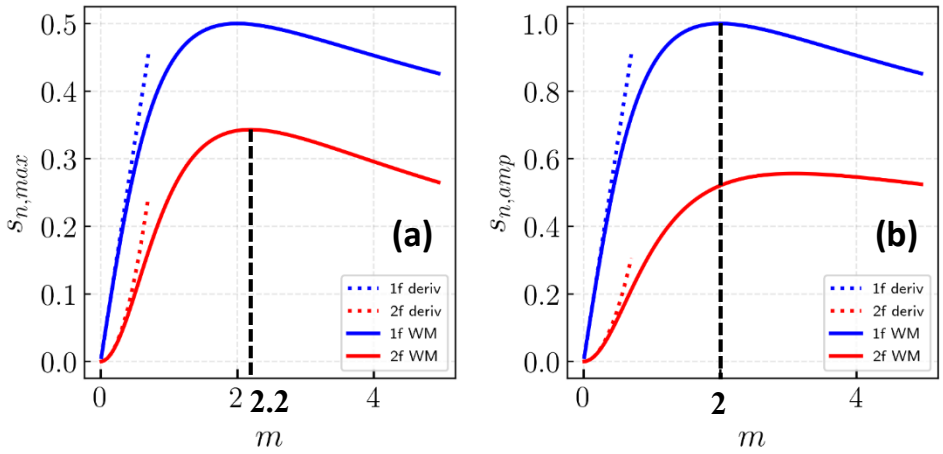

Figure 1.8: Maximum $s_{n,max}$ (a) and amplitude $s_{n,amp}$ (b) of the WM signal as a function of m, for the two first harmonics. The continuous and dotted lines correspond to the generalized and derivative expression, resp.

It can be seen again that the WM signals (plain lines) match with their derivative counterparts (dotted lines) only for small modulation amplitudes. The WM signal amplitude (resp maximum) increases with the modulation until the modulation amplitude becomes large compared to the linewidth and the signal starts decreasing. The optimum value of the modulation index are 2.0 in $1f$ (for $s_{n,amp}$) and 2.2 in $2f$ (for $s_{n,max}$). These values are well known in the spectroscopy community and are in very good agreement with experimental observations. However, at high modulation amplitudes, the shape of WM signal is not fully described by the FM modulation: the modulation of the laser power has to be considered.

1.1.5.3. Combined intensity and frequency modulation (IM-FM)

The optical power, or light intensity, varies with the injected current, which, upon modulation of the current, leads to an intensity modulation (IM). The IM contribution cannot be neglected in comparison to the FM contribution for high modulation amplitudes. The IM-FM model was brought by Schilt to describe accurately the transmitted signal [25]. It explains the signal distortion compared to the theory of pure FM.
First, a linear variation of the optical intensity is considered:

$$I_0(x) = I_0(p\Delta\nu_{line}x + 1) \tag{1.28}$$

with I_0 the intensity at linecenter and p [1/cm^{-1}] a coefficient related to the variation of the optical power.
Inserting (1.28) in (1.20), the WMS signal can be written as :

$$s_{IM-FM}(x) = I_0(p\Delta\nu_{line}x + 1)(1 - \alpha(x)L) \tag{1.29}$$

Then the FM modulation is applied using (1.29) and (1.18):

$$\begin{aligned} s_{IM-FM}(x) = I_0[p_\Omega \Delta\nu_{line}x_0 - p_\omega \Delta\nu_{line} m\cos(\omega_m t) + 1] \\ \times [1 - \alpha(x_0 - m\cos(\omega_m t + \Psi))L] \end{aligned} \tag{1.30}$$

The IM and FM arise from different physical effects and have no reason to be in phase, thus the IM-FM phase shift Ψ is added. Also, the FM modulation depends on the modulation frequency: the tuning rate ($\Delta\nu/\Delta I$ or $\Delta\sigma/\Delta I$) decreases with the frequency. Thus, the effect of the FM modulation is greater for the slow ramp at frequency Ω than for the sinewave modulation at frequency ω (modulation scheme on Figure 1.4) It is accounted by replacing p by two frequency-dependent parameters p_Ω and p_ω. The calculation of the IM-WM signals can be found in [25]. Compared to pure FM, in IM-FM the solution is composed with two terms s_{np} and s_{nq} in quadrature:

$$s_{IM-FM}(x) = \sum_{i=1}^{\infty} s_{np}(x)\cos(n\omega_m t) - \sum_{i=1}^{\infty} s_{nq}(x)\sin(n\omega_m t) \tag{1.31}$$

with s_{np} and s_{nq} for the two first harmonics :

$$\begin{aligned} s_{1p}(x) &= I_\Omega(x)\cos(\Psi)\, s_1(x) - p_\omega \Delta\nu_{\text{line}} \frac{m}{2}[2s_0(x) + \cos(2\Psi)\, s_2(x)] \\ s_{1q}(x) &= I_\Omega(x)\sin(\Psi)\, s_1(x) - p_\omega \Delta\nu_{\text{line}} \frac{m}{2}[\quad\quad \sin(2\Psi)\, s_2(x)] \\ s_{2p}(x) &= I_\Omega(x)\cos(2\Psi)\, s_2(x) - p_\omega \Delta\nu_{\text{line}} \frac{m}{2}[\cos(\Psi)\, s_1(x) + \cos(3\Psi)\, s_3(x)] \\ s_{2q}(x) &= I_\Omega(x)\sin(2\Psi)\, s_2(x) - p_\omega \Delta\nu_{\text{line}} \frac{m}{2}[\sin(\Psi)\, s_1(x) + \sin(3\Psi)\, s_3(x)] \end{aligned} \tag{1.32}$$

The signal at the *n-th* harmonics is constituted by the FM signal at the *n-th* harmonic (green), plus the harmonics (orange) of rank (n-1) and (n+1). Since those neighboring harmonics have different symmetries, mirror symmetry for odd harmonics and anti-symmetry for even harmonics, the IM-FM signal becomes asymmetric (except for rare sets of the (p_Ω, p_ω, Ψ) parameters). In particular, for the 1*f* signal, the harmonic of rank 0 results in an offset of the signal.

The selection of a given harmonic is realized using a lock-in amplifier. The LIA in-phase output signal can be expressed as:

$$s_{n,\Phi}(x) = s_{np}(x)\cos(\Phi_n) + s_{nq}(x)\sin(\Phi_n) \tag{1.33}$$

with Φ_n the LIA detection phase.

When the contribution of the intensity modulation is added to the frequency modulation, the WM signal is described with a set of new parameters: the IM-FM phase shift Ψ, the power variation factors p_Ω, and p_ω, and the detection phase Φ. The parameters p_Ω, p_ω and Ψ are intrinsically related to the laser and they can be characterized. The detection phase can be used to maximize the WM signal.

1.1.5.4. Influence of the IM-FM parameters

The complete study of the influence of Ψ, p_Ω, p_ω and Φ_n onto the WM signal can be found in Schilt [23]. We briefly illustrate them as it helps to understand the shape of the signal and how to prevent signal distortion.

In order to obtain high sensitivity, the WM signal can be maximized by taking the phase detection as:

$$\Phi_{n,max} = n\Psi + k\pi \quad , \; k \in \mathbb{Z} \tag{1.34}$$

The influence of the p_Ω, p_ω and Ψ on the $2f$ signal is represented on Figure 1.9. They all contribute to the asymmetry of the WM signal. The two negative wings are the most affected whereas the peak center does not vary greatly. Schilt generalized this observation and showed that, for the even (resp odd) harmonics the maximum (resp the amplitude) of the signal is practically constant for any set of parameters (Ψ, p_Ω, p_ω), whereas the amplitude (resp the maximum) is strongly affected by the intensity modulation.

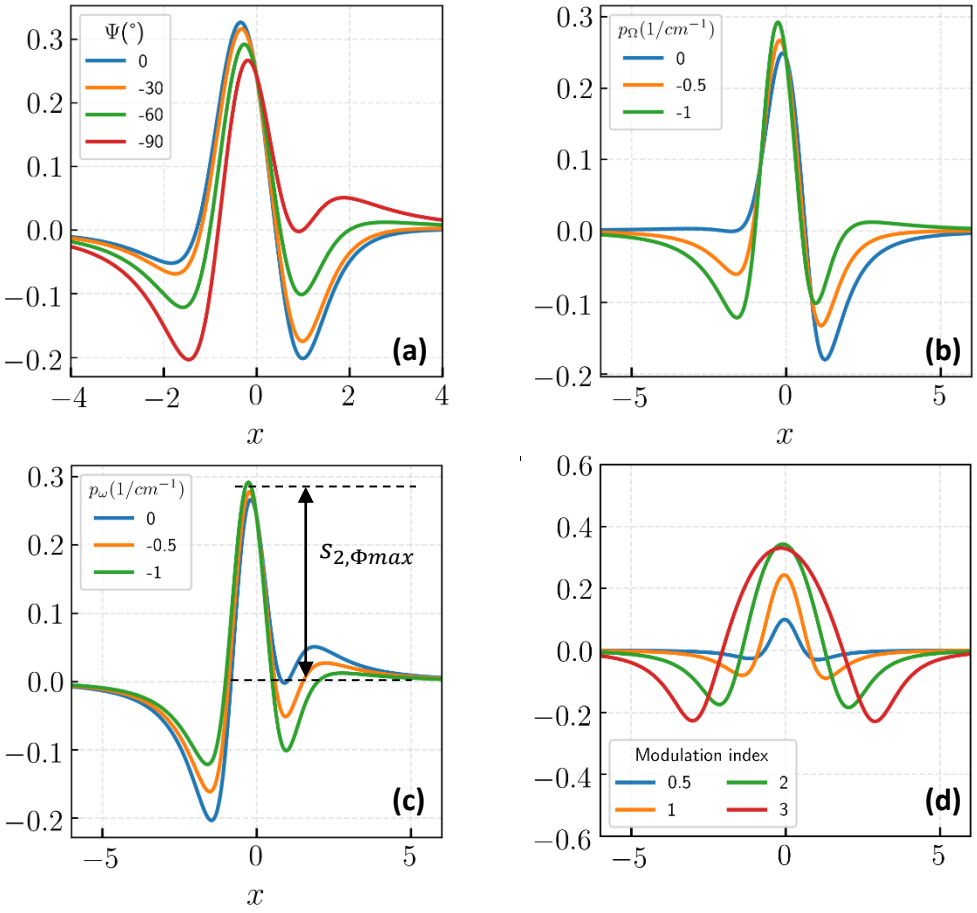

Figure 1.9: Effect of the parameter Ψ ($p_\Omega = p_\omega = -1$cm, m=1), p_Ω ($\Psi = -60°$, $p_\omega = -1$cm, m=1) and p_ω ($\Psi = -60°$, $p_\Omega = -1$cm, m=1) and m ($\Psi = 0$, $p_\Omega = p_\omega = 0$cm, m=1) onto the $2f$ signal . The detection phase Φ_n is set equal to 2Ψ in order to maximize the signal.

1.1.5.5. Measurement of the parameter p

The WM signal was accurately described using the IM-FM model. It can be employed for the characterization of the modulation parameter p (or equivalently the current tuning rate $\Delta\sigma/\Delta$i) as a function of the modulation frequency.

First, the detection phase is set as to obtain the maximum of the WM signal, as given by equation (1.34). For instance for the 2*f* mode it means $\Phi_{2,max} = 2\Psi$. As we saw, the center of the peak is practically unaffected by the effect of the IM. The laser frequency is set to match with the linecenter ($x = 0$). Schilt showed that the difference between the maximum of the 2*f* signal and the value at linecenter leads to a relative error of less than 2%. Under these conditions, the maximum of the 2*f* signal does not depend on the IM modulation but only on the FM modulation. It can be described using (1.32):

$$s_{2,max} = I_0 a_0 \left[-\frac{4}{m^2} + \frac{2}{m^2} \frac{m^2+2}{\sqrt{m^2+1}} \right] \tag{1.35}$$

Experimentally, $s_{2,max}$ can be measured as a function of the current modulation amplitude Δi, which is proportional to m:

$$m = K\Delta i \tag{1.36}$$

with K [mA^{-1}] a linear coefficient that can be obtain by fitting the experimental data with equation (1.35). Using the linewidth of the target absorption line, the current tuning rate can be obtained as:

$$\frac{\Delta\sigma}{\Delta i} = \frac{1}{c} K \Delta\nu_{\text{line}} \tag{1.37}$$

as well as the modulation parameter p, by using (1.28) and (1.37):

$$p = \frac{1}{K I_0 \Delta\nu_{\text{line}}} \frac{\Delta \text{I}}{\Delta \text{i}} \tag{1.38}$$

The knowledge of the parameter p can be employed for refining the simulation of the WMS signal, for instance with a different harmonic or with a different modulation amplitude.

The theoretical model that was presented considers the effect of the wavelength modulation onto a simple absorption spectrum composed of a single feature, typically a lorentzian function. Although some species exhibit isolated absorption lines, many others present a composite spectrum with many overlapping bands, that can hardly be separated spectrally even at low pressure. The extraction of the parameter p would require to take into account the contributions from multiples absorption lines that would make the fitting procedure more complex.

1.1.5.6. Summary of the important results

The modulation index m describes the amplitude of the FM modulation with respect to the gas absorption linewidth. For small signals (m<<1), the WM signal is proportional to the derivatives of the absorption. For higher values, the signal is a combination of the derivative harmonics, leading to a distortion of the WM signal. The optimum values for each harmonic can be obtained. Finally, the laser intensity modulation is combined with the FM modulation by introducing a set of new parameters (Ψ, p_Ω, p_ω, Φ_n) The IM contribution results in an asymmetry of the signal. Nonetheless, optimal conditions of detection, depending on the parity

of the harmonics, can be selected to limit the effect of the IM. For species exhibiting a composite spectrum, a theoretical model describing the effect of the modulation would be a useful tool for the optimization of the modulation scheme. The topic is discussed in Chapter 2.

1.1.6. From WMS to PAS

The performances can be improved by using WMS due to the significant reduction of noise. Further improvements can be done in increasing the absorption by achieving longer optical path length. Long optical paths have been obtained by two different techniques: using multipass cells or optical resonant cavities. They are both based on multiple mirror reflections. The multipass cells consists in making multiple passes in a small volume without overlapping the passes. Common designs are the Heriott [26] and the White cells [27]. Extensive work has been done to obtain compact multipass cells [28,29] while limiting interferences fringes (worst enemy of multipass cells). In Cavity Ring Down Spectroscopy (CRDS) and Cavity Enhanced Absorption Spectroscopy (CEAS), an optical cavity allows to obtain equivalent path length of up to kms [5,30,31]. The design of the cavity, its alignment and its electronic stabilization makes the setup seriously more complicated than WMS. Various designs were presented to make alignment less critical with ICOS (Integrating Cavity Output Spectroscopy) and to obtain a low noise cavity with NICE-OHMS (Noise-Immune Cavity-Enhanced Optical Heterodyne Molecular Spectroscopy) [32]. Multipass cells and cavities allow great improvements but these techniques remain expensive, hard to downscale and difficult to align. A nice alternative is based on the photoacoustic effect, which directly detects the absorption and does not require a long optical path.

1.2. Photoacoustic spectroscopy

Photoacoustic spectroscopy (PAS) was discovered in 1880 by Alexander Graham Bell [33]. As indicated by its name PAS is the conversion of optical energy to acoustic energy through molecular absorption. The generated acoustic signal is weak and could hardly be exploited at that time without the modern equipment such as powerful light sources and sensitive microphones that did not exist. The development of PAS re started in 1938 with Viegerov for the study of a gas composition [34]. Few years later, PAS measurements at the ppm level were realized using a broadband light source and a microphone. But the real boom of photoacoustic came in the 1960s with the advent of laser sources [35]. Various designs were proposed, with different shapes of acoustic resonators. Detection limits in the ppb range were achieved, notably with CO_2 lasers [36]. More recently, new designs, such as the differential Helmholtz resonator, allowed better signal enhancement and the miniaturization of the photoacoustic cell [37–39]. Further development, the integration of a QCL and a PA cell on a silicon platform was realized [15]. PAS is therefore a prominent candidate for making sensitive and miniature optical gas sensors.

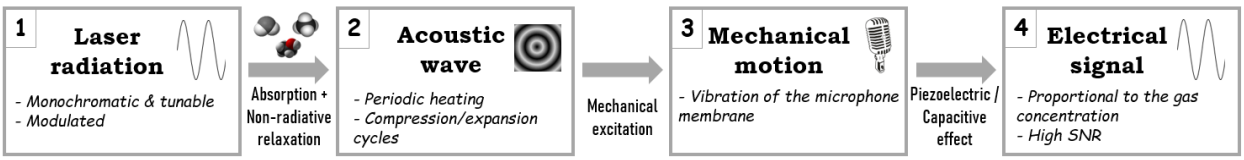

Figure 1.10: Block representation of the principle of photoacoustic spectroscopy

The principle of PAS is represented on Figure 1.10. First, photons emitted at a given wavelength by a single-mode laser are selectively absorbed by a molecule. The molecule is thus excited to a higher energy level (electronic, vibrational, rotational). Then, the excited molecules return to a lower energy level, through a process called relaxation. There exist 3 main relaxation pathways: spontaneous/stimulated emission / chemical reaction / collisional relaxation. In spontaneous /stimulated emissions, the energy of the excitation is converted back to optical energy by a photon emission while in a chemical reaction the energy is spent in the change of the chemical potential. The collisional pathway is a non-radiative relaxation and is responsible for the photoacoustic (PA) effect. The energy from the molecular excitation (mostly vibrational in the infrared region) is converted into kinetic energy (a translation), hence the name Vibrational-Translational (V-T) relaxation. The VT-relaxation causes an increase of temperature, and consequently an increase of pressure. A sensor measuring the absolute variation of temperature (or pressure) would require an extremely well controlled gas temperature or pressure, which is practically difficult and would lead to poor sensor accuracy. Instead, the light source is modulated, creating a periodic heating and thus giving rise to an acoustic wave. This acoustic wave is then amplified using an acoustic resonator and recorded using a microphone.

PAS has proven to be competitive with state of the art spectroscopic techniques such as WMS, direct absorption spectroscopy with multipass cells, CRDS, CEAS. A number of advantages can be listed, distinguishing PAS from other optical methods:

- Achromaticity: as the optical energy is converted to acoustic energy, the PA cell does not depend on the wavelength of the light source. This feature is unique in optical based gas sensing, and makes PAS a versatile method for multi gas and multi wavelength detection.
- Background free: WMS relies on a differential measurement of the transmitted energy to the incoming energy from the light source. The transmitted energy is maximum when there is no absorption. Oppositely, PAS shows no signal when the gas is not absorbing, thus no background has to be taken into account.
- Compact size: The volume of a PA cell can range from hundreds of cm^3 down to less than one cm^3.
- Low cost: microphones are very cheap compared to photodetectors (in particular IR photodetectors).

PAS can be considered both a direct and an indirect detection technique. Direct because it is directly proportional to the gas concentration, or background free. Indirect because it requires an additional step compared to WMS, that is the molecular relaxation. This latter step introduces various noises that can be detrimental to PAS sensitivity:

- window noise: the energy absorbed by the cell window results in a temperature change of the window and thus the surrounding air. It is particularly true in the mid-IR due to a lack of perfectly transparent materials in this spectral range.
- wall noise: similar to the window absorption, photons impinging the side walls of the acoustic cell can result in a background signal.
- flow noise: broadband sound emission can occur during the propagation of the gas in pipes, specifically at high flow velocities. The environmental noise can also be carried by the pipes.
- microphone noise: it is generally the limit of the system when all other noise sources have become negligible.

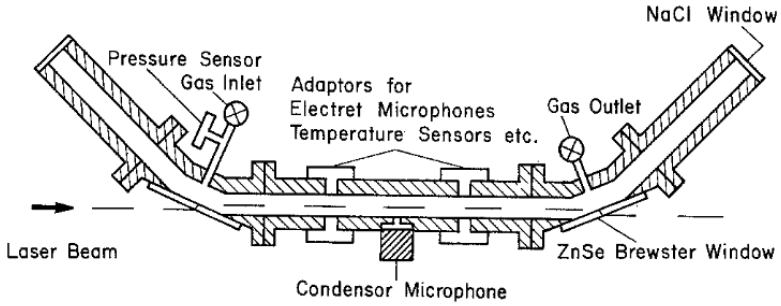

Figure 1.11: Schematic of an optimized PA cell proposed by Sigrist et al [40].

All these issues were thoroughly studied more than 20 years ago, for instance by Harren et al [41] and Sigrist et al [40]. Notably, the noise in the PA cell was reduced by tilting the windows at the Brewster angle, adding buffer volume near the window for acoustic isolation, using polished wall surfaces to prevent wall noise, placing acoustic notch filter at the gas inlets, etc (Figure 1.11). Although technical solutions were brought, similar issues pop up for every new PA designs and so are still up-to-date concerns.

The PA signal is equal to the molecular absorption coefficient α, the optical power P_L and the cell constant C:

$$S = \alpha P_L C \tag{1.39}$$

The strength of the absorption can vary over several orders of magnitude, as well as the optical power. The cell constant is a figure of merit, expressed in $Pa/(W \cdot cm^{-1})$, and describes the sensitivity of the PA cell. It is employed to compare the performances of different acoustic cells independently from the amplitude of the acoustic wave. An important part of the cell design is the choice of the acoustic resonator.

1.2.1. Acoustic resonators

Acoustic waves generated by the absorption of the modulated light are of small amplitude. Acoustic resonators are therefore employed for acoustic amplification. As optical cavity made of mirrors, acoustic cavity can be built to confine the energy of the wave spatially. The cavity has geometrical symmetries to favor the constructive buildup of the standing waves. Typical acoustic resonators are: cylindrical resonators, cavity resonators and Helmholtz resonator [42]. Cylindrical cavities are probably the most used resonators in PAS as they offer a simple and efficient design [43]. If the cavity length L is much greater than the radius R is great (L/R>>1),

the resonator can be considered as a 1D longitudinal cavity, whose resonant frequencies are the harmonics of the fundamental frequency:

$$f = \frac{nc_s}{2L} \quad , \quad n \in \boldsymbol{N}^* \tag{1.40}$$

with c_s the speed of sound [44]:

$$c_s = \sqrt{\frac{\gamma RT}{M}} \tag{1.41}$$

where γ is the adiabatic index, R the molar gas constant, T the temperature, and M the molar mass of the gas.

If the length-to-radius ratio is small, azimuthal and radial modes of the cavity can occur (Figure 1.12). The combination of the three different types of modes gives the following resonant frequencies [42]:

$$f_{jmq} = \frac{c_s}{2}\left[\left(\frac{\alpha_{jm}}{R_c}\right)^2 + \left(\frac{q}{L}\right)^2\right]^{1/2} \quad , \tag{1.42}$$

where R_c and L correspond to the cylinder radius and length, the *jmq* indices to the eigenvalues of the radial, azimuthal and longitudinal modes and α_{jm} to the j_{th} zero of the m_{th} Bessel function divided by π.

The position of the laser beam affects the allowed modes in the cavity [23]. For instance, radial modes cannot be excited by a Gaussian beam whose optical axis corresponds to the axis of the cylinder. The microphone is located at a pressure antinode to maximize the movement of the membrane. It can affect the behavior of the resonator and thus should be taken into account when simulating the resonator behavior [41].

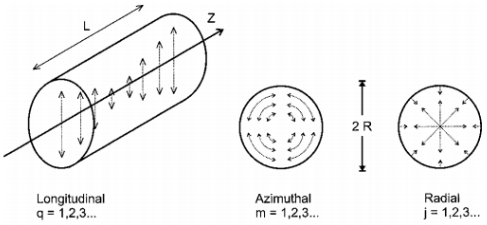

Figure 1.12: Representation of the three types of acoustic modes in a cylindrical cavity.

The cell constant can be expressed as in [42]:

$$C_n(\omega_n) = \frac{(\gamma - 1)LF_nQ_n}{V_{cell}\,\omega_n} \tag{1.43}$$

with γ the adiabatic coefficient of the gas, L the cell length, F_n the normalized overlap integral, Q the quality factor of the cell, V_{cell} the volume of the cell and $f_n = \omega_n/2\pi$ the resonant frequency.

Although it is named the cell constant, it does not depend only on the cell geometry but on the whole PA setup design. For instance, F_n represents the overlap between the spatial optical distribution and the pressure distribution, which depends on the optical arrangement. Since the resonant frequency and the quality factor depends on the cell geometry, the cell constant eventually depends on the cell length and diameter [45]. Theoretically, the best acoustic amplification are obtained for a cell of infinitely large length and infinitely small radius (Figure 1.13). However, other factors must be considered for practical application.

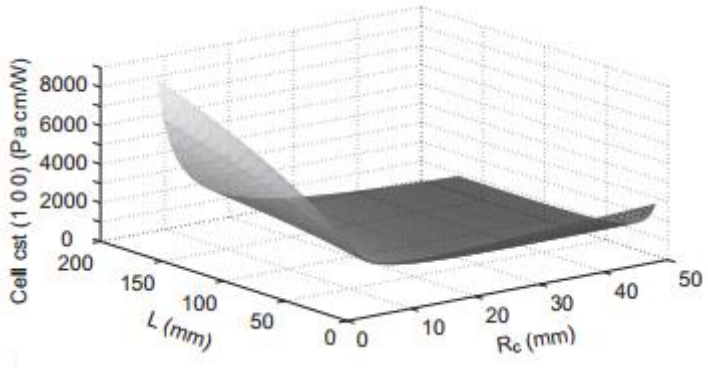

Figure 1.13: Optimization of the cell dimensions for the first longitudinal mode using the cell constant [45]. The cell constant increases with the cell length L and decreases with the cell radius R_c.

We saw in section 1.1.4.1, that low frequencies (<100Hz) suffer high noise intensity due to the 1/f noise. At high frequencies (>10kHz), the photoacoustic generation efficiency decreases (due to molecular relaxation times). Therefore, most PA cell are designed to work in the kHz range. Moreover, in this frequency range microphones offer a good SNR (up to 20kHz). A desired frequency gives the resonator length.

An important parameter of the cell is the Q factor. It represents the capacity of the resonator to conserve the stored energy. The definition of the Q factor is discussed in section 1.3.1.3. A high Q factor means a good acoustic confinement, or equivalently low acoustic losses. For the longitudinal mode of a cylindrical resonator with closed ends, the Q factor increases with the resonator radius (it must be noted that is different in the case of an open ended resonator, the losses due to radiations at the ends must be taken into account, which provokes the decrease of the Q factor with an increasing resonator radius R_c). From equation (1.43), we can see the cell constant is proportional to the Q factor which is an opposite trend to the ratio L/V_{cell} that decreases with the square of the radius R_c. Finally, multiplying the two contributions (Q and L/V_{cell}), the cell constant depends on the inverse of the resonator radius R_c. However, the laser beam should be able to pass through the cell. The smallest acceptable radius depends on the laser beam diameter, which in turn, depends on the length of the resonator (the optimization is not as sequential as it could look like).

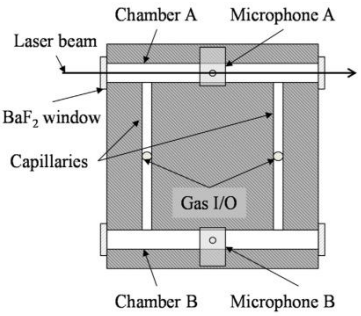

Figure 1.14: Cross cut view of a differential Helmholtz resonator made of two chambers A and B, connected by two capillaries. [38] The air in the capillaries is equivalent to a moving mass of air that is pushed back and forth by the air in chamber acting as acoustic springs. The microphone A monitors the photo-generated acoustic pressure while the microphone B is used to measure the environmental noise which can then be subtracted from the microphone A signal.

Interestingly, it can also be pointed out that a high Q will render the sensor more sensitive to drift with temperature and gas composition changes [40]. However, it can be prevented by

tracking the resonance shift of the PA cell using another resonance mode of the cell [45]. The increase of the Q factor leads to a higher signal, but may also amplify the noise. A solution is the use of differential measurement with two microphones: one measuring the noisy photoacoustic signal and a second one measuring the noise only. The second microphone is then used for subtracting the noise from the first microphone. A successful and well-known implementation is the differential Helmholtz resonator (Figure 1.14) [37].

1.2.1.1. Theoretical expression of the photoacoustic signal

The photoacoustic signal is obtained similarly to the WM signal that was thoroughly described for the case of pure FM and combined IM-FM modulation. The main difference between the two sensing techniques is that WMS is based on the gas sample transmission whereas the photoacoustic generation relies on the sample absorption. The absorbed intensity is simply expressed as the difference between the laser intensity and the transmitted intensity:

$$I_{abs}(x) = I_0(x) - I_t(x) = I_0(x)\left[1 - e^{-\alpha(x)L}\right] \tag{1.44}$$

Then the expression of the theoretical photoacoustic signal s_{PA} can be obtain following the same steps as for the transmitted signal (section 1.1.5). The details of the calculation are given in [46].

$$s_{PA}(x) = \sum_{i=1}^{\infty} s_{np}(x)\cos(n\omega_m t) - \sum_{i=1}^{\infty} s_{nq}(x)\sin(n\omega_m t) \tag{1.45}$$

For the combined IM-FM modulation, for the two first harmonics, the PA signal is obtained as:

$$\begin{aligned} s_{PA,1p}(x) &= -s_{1p}(x) - p_\omega \Delta\nu_{line} m \\ s_{PA,1q}(x) &= -s_{1q}(x) \\ s_{PA,2p}(x) &= -s_{2p}(x) \\ s_{PA,2q}(x) &= -s_{2q}(x) \end{aligned} \tag{1.46}$$

with $s_{nq}(x)$ as defined in equation (1.32).
For most components, the PA signal is equal to the WM signal plus a π phase shift. Except for the 1st harmonic where there is an additional offset (orange).

Photoacoustic has proved to be a successful technique in gas sensing. It shows a number of advantages compared to WMS: it is achromatic, background free and does not depend on the path length. The PA cell design plays a key role in order to prevent parasitic noises which would otherwise lower the detection limit. Conventional PA relies on audio microphones as transducing devices, which have a flat frequency response. Alternative techniques of PAS employ highly resonant transducers, such as a cantilever or a tuning fork, showing a potential for the miniaturization of the PA cell.

1.3. Quartz Enhanced Photoacoustic Spectroscopy

Quartz Enhanced Photoacoustic Spectroscopy (QEPAS) was proposed in 2002 by Kosterev et al. [7] as an alternative of conventional PAS. A Quartz Tuning Fork (QTF) is used as a sensitive piezoelectric transducer. The QTF is a low cost, mass-produced and small footprint component which renders QEPAS competitive with PAS for making compact gas sensors. The QTF can be directly excited by the acoustic wave, without the use for a resonant cell as in PAS (Figure 1.15). The QTF is a sharply resonant transducer compared to the flat frequency response microphone. Its high Q factor makes the QEPAS very sensitive and naturally immune to noise. It is important to accurately understand the mechanical and electrical QTF behavior before visiting the various implementation of QEPAS.

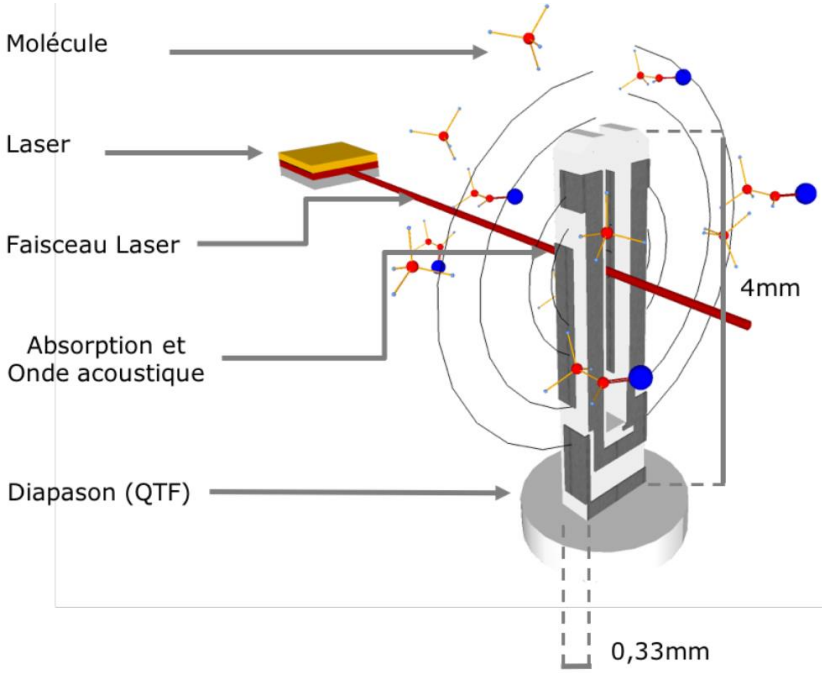

Figure 1.15: Illustration of the QEPAS technique (Quartz Enhanced Photoacoustic Spectroscopy), whose main components are a laser and a QTF (Quartz Tuning Fork) [47].

1.3.1. The Quartz tuning fork

The quartz tuning fork (QTF) is a piezoelectric transducer with a high quality factor (above 10000 at atmospheric pressure). It was initially manufactured by the watch industry as a standard 32768Hz (2^{15}) clock oscillator. Industry standards made the QTF reliable, available and affordable. Owing to his great features, it was employed as the sensitive element in many fields and systems:

- Scanning Probe Microscopy:
  First use in scanning near field acoustic microscopy [48] and soon after in atomic force microscopy [49] with atomic resolution. Deeply studied topic obtaining results close to theoretical limitations [50]. Complex design of resonators: Akiyama probe [51].

- Mass sensor [52], liquid viscosity [53,54], gas density sensor [55]
- gas sensing using Quartz-Enhanced Photo-Acoustic Spectroscopy (QEPAS) [56] , Resonant OptoThermoAcoustic Detection (ROTADE) [57] and Quartz-Enhanced Photothermal Spectroscopy (QEPTS) [58]

The standard QTF is fabricated out of a quartz substrate. Quartz is well-known for making high Q factor crystal oscillator. Indeed, due to its high crystalline quality and high stiffness, it has a high intrinsic quality factor. There are mostly two types of quartz resonators used for making clock oscillators: the quartz tuning fork and the Thickness Shear Mode (TSM). QTFs are based on a flexural mode and operate in the kHz range while TSMs, as indicated by their name, rely on shear modes and have resonant frequencies in the MHz range. TSMs are also known as Quartz Crystal Microbalances (QCM) and are used for mass, chemical, viscosity [59] and surface acoustic wave sensors [60]. As the efficiency of the photoacoustic effect is very low at MHz frequencies, QTFs are more suitable than QCMs for resonant acoustic detection.

The quartz is a piezoelectric material: the mechanical deformation of the crystal lattices leads to charge separations and thus to a potential difference. The piezoelectric properties strongly depend on the crystal orientation. The substrate angle cut is used to optimize piezoelectric properties and to improve the resonance stability with temperature. QTFs are cut at 0-5° from the xy plane [61]. The metal electrodes are positioned on the quartz surface to effectively collect the charges. Due to the symmetry of the two QTF branches (called 'prongs'), it is represented as a quadrupole component, which results in a very good noise immunity [62]. Another very important feature of the QTF is its very high dynamic range. It shows a perfectly linear response over more than 4 decades (Figure 1.16). Therefore, it can be employed for sensing traces of gas as well as high concentrations. It is also extremely stable in extreme environment [63] such as liquid helium temperatures [64], ultra-high vacuum, high pressure [65] and high magnetic fields.

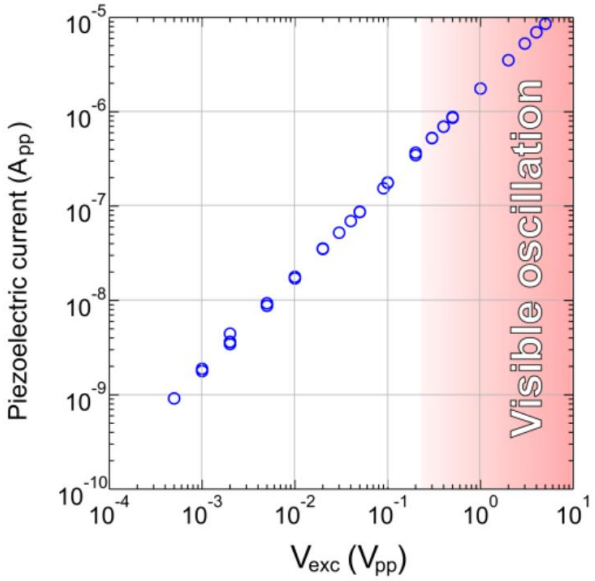

Figure 1.16: Evolution of the QTF current as a function of the applied voltage. [66]

1.3.1.1. The mechanical response

Mechanically, the QTF can be described as two separate cantilever beams (Figure 1.17(a)). A cantilever beam is a specific case of beam in terms of boundary conditions, with one free end and one fixed end. Using Euler-Bernoulli beam theory and considering small displacements, the beam deflection can be described by considering the neutral axis, i.e. the stress free location of the beam where compression and tension forces compensate each other. Torsion and shear forces are neglected. The beam deflection, i.e. the displacement in the y direction, can be written as [62]:

$$EI\frac{\partial^4 W(x,t)}{\partial x^4} + \gamma\frac{\partial W(x,t)}{\partial t} + (\rho A + \mu)\frac{\partial^2 W(x,t)}{\partial t^2} = f_i(x,t) \tag{1.47}$$

W(x,t): the displacement of the beam in the y direction [m]
E: Young's Modulus [Pa]
I: Second moment of area in the z direction [m^2]
γ: Damping coefficient [kg/s]
ρ: Volumetric mass density [kg/m^3]
A: Prong cross section [m^2]
μ: added mass due to the pressure load [kg]
f_i(x,t): the external forces [N]

The equation can be solved using a Fourier decomposition. The frequency Eigen modes w_i form a basis, associated to a given mode shape ϕ_i and to a given vibration frequency ω_i (Eigen frequency):

$$W(x,\omega) = \sum_i w_i(\omega)\phi_i(x) \tag{1.48}$$

The modes shapes ϕ_i can be described as a weighted sum of trigonometric and hyperbolic functions whose coefficients are numerically determined [67].

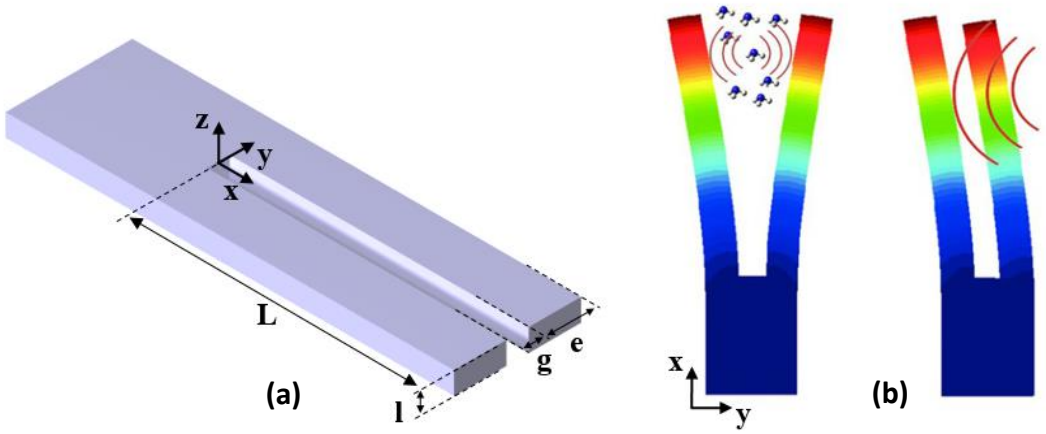

Figure 1.17: (a) Schematic of the QTF (b) Representation of the QTF in-plane flexural symmetric mode (left) and antisymmetric (right) mode of the QTF. The symmetric mode is active when an acoustic source is in between the prongs, as in QEPAS, while the antisymmetric reacts to a source located outside of the prongs. The color represent the amplitude of the mechanical displacement [12].

The two QTF prongs add some complexity in the resonance mode compared to the cantilever. At resonance, they necessarily move synchronously, i.e. at the same frequency, but spatially, the movement can be symmetric (i.e. in antiphase in time) or antisymmetric (i.e. in

phase in time), and in-plane or out of plane. The common mode used in a 32kHz QTF is the fundamental of the symmetric in-plane flexural mode (Figure 1.17(b)). This same mode is exploited in QEPAS, resulting in the best acoustic coupling and oscillation amplitude. Since it is the first order flexural mode, it can be approximated with the static response of the cantilever:

$$EI\frac{\partial^2 W(x)}{\partial x^2} = M(x) \tag{1.49}$$

with M the internal bending moment. The normalized solution[9] is easily expressed as a third order polynomial:

$$\phi(x) = \frac{3Lx^2 - x^3}{2L^3} \tag{1.50}$$

The solution is thus conveniently linearized expression compared to the solution using (1.47). The frequency response of the cantilever can be expressed as [67]:

$$w_i(\omega) = \frac{F_i}{K_i + j\gamma_i\omega - M_i\omega^2} \tag{1.51}$$

With F_i the generalized acoustic force, K_i the generalized stiffness, γ_i the damping factor and M_i the generalized mass. The cantilever response can be viewed as a harmonic oscillator constituted by a mass M_i, a spring of stiffness K_i, giving a resonance frequency $\omega_i^2 = K_i/M_i$. γ accounts for the losses and depends on the quality factor.

The QTF resonant frequency for the fundamental mode is given by [68] :

$$f_0 = \frac{1}{2\pi}\frac{\alpha_0^2}{L^2}\sqrt{\frac{EI}{\rho A + \mu}} \tag{1.52}$$

with α_0 (=1.875) a modal coefficient.
In vacuum (μ=0), the expression can be simplified to:

$$f_{0,vac} = \frac{1}{2\pi}\frac{\alpha_0^2}{L^2}e\sqrt{\frac{E}{12\rho}} \tag{1.53}$$

with e the width of the QTF prong (y direction). Other expressions can be found in the literature [69][70].

In order to model the QTF behavior, it is convenient to obtain its electrical equivalent model. It can be derived from the mechanical response thanks to the QTF piezoelectric property.

1.3.1.2. The electrical equivalent circuit

The QTF current has two different contributions: one from the piezoelectric effect and one from the capacitive effect. The piezoelectricity is directly related to the motion of the QTF, thus follow the same frequency response, whereas the capacitance is due to the conductive electrodes spaced by a nonconductive material (the quartz). The total charge on the QTF electrodes can be written as the sum of the two contributions:

$$q = c_p w_0(\omega) + C_0 V \tag{1.54}$$

[9] The normalization is taken so that $\max(\phi(x)) = 1$

where c_p is the piezoelectric coefficient (c_p=1.38·10^{-5} C/m for a standard QTF [67]), C_0 the inter-electrode capacitance and V the voltage at the QTF terminals. Introducing (1.51) in (1.54) and taking the derivative, it gives the total current generated by the QTF:

$$i = \underbrace{\left[\frac{1}{R + \frac{1}{jC\omega} + jL\omega} + jC_0\omega\right]}_{1/Z_{QTF}} V \tag{1.55}$$

with the parameters of the electrical model calculated from the mechanical model using the piezoelectric coefficient γ_0:

$$\begin{aligned} R &= \frac{\gamma_0}{C_p^2} \\ L &= \frac{M_0}{C_p^2} \\ C &= \frac{C_p^2}{K_0} \\ V &= \frac{F_0}{C_p} \end{aligned} \tag{1.56}$$

The inductance L is proportional to the generalized mass, storing the kinetic energy, the capacitance C is the inversely proportional to the stiffness, accounting for the potential energy, and finally the resistance R is proportional to the damping, representing the system losses. The admittance obtained in (1.55) corresponds to the Butterworth Von Dyke model (Figure 1.18(a)), and can be represented in terms of complex magnitude and phase (Figure 1.18(b)). C_0 accounts for the parasitic capacitance due to metal electrodes and cables.

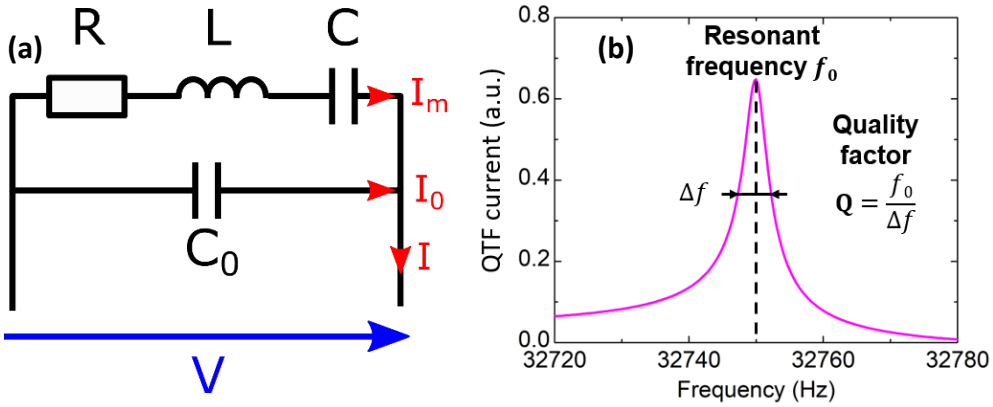

Figure 1.18: (a) Butterworth Von Dyke model (b) Frequency response of the QTF.

By introducing the resonant frequency and the quality factor, (1.55) can be rewritten as:

$$\frac{1}{Z_{QTF}} = \frac{\frac{1}{jL\omega}}{1 - \left(\frac{\omega_0}{\omega}\right)^2 - j\frac{1}{Q}\frac{\omega_0}{\omega}} + jC_0\omega \tag{1.57}$$

with $\omega_0 = 1/\sqrt{LC}$ the natural undamped angular frequency and $Q = (1/\mathrm{R})\sqrt{L/C}$ the quality factor.

The frequency ω_0 correspond to the maximum of the frequency response of a lossless LC circuit. It also corresponds to the frequency for which the reactance becomes zero, meaning the inductor and the capacitor behave synchronously, without phase lag, therefore the sum of the two reactive components is zero. The second definition of ω_0 is convenient for visualizing the concept of resonance. The contribution of the parallel capacitance is generally low at resonance ($|I_m/I_0|=(RC_0\omega_0)^{-1}\approx 10$ at $\omega=\omega_0$), though it can become non negligible for lower Q values. Also, the effect of C_0 is markedly visible on the QTF frequency response as an anti-resonance at a few hertz after the resonant frequency. If the parasitic contribution is neglected ($C_0=0$), the squared magnitude of the QTF response gives a Lorentzian function (Appendix A):

$$\left|\frac{1}{Z_{QTF}}\right|^2 = \frac{1}{R^2}\frac{1}{1+\left(\frac{2Q(\omega-\omega_0)}{\omega_0}\right)} \tag{1.58}$$

1.3.1.3. The quality factor

The quality factor is related to the resonator's ability to sustain his own motion, to conserve its own energy, thus it is inversely proportional to the losses. The quality factor can be defined in different manners. Q can be defined as the ratio of the total stored energy E_t to the energy loss δE_t for one oscillation cycle:

$$Q = 2\pi\frac{E_t}{\delta E_t} \tag{1.59}$$

It is the original expression but the less meaningful practically speaking. Using the transient response of the QTF, the envelope of the oscillations follows an exponential growth (or decay). The exponential decay time τ is related to the Q factor:

$$Q = \pi\tau f_0 \tag{1.60}$$

A high Q factor means that the reaction time of the QTF is increased. It can be understood as an "averaging effect" that tends to reduce the system fluctuations (noise) at the price of an increase response time. Q can also be obtained from the frequency response (Figure 1.18(b)), as it appears in the QTF impedance. If the frequency response is represented as a Lorentzian, the Q factor is the ratio of the resonant frequency to the full width at half maximum Δf :

$$Q = \frac{f_0}{\Delta f} \tag{1.61}$$

For a QTF Q factor of 8000, a moderate value in standard conditions (P_{atm}, 20°C), the response time is about 80ms and the bandwidth about 4Hz.
The expression (1.59) is equivalent to (1.60) and (1.61) for a harmonic oscillator with a sufficient quality factor (Q>10) [71]. The characterization methods for the Q factor and their respective accuracy are detailed in Chapter 3. The QTF mechanical losses originates from multiples mechanisms. The total quality factor Q_{tot} can be written as the sum of the independent contributions:

$$\frac{1}{Q_{tot}} = \frac{1}{Q_{struc}} + \frac{1}{Q_t} + \frac{1}{Q_v} + \frac{1}{Q_r} \tag{1.62}$$

Q_{struct}, Q_t, Q_v and Q_r represents the quality factor related to the resonator structure, the thermoelasticity, the viscosity and the acoustic radiation. Typical values for a standard 32kHz QTF are given in Table 1-1.

In standard conditions of pressure, the QTF interaction with the fluid media is the dominant effect (Q_v). The viscosity of the fluid creates a stress on the QTF surfaces, reducing the oscillation amplitude. When the resonator is in vicinity with another object, typically the case for the micro fabricated MEMS attached close to the native substrate, the viscosity affects the moving object by the squeeze film effect. This effect is particularly important when the direction of the movement is normal to the fixed object.

Q_{struct} represents the losses of the attachment anchors and is not negligible. It mostly depends onto the position of the anchors, the oscillation mode and the geometry.

Another source of losses due to the presence of the fluid is the acoustic radiation (Q_r). The coupling of the fluid with the mechanical oscillator will produce an acoustic wave, thus some energy is lost through the radiation of the wave. Q_r mostly depends on the density of the resonator material, the density of the fluid and the dimensions of the resonator [67].

During the QTF displacement, the domains under compression (resp traction) undergo a temperature increase (resp decrease). The temperature gradient results in a heat flow and therefore a loss of energy. The thermoelastic damping decreases with the operating frequency and the material specific heat [72]. In the case of the QTF, Q_r and Q_t are negligible.

Frequency f_0 (Hz)	32764
Quality factor Q_{struct}	77000
Quality factor Q_t	$4.81 \cdot 10^5$
Quality factor Q_v	20224
Quality factor Q_r	$2.29 \cdot 10^6$
Quality factor Q_{tot}	15400

Table 1-1: Q values for a standard clock QTF for the different loss mechanism [67].

Integrated MEMS, for applications such as inertia measurement or clock timing, are generally packaged under vacuum where the viscous and acoustic losses can be neglected. Therefore, they are not designed to be operated at atmospheric pressure, where the viscous damping is the dominant effect [73]. A very nice work was done to optimize the QTF geometry for atmospheric pressure operation, obtaining a quality factor up to 41 000 [74]. Other QTF designs dedicated to QEPAS have been presented [75,76].

We saw that the quality factor of a QTF standing in a fluid can be accurately modeled, accounting for different loss sources. Next, the implementation of the QTF in a system generally further degrades the quality factor. Approaching the QTF to an object will lead to more squeeze film effect. Attaching a little mass onto one of the prong, for instance a thin probe for microscopy, create an imbalance between the two prongs, leading to a brutal drop of the Q value (though f_0 is less affected relatively). Adding the same mass to the second prong (or rather the same moment of inertia) can partially restore the quality factor [77]. The tuning of the QTF

geometry by simple part gluing could be interesting to adapt the QTF to the specific application of photoacoustics, thus avoiding the complete redesign of the QTF and the microfabrication, and allowing more fancy shapes that cannot be made out of the quartz substrate. The quality factor is also affected by the readout electronics, notably the quality factor can be electronically or controlled [78,79].

1.3.1.4. The readout circuit and the noise

Due to the high impedance of the QTF (approx. 100kΩ at resonance), it can be considered as a current source. The generated current is in the range of pA in a typical QEPAS experiment [80]. In order to convert it into a readable voltage a high-gain transimpedance amplifier (TA) is generally used (Figure 1.19).

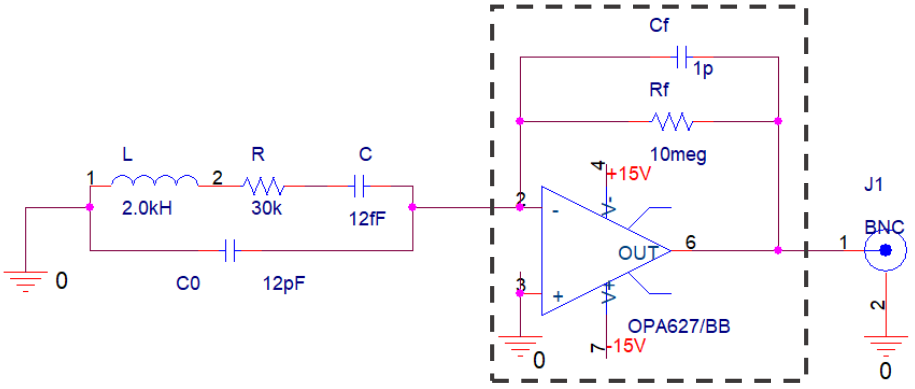

Figure 1.19: Schematic of the QTF and the transimpedance amplifier (TA) (black dotted square) used for simulation on ORCAD Pspice.

This type of circuit is typically employed with photodiodes. The ultimate noise in the case of photodiodes is the shot noise. Appropriate TA circuits are shot noise limited, meaning the signal is amplified without adding noise. However, their design is far from straight forward [81]. It is based on a non-inverting circuit, that is an operational amplifier with a feedback impedance. The feedback impedance is typically composed of a high resistor (R_f=10MΩ) and a small capacitor (C_f=1pF). The QTF is connected to the ground on one side and to the non-inverting input of an operational amplifier (OPA) onto the other side. The amplifier output voltage can be written as:

$$V_{amp} = -Z_f\, i \tag{1.63}$$

The higher the feedback resistor, the higher the gain. However, as any operational amplifier the gain is increased at the expense of the bandwidth: this effect is quantified by the gain-bandwidth product. The gain-bandwidth product is an intrinsic feature of an OPA and must be high enough in order to achieve a high gain at a given working frequency. This is a direct consequence of the close-loop transfer function being limited by the open-loop transfer function.

The QTF current equivalent noise i_b can be expressed as [50]:

$$i_b(\omega) = \frac{\sqrt{4kTR\Delta f_{BW}}}{Z_m} \tag{1.64}$$

with i_b expressed in Volts, Δf_{BW} the lock-in amplifier bandwidth and Z_m the QTF motional impedance:

$$Z_m = R + \frac{1}{jC\omega} + jL\omega \tag{1.65}$$

Equation (1.64) corresponds to the product of the thermal noise of the QTF equivalent resistor R and the QTF motional response. It is important to note that a change in the QTF response (frequency shift, Q decrease) also has an effect onto the noise. However, as the noise scales with the square root of the resistance, the best SNR is obtained at resonance. At resonance, the QTF impedance is equal to R, thus i_b simplifies to $\sqrt{4kT\Delta f_{BW}/R}$.

Physically, the thermal noise corresponds to the molecular agitation of the fluid surrounding the prongs, also called the Brownian motion. It can be lowered by reducing the pressure or the temperature. However, the photoacoustic signal generation depends on those parameters as well, thus it opens up a more complex optimization, that is considered out of the scope here. For practical operation of the sensor, only standard conditions of pressure and temperature are considered. Another strategy for noise reduction is playing on the bandwidth. The Johnson noise is a white noise, i.e. a noise with a flat frequency distribution. The increase of the SNR is proportional to the square root of the bandwidth.

The purpose of the TA is to amplify the very low current while keeping the noise to a minimum. The total current noise at the frequency f_0 at the input of the transimpedance amplifier (Figure 1.20) can be written as [81]:

$$i_{total} = \sqrt{\frac{4kT}{R} + i_{BN}^2 + \left(\frac{e_N}{R_f}\right)^2 + \frac{4kT}{R_f}}\sqrt{\Delta f_{BW}} \tag{1.66}$$

where e_N and i_{BN} are the OPA input voltage noise and the OPA input current noise, resp. The TA circuit design aims to make the contribution of the three last terms of equation (1.66) negligible compared to thermal noise of the QTF (first term). Due to the high value of R_f, the contribution of e_N is negligible compared to i_{BN}. OPAs based on FET amplifiers, such as the OPA657, present low current noise compared to bipolar OPA. Therefore, the OPA657 is a good candidate for high gain (>10^3) transimpedance amplifier. Considering the fourth term, the feedback resistor is very large compared to the QTF equivalent resistor, making the noise contribution negligible.

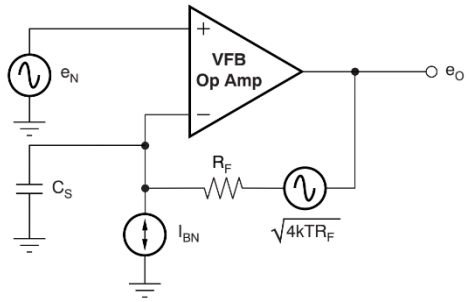

Figure 1.20: Schematic of the TA for noise analysis [81]

Final considerations are external sources of noise. The most prominent ones are the power supply and electromagnetic noise. A battery will produce a very stable DC voltage compared to all benchtop power supply. Electromagnetic radiation is prevented by placing the QTF as close as possible to the TA, using shielded cables and metallic cases.

The high gain TA we described is the most common electronic setup used in QEPAS, but other designed were presented, notably with a differential measurement of each QTF prongs [67] and also with a buffer for impedance matching [82].

For a properly designed TA, the thermal noise is the dominant source of noise. It can be verified experimentally by measuring the noise spectral density at the output of the TA. This measurement is usually made with a network analyzer. Alternatively, we used a lock-in amplifier. to measure the noise at the output of the amplifier. The lock-in amplifier bandwidth was set to 0.1Hz, in order to selectively measure the noise around the demodulation frequency. The demodulation frequency was swept over a few Hz, and for each measured frequency, a few hundreds of points were acquired. The noise spectral density was then computed as the ratio of the standard deviation of the measured voltage points to the Equivalent Noise BandWidth (ENBW). The results (Figure 1.21) are in good agreement with the theory obtained with equation (1.64) with an offset that can possibly be attributed to a calibration error of the transimpedance amplifier gain or a voltage offset of the OPA.

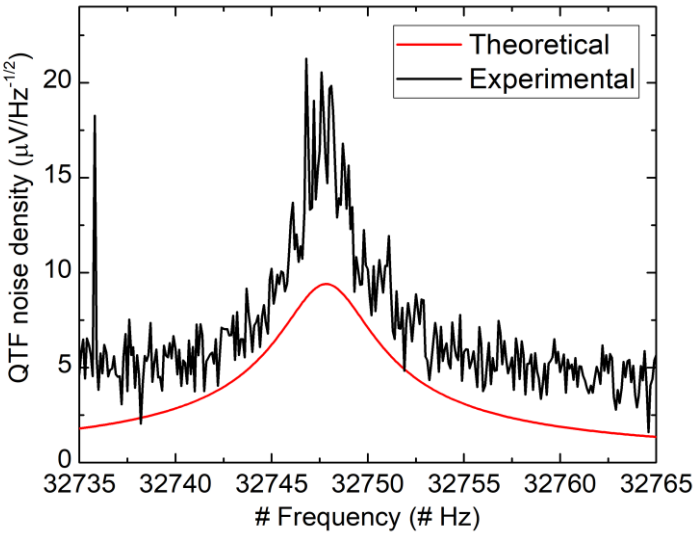

Figure 1.21: QTF noise power spectral density. The theoretical curve is obtained using (1.64). The experimental data were measured with a setup based on a lock-in amplifier.

Those results correspond well with previously reported values [67].

The QTF can be described mechanically using the beam theory. We are interested in the first order in-plane symmetrical flexural mode which yields a resonance at 32kHz. The high stiffness of the quartz material renders some loss contribution negligible and allows to obtain a high Q factor, around, mostly limited by the viscous damping and the squeeze film effect. The electrical equivalent model can be deduced from the mechanical model thanks to the piezoelectric properties. The QTF thermal noise is the fundamental limitation. The transimpedance amplifier is the typical electronic setup used to recover the very low current generated by the QTF in the range of pA, and is essential for achieving a sensitive QEPAS detection.

1.3.2. QEPAS operation

In QEPAS, similarly to PAS, a modulated laser is used to excite a gas specie in order to create a sound wave thanks to the photoacoustic effect. Then, the acoustic energy is used to excite mechanically the QTF. The QTF is a piezoelectric transducer which upon mechanical excitation will generate an electrical signal which is proportional to the amplitude of the acoustic wave (Figure 1.22). The QEPAS signal can be expressed as [12]:

$$S \propto \frac{\alpha_{LOD} \cdot P_L \cdot Q}{\sqrt{1 + (2\pi f_0 \tau_{V-T})^2}} C_{ppmv} \qquad (1.67)$$

with α_{LOD} the absorption coefficient at the limit of detection, P the laser power, Q the QTF quality factor, f_0 the QTF resonant frequency, $\tau_{v\text{-}t}$ the V-T relaxation rate and C_{ppmv} the concentration of the target specie.

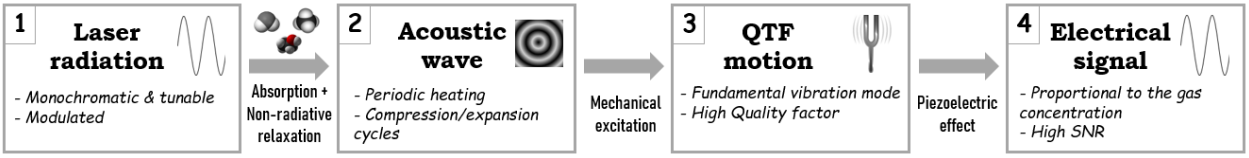

Figure 1.22: Block representation of the QEPAS technique. : A laser radiation (1) is used to generate a pressure wave (2) through the photoacoustic effect. Detection is then realized by a QTF (3), that generates in turn an electrical signal (4) by a piezoelectric effect

QEPAS and PAS have many similarities, as they are both based on the photoacoustic generation, are background free, achromatic, do not depend on the optical path length and are proportional to the absorbed optical power (corresponding to the product $\alpha \cdot P$). The two techniques also exhibit some differences. The QTF has a very small footprint, which allows its integration into gas cell of a few cm^3, smaller than a standard photoacoustic cell. In QEPAS, the energy is stored in the form of mechanical motion of the QTF prongs, differently from PAS in which the energy is stored in the acoustic resonator. We can remark that the quality factor of the QTF ($\approx 10^4$) is about two orders higher than the one for an acoustic resonator (typ. $\approx 10^2$). It has direct implications: a higher Q means a higher amplification (Equation (1.67)), a longer response time (section 1.3.1.3) and narrower bandwidth. A higher Q factor will contribute to increase the signal to noise ratio and subsequently improve the sensor's limit of detection. However, it also increases the sensitivity to environmental changes. The influence of the humidity and temperature onto the QTF are discussed in the Chapter 3.

Another important difference is the operating frequency. When the modulation frequency has the same order of magnitude compared to the molecular relaxation rate, the efficiency of the photoacoustic conversion starts to decrease ($(2\pi f_0 \tau_{V-T})^2 > 1$ in equation (1.67)). In QEPAS, the conventional QTF resonates around 32.8kHz, which is greater than in PAS where the selected resonance is generally below the kHz. QEPAS is thus more affected by the effect of the relaxation rate, as it was reported for instance for the detection of CH_4 [83], CO [84] and NO [85].

The target specie interacts with the other species in the gas mixture through molecular collisions. During those collisions, energy transfers can occur and create new pathways for the molecular relaxation. Therefore the molecular relaxation rate depends the composition of the gas mixture and not only the target species. It can be difficult to predict in the presence of many

species as they can exhibit multiple relaxation pathways. Certain mixtures, such as dilute CO in air, have long relaxation rate, which lowers the photoacoustic efficiency. This issue can be tackled by forcing a faster relaxation path with the addition of another specie to the gas sample, 'a relaxation promoter', often H_2O [86] but also He [87] or SF_6 [88].

Compared to a simple cantilever beam or a membrane which can be considered as a dipole, the QTF is a quadrupole. In order to activate the symmetric flexural mode, the acoustic source must be located between the two prongs to apply an opposite force on the two QTF prongs. Any acoustic source located around the QTF will apply a force on the two prongs in the same direction, which will not contribute to the symmetric mode (Figure 1.17(b)) Therefore, the QTF exhibits good immunity to external acoustic noise.

The QEPAS technique was theoretically studied by Petra et al [89]. The laser beam is absorbed by the gas, which delivers a given amount of heat and can be used to formulate a source term for the acoustic wave generation. The laser is considered to have Gaussian beam profile and a constant beam width over the thickness of the tuning fork, therefore the solution for the acoustic profile is a cylindrical wave, whose amplitude decreases as a function of the radius r. The exact expression has been described in [67], but the numerical solutions do not converge readily. The pressure distribution is well approximated by [89]:

$$\begin{aligned} \mathrm{P(r,t)} &\approx \mathrm{A}\left[\mathrm{J}_0\left(\frac{\omega r}{c}\right)\cos(\omega t) + Y_0\left(\frac{\omega r}{c}\right)\sin(\omega t)\right] \\ A &= (\gamma_H - 1)\omega\alpha_{eff}\frac{W_L}{8c^2} \end{aligned} \tag{1.68}$$

with A the amplitude of the pressure, γ_H the adiabatic index of the gas, ω the modulation angular frequency, α_{eff} the effective absorption coefficient, W_L the laser power and c the speed of sound, J_0 and Y_0 are the zero-order Bessel functions of the first and the second kind.

On the inner surface of the QTF prongs, i.e. approximately 150μm far from the optical axis, the amplitude of the pressure is approximately of 20 mPa, for the detection of 100% CH_4 at 4246.46 cm^{-1} (2.35μm) with a linestrength of $1{\cdot}10^{-21}$ $cm^{-1}/(molecule{\cdot}cm^{-2})$ and a laser power of 25 mW [80]. In the same condition but a concentration of 1ppmv, the pressure would be 10^{-6} lower 20 nPa.

For an optimal QTF excitation, the laser is focused between the two prongs, in the xz plane matching the QTF symmetry and at a distance h from the bottom of the prongs (Figure 1.23(a)). Using equation (1.68), the pressure profile can be calculated on the inner surface of the QTF prong (y=g/2). It is represented here for h=3mm (Figure 1.23(b)). It can then be integrated along the QTF mode shape $\phi_0(x)$ (equation (1.50)) to deduce the photoacoustic force F_0 as it was suggested by Aoust [67]:

$$\begin{aligned} \mathrm{F}_0(h) = \int_0^L \Bigg[\int_{-\frac{l}{2}}^{\frac{l}{2}} \Bigg[& \underbrace{P\left(x', y = \frac{g}{2}, z\right)}_{prong\ inner\ surface} \\ & - \underbrace{P\left(x', y = \frac{g}{2} + e, z\right)}_{prong\ \ outer\ surface} \Bigg] \phi_0(x) dz \Bigg] dx' \end{aligned} \tag{1.69}$$

with $x' = x - h$.

The force increases with the position of the laser beam h (Figure 1.23(c)) due to the greater leverage onto the prongs of the QTF and reaches a maximum just below the top of the prong. Our simulation yields a maximum when the laser spot is 0.53mm below the top of the prongs, similar to the theoretical value obtained by Petra et al, and very close to the value of 0.7mm observed experimentally [89].

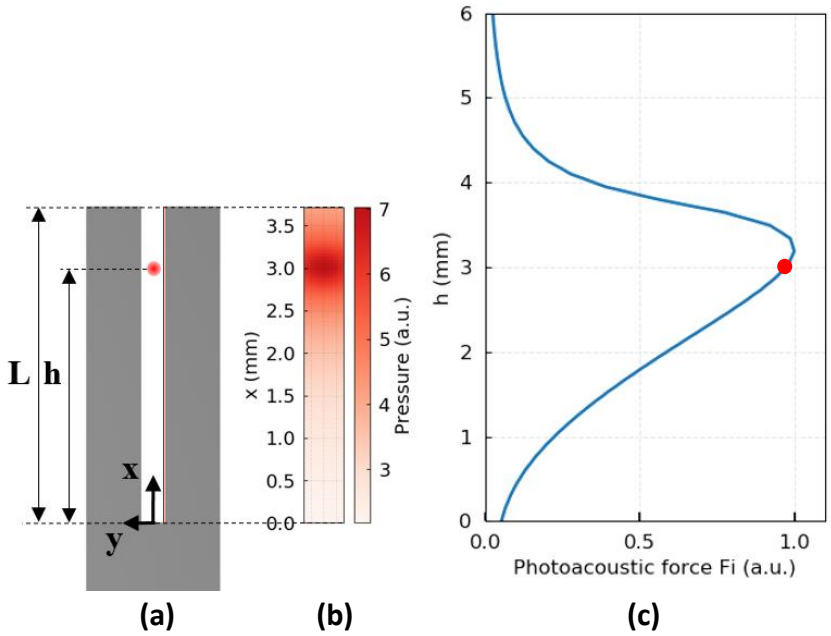

Figure 1.23: (a) Schematic of the QTF and the laser spot at a distance h from the bottom of the prongs.(b) 2D pressure distribution on the inside of one prong. The laser spot size is assumed to be small compared to the QTF gap (distance g). (c) Evolution of the photoacoustic force with the position of the laser beam. The red dot correspond to the integration of the pressure distribution of Figure 1.23(b). (b) and (c) are the results of a simulation on Python.

We have shown that the photoacoustic force depends on the position of the laser beam and the amplitude of the acoustic wave. The latter can be enhanced by the addition of acoustic resonators, called microresonators.

1.3.3. Signal enhancement with microresonators

1.3.3.1. The on-beam spectrophone

In the first QEPAS experiment, the laser was focused in the middle of the two QTF prongs and the acoustic wave was directly sensed by the 'bare QTF'. Soon after, acoustic microresonators were added to further enhance the acoustic wave. The QTF and the microresonators (mR) form a double resonant system called the spectrophone. The mR is a cylindrical tube, which can be considered as a 1 dimensional longitudinal resonator, and amplifies the acoustic wave before detection by the QTF. The spectrophone provides maximum enhancement when both elements are resonantly coupled. As the QTF operates at a fixed frequency, that depends on its geometry and material, and that cannot be adjusted, the mR is designed to match the QTF resonant frequency. The frequency of 32.7kHz of a standard QTF corresponds to a wavelength of 10 mm approximately (in air). Therefore, the mR length is below 1cm, which is small compared to acoustic resonators used in PAS.

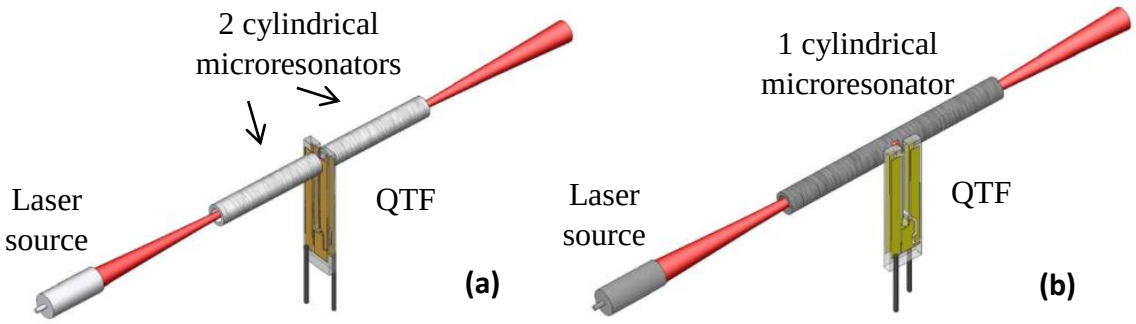

Figure 1.24: QEPAS spectrophone in the on-beam (a) and off-beam configuration (b). [90]

There are mostly two configurations for coupling the mR and the QTF: the on-beam and the off-beam spectrophone (Figure 1.24). In the on-beam configuration two cylindrical tubes are placed on both sides of the QTF. The laser beam passes through both tubes and the QTF gap (the space between the two prongs). The coupling efficiency mostly depends on two parameters: the length of the mRs and the distance between the QTF and the mR. The optimal mR length was found to be between $\lambda/4$ and $\lambda/2$ [90]. When the mR and the QTF are critically coupled, it can result in a decrease of the QTF factor, but an improvement of the signal-to-noise ratio [67]. The Q factor decrease has been seen as an advantage as it reduces the QTF response time [91].

The major limitation of the on-beam configuration is related to the narrow QTF gap (300μm). Indeed, similarly to the window noise in PAS, if some laser light impinges the inner surface of the mR (the mR walls) or the QTF surface, a background noise will be generated due to photothermal effects, leading to a serious degradation of the spectrophone SNR. Therefore, the laser beam must be able to pass entirely through the spectrophone. When using near IR laser diodes with nice Gaussian shape beam profile and moderate divergence, the beam can be easily focused into the spectrophone. However, it becomes more difficult with lasers operating a longer wavelength. QCLs have been used in the on-beam configuration, but they require more complex optical setups [92]. An alternative is to use the off-beam configuration.

1.3.3.2. The off-beam spectrophone

In the off-beam configuration, the mR is composed of two tubes (Figure 1.25): the main hole (red) and the side slit (blue). The laser beam is passed through the main tube. The acoustic generation in this tube provokes the creation of a standing wave. A side slit is located in the middle of the main tube, at the pressure antinode, and transfers the acoustic energy to the QTF. The QTF is located on the side of the mR, facing the slit, therefore in an off-beam position. The optical beam is not limited by the QTF gap as in on-beam, but only by the size of the main hole. The off-beam can be employed with optical sources having a high divergence and a large beam diameter such as QCLs at long wavelengths as will be presented in chapter 2.

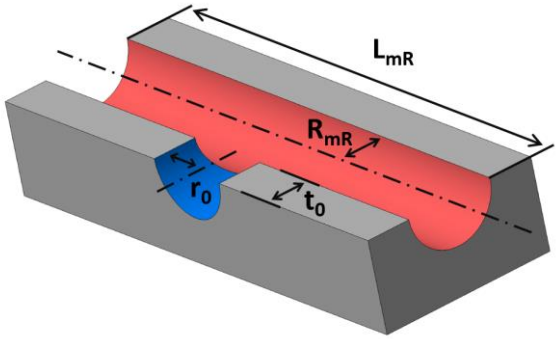

Figure 1.25: 3D Section view of the off-beam mR, with a T-shape, composed of the main tube (red) of length L_{mR} and radius R_{mR} and the side opening (blue) of radius r_0 and length t_0.

Oppositely to the on-beam spectrophone, there is a weak coupling between the mR and the QTF. The two elements can be modeled independently and the spectrophone transfer function equals to the product of the transfer functions of the two elements [93]. The QTF is not affected by the mR due to coupled resonances, but only due to the viscous damping. When the QTF is in the vicinity of the outer surface of the mR, the viscous damping increases, resulting in a shift of the resonance frequency and the quality factor (Figure 1.26).

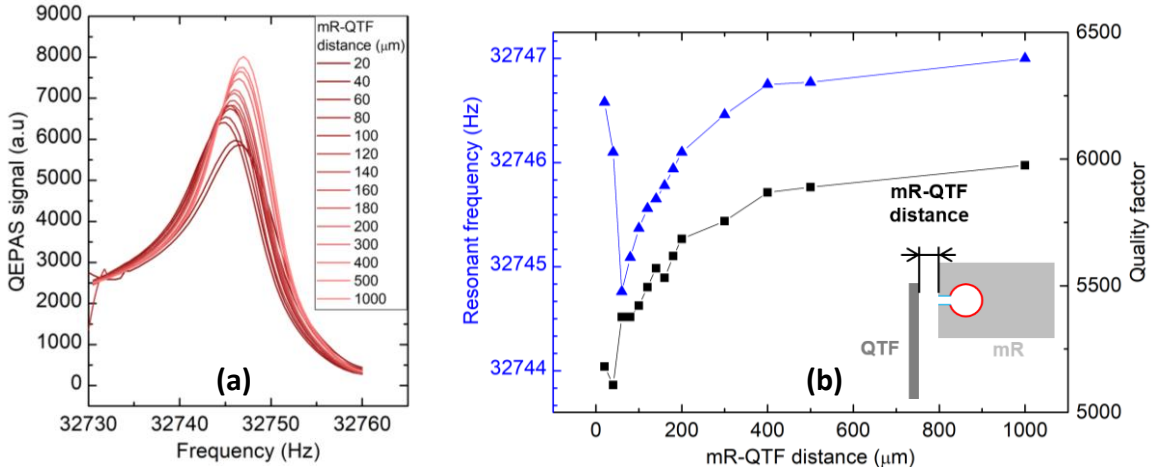

Figure 1.26: Influence of the mR-QTF distance onto the QEPAS signal represented in terms of frequency response (a) or in terms of resonant frequency and quality factor (b).

The resonant frequencies for the longitudinal modes of a cylindrical resonator were described in equation (1.42). However, there is a significant deviation of the mR resonance due to the presence of the opening in the main tube and the imperfect reflection at the tube open ends. Theoretical models using acoustic impedance based calculations have been presented for the original off-beam mR and a more refined T-shape model [94,95].

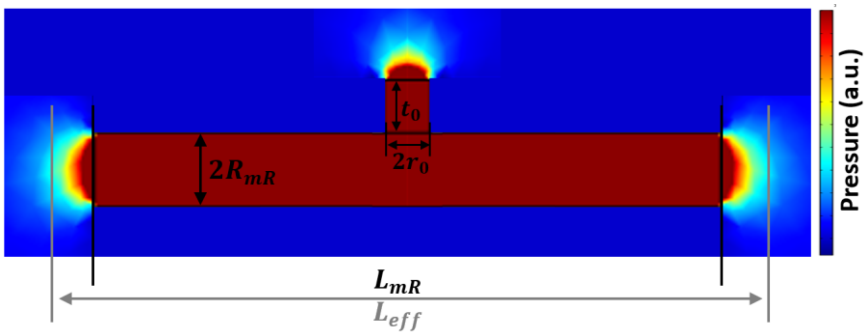

Figure 1.27 : Illustration of the acoustic confinement in the off-beam mR, obtained with a finite elements simulation on COMSOL.

The acoustic wave is reflected on both ends of the main tube. However the tube ends are open and cannot be considered as perfectly rigid walls, therefore the reflection does not occur exactly at the tube end but partially outside of the tube (Figure 1.27). Therefore, the effective cavity length L_{eff} is longer that the physical length L_{mR}, and can be calculated by applying an end correction for open tubes [96]:

$$L_{eff} = L_{mR} + C_{mR} \times R_{mR} \tag{1.70}$$

C_{mR} is the correction factor for the main tube. For a given resonant frequency f_{mR}, the effective length can be calculated as [94]:

$$L_{eff} = \frac{c}{f_{mR}} - \frac{c}{\pi f_{mR}} \tan^{-1}\left(\frac{4\pi S t_{eff}}{s_s}\frac{f_{mR}}{c}\right) \tag{1.71}$$

S and s_s are the cross section of respectively the main tube and the opening. t_{eff} is the effective length of the opening considering open-end corrections:

$$t_{eff} = t_0 + C_{t0} \times r_0 \tag{1.72}$$

C_{t0} is the correction factor for the side slit.
The details of the calculations are given in Appendix B.

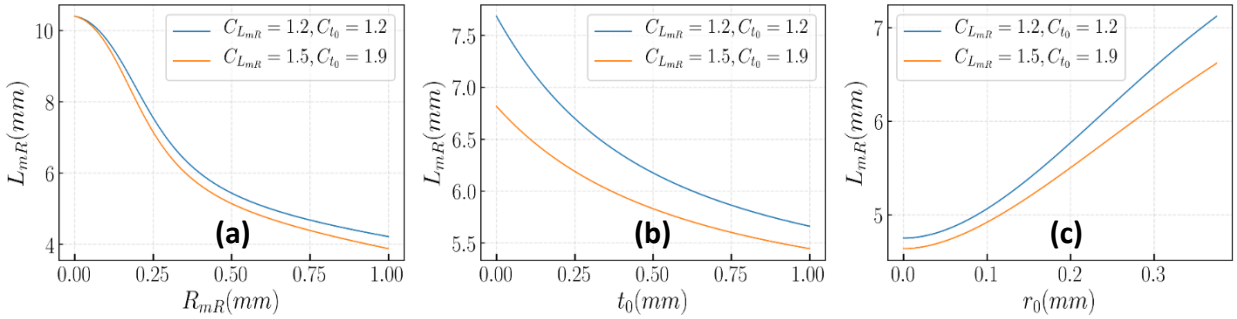

Figure 1.28: Optimum length of the off-beam microresonator as a function of the radius of the main hole (a) (with t_0=0.5mm, r_0=0.25mm), the length of the orifice (b) (with R_{mR}=0.375mm, r_0=0.25mm) and the radius of the orifice (c) (with R_{mR}=0.375mm, t_0=0.5mm). The mR frequency is set equal to the QTF frequency (f_{mR}=32700Hz) and the optimum length is obtained using equation (1.70) and (1.71).

The effect of the different parameters are presented on Figure 1.28. The following trends can be observed: The mR optimal length decreases with the radius of the main hole R_{mR} and the length of the orifice t_0 but increases with the radius of the orifice r_0. For PAS resonators, the correction factors C_{mR} and C_{t0} are empirically taken as 1,2 [96,97]. However, for QEPAS

microresonators, the dimensions of the tubes are very inferior and the values of the correction factors might be inappropriate. In chapter 2, we suggest to adjust these factors to the experimental results and thereby, obtain a semi-theoretical model with better accuracy (C_{mR}=1.5, C_{t0}=1.9).

The performance of the different mRs cannot be solely compared, but the whole spectrophones can be. Although the quality factor and the resonance frequency of the mR can be simulated and compared, the acoustic coupling between the mR and the QTF must be considered for the comparison between the on-beam and the off-beam spectrophone. The acoustic coupling is subtler to simulate, notably in the case of on-beam where the coupling is strong. In the literature, the mRs are compared using the SNR gain which correspond to the ratio of the SNR with the mR to the SNR with the 'bare QTF' [90]. A gain of 30 is a widely accepted value in the literature for on-beam [90,98]. Similar values were obtained with off-beam spectrophones [95].

1.3.4. A variety of other designs

Since its invention in 2002, a variety of QEPAS designs were presented. The main objective of those designs is to improve the sensor sensitivity, that is to lower the limit of detection. It can be realized by increasing the signal at any stage of the sensor: optical, acoustic, mechanical or electrical. The QEPAS signal is directly proportional to the absorbed optical power (αP). The optical power can be increased by using high power sources such as QCLs [99], OPOs [100], fiber amplifiers [101]. Multiple optical passes can also provide an additional optical energy between the QTF prongs. Another possibility is to place the QTF in an optical cavity [102,103]. After the photoacoustic generation, the acoustic wave is generally further amplified using acoustic microresonators (section 1.3.3). Many mR configurations were proposed, often based on on-beam and off-beam, using multiple cylindrical mR [104,105], single on-beam mR [106,107] which improves the mR-QTF acoustic coupling. Multiple QTFs can be combined to collect more acoustic energy [105]. The QTF current can be enhanced by employing a material with a higher piezoelectric coefficient such as lithium niobate [108]. The SNR can be reduced by designing a low-noise electronic circuit [82]. QEPAS was combined with gas chromatography, forming a very sensitive sensor [109,110].

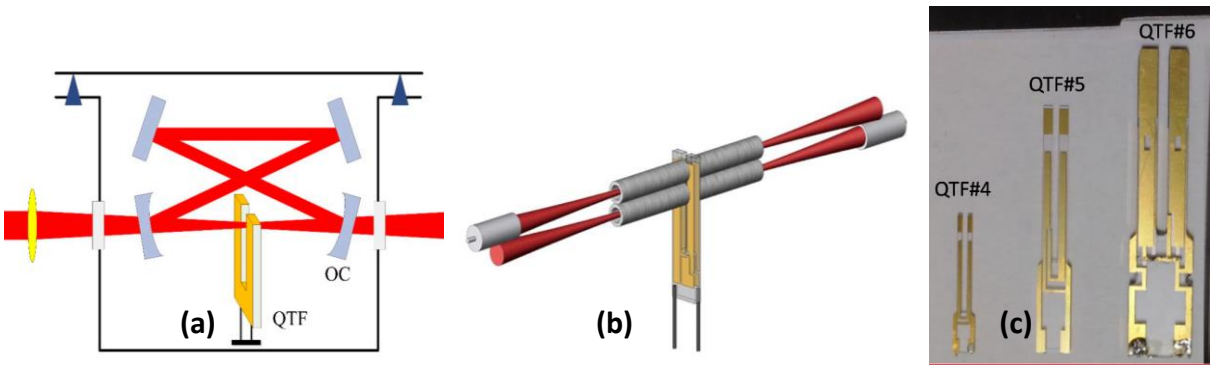

Figure 1.29: The QEPAS signal can be enhanced optically, for instance with an optical cavity [103] (a), acoustically, typically by using microresonators such as the double mR [104] (b), and mechanically, as by using custom QTFs optimized for the QEPAS [75] (c).

The alternative configurations tend to provide from a moderate improvement to very large improvement, up to 250 claimed for I-QEPAS. The gain in sensitivity is often balanced by a more complex setup which translates to a more expensive sensor, though the cost-to-sensitivity-gain ratio could be justified for certain applications such as military or medical applications. The robustness of the sensor can also be affected by a complex setup, for instance adding the mR renders the spectrophone prone to drifts upon gas density variations. Some authors have suggested to use the most simple configuration with a bare QTF to keep the QEPAS sensor robust and low-cost [111].

Aside sensitivity-improved complex system, efforts have been made to tackle the common QEPAS specific issues. The narrow QTF gap has always been a limitation to use lasers with coarse and divergent beam profiles. We saw that the off-beam configuration was a possibility to overcome the issue, but there are others, such as the use of optical fibers to guide the laser between the prongs. In the mid-Infrared, both hollow [112] and solid core [113] fibers were employed. An all optical fiber system was also demonstrated by tapering the fiber to generate an evanescent wave which interacts with the gas sample [114]. A great work has also been done on fabricating custom QTFs, i.e. QTFs adapted to QEPAS [74,115]. The custom QTFs benefit from a larger QTF gap, which makes them suitable for working in the mid-infrared and even in the THz region [115]. Additionally, they were designed to work at a lower frequency (4kHz in [115]) than the standard QTF, which enables the detection of molecules with slow relaxation rates.

Many configurations have been presented to improve the sensitivity of the QEPAS sensor, though sometimes at the expanse of the sensor cost and complexity. The performances of the different configuration are often compared by measuring the limit of detection and a figure of merit called the NNEA.

1.3.5. Evaluation of the limit of detection using the Allan plot

The limit of detection (LOD) is the minimum concentration that can be detected by the sensor. The concept of ‘sensitivity’ in gas sensing does not correspond to the usual definition in physics: a sensor with a low LOD is qualified as “sensitive”. The LOD is reached when the sensor signal equals the sensor noise, i.e. the SNR equals to 1 (1σ), (or sometimes three times the noise (3σ)). If the SNR is below 1, the signal is not readable among the noise, hence the criterion for the LOD. What we call noise is the measurement dispersion, i.e. the random variations of the measured value around its mean value. Signal averaging is a well-known technique to reduce the noise, which consequently improves the sensor LOD, as illustrated on Figure 1.30. The longer the integration time is, the smaller the dispersion and the higher the SNR. However, over long period of time, the sensor is prone to instabilities (the topic is discussed in Chapter 3), for instance due to the variation of the temperature, which limits the SNR improvement by signal averaging. Therefore, there is an optimum averaging time that maximizes the LOD. This optimum can be found using the Allan variance.

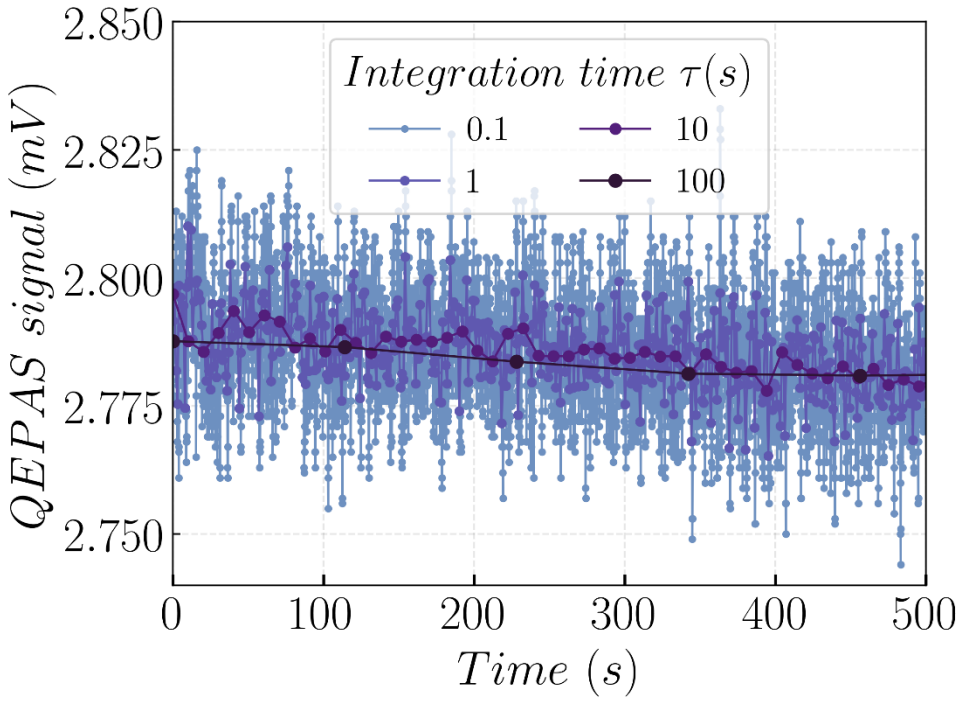

Figure 1.30: Effect of the averaging on the QEPAS signal. The light blue curve corresponds to the raw data recorded at a sample rate of 10Sa/s. The LIA integration time is set to 100ms which corresponds to a filter bandwidth of 0.81Hz.

The Allan variance is a statistical tool used to measure the time domain stability of oscillators [116]. The tool can be transposed to study the stability over time of any physical parameter. It was introduced by Werle [117] in the field of optical gas sensors, and since that, has been widely applied in laser spectroscopy and particularly in QEPAS, and is known as the Allan-Werle variance.

The output signal of a gas sensor, when measuring a concentration C_{ppmv} of the target specie (light blue curve on Figure 1.30) is typically a set N data points y_i, with a step time Δt between two consecutive points (Figure 1.31). In order to smooth the signal, the original data can be resampled with a longer timestep $\tau=k\Delta t$ by applying a moving average. The new sample contains M=N/k subsets and the value A_m of each subset m is calculated as the average over k data points:

$$A_m(\tau) = \frac{1}{k}\sum_{i=1}^{k} y_{(m-1)k+i} \tag{1.73}$$

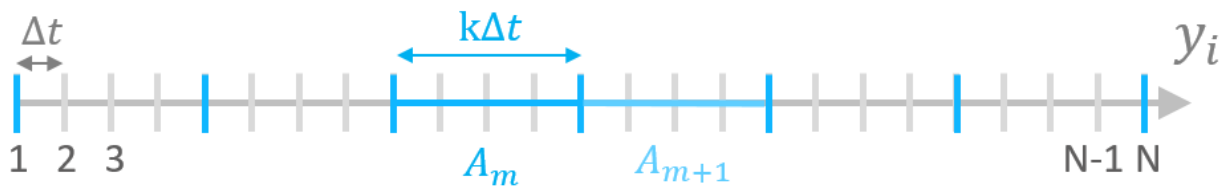

Figure 1.31: Illustration of the construction of the A_m subsets from the original data points y_i.

Then, the Allan variance is defined as:

$$\sigma_A{}^2(\tau) = \frac{1}{2(M-1)} \sum_{m=1}^{M} [A_m(\tau) - A_{m-1}(\tau)]^2 \quad (1.74)$$

Taking the square root to obtain the Allan deviation, the SNR can be defined as:

$$SNR(\tau) = \frac{\bar{x}}{\sigma_A(\tau)} \quad (1.75)$$

with $\bar{x}$ the average value of the variable x_i. The limit of detection of the sensor can be obtained as:

$$LOD(\tau) = \frac{C_{ppmv}}{SNR(\tau)} \quad (1.76)$$

with C_{ppmv} the concentration of the target species (defined as in equation (1.10)).

The Allan deviation highly depends on the measurement conditions, which are not equivalent in the literature: for instance, some authors record the QEPAS signal with a neutral gas to measure the noise while others measure it with the cell filled with the target specie [118]. In order to obtain the real conditions of the sensor and accounts for the noise sources at the different stages (laser emission, gas absorption), it seems logical to have the sensor under operation and the gas cell filled with a given concentration of target gas before measuring the sensor output.

A typical curve of the Allan deviation (adev) is presented on Figure 1.32, calculated using the data from Figure 1.30. The first point of the curve (blue dot, Figure 1.32) corresponds to the LOD obtained for the raw data (blue curve, Figure 1.30). On the short-term, the Allan deviation (grey curve) decreases, which indicates an improvement of the LOD due to the signal averaging. The curve slope (here $\tau^{-1/2}$) depends on the type of noise, here it is a white noise (blue curve), as expected for the QTF Brownian noise. The deviation from the $\tau^{-1/2}$ curve at short integration times is due to the low-pass filter of the lock-in amplifier which causes an anti-aliasing effect [119]. The LOD reaches a minimum at t = 50s. On the long term, the Allan deviation increases due to the drift of the system (orange curve). As the integration time increases, the number of subset decreases, which results in a larger error as indicated by the error bars. The number of subsets can be increased 'numerically' by taking the average of multiple Allan deviations, this is called the overlapped Allan deviation (oadev). The Allan deviation is repeated k times, and each subset is offset by k, thus increasing the number of subsets and consequently increasing the confidence of the deviation of oadev compared to adev one. The complete expression of the oadev is tedious and can be found in [116]. It is shown on Figure 1.32 (dark blue curve) and exhibits a smaller error than the Allan deviation for large values of τ.

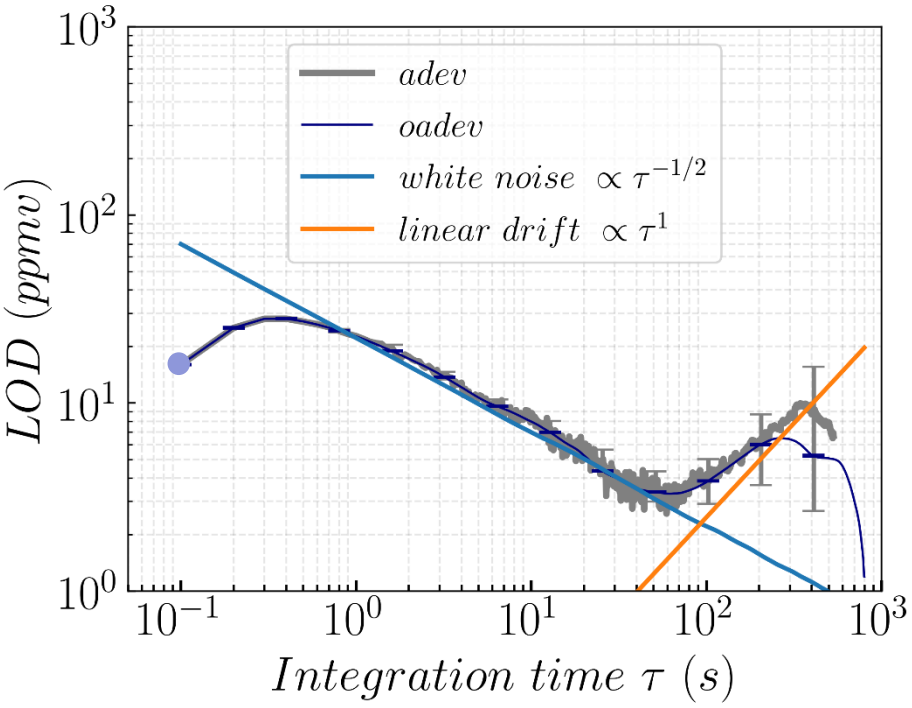

Figure 1.32: Allan deviation (adev) and overlapped Allan deviation (oadev), and the corresponding errors, are calculated with the allantools library on Python. The blue dot corresponds to the measured value with the raw data.

The Allan deviation is a good indicator of the system stability and allows to determine the sensor LOD at a given integration time. However, the Allan deviation cannot be used to compare the performance of the different QEPAS spectrophones. Another criterion is used, the Normalized Noise Equivalent Absorption (NNEA), which is defined as:

$$NNEA = \frac{\alpha_{LOD} \cdot P}{\sqrt{\Delta f}} \tag{1.77}$$

The NNEA, expressed in $cm^{-1} \cdot W \cdot Hz^{-1/2}$, takes into account the laser power P, the absorption coefficient at the limit of detection α_{LOD} and the integration bandwidth Δf. It can be used to compare QEPAS spectrophones independently from the absorbed optical power, the intensity of the absorption and the LIA integration time. Its value typically ranges from 10^{-8} to 10^{-9} $cm^{-1} \cdot W \cdot Hz^{-1/2}$ [76]. The lower the NNEA is, the more sensitive the QEPAS sensor. Although the NNEA does not take into account all the parameters, such as the modulation scheme or the shape of the absorption profile, it is a practical tool for the quick prediction of the LOD of a given QEPAS sensor with a given laser power and a given absorption line. We employ it in the next chapter for assessing the feasibility of the QEPAS sensor for the detection of our target species of the project MULTIPAS.

1.4. Conclusion

Laser spectroscopy distinguishes from other gas sensing techniques by offering very good sensitivity and selectivity. It became even more attractive with the recent availability of powerful and compact mid-infrared lasers such as the QCLs. The direct optical detection of the absorption has limited performances, but can be improved by increasing the path length, for instance using multipass or resonant cells, or by reducing the noise by applying a modulation. The modulation can be applied onto the laser wavelength, and the resulting signals were theoretically described and can be used to improve the sensor's performances. The modulated absorption can also be measured through to the generation of an acoustic wave. The sensors based on photoacoustic spectroscopy allow to achieve small footprints while preserving the sensitivity and the selectivity of laser-based sensors. Photoacoustic detectors are achromatic and therefore compatible with any mid infrared lasers. The acoustic wave is detected by a very sensitive transducer, such as the Quartz Tuning Fork. Further enhancement can be obtained by adding microresonators. The next chapter is dedicated to the study and optimization of a QEPAS sensor in the off-beam configuration and its implementation with quantum cascade lasers. The sensor is tested at two different wavelengths: at 11μm for the detection of ethylene and at 4.6μm the detection of carbon monoxide with an application on breath analysis.

1.5. References

1. Gordon, I.E.; Rothman, L.S.; Hill, C.; Kochanov, R. V.; Tan, Y.; Bernath, P.F.; Birk, M.; Boudon, V.; Campargue, A.; Chance, K. V.; et al. The HITRAN2016 molecular spectroscopic database. *J. Quant. Spectrosc. Radiat. Transf.* **2017**, *203*, 3–69.
2. Griffiths, P.R.; de Haseth, J.A. *Fourier Transform Infrared Spectrometry*; Sons, J.W.&, Ed.; 2007;
3. Vandenbroucke, A. Abatement of Volatile Organic Compounds by Combined Use of Non-Thermal Plasma and Heterogeneous Catalysis, Ghent University, 2015.
4. Hodgkinson, J.; Smith, R.; Ho, W.O.; Saffell, J.R.; Tatam, R.P. Non-dispersive infra-red (NDIR) measurement of carbon dioxide at 4.2 μm in a compact and optically efficient sensor. *Sensors Actuators, B Chem.* **2013**, *186*, 580–588.
5. Hodgkinson, J.; Tatam, R.P. Optical gas sensing: A review. *Meas. Sci. Technol.* **2013**, *24*.
6. Makeenkov, A.; Lapitskiy, I.; Somov, A.; Baranov, A. Flammable gases and vapors of flammable liquids: Monitoring with infrared sensor node. *Sensors Actuators, B Chem.* **2015**, *209*, 1102–1107.
7. Fanchenko, S.; Baranov, A.; Savkin, A.; Petukhov, A.; Kalinina, K.; Zhurtanov, B.; Velikotny, M. Non-dispersive LED-based methane open path detector capabilities. *2015 IEEE Work. Environ. Energy, Struct. Monit. Syst. EESMS 2015 - Proc.* **2015**, 146–151.
8. Fanchenko, S.; Baranov, A.; Savkin, A.; Sleptsov, V. LED-based NDIR natural gas analyzer. *IOP Conf. Ser. Mater. Sci. Eng.* **2016**, *108*, 012036.
9. Von Bandel, N.; Myara, M.; Sellahi, M.; Souici, T.; Dardaillon, R.; Signoret, P. Time-dependent laser linewidth: beat-note digital acquisition and numerical analysis. *Opt. Express* **2016**, *24*, 27961–27978.
10. Tournié, E.; Baranov, A.N. *Mid-Infrared Semiconductor Lasers. A Review.*; 1st ed.; Elsevier Inc., 2012; Vol. 86; ISBN 9780123910660.
11. Tacke, M. Lead–salt lasers. *Philos. Trans. R. Soc. London A Math. Phys. Eng. Sci.* **2001**, *359*, 547–566.
12. Tournié, E.; Cerutti, L. *Mid-infrared Optoelectronics Materials, Devices, and applications*; Elsevier, Ed.; 2020; ISBN 978-0-08-102738-7.
13. Yao, Y.; Hoffman, A.J.; Gmachl, C.F. Mid-infrared quantum cascade lasers. *Nat. Photonics* **2012**, *6*, 432–439.
14. mirSense Available online: http://mirsense.com/products/.
15. Nicoletti, S.; Barritault, P.; Boutami, S.; Brun, M.; Glière, A.; Labeye, P.; Rouxel, J.; Czarny, J.; Lhermet, H.; Carras, M.; et al. Challenges in the realization of a fully integrated optical lab-on-chip. *Proc. IEEE Sensors* **2014**, 649–652.
16. Reed, G.T.; Mashanovich, G.; Gardes, F.Y.; Thomson, D.J. Silicon optical modulators. *Nat. Photonics* **2010**, *4*, 518–526.
17. Michel, J.; Liu, J.; Kimerling, L.C. High-performance Ge-on-Si photodetectors. *Nat. Photonics* **2010**, *4*, 527–534.
18. Schwaighofer, A.; Brandstetter, M.; Lendl, B. Quantum cascade lasers (QCLs) in biomedical spectroscopy. *Chem. Soc. Rev.* **2017**, *46*, 5903–5924.
19. Hugi, A.; Villares, G.; Blaser, S.; Liu, H.C.; Faist, J. Mid-infrared frequency comb based on a quantum cascade laser. *Nature* **2012**, *492*, 229–233.
20. Gaida, C.; Gebhardt, M.; Heuermann, T.; Stutzki, F.; Jauregui, C.; Antonio-Lopez, J.; Schülzgen, A.; Amezcua-Correa, R.; Tünnermann, A.; Pupeza, I.; et al. Watt-scale super-octave mid-infrared intrapulse difference frequency generation. *Light Sci. Appl.* **2018**, *7*, 1–8.
21. Kiely, R. Understanding and Eliminating 1 / f Noise. *Analog Devices* **2017**, 1–12.
22. Kosterev, A.A.; Dong, L.; Thomazy, D.; Tittel, F.K.; Overby, S. QEPAS for chemical analysis of multi-component gas mixtures. *Appl. Phys. B Lasers Opt.* **2010**, *101*, 649–659.
23. Schilt, S. Mesure de traces de gaz à l'aide de lasers à semi-conducteur, EPFL, 2002.
24. Arndt, R. Analytical line shapes for Lorentzian signals broadened by modulation. *J. Appl. Phys.*

1965, *36*, 2522–2524.
25. Schilt, S.; Thevenaz, L.; Robert, P. Wavelength modulation spectroscopy : combined frequency and intensity laser modulation. *Appl. Opt.* **2003**, *42*, 6728–6738.
26. Herriott, D.; Kogelnik, H.; Kompfner, R. Off-Axis Paths in Spherical Mirror Interferometers. **1964**, *3*, 523–526.
27. White, J.U. Very Long Optical Paths in Air. *J Opt Soc Am* **1976**, *66*, 411–416.
28. Tuzson, B.; Mangold, M.; Looser, H.; Manninen, A.; Emmenegger, L. Compact multipass optical cell for laser spectroscopy. **2013**, *38*, 257–259.
29. Aeris Technologies Available online: http://aerissensors.com/technology/.
30. Romanini, D., Kachanov, A. A., Sadeghi, N., & Stoeckel, F. Cavity Ring-Down Spectroscopy. *Chem. Phys. Lett.* **2009**, *264*, 316–322.
31. ap2e Available online: https://www.ap2e.com/en/enhanced-ir-laser-technology/.
32. Foltynowicz, A.; Schmidt, F.M.; Ma, W.; Axner, O. Noise-immune cavity-enhanced optical heterodyne molecular spectroscopy: Current status and future potential. *Appl. Phys. B Lasers Opt.* **2008**, *92*, 313–326.
33. Bell, A.G. On the production and reproduction of sound by light: The photophone. *Am. J. Sci.* **1880**, *20*, 305–324.
34. Viegerov, M.L. Eine methode der gasanalyse, beruhend auf der optisch-akustischen tyndall-rontgenerscheinung. ¨. *Dokl. Akad. Nauk SSSR* **1938**, *19*, 687–688.
35. Kreuzer, L.B. Ultralow gas concentration infrared absorption spectroscopy. *J. Appl. Phys.* **1971**, *42*, 2934–2943.
36. Kerr, E.L.; Atwood, J.G. The Laser Illuminated Absorptivity Spectrophone: A Method for Measurement of Weak Absorptivity in Gases at Laser Wavelengths. *Appl. Opt.* **1968**, *7*, 915.
37. Zeninari, V.; Kapitanov, V.A.; Courtois, D.; Ponomarev, Y.N. Design and characteristics of a differential Helmholtz resonant photoacoustic cell for infrared gas detection. *Infrared Phys. Technol.* **1999**, *40*, 1–23.
38. Rouxel, J.; Coutard, J.G.; Gidon, S.; Lartigue, O.; Nicoletti, S.; Parvitte, B.; Vallon, R.; Zéninari, V.; Glière, A. Miniaturized differential Helmholtz resonators for photoacoustic trace gas detection. *Sensors Actuators, B Chem.* **2016**, *236*, 1104–1110.
39. Bauer, R.; Stewart, G.; Johnstone, W.; Boyd, E.; Lengden, M. 3D-printed miniature gas cell for photoacoustic spectroscopy of trace gases. *Opt. Lett.* **2014**, *39*, 4796–4799.
40. Bernegger, S.; Sigrist, M.W. Longitudinal resonant spectrophone for CO-laser photoacoustic spectroscopy. *Appl. Phys. B* **1987**, *44*, 125–132.
41. Bijnen, F.G.C.; Reuss, J.; Harren, F.J.M. Geometrical optimization of a longitudinal resonant photoacoustic cell for sensitive and fast trace gas detection. *Rev. Sci. Instrum.* **1996**, *67*, 2914–2923.
42. Miklós, A.; Hess, P.; Bozóki, Z. Application of acoustic resonators in photoacoustic trace gas analysis and metrology. *Rev. Sci. Instrum.* **2001**, *72*, 1937–1955.
43. Pao, Y.-H. *Optoacoustic spectroscopy and detection*; Elsevier, Ed.; 2012;
44. Bohn, D.A. Environmental effects on the speed of sound. *83rd AES Conv.* **1987**.
45. Besson, J.P.; Thévenaz, L. Photoacoustic spectroscopy for multi-gas sensing using near infrared lasers, EPFL, 2006.
46. Schilt, S.; Thévenaz, L. Wavelength modulation photoacoustic spectroscopy: theoretical description and experimental results. *Infrared Phys. Technol.* **2006**, *48*, 154–162.
47. CHAMASSI, K. Détecteur de gaz multi-espèces par mesure photo-acoustique à effet capacitif, University of Montpellier, 2018.
48. Günther, P.; Fischer, U.C.; Dransfeld, K. Scanning near-field acoustic microscopy. *Appl. Phys. B* **1989**, *48*, 89–92.
49. Karraï, K.; Grober, R.D. Piezoelectric tip-sample distance control for near field optical microscopes. **1995**, *66*, 1842–1844.
50. Grober, R.D.; Acimovic, J.; Schuck, J.; Hessman, D.; Kindlemann, P.J.; Hespanha, J.; Morse, A.S. Fundamental limits to force detection using quartz tuning forks. **2000**, *71*, 2776–2780.
51. Akiyama, T.; Staufer, U.; De Rooij, N.F.; Frederix, P.; Engel, A. Symmetrically arranged quartz tuning fork with soft cantilever for intermittent contact mode atomic force microscopy. *Rev. Sci. Instrum.* **2003**, *74*, 112–117.

52. Zhang, J.; O'Shea, S. Tuning forks as micromechanical mass sensitive sensors for bio- or liquid detection. *Sensors Actuators, B Chem.* **2003**, *94*, 65–72.
53. Toledo, J.; Manzaneque, T.; Hernando-García, J.; Vázquez, J.; Ababneh, A.; Seidel, H.; Lapuerta, M.; Sánchez-Rojas, J.L. Application of quartz tuning forks and extensional microresonators for viscosity and density measurements in oil/fuel mixtures. *Microsyst. Technol.* **2014**, *20*, 945–953.
54. Matsiev, L.F. Application of flexural mechanical resonators to simultaneous measurements of liquid density and viscosity. *Proc. IEEE Ultrason. Symp.* **1999**, *1*, 457–460.
55. Zeisel, D.; Menzi, H.; Ullrich, L. Precise and robust quartz sensor based on tuning fork technology for (SF6)-gas density control. *Sensors Actuators, A Phys.* **2000**, *80*, 233–236.
56. Kosterev, A.A.; Bakhirkin, Y.A.; Curl, R.F.; Tittel, F.K. Quartz-enhanced photoacoustic spectroscopy. *Opt. Lett.* **2002**, *27*, 1902–1904.
57. Kosterev, A.A.; Doty, III, J.H. Resonant optothermoacoustic detection: technique for measuring weak optical absorption by gases and micro-objects. *Opt. Lett.* **2010**, *35*, 3571.
58. Ma, Y.; He, Y.; Tong, Y.; Yu, X.; Tittel, F.K. Quartz-tuning-fork enhanced photothermal spectroscopy for ultra-high sensitive trace gas detection. *Opt. Express* **2018**, *26*, 32103.
59. Martin, S.J.; Frye, G.C.; Wessendorf, K.O. Sensing liquid properties with thickness-shear mode resonators. *Sensors Actuators A. Phys.* **1994**, *44*, 209–218.
60. Vashist, S.K.; Vashist, P. Recent advances in quartz crystal microbalance-based sensors. *J. Sensors* **2011**, *2011*.
61. Vig, J.. R. Quartz crystal resonators and oscillators. *US Army Commun. Command* **2001**.
62. Patimisco, P.; Scamarcio, G.; Tittel, F.K.; Spagnolo, V. Quartz-enhanced photoacoustic spectroscopy: a review. *Sensors* **2014**, *14*.
63. Gagnepain, J. Sensitivity of Quartz Oscillators to to the environment: characterization methods and pitfalls. *IEEE Trans. Ultrason. Ferroelectr. Freq. Control* **1990**, *37*, 347–354.
64. Rust, H.; Heyde, M.; Freund, H. Signal electronics for an atomic force microscope equipped with a double quartz tuning fork sensor. *Rev. Sci. Instrum.* **2006**, *77*, 1–8.
65. Sell, J.K.; Niedermayer, A.O.; Babik, S.; Jakoby, B. Real-time monitoring of a high pressure reactor using a gas density sensor. *Sensors Actuators, A Phys.* **2010**, *162*, 215–219.
66. Castellanos-gomez, A.; Agraït, N.; Rubio-Bollinger, G. Characterization and Optimization of Quartz Tuning Fork-Based Force Sensors for Combined STM / AFM. In *Scanning Probe Microscopy in Nanoscience and Nanotechnology 3*.; 2012; pp. 23–53 ISBN 9783642254147.
67. Aoust, G. Developpements de sources infrarouges et de resonateurs en quartz pour la spectroscopie photoacoustique, Paris-Saclay.
68. Christen, M. Air and gas damping of quartz tuning forks. *Sensors and Actuators* **1983**, *4*, 555–564.
69. Nakamura, Y.; Miyashita, S. Frequency-Temperature Characteristics of Quartz Crystal Flexure Bars and Quartz Crystal Tuning Forks. *IEEE Trans. Sonics Ultrason.* **1979**, *26*, 369–376.
70. Hirata, M.; Kokubun, K.; Ono, M.; Nakayama, K. Size effect of a quartz oscillator on its characteristics as a friction vacuum gauge. *J. Vac. Sci. Technol. A Vacuum, Surfaces, Film.* **1985**, *3*, 1742–1745.
71. Friedt, J.-M.; Carry, É. Introduction to the quartz tuning fork. *Am. J. Phys.* **2007**, *75*, 415–422.
72. Le Foulgoc, B.; Bourouina, T.; Le Traon, O.; Bosseboeuf, A.; Marty, F.; Breluzeau, C.; Grandchamp, J.P.; Masson, S. Highly decoupled single-crystal silicon resonators: An approach for the intrinsic quality factor. *J. Micromechanics Microengineering* **2006**, *16*.
73. Aoust, G.; Levy, R.; Bourgeteau, B.; Traon, O. Le Acoustic damping on flexural mechanical resonators. *Sensors Actuators, A Phys.* **2016**, *238*, 158–166.
74. Aoust, G.; Levy, R.; Verlhac, B.; Le Traon, O. Optimal quality factor for tuning forks in a fluid medium. *Sensors Actuators, A Phys.* **2016**, *243*, 134–138.
75. Patimisco, P.; Sampaolo, A.; Dong, L.; Giglio, M.; Scamarcio, G.; Tittel, F.K.; Spagnolo, V. Analysis of the electro-elastic properties of custom quartz tuning forks for optoacoustic gas sensing. *Sensors Actuators, B Chem.* **2016**, *227*, 539–546.
76. Patimisco, P.; Sampaolo, A.; Dong, L.; Tittel, F.K.; Spagnolo, V. Recent advances in quartz enhanced photoacoustic sensing. *Appl. Phys. Rev.* **2018**, *5*.
77. Hussain, D.; Song, J.; Zhang, H.; Meng, X.; Yongbing, W.; Xie, H. Optimizing the quality factor

of quartz tuning fork force sensor for atomic force microscopy: Impact of additional mass and mass rebalance. *IEEE Sens. J.* **2017**, *17*, 2797–2806.
78. Ctistis, G.; Frater, E.H.; Huisman, S.R.; Korterik, J.P.; Herek, J.L.; Vos, W.L.; Pinkse, P.W.H. Controlling the quality factor of a tuning-fork resonance between 9 and 300 K for scanning-probe microscopy. *J. Phys. D. Appl. Phys.* **2011**, *44*.
79. González, L.; Otero, J.; Cabezas, G.; Puig-vidal, M. Physical Electronic driver with amplitude and quality factor control to adjust the response of quartz tuning fork sensors in atomic force microscopy applications. *Sensors Actuators A. Phys.* **2012**, *184*, 112–118.
80. Ba, T.N. Mesures de traces de gaz par spectroscopie d ' absorption par diodes laser accordables . Application à la surveillance de l ' environnement ., University of Montpellier, 2014.
81. Ramus, X. Transimpedance Considerations for High-Speed Amplifiers. *Appl. Rep.* **2009**.
82. Winkowski, M.; Stacewicz, T. Low noise, open-source QEPAS system with instrumentation amplifier. *Sci. Rep.* **2019**, *9*, 1–6.
83. Schilt, S.; Besson, J.P.; Thévenaz, L. Near-infrared laser photoacoustic detection of methane : the impact of molecular relaxation. *Appl. Phys. B* **2005**, *82*, 319–328.
84. Dong, L.; Lewicki, R.; Liu, K.; Buerki, P.R.; Weida, M.J.; Tittel, F.K. Ultra-sensitive carbon monoxide detection by using EC-QCL based quartz-enhanced photoacoustic spectroscopy. *Appl. Phys. B Lasers Opt.* **2012**, *107*, 275–283.
85. Ren, W.; Shi, C.; Wang, Z.; Yao, C. QEPAS nitric oxide sensor based on a mid-infrared fiber-coupled quantum cascade laser. In Proceedings of the 2017 25th Optical Fiber Sensors Conference (OFS); IEEE; pp. 3–6.
86. Wysocki, G.; Kosterev, A.A.; Tittel, F.K. Influence of molecular relaxation dynamics on quartz-enhanced photoacoustic detection of CO2 at λ =2 μm. *Appl. Phys. B* **2006**, *85*, 301–306.
87. Mordmueller, M.; Schade W; Willer, U. QEPAS with electrical co - excitation for photoacoustic measurements in fluctuating background gases, 2017, Vol. 123.
88. Kosterev, A.A.; Bakhirkin, Y.A.; Tittel, F.K. Ultrasensitive gas detection by quartz-enhanced photoacoustic spectroscopy in the fundamental molecular absorption bands region. *Appl. Phys. B Lasers Opt.* **2005**, *80*, 133–138.
89. Petra, N.; Zweck, J.; Kosterev, A.A.; Minkoff, S.E.; Thomazy, D. Theoretical analysis of a quartz-enhanced photoacoustic spectroscopy sensor. *Appl. Phys. B Lasers Opt.* **2009**, *94*, 673–680.
90. Dong, L.; Kosterev, A.A.; Thomazy, D.; Tittel, F.K. QEPAS spectrophones: Design, optimization, and performance. *Appl. Phys. B Lasers Opt.* **2010**, *100*, 627–635.
91. Kosterev, A.A.; Buerki, P.R.; Dong, L.; Reed, M.; Day, T.; Tittel, F.K. QEPAS detector for rapid spectral measurements. *Appl. Phys. B Lasers Opt.* **2010**, *100*, 173–180.
92. Wang, Z.; Li, Z.; Ren, W. Quartz-enhanced photoacoustic detection of ethylene using a 10.5 μm quantum cascade laser. *Opt. Express* **2016**, *24*, 4143–4154.
93. Rück, T. Development, characterization and miniaturization of a trace gas detection system for NO2 in air based on photoacoustic spectroscopy, 2019.
94. Yi, H.; Liu, K.; Sun, S.; Zhang, W.; Gao, X. Theoretical analysis of off beam quartz-enhanced photoacoustic spectroscopy sensor. *Opt. Commun.* **2012**, *285*, 5306–5312.
95. Yi, H.; Chen, W.; Sun, S.; Liu, K.; Tan, T.; Gao, X. T-shape microresonator-based high sensitivity quartz-enhanced photoacoustic spectroscopy sensor. *Opt. Express* **2012**, *20*, 9187–9196.
96. Kinsler, L.E.; Frey, A.R.; Coppens, A.B.; Sanders, J. V *Fundamentals of acoustics*; 4th Editio.; Wiley-VCH;
97. Miklós, A.; Hess, P.; Bozóki, Z. Application of acoustic resonators in photoacoustic trace gas analysis and metrology. *Rev. Sci. Instrum.* **2001**, *72*, 1937–1955.
98. Yi, H.; Chen, W.; Guo, X.; Sun, S.; Liu, K.; Tan, T.; Zhang, W.; Gao, X. An acoustic model for microresonator in on-beam quartz-enhanced photoacoustic spectroscopy. *Appl. Phys. B* **2012**, *108*, 361–367.
99. Ma, Y.; Lewicki, R.; Razeghi, M.; Tittel, F.K. QEPAS based ppb-level detection of CO and N 2 O using a high power CW DFB-QCL. **2013**, *21*, 1008–1019.
100. Ngai, A.K.Y.; Persijn, S.T.; Lindsay, I.D.; Kosterev, A.A.; Groß, P.; Lee, C.J.; Cristescu, S.M.; Tittel, F.K.; Boller, K.J.; Harren, F.J.M. Continuous wave optical parametric oscillator for

quartz-enhanced photoacoustic trace gas sensing. *Appl. Phys. B Lasers Opt.* **2007**, *89*, 123–128.
101. Wu, H.; Dong, L.; Zheng, H.; Liu, X.; Yin, X.; Ma, W.; Zhang, L.; Yin, W.; Jia, S.; Tittel, F.K. Enhanced near-infrared QEPAS sensor for sub-ppm level H2S detection by means of a fiber amplified 1582 nm DFB laser. *Sensors Actuators, B Chem.* **2015**, *221*, 666–672.
102. Hayden, J.; Giglio, M.; Sampaolo, A.; Patimisco, P.; Spagnolo, V.; Lendl, B. Intracavity quartz-enhanced photoacoustic spectroscopy for CO/N2O detection in the part-per-trillion concentration range. **2020**, *1128821*.
103. Spagnolo, V.; Borri, S.; Patimisco, P.; Galli, I.; Mazzotti, D.; Giusfredi, G.; Akikusa, N.; Yamanishi, M. Intracavity quartz-enhanced photoacoustic sensor. *Appl. Phys. Lett.* **2014**, *104*, 091114.
104. Dong, L.; Wu, H.; Zheng, H.; Liu, Y.; Liu, X.; Jiang, W.; Zhang, L.; Ma, W.; Ren, W.; Yin, W.; et al. Double acoustic microresonator quartz-enhanced photoacoustic spectroscopy. *Opt. Lett.* **2014**, *39*, 2479.
105. Zheng, H.; Dong, L.; Wu, H.; Yin, X.; Xiao, L.; Jia, S.; Curl, R.F.; Tittel, F.K. Application of acoustic micro-resonators in quartz-enhanced photoacoustic spectroscopy for trace gas analysis. *Chem. Phys. Lett.* **2018**, *691*, 462–472.
106. Serebryakov, D. V; Morozov, I. V; Kosterev, A.A.; Letokhov, V.S. Laser microphotoacoustic sensor of ammonia traces in the atmosphere. *Quantum Electron.* **2010**, *40*, 167–172.
107. Zheng, H.; Dong, L.; Sampaolo, A.; Patimisco, P.; Ma, W.; Zhang, L.; Yin, W.; Xiao, L.; Spagnolo, V.; Jia, S.; et al. Overtone resonance enhanced single-tube on-beam quartz enhanced photoacoustic spectrophone. *Appl. Phys. Lett.* **2016**, *109*.
108. Liu, Y.; Difoggio, R.; Sanderlin, K.; Perez, L.; Zhao, J. Measurement of density and viscosity of dodecane and decane with a piezoelectric tuning fork over 298-448 K and 0.1-137.9 MPa. *Sensors Actuators, A Phys.* **2011**, *167*, 347–353.
109. Zampolli, S.; Mengali, S.; Liberatore, N.; Elmi, I.; Masini, L.; Sanmartin, M.; Viola, R. A MEMS-enabled deployable trace chemical sensor based on fast gas-chromatography and quartz enhanced photoacousic spectoscopy. *Sensors* **2020**, *20*, 120.
110. Viola, R.; Liberatore, N.; Luciani, D.; Mengali, S. Quartz Enhanced Photoacoustic Spectroscopy for Detection of Improvised Explosive Devices and Precursors. *Adv. Opt. Technol.* **2016**, *2016*.
111. Breitegger, P.; Schweighofer, B.; Wegleiter, H.; Knoll, M.; Lang, B.; Bergmann, A. Towards Low-Cost QEPAS Sensors for Nitrogen Dioxide Detection. *Photoacoustics* **2020**, 100169.
112. Spagnolo, V.; Patimisco, P.; Borri, S.; Scamarcio, G.; Bernacki, B.E.; Kriesel, J. Mid-infrared fiber-coupled QCL-QEPAS sensor. *Appl. Phys. B Lasers Opt.* **2013**, *112*, 25–33.
113. Li, Z.; Shi, C.; Ren, W. Mid-infrared multimode fiber-coupled quantum cascade laser for off-beam quartz-enhanced photoacoustic detection. *Opt. Lett.* **2016**, *41*, 4095–4098.
114. Li, Z.; Wang, Z.; Qi, Y.; Jin, W.; Ren, W. Sensors and Actuators B : Chemical Improved evanescent-wave quartz-enhanced photoacoustic CO sensor using an optical fiber taper. *Sensors Actuators B. Chem.* **2017**, *248*, 1023–1028.
115. Patimisco, P.; Borri, S.; Sampaolo, A.; Beere, H.E.; Ritchie, D. a; Vitiello, M.S.; Scamarcio, G.; Spagnolo, V. A quartz enhanced photo-acoustic gas sensor based on a custom tuning fork and a terahertz quantum cascade laser. *Analyst* **2014**, *139*, 2079–87.
116. Riley, W.J. *Handbook of Frequency Stability Analysis*; National Institute of Standards and Technology: Washington, US, 2008; ISBN 3019753058.
117. Werle, P.; Mücke, R.; Slemr, F. The limits of signal averaging in atmospheric trace-gas monitoring by tunable diode-laser absorption spectroscopy (TDLAS). *Appl. Phys. B Photophysics Laser Chem.* **1993**, *57*, 131–139.
118. Yi, H.; Liu, K.; Chen, W.; Tan, T.; Wang, L.; Gao, X. Application of a broadband blue laser diode to trace NO_2 detection using off-beam quartz-enhanced photoacoustic spectroscopy. *Opt. Lett.* **2011**, *36*, 481.
119. Calosso, C.E.; Clivati, C.; Micalizio, S. Avoiding aliasing in fiber link data analysis. *2016 Eur. Freq. Time Forum, EFTF 2016* **2016**, *63*, 646–655.

Chapter 2

Experiments

2.1. MULTIPAS project: Selected gases and required laser power

Laser spectroscopy offers high selectivity and sensitivity over other sensing methods. While most of the light sources are broadband, single-mode lasers offer this incredible property to concentrate the optical power in a very narrow spectral band. Because the laser linewidth is inferior to the molecular absorption linewidth, the whole laser spectra is efficiently contributing to the absorption, giving the high sensitivity of laser based spectroscopic methods. The selectivity is obtained by a careful selection of the absorption line where only absorption of the target specie occurs while the sensitivity depends on the amplitude of the absorption line (linestrength). Once the absorption line is selected and a suitable laser source is available, the sensor can be easily implemented since the QEPAS is wavelength-independent. Each specie presents specific absorption lines. Case study needs to be replicated for every target species.

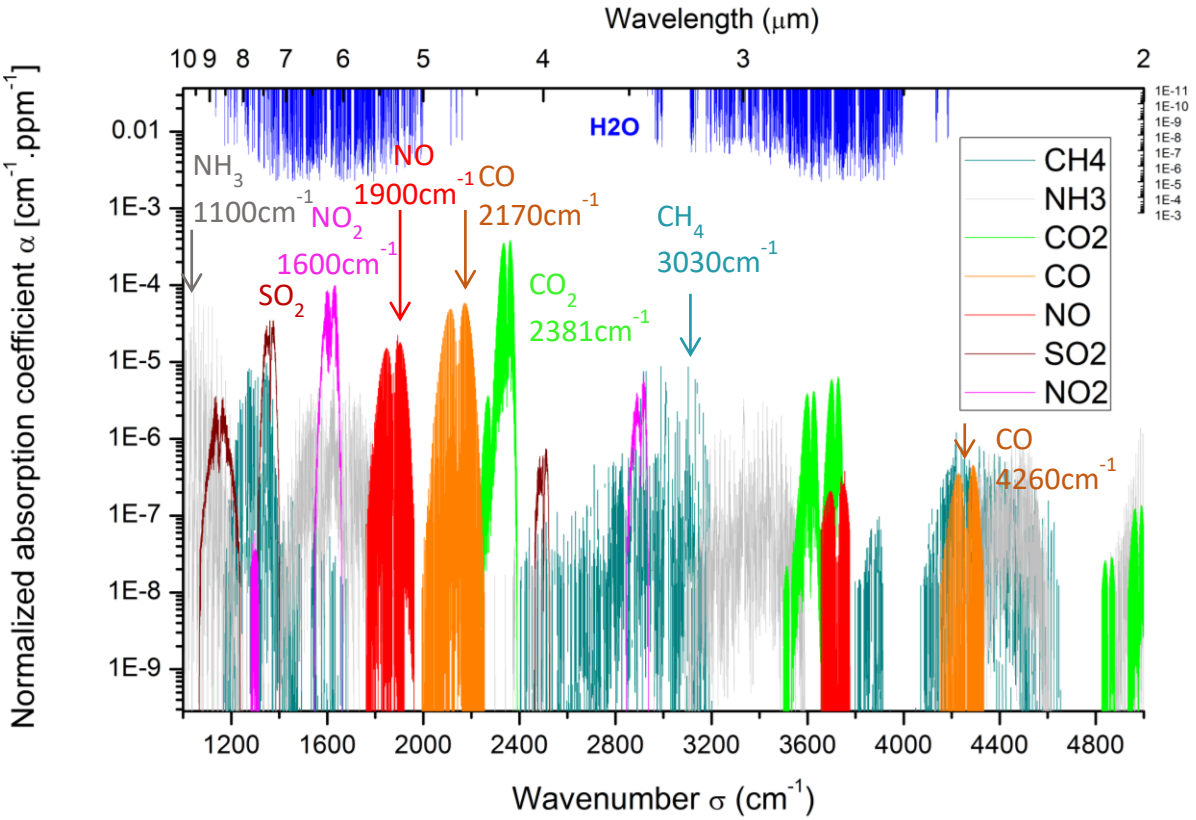

Figure 2.1: Mid-infrared absorption spectra of the MULTIPAS target species, and the main interfering specie H_2O.

According to the specifications of the MULTIPAS project, we focused onto the following species: CO, SO_2, NO, NO_2, NH_3 and CH_4. The absorption profiles are presented on Figure 2.1. In QEPAS, as a convention, the path length is taken as 1 cm. For convenience, the concentration is set to 1ppmv as a reference, the normalized absorption coefficient is thus expressed in 'cm^{-1}·$ppmv^{-1}$'. Molecular fingerprints are also often represented in terms of linestrengths i.e. the area under the curve of a given molecular transition expressed in $cm^{-1}/(molecule \cdot cm^{-2})$. The linestrength describes the ability of a specie to absorb the light for a given transition line. However, when multiple absorption lines are spectrally close, they overlap due to line broadening and form a peak with the contribution of multiple lines. Using the absorption coefficient instead of the linestrength is more appropriate in such situations of composite spectra. Observing Figure 2.1, it can be seen that the absorption coefficient is stronger in the mid-IR than in the near-IR. For the CO, there are 2 orders of magnitude between the absorption lines around 4260 cm^{-1} (2.35μm) and the lines around 2170 cm^{-1} (4.61μm). The increase in absorption coefficient will be a direct gain of the same amount in the energy converted into an acoustic wave and thus a net gain in the sensor's LOD (for $\alpha L \ll 1$).

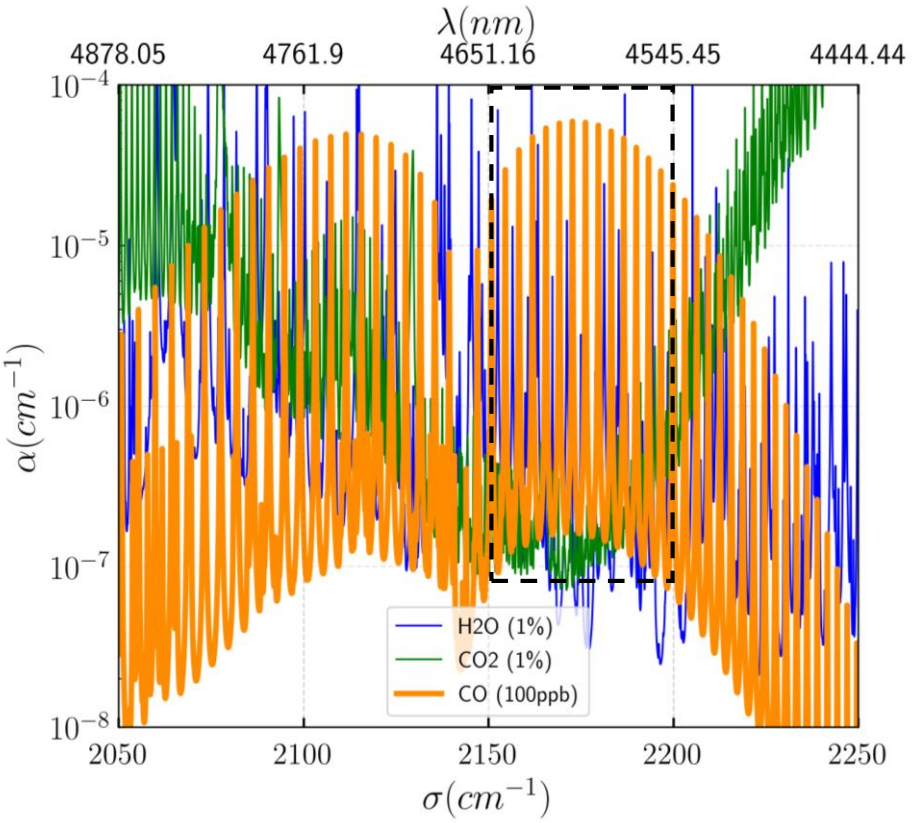

Figure 2.2: CO absorption coefficient in the mid-infrared (orange), along with the main interferent H_2O (blue) and CO_2 (green), at atmospheric pressure and room temperature. Between 2150 and 2200 cm^{-1} (dashed square), the CO_2 absorption is negligible compared to the CO absorption.

Let the CO be our reference example for the peak selection. The CO shows strong absorption in the mid-IR between 2050 and 2250 cm^{-1} (Figure 2.2). At this graph scale, the CO spectral envelope has a butterfly shape with two wings. The peaks are very distinctive and regularly spaced, with a distance between two consecutive peaks of about 4 cm^{-1}. Semiconductor lasers typically cover a few cm^{-1} at a given temperature, using the current for tuning the emission wavenumber. Therefore, a given laser will be able to target 1 to 2 peaks, and probably only one with an appropriate optical power. With the specific shape of the CO spectra, neighboring peaks offer very similar absorption coefficient. A spectral region made of a few peaks can be targeted instead of just a single peak. It gives some flexibility for the laser fabrication. Besides, the common interferents, H_2O and CO_2 show strong absorption. The effect of the interferents can be minimized by choosing an appropriate window. Here for instance between and 2150 and 2200 cm^{-1} (dashed square on Figure 2.2), the CO_2 background is two orders of magnitude below the 100 ppbv CO absorption coefficient, thus ensuring a good selectivity down to a few ppbv. H_2O lines are stronger, but are spectrally distinguished from the CO peaks. The suitable laser modulation amplitude will prevent the overlap with H_2O lines.

As suggested by the project partner ENVEA, two types of specifications standards were considered: Air Quality Monitoring Systems (AQMS) and Continuous Emission Monitoring Systems (CEMS). Those standards define the limit of detection to reach, the measurement range and the concentration of interferents. During cross sensitivity tests, the sensor response to an interfering species is measured. It should be as low as possible. For H_2O and CO_2, the concentrations are set to 30% by volume and 15% by volume, resp, for the cross sensitivity test.

It is clear that such concentrations are serious constraints for a sensor based on optical absorption. If the desired limit of detection is of 1 ppbv, the ratio of the target concentration to the interferent concentration is about 10^{-8}. It means that even a very weak absorption line of the interferent, 10^{-8} smaller than the one of the target species, would lead to similar absorptions. The lorentzian line shape has broad wings that are spreading spectrally and can affect the neighboring absorption lines of low absorption coefficient.

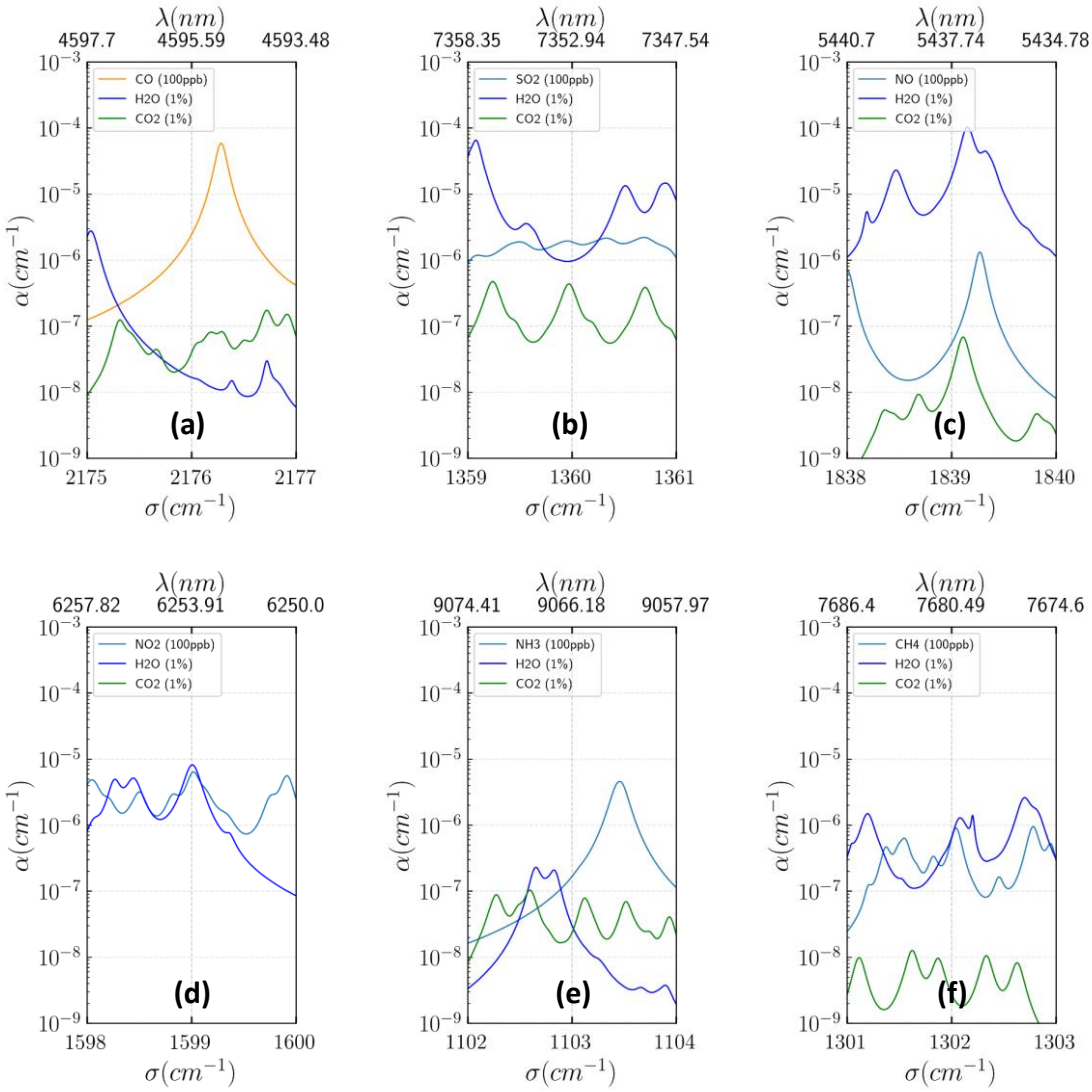

Figure 2.3: Focused spectra of the selected absorption peak for the target species CO (a), SO_2 (b), NO (c), NO_2 (d), NH_3 (e) and CH_4 (f) along with the main interferent H_2O (blue) and CO_2 (green), at atmospheric pressure and room temperature.

For each molecule of interest, ideal absorption lines can be identified (Figure 2.3), i.e. lines with a high absorption coefficient of the target specie and a low absorption of interferents. In this study, the interferent concentration is set to the more reasonable value of 1% for both H_2O. and CO_2. Concerning CO, NO_2, NH_3 and CH_4, the absorption coefficient is at least one order of magnitude higher than the interferents, while for NO and SO_2, the absorption is close or superior to the interferent absorption. Nonetheless, even if the interfering species are strongly absorbing in the region of interest, it might not prevent the detection of the target species. Some

strategies, such as lowering the pressure [1] , multivariate analysis [2,3], differential measurement with a reference cell and dehumidification of the sample [4], can be employed to overcome these issues.

Now that the ideal region has been identified, the theoretical limit of detection can be estimated. For instance for CO, the absorption line at 2176.3 cm^{-1}, shows an absorption coefficient of $5.85 \cdot 10^{-5}$ $cm^{-1} \cdot ppmv^{-1}$, associated with a single transition of linestrength of $4.4 \cdot 10^{-19}$ $cm^{-1}/(molecule \cdot cm^{-2})$. Taking the typical figure of merit for a QEPAS sensor (NNEA=10^{-8} $W \cdot cm^{-1} \cdot Hz^{-1/2}$) [5], and a typical laser power (10mW), the limit of detection of the sensor can be determined using Equation (1.77). For a 100 seconds integration time, it gives 20 ppbv. The LOD is thus obtained for a given absorption line, laser power and integration time. The process can be reversed, fixing the LOD according to the MULTIPAS specifications and deducing the required laser power. The results for each molecule are summarized in Table 2-1.

Molecule	Wave number	Wave length	α_{target}	α (1%H_2O)	α (1%CO_2)	LOD		P_{min}	
						AQMS	CEMS	AQMS	CEMS
	cm^{-1}	um	cm^{-1}	cm^{-1}	cm^{-1}	ppb	ppb	mW	mW
CO	2176.3	4.59	5.85E-05	1.00E-08	8.30E-08	80	100	0.22	0.17
SO_2	1360	7.35	2.12E-05	5.26E-06	3.80E-07	1	100	47	0.47
NO	1839.3	5.44	1.32E-05	4.19E-05	1.11E-08	1	100	76	0.76
NO_2	1599	6.25	6.37E-05	8.02E-06	/	1	100	16	0.16
NH_3	1103.5	9.06	4.57E-05	4.01E-09	4.19E-08	100	100	0.22	0.22
CH_4	1302	7.68	9.45E-06	1.87E-06	2.34E-08	100	100	1.1	1.1
	3067.3	3.26	4.94E-05	1.17E-04	1.02E-09			0.203	0.203

Table 2-1: Summary of the selected absorption peaks. At a given wavelength corresponds an absorption coefficient α_{target} (for a concentration of 1ppm) from which can be calculated the minimum laser power P_{min} to obtain the required limit of detection LOD, both for the AQMS and CEMS standards. The integration time is set to 100s. The absorption coefficients for 1%H_2O and for 1% CO_2 are also mentioned.

For CEMS specifications, the minimum laser power is inferior to 1 mW, which is totally achievable, while for AQMS it goes over 10 mW for NO, NO_2 and SO_2, which corresponds to high power lasers. Combining high power and a specific emitted wavelength puts a heavy stress on the laser fabrication, increasing the cost of the device. We listed some literature results on QEPAS for MULTIPAS' target molecules (Table 2-2). The LOD for most of the molecules lies within a few ppbs to hundreds of ppbs, which is in the order of magnitude of the AQMS and CEMS requirements. The best performances are obtained for high power and mid infrared laser sources.

Molecule	Wave number	Wave length	Pressure	NNEA	Power	LOD	Integration time	Ref
	cm^{-1}	*nm*	*Torr*	$W \cdot cm^{-1} Hz^{-1/2}$	*mW*	*ppbv*	*s*	
CH_4	6057.09	1650.95	760	$3.7\ 10^{-9}$	16	240	1	[6]
CH_4	2958.23	3380.4	760	$4.1\ 10^{-9}$	1	100	12	[6]
CO	2169.2	4609.99	760	$1.6\ 10^{-8}$	400	1.5	1	[6]
CO	2176.28	4594.99	100	$1.4\ 10^{-8}$	71	2	1	[6]
NO	1900.08	5262.94	210	$5.7\ 10^{-9}$	66	4.9	1	[7]
NH_3	967.35	10337.52	130	$7.9\ 10^{-9}$	24	6	1	[8]
NO_2	22222.22	450		$4.1\ 10^{-9}$	7	18	1	[9]
SO_2	1380.94	7241.44	150		140	100	1	[10]
C_2H_4	949.3	10534.07	760	$1.78\ 10^{-7}$	23	50	70	[11]

Table 2-2: Literature results for the target molecules of the MULTIPAS project.

5 partners were involved within the MULTIPAS project, interacting at different levels of the development of the gas sensor (Figure 2.4). QCLs were provided from the company mirSense and also from the IES. The QCLs were mounted and characterized at the IES (see Section 2.4), and implemented for gas sensing at the IES (for CO, CH_4 and NH_3) and at the LPCA (NO, NO_2). The IES focused on the development of a robust QEPAS sensor adapted to QCLs while the LPCA studied a more complex and sensitive system based on intracavity-QEPAS. The operation of the QCL requires dedicated electronics to ensure a finely adjustable and highly stable laser emission. A bill of specifications was written by the IES and mirSense and delivered to ValoTec, which was in charge of the design of the QEPAS specific electronics. The board had to fulfill multiple functions: laser control (temperature, control), signal generation (laser modulation), amplification, digitization and processing. The board was tested on the QEPAS prototype at the IES with ValoTec staff.

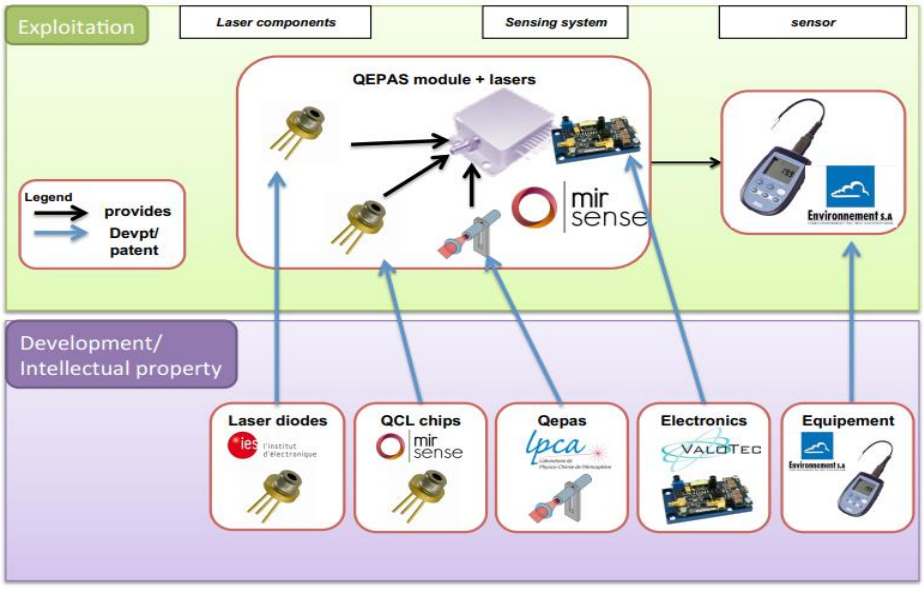

Figure 2.4: Roles of the partners in the MULTIPAS project.

2.2. Optimized spectrophone

The spectrophone is at the heart of the QEPAS system. The spectrophone comprises the acoustic microresonator (mR) and the Quartz Tuning Fork (QTF). The acoustic microresonator confines and amplifies the acoustic energy while the QTF converts the acoustic wave into a mechanical movement, and then to an electrical signal thanks to the piezoelectric effect. The dimensioning of the microresonator and its relative position with the QTF can lead to a consequent improvement of the QEPAS performances. In this section, we will discuss the various functions of the spectrophone and their optimization.

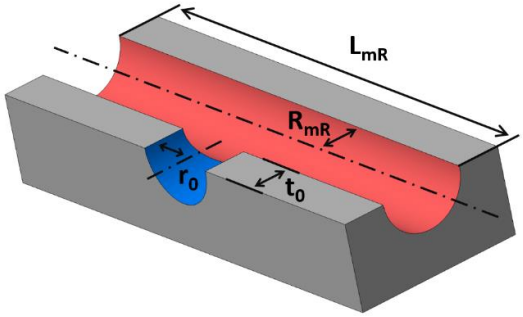

Figure 2.5: 3D Section view of the off-beam mR composed of the main tube (red) of length L_{mR} and radius R_{mR} and the slit (blue) of radius r_0 and length t_0. The laser beam passes in the main tube. The QTF is positioned in front of the slit.

The QEPAS spectrophone is known to have two main configurations: on-beam and off-beam, as we described in chapter 1 (paragraph 1.3.3). The off-beam spectrophone was chosen to be the most suitable for the combination with highly divergent QCLs. Indeed, in on-beam the beam diameter is limited by the gap between the two QTF prongs (300µm) while in off-beam, it can be increased up to 1mm. Off-beam thus offers optical versatility. The off-beam microresonator (Figure 2.5) is composed of a main tube (red) and a side slit (blue). The laser beam passes in the main tube and the photoacoustic generation occurs upon optical absorption. The side slit allows the coupling with the QTF, by radiating the acoustic standing wave outside the cavity (main tube).

The microresonator has multiple functions: acoustic amplification, light shielding, acoustic coupling. Acoustic amplification is mostly related to the dimensions and surface aspect of the main tube. Larger main tube diameters might decrease the amplification, but this signal loss is mild compared to the photothermal noise due to beam collision with the main tube walls occurring if it is to narrow. Also, by placing the QTF off the optical axis, it is physically protected from divergent rays. Light shielding is a serious advantage in the off-beam configuration. The acoustic coupling with the QTF is realized by the side slit.

In this section, we present a setup to characterize the QTF response and to optimize its dimensions. Then, the resonance is studied as a function of the main hole length and diameter. Finally, 3D printed mRs are fabricated, allowing to adjust the slit shape and improve the acoustic coupling between the mR and the QTF.

2.2.1. Acoustic characterization setup

The mR frequency response was studied theoretically in order to optimize the length of the mR. Some expressions of the optimum length were presented for the off-beam mR (Section 1.3.3.2). Even if the expressions were obtained with the well-established acoustic equations, experimental validations were missing from the literature. The acoustic response of on-beam mR was obtained from the deduction of the measured QEPAS signal with or without the mR [12,13]. However, regarding the sensitivity to the QTF position and the narrow QTF response compared to the one of the mR, this method seems to be of a relatively low accuracy. Indeed, mR Q factors are in the range of 10-100, giving a bandwidth of a few kHz that is very large compared to the few Hz bandwidths of the QTF.

Another technique consists in varying the speed of sound to measure the frequency response [14]. By varying the gas matrix, the speed of sound varies and so does the mR acoustic resonance. The experiment can be conducted as follows. First, the acoustic wave is generated at the QTF resonance frequency. Second, the gas matrix is changed, thus the amplitude of the acoustic wave inside the mR changes due to acoustic detuning. Third, the amplitude of the QEPAS signal is recorded. Finally, the amplitude of the QEPAS signal, as a function of the speed of sound, can be used to obtain the mR frequency response. This technique suffers from several drawbacks. The frequency span is limited to a few kHz, due to the finite available range of gas density. Also, the change in the gas matrix will affect the molecular relaxation rate, and consequently the amplitude of the PA signal.

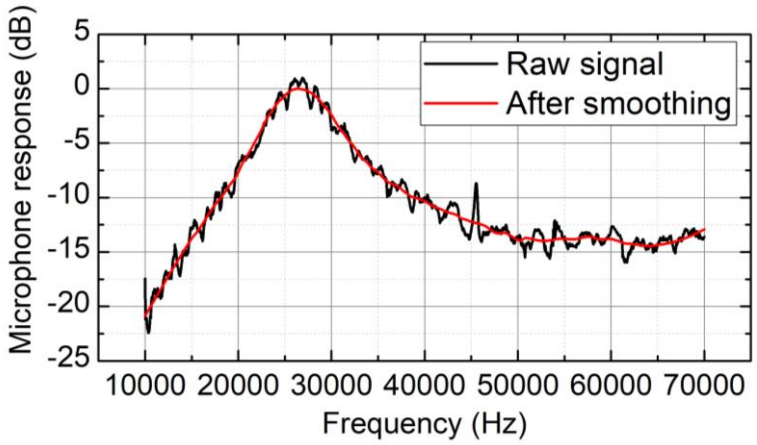

Figure 2.6: Measured acoustic response of the microphone (Knowles SPU0410LR5H-QB). The input acoustic wave is generated photoacoustically through water absorption. The response is normalized by the maximum.

The limitations in the previous techniques are due to the QTF narrow-bandwidth. That is why we decided to replace it with a flat bandwidth electro-acoustic transducer, also known as a microphone. It might be said that using a microphone instead of a QTF is a move backward to the classical PA setup, but here the microphone is only an instrument employed for acoustic characterization. Most microphones are designed for audio applications, i.e. operating in the 20Hz-20kHz range, although some of them are designed for ultrasonic applications (>20kHz) [15]. In particular, they are used for recording the ultrasonic sounds emitted by the bats. Some resources can be found online about DIY bat detector, as well as engineered products [16,17].

MEMS microphones have a wide response up to 80 kHz (Figure 2.6). The sensitivity tends to decreases above 25kHz but is high enough for the characterization.

The typical QEPAS setup used in our laboratory was based on the detection of methane. The mR was enclosed in a gas cell in order to add the methane. The microphone was placed facing the side slit instead of the QTF. Upon our first experiments, a weak signal background without any significant resonance was obtained. We attributed the background to acoustic mode of the gas cell. In order to prevent those unwanted modes, the cell was insulated with foam, to efficiently avoid reflection on the cell walls.

Some results were obtained, but we quickly realized the setup was inappropriate, since the position of the mR was not adjustable during the experiment. A smart way to overcome this issue was by removing the gas cell. The use of a baffle was considered in order to generate the input acoustic wave. However, it raised another problematic: is a baffle response constant with frequency? If not calibration would be required, and thus a calibrated reference microphone. Another issue with the baffle is that sound pressure level can be higher outside the mR than inside the mR, since the mR is by definition an acoustic filter. Differently from the baffle, the photoacoustic generation is localized inside of the mR which is therefore more efficient. However, the drawback of the PA generation is the need for a gas cell to provide the suitable environment around the mR. Hence the question: is it possible to find is a target gas in the ambient environment and an appropriate laser source suitable for PA generation?

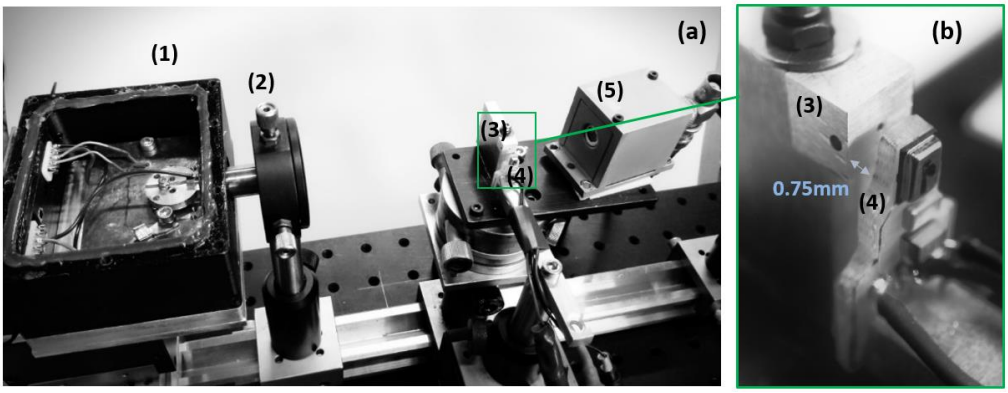

Figure 2.7: Photography of the acoustic test bench with, from left to right, the 2.62µm laser enclosed in a temperature regulated module for operation at 8°C (1), the focusing lens (2), the mounted microresonator (3) facing the MEMS microphone (4) placed on a xyz translation stage, and a tilted photodiode (5). (b) Close-up picture of the mR and the microphone.

N_2 and O_2 are not good candidates for PA generation. CO_2 is commonly employed but the concentration is low in air (400ppm). Ambient air has a certain level of humidity, often around 50%RH in our building, that is an absolute concentration of 1.16% H_2O (20°C, 1atm). H_2O shows strong absorption lines between 2.4 and 2.7µm. We found a laser fabricated at the IES and matching the H_2O lines around 2600 nm. It was used for making the proof of concept, that turned out to be successful. The experimental setup is presented on Figure 2.7. Regular mode hopes of the 2.6µm laser complicated the experiment and made us purchase a more reliable single frequency laser at emitting 1392nm (EBLANA). The laser was fully characterized, as shown on Figure 2.8. The target H_2O line has a linestrength $1.5 \cdot 10^{-20}$ $cm^{-1}/(molecule \cdot cm^{-2})$. Thus the amplitude of the acoustic wave, based on ambient water absorption, is very strong, comparable to the one obtained with 100% CH_4, as required for the acoustic characterization.

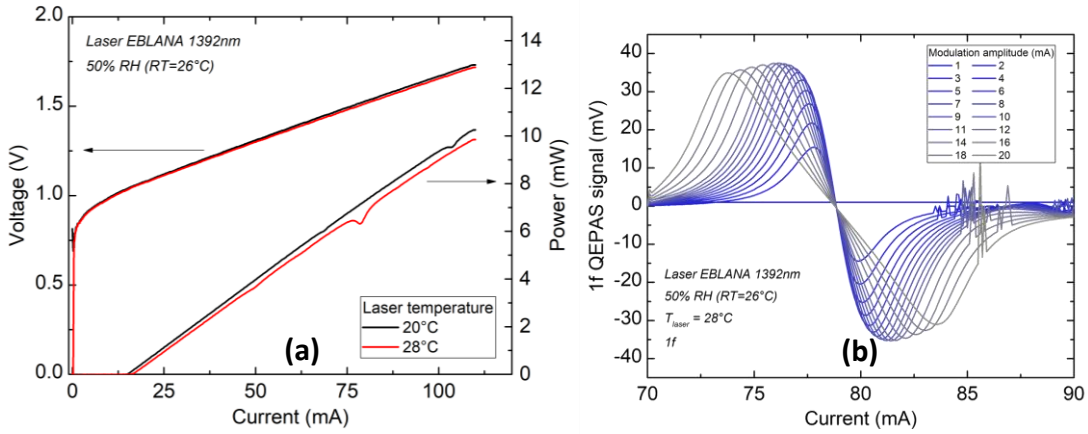

Figure 2.8: Characteristics of the EBLANA laser: LIV curves (a) and QEPAS response (b). The 1*f* QEPAS response was obtained for a laser temperature of 28°C and ambient humidity around 50%RH.

The mR frequency response is represented on Figure 2.9 for different distances between the mR and the microphone. When the two elements are in contact, the volume of the air gap at the output of the side slide is very small, thus the side slit behaves almost as in a close-ended configuration. The resonance is located around 28.3kHz (red dotted line). When the distance is increased, the resonance shifts towards the high frequencies. It can be explained by the shorter equivalent length of the mR due to the loss of energy through the side slit. The resonance converges to a value of 31.3 kHz (blue dotted line), where the side slit is in open-ended configuration. This study was repeated on mRs of various dimensions and allowed us to conclude that a distance superior to 0.75mm ensures that the side slit is in open-ended configuration (though the side slit cannot be considered totally opened when the QTF is added).

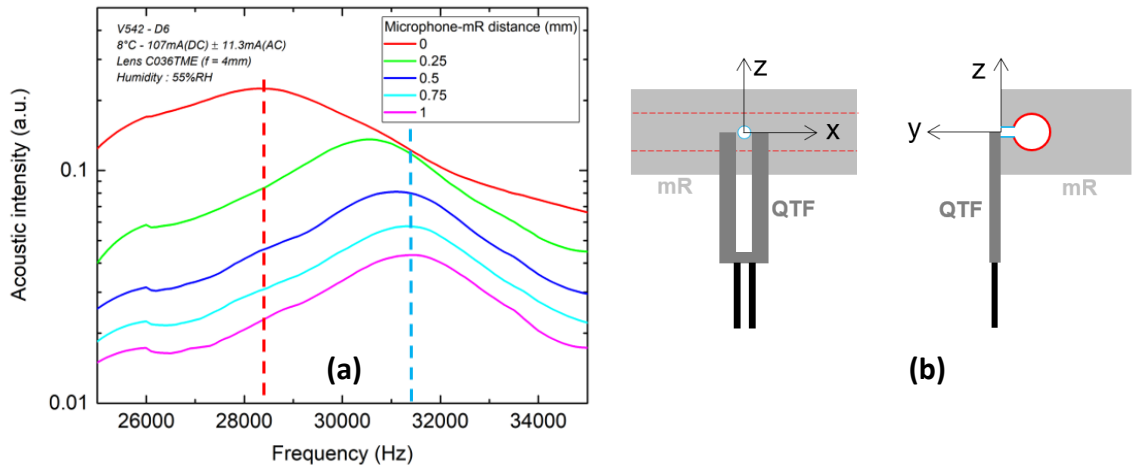

Figure 2.9: Frequency response of a mR (a6) while varying the distance between the microphone on the mR. The red dotted line corresponds to the close-ended configuration of the slit while the blue dotted line corresponds to the open-ended configuration.

From these results, we designed a protocol for positioning the mR using the translation stage, that relies on the following steps:

- the microphone is put into physical contact with the mR, moving in the y direction,

- the signal from the microphone is maximized by moving in the xz plane,
- the microphone is moved 0.75mm backward in the y direction, using the micrometer screw.
- the frequency response of the mR is measured.

The protocol was applied before each mR characterization and ensures the consistency of the results.

2.2.2. Frequency response of micromachined microresonators

Once the characterization setup was validated, microresonators were fabricated and tested. The first mRs were fabricated from aluminum blocks by milling and drilling in the IES workshop. With this process, the surface aspect was correct (the judgement is very qualitative since no instrument for quantifying the internal roughness were used). 9 microresonators with various lengths L_{mR} and radius R_{mR} were selected (Table 2-3). Different radius would allow to adjust the mR for the future use of lasers with various optical waist size. The parameters r_0 and t_0 are set to fixed values, 0.25 and 0.5mm respectively, for the all 9 mRs. For each diameter, 3 values of the length are chosen around the theoretical optimal length, obtained with the equation (1.71) from H.Yi . As a reminder, at the optimal length, the mR resonant frequency (f_{mR}) matches with the QTF one (f_0).

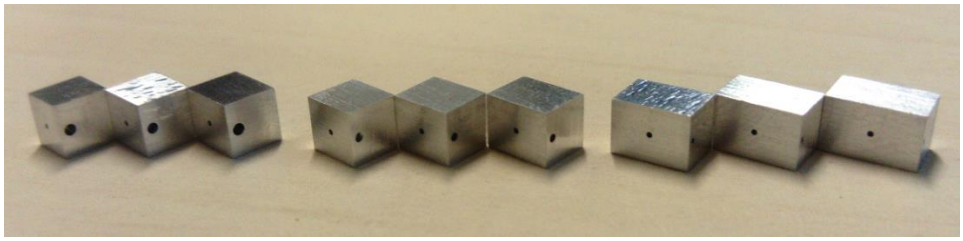

Figure 2.10: Set of fabricated microresonators from aluminum blocks, from a1 (left) to a9 (right).

Ref	A1	A2	A3	A4	A5	A6	A7	A8	A9
R_{mR} (mm)	0.25	0.25	0.25	0.35	0.35	0.35	0.5	0.5	0.5
L_{mR} (mm)	7	7.5	8	5.5	6	6.5	5	5.5	6

Table 2-3: Dimensions of the fabricated microresonators.

Applying the protocol described in Section 2.2.1, the mR frequency response were obtained (Figure 2.11(a)). The quality factors of the different mRs are in the range of 10, in agreement with the literature. As can be seen the microphone response is not perfectly flat, thus leading to a higher measurement error on the Q factor. Nonetheless, the resonant frequency, that is the crucial information for us, can be well estimated by taking the maximum of the peak.

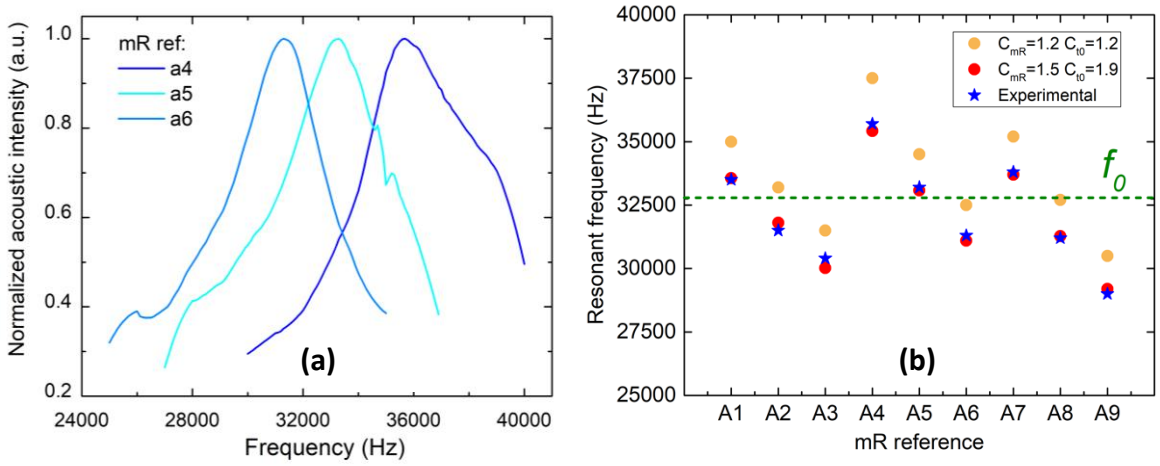

Figure 2.11: (a) Frequency response of the mRs a4, a5 and a6, sharing the same radius and different lengths. (b) Acoustic resonance for resonators from Table 2-3. The correction factors are adjusted to fit the experimental results. f_0 is the QTF resonant frequency, i.e the target frequency for the mR.

The resonant frequency can be plotted for the 9 mRs (Figure 2.11(b)). We observe the expected trend: f_{mR} decreases with increasing L_{mR} and increasing R_{mR}. We compared the results to the H. Yi model. The original expression of Equation (1.71) with $C_{mR} = C_{t0} = 1.2$ (orange dots on Figure 2.11(b)) is clearly off the experimental results (blue stars) by approximately 1400Hz. As we discussed in Chapter 1, the value 1.2 is rather empirical and has not been verified for millimeter sized mRs. That is why we suggest to adjust these factors to the experimental results and thereby, obtain a semi-theoretical model with better accuracy. The H. Yi model was codded as a function in Python, with parameters R_{mR}, f_{mR}, C_{mR} and C_{t0} and returning the optimal LmR. The optimization of the model was done using the non-linear fitting function *curve_fit* from the *scipy.optimize* library. R_{mR} and f_{mR} were used as the input variable vector, L_{mR} the dependent vector while C_{mR} and C_{t0} were the adjustable parameters. Thus, *curve_fit* returns the optimal values for C_{mR} and C_{t0} that give the best fit of the H.Yi model to the experimental data. In our case, we obtained for $C_{mR} = 1.5$ and $C_{t0} = 1.9$. The corrected theoretical model exhibits a good fit of the experimental data. For this model, the mean error over the 9 mRs tested, is of 200Hz, that is about a factor 7 error reduction compared to the original model.

2.2.3. 3D printed microresonators using stereolithography

Most of the machining techniques, e.g. milling, turning, start with bulk material and remove the excess material to obtain the desired part. Oppositely, 3D printing is an additive manufacturing technique [18], meaning that the right amount of material is added at the right location. Layers of material are deposited successivelly until they form a three dimensionnal shape. 3D printing offers fast prototyping at low cost with a high resolution, which is beneficial for applications such as biomedicine, aerospace and the mechanical industry in general. A wide range of materials are available, such as a polymers, metal alloys, ceramics and composites. The most widespread 3D printing technique is Fused Deposition Modeling (FDM) but additive manufacturing regroups many others such as Stereolithography (SLA), inkjet printing, Selective Laser Sintering (SLS).

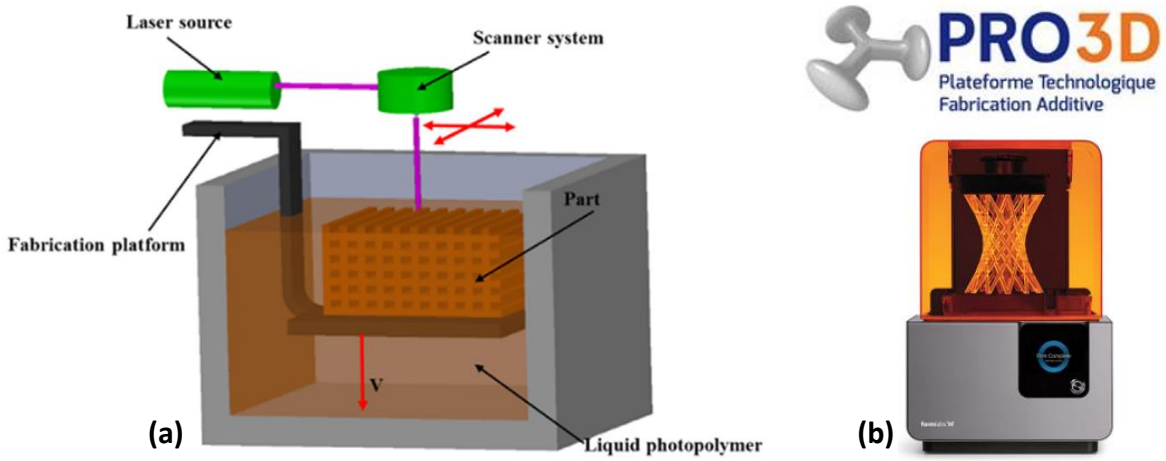

Figure 2.12: (a) Schematic of a stereolithography (SLA) setup [19]. (b) SLA printer (Form 2, Formlabs) used for the fabrication of custom microresonators at the 3D printing plateform PRO3D.

SLA was one the first additive manufacturing technique, invented in 1986 by Charles Hull [19]. The principle is to selectively illuminates a liquid resin with a UV laser to initiate the polymerization. A schematic of the SLA is presented on Figure 2.12. A container is filled with a photosensitive resin. A UV laser is focused onto a specific spot to initiate the polymerization of the resin, and thus the solidification. A set of mirrors allows the movement of the laser spot to enscribe the desired 2D pattern. The fabrication plateform is then moved downward, allowing a thin film of liquid to flow on top of the initial 2D pattern. The next layer is ready to be illuminated. SLA is known for the production of high quality parts with resolution down to 5µm [20,21]. The maindrawbacks of SLA is the limited printing speed and the non negligible cost of the resin. Therefore, the technique is more suitable to build objects with small footprints. The SLA technique, and more generally additive manufacturing techniques, have an oustanding capacity of making complex shapes and surfaces, that cannot be obtained with standard machining techniques. For instance, inner cavities and sophiticated latices can be fabricated. The versatily of the SLA seems ideal for the fabrication of customized parts and we decided to exploit it for the fabrication of new microresonator designs.

The University of Montpellier possesses its own 3D printing platform, called PRO3D, offering fabrication techniques such as FDM and SLA for polymers, SLS for metals and more [22]. The mR were fabricated using a printer (Form 2, Formlabs) which is based on inverted SLA, with a spot size of 140µm and minimum layer thickness of 25µm. The 3D model were made using a CAD software (Catia V5R19, Dassault system) and used for generating a typical 3D printed file in the '.stl' format. The graphical settings of the software were adjusted to make sure the resolution of the stl file was sufficient.

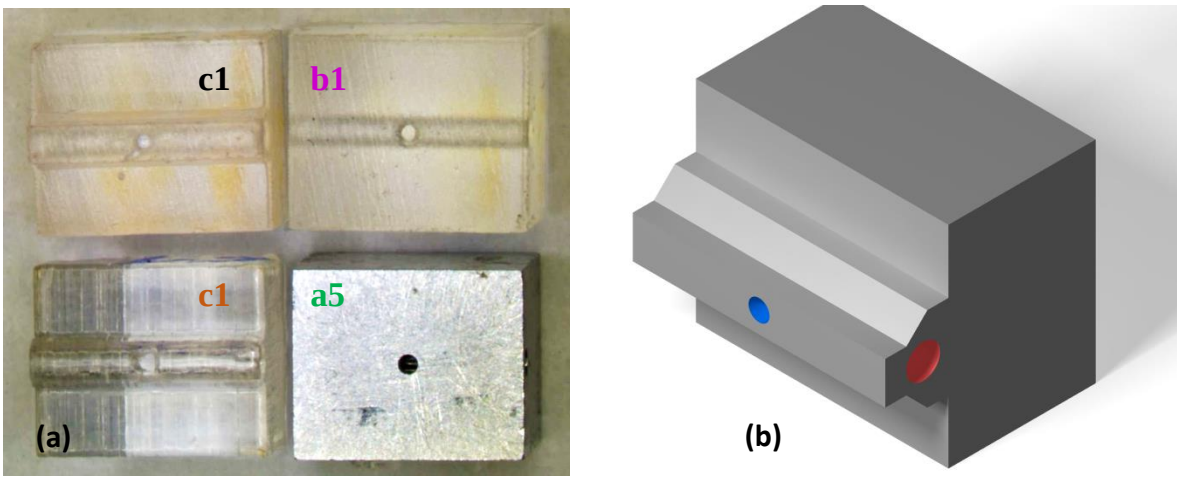

Figure 2.13: (b) Picture of the 3D printed mRs inspired from the reference micromachined mR (a5, bottom right). b1 (top right) and c1 (top right) were fabricated at PRO3D while c1 (bottom left) was from CRESILAS. (b) CAD drawing of the mR c1.

The first mRs were designed with similar dimensions to the mR a5, which was correctly matched with the QTF resonant frequency. One mR (b1) was the exact replica of the mR a5 while on the other one (c1) some material was removed around the main hole (Figure 2.13(b)). This modification was realized to minimize the effect of the mR onto the QTF. Indeed, when the QTF is in the vicinity of the mR, a thin layer (tens of μm) of air (the squeeze film) applies a reactive force onto the QTF prongs, which lowers the QTF Q factor. Decreasing the surface of interaction between the mR and the QTF will result in a higher Q factor, hence the new design of the mR c1.

The microresonators were characterized, following three major steps:

1. Visual inspection under the optical microscope
2. Characterization of the frequency response with a microphone
3. Measurement of the amplitude of the QEPAS signal

The visual inspection was useful to check for any apparent fabrication faults, the surface aspect and the dimension of the holes. Those three parameters might affect the mR resonance and contribute to explain experimental deviations of the frequency response and the QEPAS signal. For instance, the roughness of the cavities can induce higher losses, thus lower acoustic Q factor. The dimension of the main hole can lead to a shift of the resonant frequency while the dimension of the side slit can affect the coupling between the mR and the QTF. The measurement of the frequency response was carried out following the protocol described in section 2.2.2. For the QEPAS experiment, the same setup was used, replacing the microphone by the QTF. While the microphone is omnidirectional and tolerate slight spatial deviations, the QTF positioning is critical and the QEPAS experiment might be affected by a slight translation or rotation of the QTF. Also, the position of the laser beam has to be fine-tuned to ensure optimal photoacoustic generation inside each mR.

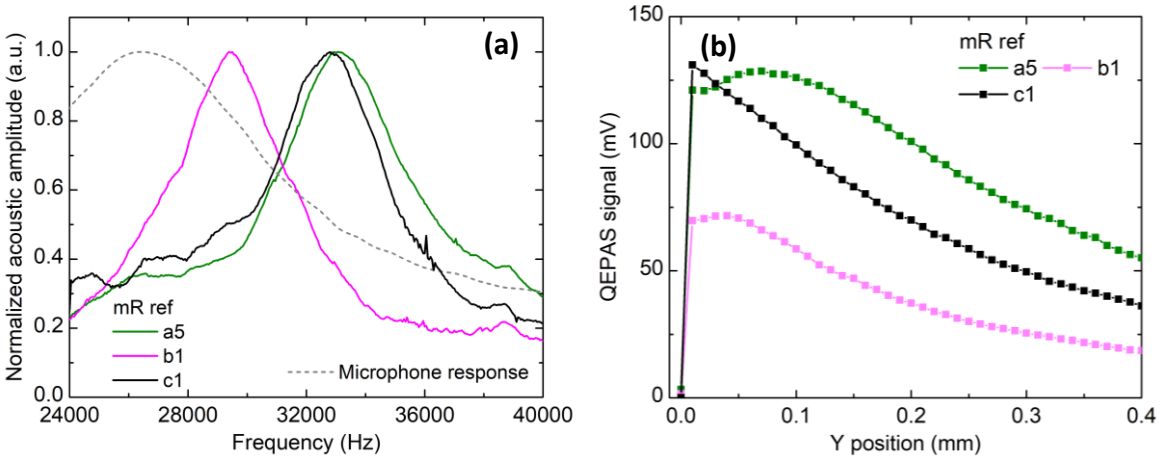

Figure 2.14: (a) Frequency responses of the 3D printed mRs compared to the reference mR a5. The mR response was normalized by the microphone response (dotted line). (b) QEPAS signal for the different mRs versus the Y position, corresponding to the distance between the mR and the microphone (schematic on Figure 2.9).

The frequency responses of the mRs (Figure 2.14(a)) were obtained by normalizing the signal from the microphone by the lone microphone response (dotted line). The response of the first 3D printed mR (b1, pink) is shifted compared to the mR a5. It is explained by the radius of the main hole R_{mR} being too narrow. This deviation was corrected in the next batch of printed parts, as it can be seen the mR c1 resonates at the proper frequency. The 3 mRs were then tested in the QEPAS experiment (Figure 2.14 (b)). Regarding the high sensitivity of the QEPAS towards the mR-QTF distance (y-axis), a sweep of the mR position was made along the y-axis. For very small mR-QTF distances the QEPAS signal decreases for the microresonator a5 and b1, indicating a drop in the Q factor. It does not occur with the c1, confirming that the modified shape of the mR reduces the squeeze film effect. Although c1 does not decreases for small mR-QTF distances, the signal maxima for a5 and c1 are similar. it might be explained by the increase roughness of the 3D printed parts compared to the micromachined mRs.

The 3D printed mRs offer good QEPAS performances and demonstrate the potential of stereolithography for making more complex shape of mRs.

2.2.4. Improving the acoustic coupling by adjusting the slit shape

Acoustic amplification is mostly related to the dimensions and surface aspect of the main hole while the acoustic coupling with the QTF is realized by the side slit. To describe it, we can use the metaphor of the organ pipe for which the size of the tube is dimensioned to output a given note pitch. The wave resonates inside the pipe and is re emitted through a slit positioned at a pressure antinode. The size of the slit is important because it affects the mR resonance. In the H. Yi model the impedance of the slit is accounted to deduce the mR resonant frequency. It is important to note that the acoustic cavity and the slit are basically counter interacting: the cavity confines the energy while the slit radiates the energy out of the cavity. Dimensioning the slit relies on finding the optimum size and shape which will maximize the energy transfer to the QTF. The optimization may also include the adjustment of the acoustic cavity itself (not only the slit) to ensure the proper resonance frequency.

The topic was discussed with Pr Le Clezio (IES, University of Montpellier), whose research field is the characterization of complex materials by acoustic methods. When looking at the development of musical instrument such as the organ pipe, the improvements of the instrument geometry were mostly empirical. Empiricism is possible in acoustics using human's ear, in the audio range. In the ultrasonic domain the microphone will be our ear. And remembering the slit size (0.1-0.5mm), measuring the pressure field would require with a spatial accuracy we cannot obtain with a basic microphone. Moreover the microphone is likely to affect the pressure distribution. The characterization of the pressure field is more complex for the mR than for the organ pipe. That is why, we decided to simulate the pressure field at the output of the mR slit.

As the slit is small compared to the length of the main hole, we make the assumption that no reflection occurs at the slit, thus the system is considered feedback free. Then the slit emission can be obtained using Huygens' principle. Huygens stated that the wavefront of a continuous source can be obtained by considering the source as multiple equivalent spherical secondary point sources. Illustrating Huygens' principle in the case of a 1D acoustic emitter, if the slit width-to-thickness ratio is much larger than 1, it can be represented by a as a line source (Figure 2.15(a)). In order to discretize the problem, secondary sources are equally distributed along the line. By drawing the wavefronts of every secondary sources, the wave front of the emitter can be well approximated. Close to the emitter, the secondary sources interfere with the closest neighbors creating various patterns, this is the near field or Fresnel diffraction. At a larger distance from the emitter, all wave fronts merge together, forming the far field pattern or Fraunhofer diffraction, e.g. a plane wave on Figure 2.15(a). The near and far field are spatially separated by the Fresnel length:

$$d = \frac{a^2}{\lambda} \tag{2.1}$$

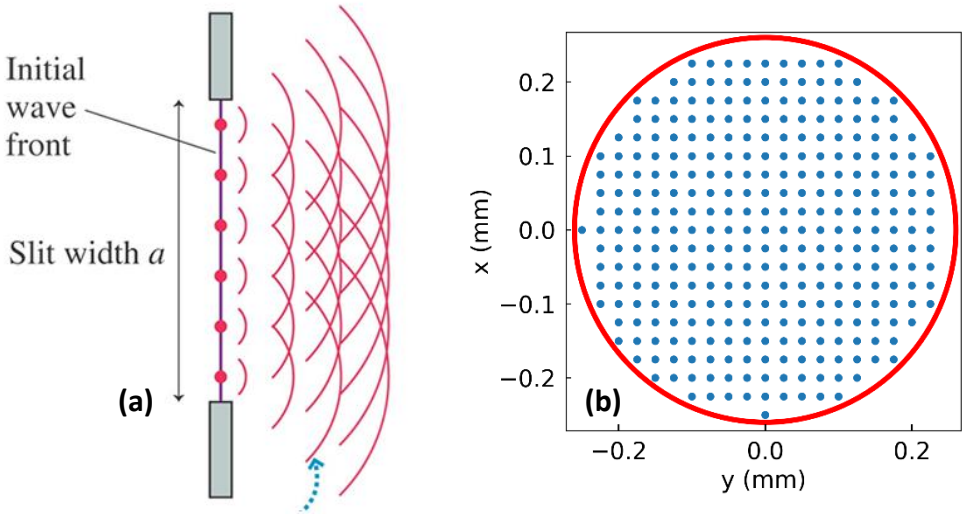

Figure 2.15: (a) Representation of Huygens' principle for a line source. Secondary spherical sources are equally distributed along the line, from which the wave fronts are drawn. In the far field, the spherical wave fronts merge to form a plane wave (b) Secondary sources (blue dots) arranged for the simulation of the emission of a circular slit or of radius 0.25mm (red circle). The distance between two sources is 0.025mm ($1/10^{th}$ of R_{mR}).

More generally, the pressure field at a point P can be obtained by integrating the infinitesimal contribution dP of each secondary source over the surface of the acoustic emitter, as given by Rayleigh's integral [23,24] :

$$p(r,\theta,t) = \frac{j\rho_0 c U_0}{\lambda} \int \frac{1}{r'} e^{j(\omega t - kr')} dS \qquad (2.2)$$

Where ρ_0 is the fluid density, U_0 the initial fluid velocity, λ the acoustic wavelength, ω the acoustic angular frequency and r' the distance from a field point to a point on the acoustic source.

Rayleigh's integral can be solved analytically but the solutions are complex [25]. The integral can be solved numerically as well, by discretizing the integral, and we show here a very simple model, leading to a good approximation of the solution. The mR slit is considered as a disk containing n secondary sources at locations $(x_a, y_a, 0)_i$, as represented on Figure 2.15(b). The amplitude of the complex pressure field, expressed in Cartesian coordinates, can be obtained by summing every contribution:

$$p(x,y,z) = \frac{j\rho_0 c U_0}{\lambda} \frac{S}{n} \sum_{i=1}^{n} \frac{1}{r'} \exp\left[-k\sqrt{(x-x_a)^2 + (y-y_a)^2 + z^2}\right] \qquad (2.3)$$

The simulation was realized on Python (Numpy, Scipy, Matplotlib). The results are represented on Figure 2.16 for a circular slit of radius r_0=0.25mm, at two different frequencies. At 1 MHz, a typical interference pattern is observed while at 32kHz the pressure amplitude decreases monotonously as expected for the far field pattern. The highest pressure is obtained in the vicinity of the slit where the QTF will be located.

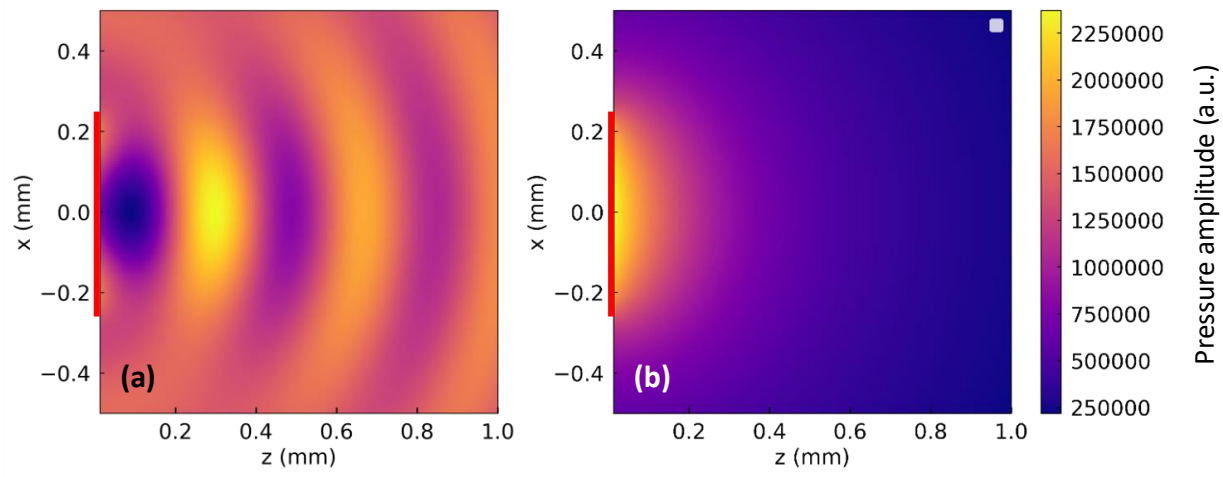

Figure 2.16: Image of the pressure field in the xoz plane, for an acoustic frequency of 1MHz (a) and 32kHz (b). High pressure values are represented in yellow while low pressure value in purple. The slit parameters are: radius R_{mR}=0.25mm, center (0, 0, 0), number of secondary sources n=309. (source code Radiation_Huygens3.py)

Let us consider now different slit shapes. The disk is convenient for conventional fabrication, but with 3D printed mR, the only limit in terms of shapes is the printing resolution and the maker's imagination. The shape of the orifice has a direct effect on the pressure field and more precisely the directivity. Paying attention to the shape of the QTF flexure mode, the

x-component of the acoustic wave applies a force in the direction of the QTF movement while the acoustic energy of the y and z components is lost. In order to increase the x-component and reduce the z-component, the slit must be elongated in the z direction. The slit shape was designed either as a rectangle or as an obround (Figure 2.17(a)&(b)). Another idea to prevent the diffraction in the z-direction is to form a horn (Figure 2.17(c)). Indeed as for the mouth of a trumpet, the sound emitted from a resonating tube has a higher directivity when the opening is progressive [26].

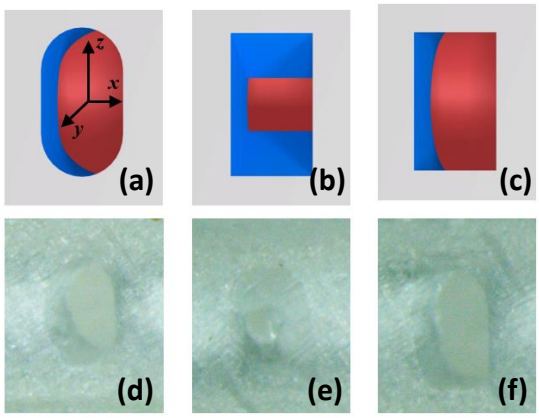

Figure 2.17: CAD images of three selected slit shapes : obround (a), rectangular cone (b), rectangle (c) and the images of the fabricated mR from the microscope (d-e-f).

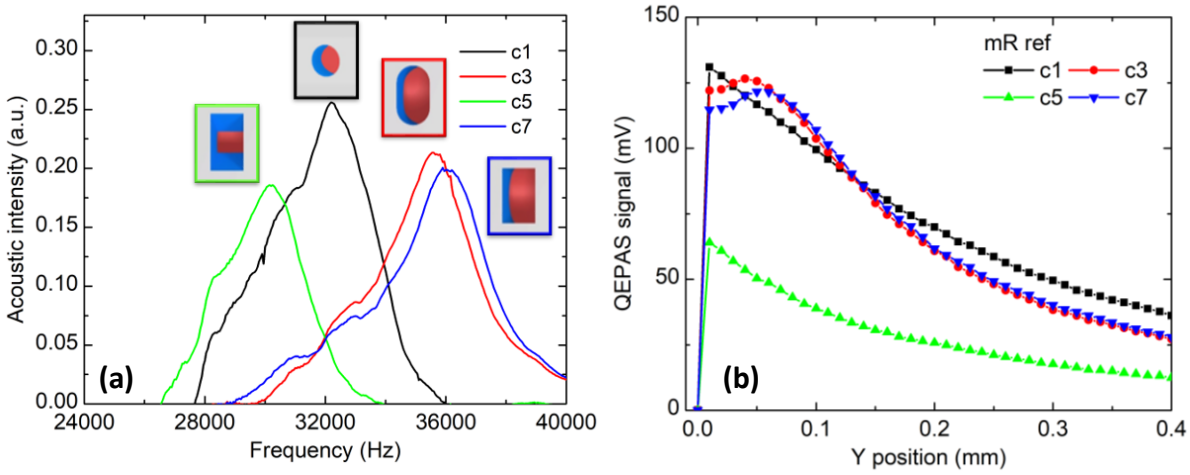

Figure 2.18: (a) Frequency response of the mRs with different slit shapes. The characterization is realized following the protocol described in section 2.2.1. (b) Profile of the QEPAS signal along the y axis.

The frequency response of the mRs is shown on Figure 2.18(a). While the mRs have a similar Q value, f_0 varies greatly, due to the different slit size. The larger the slit size the higher the f_0 as predicted by H. Yi Model. Then, we run a QEPAS experiment based on water absorption (described in section 2.2.1) with the same mRs, to assess the mR-QTF coupling efficiency (Figure 2.18(b)). The amplitude of the QEPAS signal is lower for the mR c5 than for other mRs. It is probably explained by the reduced area of the slit which limits the amount of radiated energy. All 3 mRs, the c1, c3 and c7, present a similar QEPAS response. However, the c3 and c7 are not frequency matched with the QTF. We can then deduce that the mR-QTF acoustic coupling is better for those 2 mRs than for the c1 and that it compensates the frequency mismatch. A new batch of 4 mRs with the obround slit shape was made in order to adjust the

frequency ($f_{mR} = f_0$) so to obtain a higher signal than mR-c1. PROD3D experienced issues with the SLA printer, therefore we had to have the new batch fabricated by another company (CRESILAS, [27]). The 4 mRs had the same geometry, except the length, which was varied to adjust the resonant frequency. Their frequency response is shown on Figure 2.19.

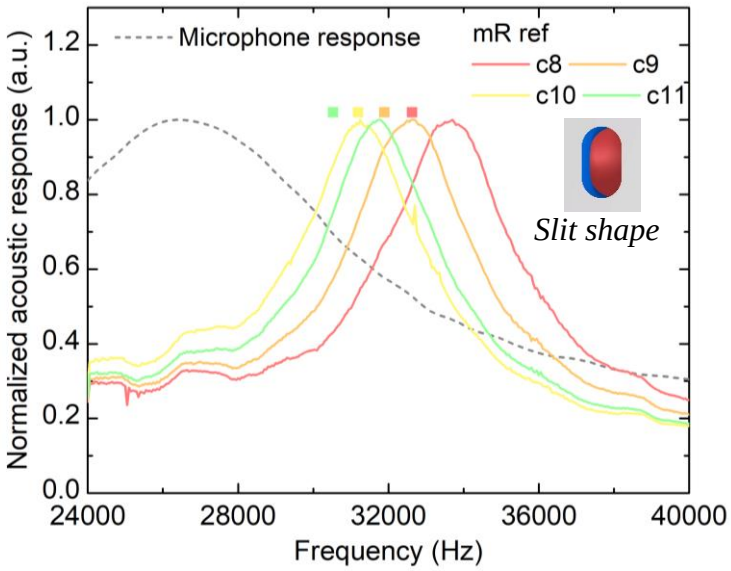

Figure 2.19: Frequency response of the mRs with an obround slit shape. The continuous lines represent the experimental results while the dots are the theoretical values of the mR resonant frequencies for the expected mR dimensions (equation (1.71)). The length of the mR c8, c9, c10 and c11 are of 6.6, 6.8,7.0 and 7.2 mm, resp.

In order to conclude nicely on the performance of the 3D printed mRs, we decided to carry out a final QEPAS experiment for testing all the mRs with the same setup and an accurate protocol.

2.2.5. Accurate comparison of the microresonators in a QEPAS experiment

We remarked an oversight in the previous QEPAS experiments (Figure 2.14(b) and Figure 2.18(b)). Indeed, the protocol we followed was similar to the one used for obtaining the mR acoustic frequency response. In the frequency response, the amplitude of the photoacoustic excitation is unimportant since we apply a normalization. It is not the case in QEPAS, in which we want to apply the same excitation amplitude to be able to compare the absolute amplitude of the QEPAS signal from the different spectrophones. The acoustic wave can be created mainly due to 2 effects: the photoacoustic effect and the photothermal effect (wall absorption). The latter must be prevented to ensure an acoustic wave of similar amplitude is generated in each mRs. Usually, in a QEPAS experiment, a flush of the cell with neutral gas allows to verify that the signal if offset free. It cannot be realized with our setup with no gas cell. Instead, we can make a sweep of the laser current in order to observe the shape of the photoacoustic signal. Zero-offset of the curve implies that there is no contribution from the photothermal effect. Additionally, since the QTF resonance can be affected by the proximity of the mR, the QEPAS signal is recorded while sweeping the laser modulation frequency.

Summarizing the experimental requirements, the protocol for each mR was the following:

1. Adjust the position of the QTF to maximize the QEPAS signal in the x and z directions
2. Adjust the QTF in the y direction until the QEPAS signal is lost (QTF barely touching the mR ⇔ y=0).
3. Withdraw the QTF in the y direction until the QEPAS signal is recovered (typically 50um)
4. Adjust the laser beam position to maximize the QEPAS signal
5. Make a sweep of the laser current to check if there is no photothermal effect (zero-offset)
6. Measure the QEPAS signal while sweeping the frequency of the laser modulation, at different mR-QTF distances.

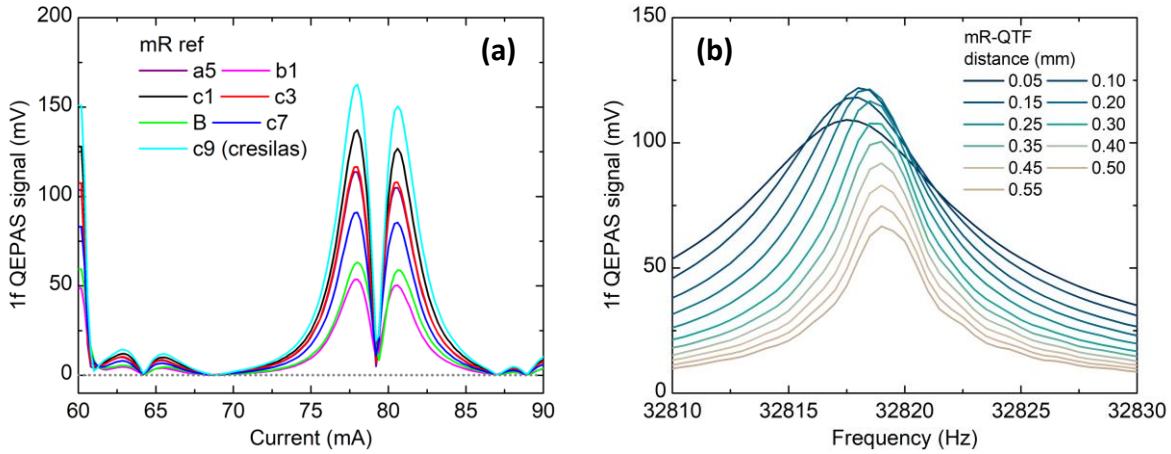

Figure 2.20: (a) The QEPAS signal versus the laser current for the different mRs. (b) The QEPAS signal as a function of the laser modulation frequency for the mR a5 at various mR-QTF distances.

The results of the laser current sweep is shown on Figure 2.20(a). The curves are offset free, indicating that only the photoacoustic effect was contributing to the measured QEPAS signal (no photothermal effect). Otherwise said, the laser passed through the mR without hitting the inside of the hole. After this verification, we measured the QEPAS signal as a function of the laser modulation frequency (Figure 2.20(b)) and the mR-QTF distance. The measurement was repeated for each mR described in Table 2-4. A Python script was employed to fit the curve and to extract the QEPAS signal at resonance, the quality factor and the resonant frequency. The results are summarized on Figure 2.21.

mR ref	a5	b1	c1	c3	c5	c7	c9
Fabrication	Aluminium block	3D printing	3D printing	3D printing	3D printing	3D printing	3D printing
Slit shape	Round	Round	Round	Obround	Square	Square Horn	Obround
Measured f_{mR} (Hz)	33 200	29 100	32 200	35 650	30 200	35 650	32 650

Table 2-4: Summary of the features of the different microresonators tested.

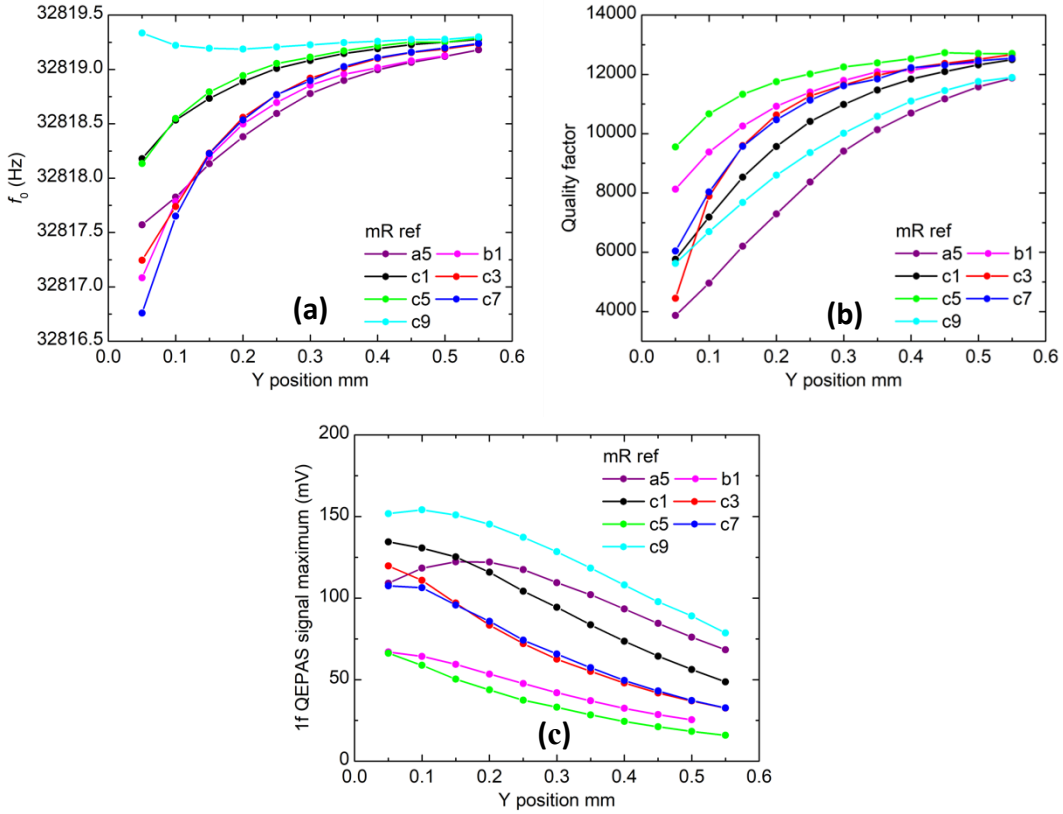

Figure 2.21: The resonant frequency (a), the quality factor (b) and the QEPAS signal (c) as a function of the mR-QTF distance along the y-axis.

From Figure 2.21(a), it can be said that the QTF resonant frequency as a function of the y position, behaves very similarly for most mRs, showing a variation of about 2 Hz when approaching the QTF to the mR, except for the mR c9 for which f_0 remains almost constant in this case (the cause is under discussion). In terms of quality factors (Figure 2.21(b)), the smallest value is obtained with the mR a5, due to the strong squeeze film effect. Except the mR a5 and b1, the mRs have an equivalent 'outer' shape that should lead to the same squeeze film effect. However, the variation of the quality factor is different for all mRs. It might be explained by a strong mR-QTF acoustic coupling which differs depending on the slit shape and the frequency mismatch.

Finally, the QEPAS performance of the different mRs can be compared. The original micromachined mR a5 shows a good QEPAS signal, but it decreases for small mR-QTF distances. The mR c1, the 3D printed equivalent of the a5, exhibits a better signal due to a higher QTF quality factor close to the mR. The 3D printed mRs (c3-c5-c7) with modified slit shape, show lower QEPAS performances due to the resonance mismatch. Finally, the mR c9, with an obround slit shape, which was accurately frequency matched with the QTF, achieved the highest QEPAS signal, about 25% greater than with the mR-a5. The results we obtained from Figure 2.14(b), Figure 2.18(b) and Figure 2.21(c) are fairly comparable, though the latter experiment is more accurate and also gives information about the evolution of the QTF resonance, giving a deeper understanding of the mR-QTF acoustic coupling.

In conclusion, we compared the mRs in terms of QEPAS performances while measuring the QTF resonance. We presented a stringent protocol to obtain consistent results. We modified the slit shape to improve the coupling between the mR and the QTF. We fabricate the mRs by

3D printing which allows complex shapes but also has some limitations in terms of resolution and repeatability. After a few iterations, we obtained the best performances with the 3D printed mRs and an obround slit shape. More iterations could lead to even better improvements. For instance, we could imagine building a new kind of mRs allowing a double optical pass in order to increase the absorption path length.

2.2.6. Effect of the QTF positioning

After the experimental dimensioning of the mR was completed, we studied the influence of the QTF position. Using the same experimental setup and replacing the microphone by a QTF gave us a suitable setup to optimize the QTF position relatively to the mR. For on-beam QEPAS, it has been theoretically described and experimentally verified [28]. However, the behavior in an off-beam configuration can differ from the one in on-beam. The acoustic source being the mR slit instead of the direct pressure wave associated with the laser beam, the pressure around the QTF prongs has a different profile in space. The QEPAS signal is thus recorded while moving the QTF in the 3 space directions (Figure 2.22).

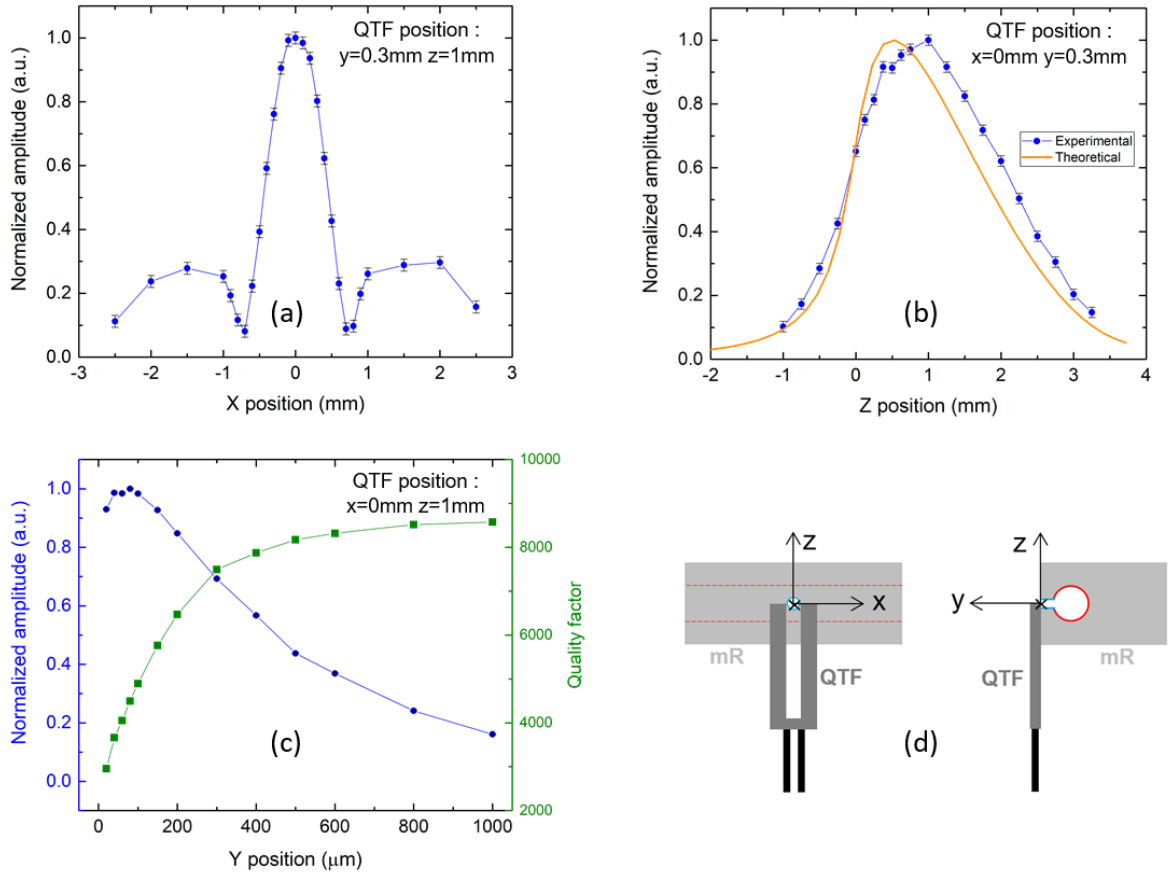

Figure 2.22: Amplitude of the QEPAS signal as a function of the relative position between the mR (ref: a5) and the QTF, in the x (a), z (b) and y (c) directions. Illustration of the referential (d) with the mR located at the origin (x = y = z = 0) corresponding to the black cross. The simulated curve (orange) for the on-beam configuration was added for the z direction (from Figure 1.23).

In the x direction (Figure 2.22(a)), the signal has a maximum at x equal to zero. The fork has a mirror symmetry relative to the yz plane, thus the signal is optimal when the source is located in the symmetry plane. The signal decreases to almost zero when one of the prong is

placed in front of the mR opening, followed by an increase due to the excitation of the external part of the prong. In the z direction (Figure 2.22(b)), the optimum is located 1 mm below the top of the QTF. It is a little below the ideal z position for the on-beam QEPAS (0.7mm) [28]. The diameter of the orifice being 0.5 mm, the acoustic energy is more widespread than in on-beam, thus displacing the optimum z position by 0.3mm. Finally, the y direction being the most crucial, the quality factor was determined as well as the QEPAS signal (Figure 2.22(c)). The Q factor decreases from 8000 to 3000 at 20 µm, due to viscous damping effects in the vicinity of the wall of the mR. The QEPAS signal exhibits a maximum around 100 µm. In conclusion, the ideal position of the QTF, relative to the mR, was determined and corresponds to an optimum acoustic coupling between the QTF and the mR.

2.2.7. A novel design using two microresonators (2mR 2cc)

The symmetrical movement of the 2 QTF prongs is best coupled with a cylindrical acoustic wave when the axis of the wave is located in between the 2 prongs. Both on-beam and off-beam satisfy this condition. One acoustic source acting on the inner surface of both prongs symmetrically. Alternatively, the QTF could be excited by applying a force on the outer surface of the prongs, but it is hardly possible with a lone acoustic source. We rethought the design of the spectrophone to be able to excite from the outside of the prongs. We used two off-beam mRs placed in a mirror symmetry and the QTF located in between (Figure 2.23(a)). The optical path is somewhat more complex. The laser beam goes through one microresonator (mR 1), undergoes 2 right-angle reflections that brings it parallel to the incoming beam with a lateral shift (δ), and finally crosses the other microresonator (mR 2).

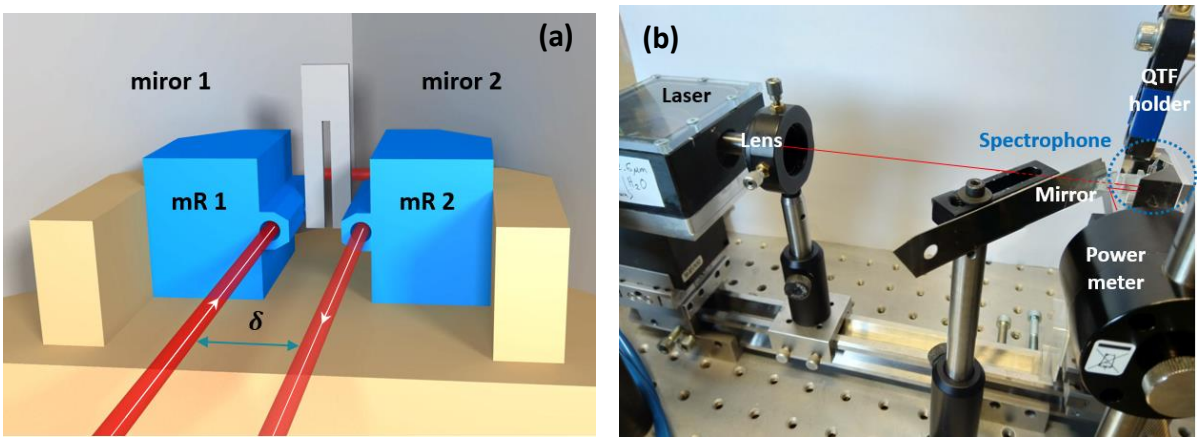

Figure 2.23: (a) CAD drawing of the new spectrophone design, with the 2 mRs, the 2 corner cubes (cc) mirrors, the QTF and the holder (orange). (b) Picture of the setup: the laser (EBLANA 1392nm) on the left is focused through a lens into the spectrophone, the exiting beam is monitored with a power meter.

In our configuration, the two mRs are accurately pre-positioned using an aluminum machined holder. The holder ensures that the main hole of the mRs are well in the optical plane and that the mRs are spaced with a distance equal to the width of the QTF plus a 100µm gap. The two corner cube mirror are glued onto a plate, thus setting an angle of 90° between the two reflective surfaces. The back plate slides along a shoulder in the back of the holder. Therefore,

the two mirrors can be translated in the normal direction of the incoming beam, offering a simple mean of adjusting the distance δ.

The setup is pre aligned using a red laser (Figure 2.23 (b)). The visible laser is positioned instead of the IR laser and sent to the mR 1. The mirrors are translated until the exiting beam consistently crosses the mR 2. Collision with the mR walls was prevented by visual inspection though the reflections on the transparent resin made the adjustments tedious.

Next, the red laser was replaced by the IR laser (EBLANA 1392nm, see specifications on Figure 2.8) and a focusing lens (similar setup as presented in section 2.2.1) and a power meter was used to monitor the output power. The exiting beam was sent to the power meter by using a tiny mirror, without cutting the incoming beam. The optical constraints are greater than with the traditional off-beam. The beam had to cross the 2 mRs without impinging their wall, meaning the beam size needs to be smaller than the mR diameter ($2R_{mR}$) over a distance equal to 2.2 cm ($2L_{mR}$ plus the optical path between the 2 mR). The laser was positioned about 20 cm far from the spectrophone so as to obtain a slowly converging beam. Approximately half of the initial optical power was measured at the output, partly associated with free water absorption.

After the first attempts to obtain the QEPAS signal, the mR was modified to simplify the alinements. The two mRs were redrawn as a single part combining the two mRs, solving 3 problems in one stroke: the gap between the 2 mRs was accurately controlled, the 2 slits were perfectly facing each other and the stray light due to the mirror reflection was prevented from hitting the QTF. Different mRs were fabricated (D-series), with different values for the QTF gap. An ideal gap of 70µm on each side of the QTF was obtained (Figure 2.24(a)) A xyz translation stage was used to accurately position the QTF inside the mR. The QTF resonance was measured by means of electronic excitation and used as a control signal during the descent. This continuous control technique was an absolute necessity to prevent the QTF collision and breakage. The frequency response of the QTF free and inside of the mR were compared, showing a Q factor of 14140 and 9300, resp (Figure 2.24(b)). The Q value decrease (about 30%) in 2mR 2cc is similar to the off-beam one. The large signal offset is due to the parallel capacitance of the long coaxial cable before the transimpedance amplifier.

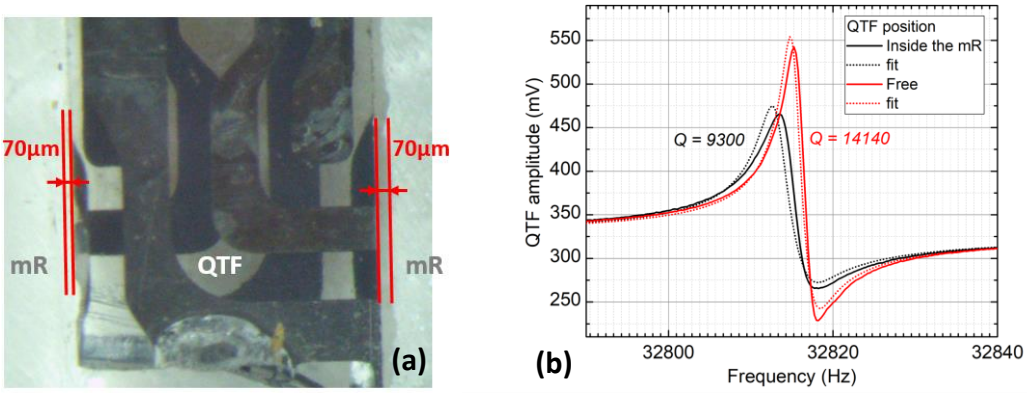

Figure 2.24: (a) Magnified (×4) picture of the QTF positioned inside the 2 mRs. (b) Frequency response of a QTF in free space (red) and positioned inside the mR (black). The Q factor is determined through the curve fitting with the Butterworth Von Dyke model.

In the 2mR 2cc configuration, there are two acoustic sources photo-generated with the same laser. In order to obtain the best excitation of the QTF, the two acoustic sources must be in-phase. Considering two perfectly similar mRs and also two similar mR-QTF gaps, the phase

shift Δφ between the two acoustic sources can be calculated with the optical path difference ΔL between the two mRs (ΔL=2.2cm) :

$$\Delta\varphi = k\Delta L = \frac{2\pi f_0}{c}\Delta L = 1.3 \cdot 10^{-5}\, rad \qquad (2.4)$$

With k the wave vector.

The phase shift is negligible; therefore the 2 mRs are considered to be acoustically in phase.

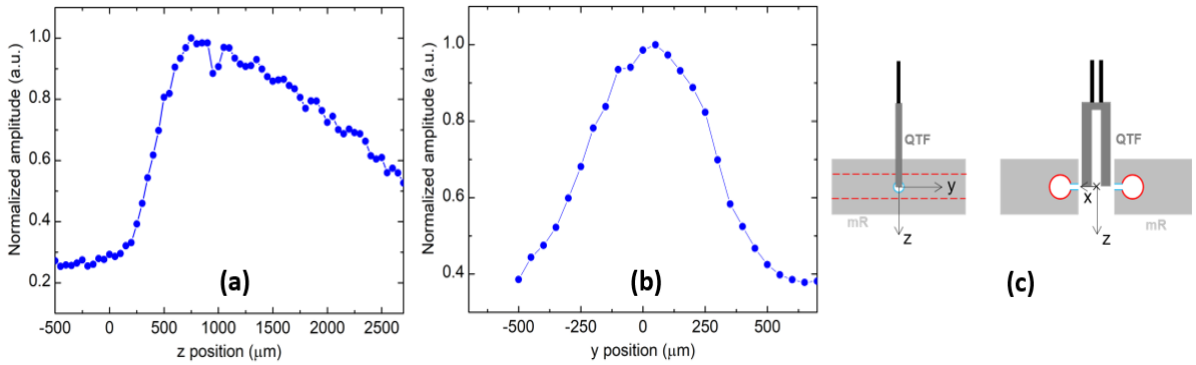

Figure 2.25: Evolution of the QEPAS signal when moving the QTF in the z (a) and y (b) direction. (c) Schematic of the mR and the QTF in the defined referential. The QTF is represented in the (0, 0, 0) position.

The QTF was inserted into the mR, and the laser beam crossed the two mRs. The QEPAS signal was monitored as a function of the QTF position, in the y and z direction (Figure 2.25). The signal amplitude directly indicates the 2mR-QTF coupling efficiency. In the z direction, the response grows significantly when the top of the prongs arrives in front of the slit and then decreases slowly as the lever becomes small. The response versus the y direction exhibits a mirror symmetry with the ordinate axis, and a maximum when y = 0, i.e the prong and the mR slit best overlap.

After the optimization of the QTF position, we studied the effect of each individual mRs and compared it to the off-beam configuration (with a single mR). To this end, we first measured the QEPAS signal as a function of the mirrors position. The mirrors were translated in the perpendicular direction with respect to the incoming beam, using a micrometric translation stage, thus changing the value of δ. At first, the laser beam travels only through the mR 1, giving a QEPAS signal maximum of about 20 mV (Figure 2.26(a)). When the mirror is translated, the beam crosses the mR 2 and the signal rises to 40mV, approximately doubling the initial value of the signal. The signal presents a nice plateau over 200μm. The results can also be presented in terms of the QEPAS signal versus the laser current, with the typical 1*f* signal shape (Figure 2.26(b)). We added the signal obtained with the conventional off-beam, whose amplitude is about 30mV. The amplitude difference between the off-beam and the misaligned 2mR 2cc is associated with the mR resonance. In the off-beam configuration, the slit is considered open while in the 2mR 2cc configuration, the slit should be considered almost as closed, thus changing the acoustic resonant frequency. The mR and the QTF resonant frequency are unmatched in the 2mR 2cc configuration. An optimization of the mR resonance might lead to doubling the signal in the 2mR 2cc compared to the conventional off-beam.

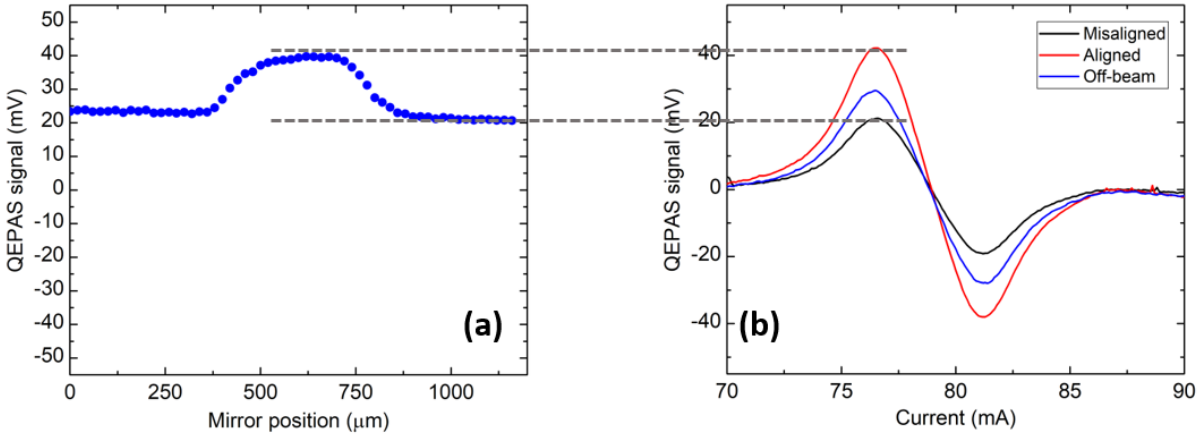

Figure 2.26: (a) Effect of the mirror position on the QEPAS signal maximum. (b) QEPAS signal versus laser current when the beam is misaligned (black) or aligned (red) with the mR 2, and comparing it with the results from conventional off-beam (blue).

The strength of the 2mR 2cc method is the large enhancement of the mR-QTF coupling. The surface of the prong is normal to the wave propagation direction; thus the pressure is efficiently actuating the QTF. The weakness of the 2mR 2cc is the sensitivity to the QTF positioning compared to the conventional off-beam. However, the required spatial accuracy (10-30μm) is definitely reachable using micropositioners.

It is important to note that a similar work [29,30] was published a few months after our work on this new design of mR was finished. The new design, proposed by Hu et al, is based on a QTF-embedded, double-pass, off-beam quartz-enhanced photoacoustic spectroscopy (DP-OB-QEPAS). Similarly to the original off-beam mR, the spectrophone is made of two cylindrical mR with a slit in the center (Figure 2.27). The QTF is embedded in the mR, the slit is large enough in order to partly immerse the QTF prong inside the mR cavity and thus having better coupling. The authors made a thorough study on the effect of the length and the radius of the mR. The optimized spectrophone shows a SNR gain of ≈20 and ≈40, without or with the right-angle prism, respectively, which correspond to a factor 2 increase. Although their setup is differently implemented, the working principle is similar to the one we developed and their results in terms of SNR gain are in good agreement with the ones we obtained.

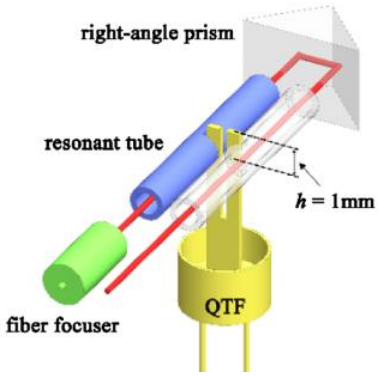

Figure 2.27: Schematic of the embedded off-beam QEPAS proposed by Hu. *et al.* [30]. The spectrophone is based on 2 off-beam microresonators. Each QTF prong is embedded in a mR. A double optical pass is realized using a right angle prism.

In summary, a novel design was proposed in order to increase the acoustic pressure, using 2 mRs actuating on the external side of the QTF prongs. The 2 mRs were successfully 3D printed, showing the ability of the SLA method in printing complex parts. The gap between the 2 mRs was adjusted at the printing level, simplifying the assembly process and the optimization the QTF positioning. Finally, the 2mR 2cc spectrophone was tested in a QEPAS experiment showing better results than the conventional off-beam spectrophone.

2.3. Off-beam QEPAS experiment with a QCL for the detection of ethylene.

In this section, we present a QEPAS sensor optimized for quantum cascade lasers. The goal of this prototype was the modification of the QTF spectrophone, originally designed to work with near-IR lasers, in order the meet the QCL optical requirements. A DFB QCL laser emitting at 11μm was fabricated at the IES. It was thoroughly characterized in terms of electrical performance and spectral emission, allowing to target a strong ethylene absorption line. Then, the QEPAS signal was optimized experimentally and compared to the simulation based on the modulation theory. Eventually, the sensor performances were assessed and compared to the literature.

2.3.1. Laser specifications and wavelength selection

The QCL used in this study was fabricated in the IES, based on the InAs/AlSb materials and grown by Molecular Beam Epitaxy (MBE) in a RIBER 412 solid-source MBE system. The laser structure is reported in [31]. The grown wafer was processed into 7-μm-wide ridge lasers. A linear grating was patterned on the top of the ridges using electron beam lithography and inductively coupled plasma etching. The ridge surface was then metallized with gold thus forming a metal DFB grating in the laser waveguide. The periodicity of the 1st order grating was selected to be 1.63 μm, giving an emission wavelength close to the maximum of the QCL gain spectrum. The fabricated devices were mounted epi-side down on copper heatsinks. The lasers operated in the continuous wave regime up to room temperature with a threshold current density of 1.3 kA/cm^2. The voltage-current and light-current characteristics of the laser at different temperatures are shown on Figure 2.28.

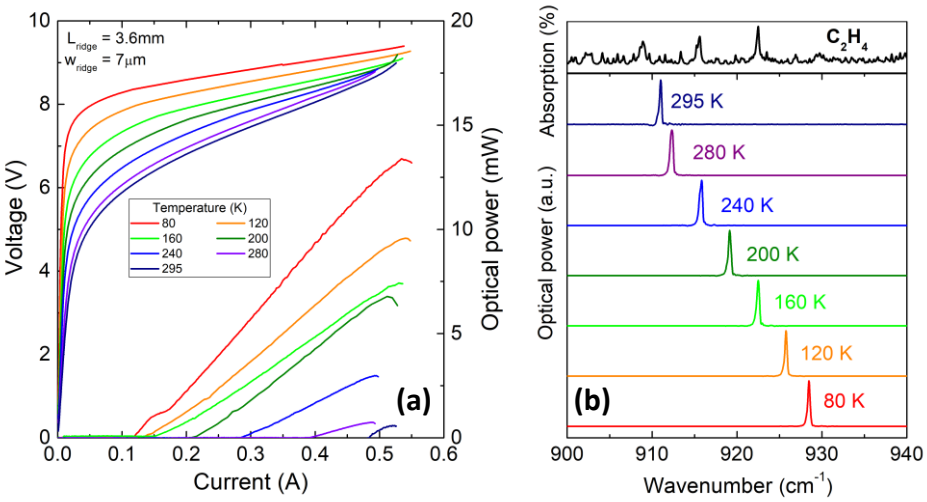

Figure 2.28: Voltage-current and light-current characteristics (a) and emission spectra (b) of a 3.6-mm-long QCL at different temperatures. The ethylene absorption spectrum, on top of graph (b), shows many features in the range covered by the QCL

For spectral characterization, a Fourier transform infrared spectrometer combined with a pyroelectric detector was used. The laser emission was tuned by varying both the current and the temperature, with respective tuning rates of -0.9 cm^{-1}/A and -0.09 cm^{-1}/K. For our purpose, the laser temperature was chosen to be around 240K for two reasons: the emission wavelength is close to a strong absorption peak and the optical power is up to 3 mW. The measurements were performed using a homemade Peltier temperature controlled module able to cool the laser at temperatures down to 240K without using liquid nitrogen, thus making the system more suitable for field deployment. In total, with a temperature span of 40K, a spectral range of about 3.5 cm^{-1} can be covered, addressing various ethylene absorption lines.

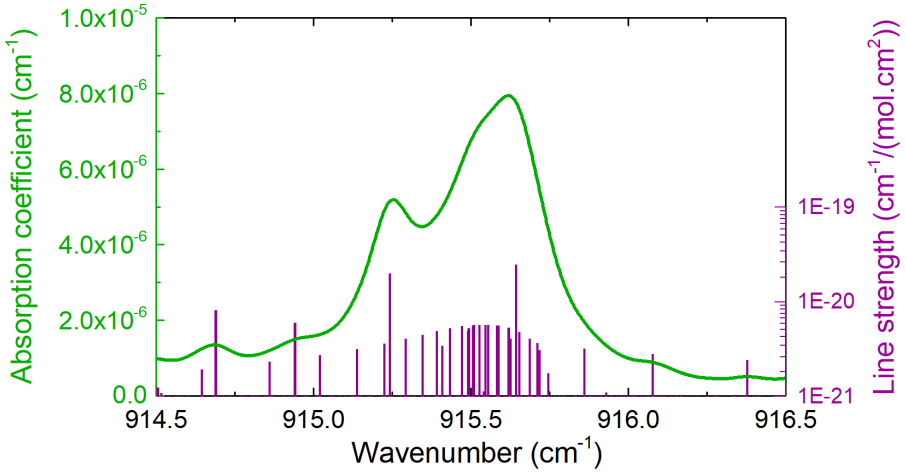

Figure 2.29: Selected absorption peaks (green) obtained from the Hitran database around 915.61 cm^{-1}, for 1ppmv of C_2H_4 at standard conditions of pressure and temperature, and the corresponding absorption lines (purple).

As shown on Figure 2.29, the composite ethylene absorption spectrum results from multiple transitions with linestrengths ranging from 10^{-21} to 10^{-19} $cm^{-1}/(mol \cdot cm^2)$. Those bands add up to form a double peak with maxima located at 915.61 and 915.25 cm^{-1}. At a concentration of 1 ppmv, it exhibits an absorption coefficient of 7.94×10^{-6} cm^{-1} (a factor 1/5

compared to the strongest peak at 951 cm^{-1}) and a half width at half maximum of about 0.28 cm^{-1}. In terms of common interfering species, the closest H_2O absorption is located far from the laser setpoint (913.97 cm^{-1}). For a usual atmospheric composition (1% H_2O, 450 ppm CO_2, in volume), absorption due to CO_2 was 1 order of magnitude lower than that of a 100 ppbv C_2H_4 target sample.

2.3.1.1. Divergence of the QCL beam.

The cross section of the active zone can be considered as the optical emitter. It has a rectangular shape of 3.2µm thickness and 7µm width. This rectangular shape leads to an elliptical optical beam. The smallest (resp larger) dimension is called the fast (slow) axis. The divergence is the largest along the fast axis. The emission was simulated using Gaussian optics with the software Gaussian Beam. For the fast (resp slow) axis, the laser waist equals to half the active zone thickness (resp width) leading to a full diverging angle (2θ) of about 120° (resp 80°). The light is then collected by a lens **(L1)** of focal *f*=4mm, located 4.18mm after the lens, in order to obtain a focal spot about 10cm after the lens. The center of the mR is located at the focal spot. The beam at the entrance ($w(z_2-l_{mR}/2)$) is calculated and should be very inferior than the mR radius (R_{mR}). As defined in Gaussian Optics, the beam width *w(z)* corresponds to the distance from the optical axis where the intensity has decreased by a factor 1/e. Some optical rays remain beyond the Gaussian width; therefore we must have $w(z_2-l_{mR}/2) << R_{mR}$. Also, it is practically difficult to ensure the exact position of the focal spot due to the short focal distance of the lens.

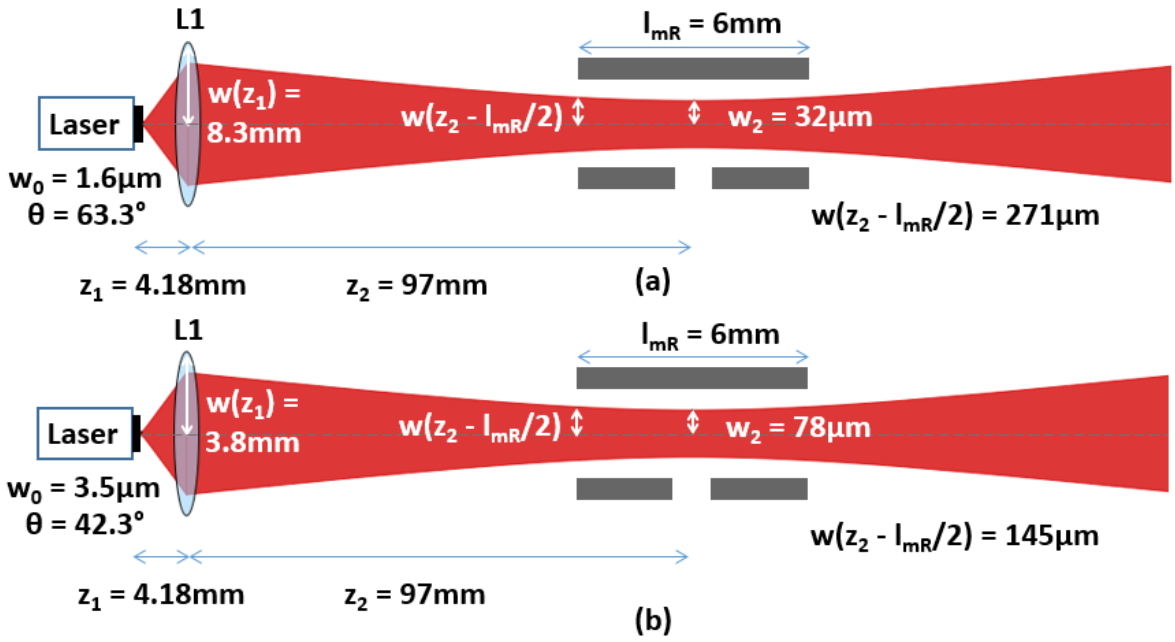

Figure 2.30: Simulation of the QCL emission using a Gaussian beam software, for the fast axis (a) and the slow axis (b). The laser of waist size w_0, emits a divergent beam, collected by a length L1 of focal *f*=4mm and directed to the mR located 97mm after the lens. The focal spot corresponds to the middle of the mR. The beam diameter is measured at the entrance of the mR. The wavelength is set to 10µm.

2.3.2. Experimental setup

A schematic of the QEPAS sensor for ethylene detection is presented in Figure 2.31:. As for a conventional QEPAS system, the photoacoustic generation is obtained using a DFB laser, and the detection is provided by a QEPAS spectrophone enclosed in a gas cell. The spectrophone, consisting of the microresonator (mR) and the QTF, is based on an off-beam geometry, adapted to the QCL optical requirements.

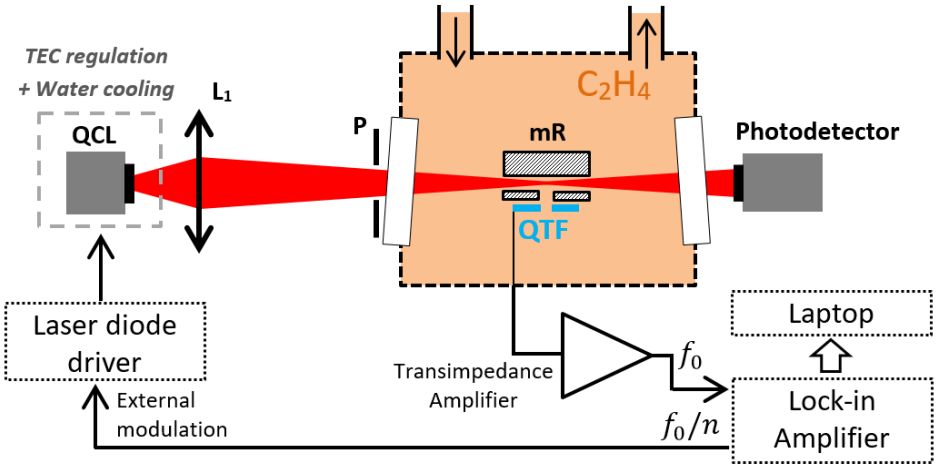

Figure 2.31: Schematic of the QEPAS setup (top view) for ethylene detection. The excitation source is a Quantum Cascade Laser (QCL). The acoustic spectrophone is made of a microresonator (mR) and a Quartz Tuning Fork (QTF).

The QCL emits an elliptic beam with a high divergence estimated to be 80x120° in the lateral and vertical directions, respectively. There are two critical points in the QEPAS optical design: an efficient light collection, and preventing the direct illumination of the mR walls. To collect the maximum optical power, the collimation lens must be chosen with a high numerical aperture. However, aberrations at high angles can result in photothermal noise due to the illumination of the mR walls. The issue can be overcome by using a two-lens optical system, forming an intermediate image between the lenses and removing divergent rays with a pinhole [11]. Another approach employing an hollow-core fiber was successfully implemented [32]. In our case, for convenience of optical procedures, a single aspheric lens **(L1)** (Thorlabs C036TME-F, f=4.0mm) was used for laser light collection and focusing. The laser light is focused in the center of the main tube of the mR. At the entrance of the mR, the beam diameter is approximately of 0.5 mm. A 2-mm-diameter pinhole **(P)** is positioned at the entrance of the gas cell for coarse beam cleaning. A pyroelectric detector (Infratec LIE-332f-66) is used for optical alignments. In the off-beam configuration, the mR offers multiple benefits to the system: (1) it increases the acoustic pressure (as in on-beam QEPAS), (2) it can be adapted to the beam width, (3) it protects the QTF from the stray light by separating light absorption and sound wave detection. The mR main hole radius was increased to 0.75mm, whereas it was 0.35mm for our former setup with near-IR laser diodes. After photoacoustic generation and amplification, the acoustic wave is converted into an electric signal by the QTF. The electrical signal is processed through a transimpedance amplifier and then a lock-in amplifier.

2.3.2.1. Issues and improvements

We faced two major issues during the first QEPAS experiments for ethylene detection: the presence of Fabry-Perot (FP) interferences and a strong signal offset. Fabry-Perot typically appear in a system when there is an optical cavity, most likely two parallel reflective surfaces allowing the rays to travel back and forth. As it can be seen on Figure 2.32(a), they give rise to periodical oscillations. The frequency interval is equal to the free spectral range (FSR):

$$\Delta f = \frac{c}{2L_{FP}} \tag{2.5}$$

With c the speed of light and L_{FP} the distance between the two reflective surfaces forming the optical cavity.

In our case and more generally in spectroscopy, FP interferences is an unwanted effect: the amplitude and the position of the oscillations can vary throughout time and thus cause a measurement artifact. They are mostly due to variations of the cavity length upon temperatures changes or mechanical stress. Also, QCL are known to be very sensitive to optical feedback, even in the case of DFB lasers. Therefore, optical feedback should be as low as possible.

As we observed the FP interferences, we translated the QEPAS cell, re measured the QEPAS signal, and found the oscillations period had changed. It showed that the cavity was made by the QEPAS cell and the laser (and not by the 2 windows of the QEPAS cell). The reflection of the QEPAS cell was not caused by the windows which were tilted but by the side of the mR. In this experiment the mR radius was of 0.35mm which is small compared to the beam radius at entrance. Increasing the mR radius to 0.75mm solved the issue.

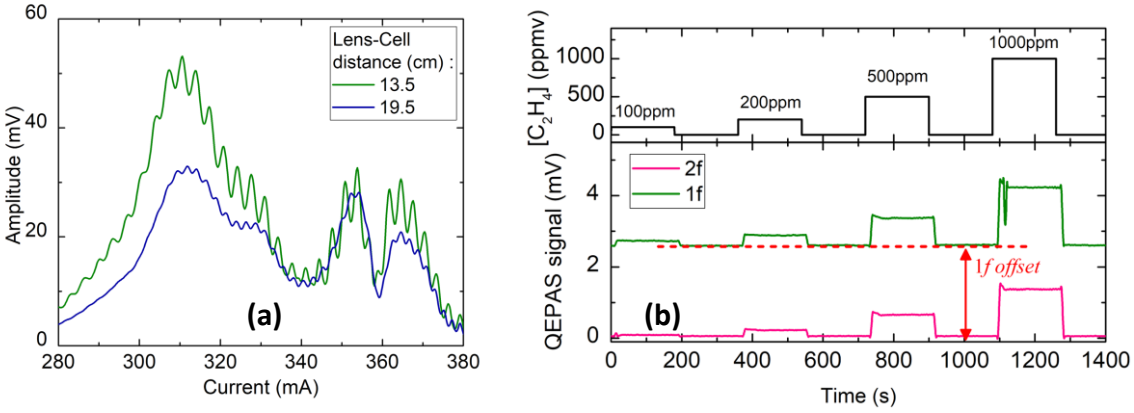

Figure 2.32: (a) QEPAS signal versus injected current for different distance of the cell. The oscillations are due to Fabry-Perot interferences. (b) QEPAS response to different steps of ethylene concentrations. In 2*f* mode (pink) the signal returns to zero when the cell is flushed (0ppm) while in 1*f* mode shows a significant offset.

The second issue concerned the large signal offset in the 1*f* mode. The QEPAS signal is represented on Figure 2.32(b) during a gas cycle. When the target gas concentration equals to zero, we expect the 1*f* QEPAS signal to be zero as well. The signal offset was attributed to the photothermal effect, i.e. direct illumination of the QTF prong resulting in a variation of the QTF surface temperature and thus a mechanical excitation of the QTF. The signal background can also be due to intensity modulation at solid-gas interfaces (cell windows, walls, …). It is present in 1*f* mode and almost negligible in the 2*f* mode [33]. 2*f* remains unaffected because of the use of the second harmonics whereas the intensity modulation occurs only at the fundamental

frequency. The 1*f* signal offset was corrected by adding a pinhole to remove divergent rays and by placing an optical shield to prevent direct illumination of the QTF.

2.3.3. Results

2.3.3.1. A wide response over temperature for small modulation amplitudes

The QEPAS sensor was then employed for spectroscopic purposes and ethylene sensing. The laser temperature was continuously adjusted from -30 to 10°C while recording the 2*f* QEPAS signal. The photoacoustic generation is proportional to the optical power. To obtain a power independent spectrum, the QEPAS signal was normalized by the optical power. The normalized signal is compared to the 2nd derivative of the ethylene spectrum (Figure 2.33), obtained with the HITRAN database and the HITRAN-PC software, exhibiting a very nice concordance. This spectroscopic acquisition provided us meaningful information for: (1) the verification of the QCL behavior with temperature, (2) an accurate calibration of the tunability with temperature (3) the selection of the laser setpoint for optimum detection. Although the normalized QEPAS signal is meaningful for the calibration, the raw QEPAS signal allows us the selection of the laser setpoint for optimum detection. The strongest acoustic intensity in 2*f* mode is obtained at 915.25 cm^{-1}, and will lead to the lowest limit of detection.

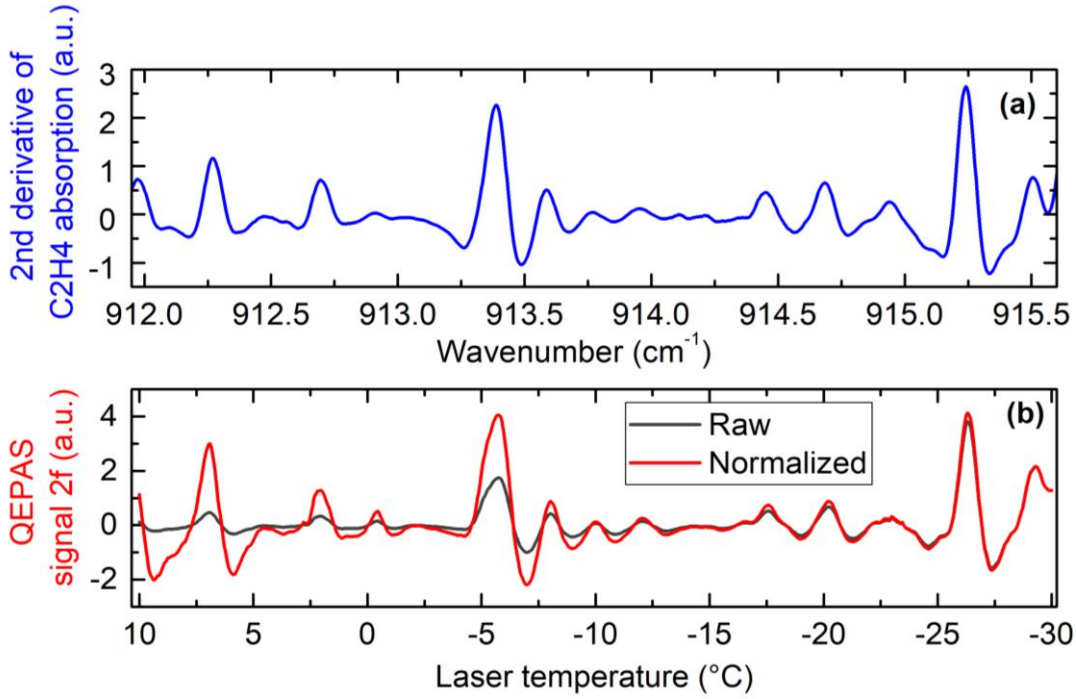

Figure 2.33: The 2nd derivative of ethylene absorption (a) is compared to the normalized 2*f* QEPAS signal (b). The laser current was of 340mA and the modulation amplitude of 0.04cm^{-1}, giving a modulation index of 0.5 for the peak located at 913.38cm^{-1}. Ethylene concentration was set to 5%.

2.3.3.2. Response for large modulation amplitudes

The QEPAS signal was measured over a broad spectra using temperature sweep, allowing to select the best laser setpoint. Next, the modulation amplitude was increased in order to obtain higher signal amplitudes. According to Schilt, the photoacoustic signal increases with the modulation amplitude till it reaches an optimum. The optimum modulation index m equals to 2 and 2.2, for the 1*f* and 2*f* modes, resp (see section 1.1.5.2). From the temperature sweep, we

identified the laser setpoint for the 1*f* and 2*f* modes. Then, we measured the QEPAS signal while increasing the modulation amplitude (Figure 2.34). We can make the following observations: the position of the optimum for the 1*f* occurs after the one for the 2*f*, the ratio of the 1*f* to the 2*f* maximum QEPAS signal is large (about 5). Those two observations do not correspond to the theoretical model, which is easily explained. Indeed, the theoretical model is based on a single Lorentzian peak whereas multiple overlapped ethylene lines are present in the region of interest (Figure 2.29). Another element to explain the large ratio (1*f* to the 2*f* maxima) is the presence of the signal offset, that was later removed.

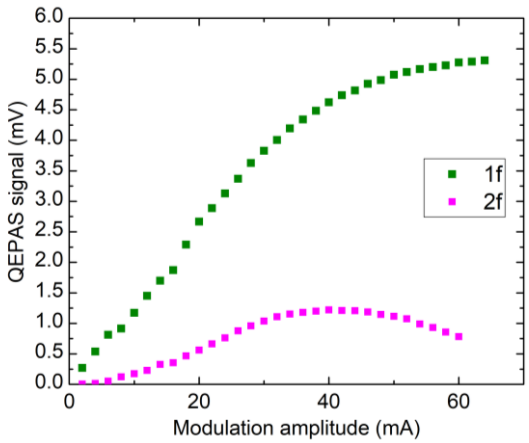

Figure 2.34: Optimization of the modulation amplitude for the 1*f* and 2*f* modes. The laser temperature is set to -26°C, and the current to 343 and 337mA, for the 1*f* and 2*f* modes, resp. The ethylene concentration is of 1000ppmv.

Unsatisfied by the incomplete optimization of the QEPAS signal, we decided to enrich the study by varying both the modulation and the laser current. The process was automated with Labview using multiple loops in order to obtain reproducible curves. (The Labview program proved to be an efficient tool and can be easily re employed for the optimization of any extra lasers) The results are presented on Figure 2.35.

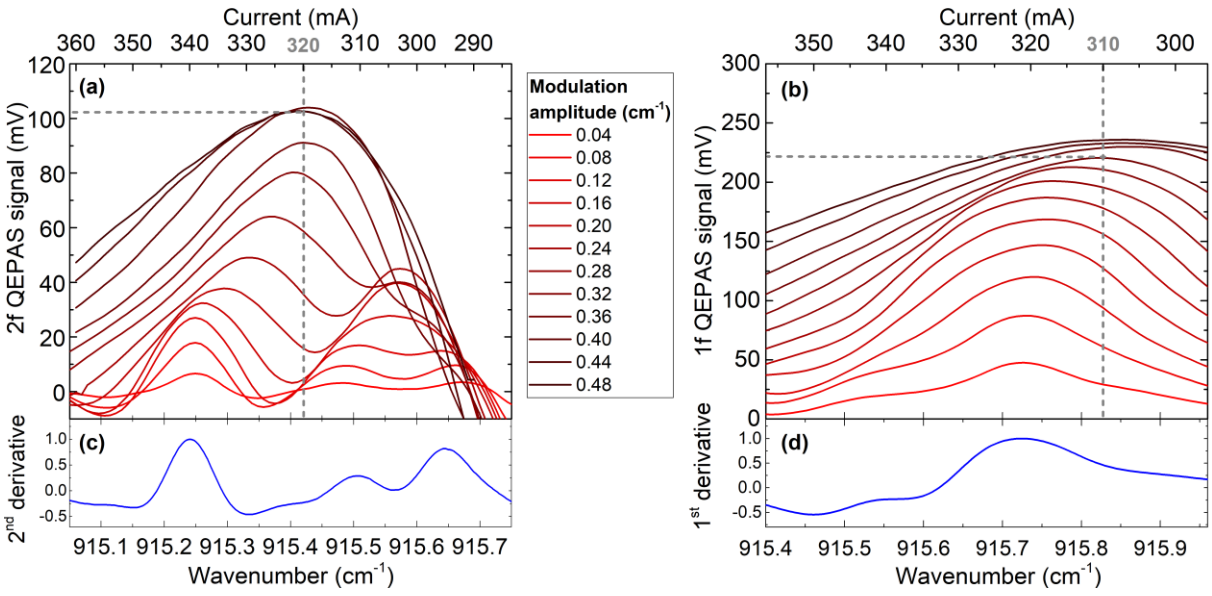

Figure 2.35: QEPAS signal measured as a function of the wavenumber, for different modulation amplitudes, for the 2*f* (a) and 1*f* mode (b). 2nd and 1st derivatives of ethylene absorption are represented in (c) and (d), resp. They are proportional to the the 1*f* and 2*f* QEPAS signals at small modulation amplitude. The grey dotted lines shows the optimum working conditions for both modulation schemes.

At small modulation amplitudes, two peaks at 915.25 and 915.61cm^{-1} can be observed, corresponding to the ethylene absorption profile. As the modulation amplitude is increased, the two features merge together to form a single broad peak with a magnified amplitude and the location of the maximum is shifted. The photoacoustic signal is not proportional to the *n-th* derivative anymore, but for gas sensing purposes it seems judicious to work with high modulation amplitudes in order to maximize the QEPAS signal. For the 2*f* mode, the optimum conditions are represented by the grey dotted lines on Figure 2.35(a) corresponding to a laser current of 320 mA and a modulation amplitude of 0.40 cm^{-1}. It seems unappropriate to deduce a modulation index for a such complex absorption. It can be noted that the modulation amplitude of 0.40 cm^{-1} is greater than the FWHM of the whole peak, that is 0.28 cm^{-1}, overlapping the two original ethylene peaks.

The study presented for the 2*f* mode was replicated for the 1*f* mode using the right side of the absorption peak at 915.61cm^{-1} (Figure 2.35(b-d)). Due to the broad feature of the ethylene spectra, the whole 1*f* signal could not be covered through a current sweep. Therefore, only the maximum of the 1*f* signal was recorded and not the amplitude. The linearity was then verified, proving that the 1*f* maximum is a meaningful quantity. From a theoretical point of view, the photoacoustic signal is stronger in 1*f* mode. It can be seen experimentally: there is a factor 2 between the 1*f* and 2*f* signal maxima for optimum conditions.

We optimized the QEPAS signal by adjusting both the laser current and modulation, in 1*f* and 2*f*. The current setpoints differ from the maximum of the absorption derivative, due to the composite ethylene spectra. Next, using Schilt's theory, the complex photoacoustic response can be theoretically fitted.

2.3.3.3. Simulation of the photoacoustic signal over a broad spectrum

Ethylene shows a composite spectrum in our region of interest. The photoacoustic signal can be accurately simulated using Schilt's model in the frame of the IM-FM modulation (section 1.1.5.3). Every absorption line is represented as a Lorentzian function. In order to simulate the PA response, the composite spectrum must be expressed as a sum of Lorentzian peaks. Using the Hitran Database, the ethylene spectrum is made of 521 peaks in the region ([911:917] cm^{-1}). (Figure 2.36(a)).

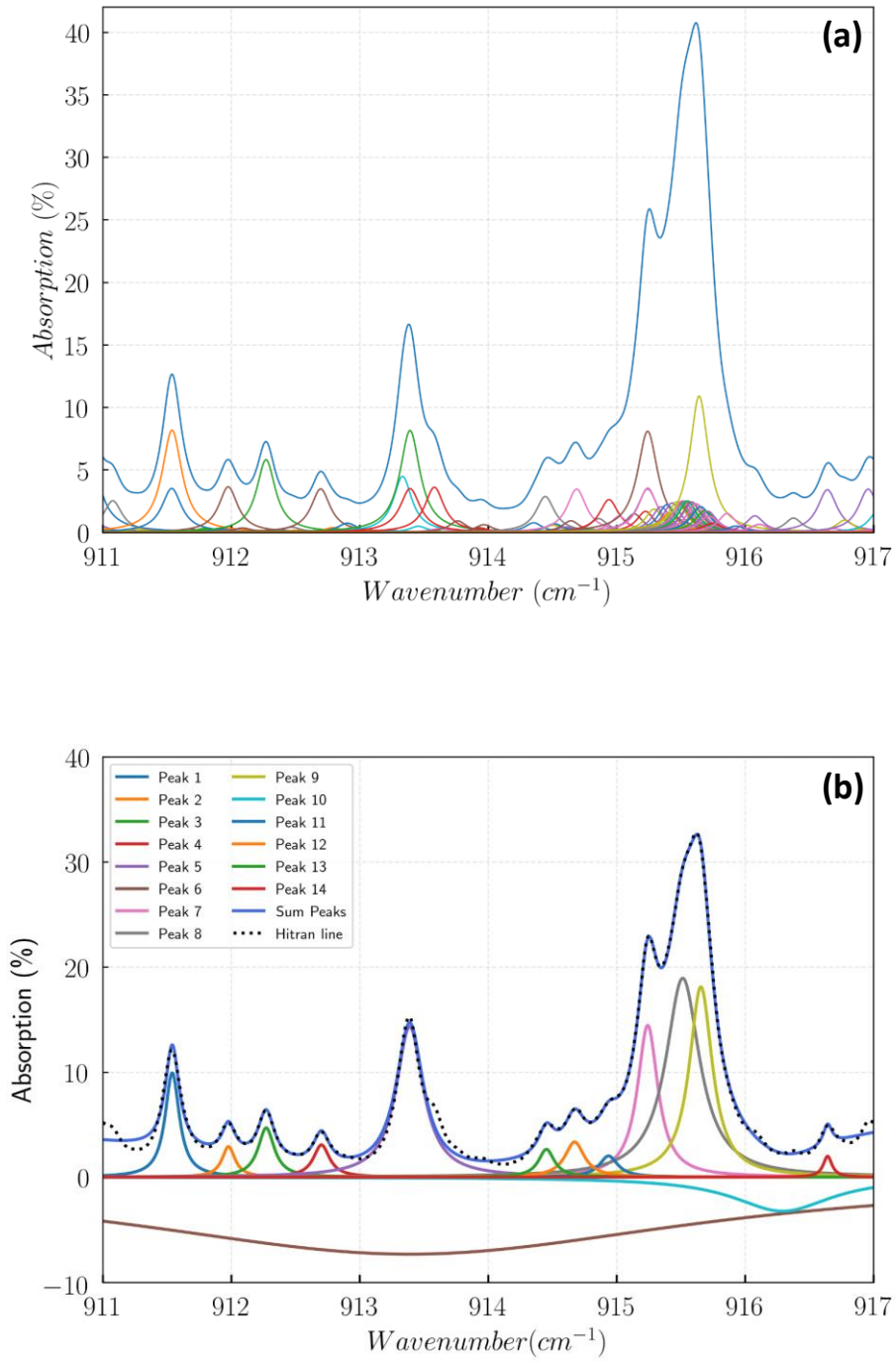

Figure 2.36: The composite ethylene absorption spectra can be represented as a sum of Lorentzian functions. In (a), the peaks originate from the HITRAN database while in (b), they are synthetic (without physical meaning). The spectrum is decomposed in 521 and 14 peaks for (a) and (b), resp. The total composite ethylene absorption is represented in blue.

Due to the high number of peaks, our first approach was to use simplified synthetic peaks instead of Hitran lines. Synthetic peaks were obtained by fitting the spectrum with multiple Lorentzian functions using the Origin software (Figure 2.36(b)). We obtained 14 peaks which, added together, provide a good enough fit of the absorption line, though the peaks have no

physical meaning. The center, width, amplitude and height of the fitted peaks were exported to txt file and imported in the Python script used for the generation of the PA signal, following the theoretical description of chapter 1 (section 1.1.5.3). The IM-FM modulation parameters (Ψ, $p_{\Omega}, p_{\omega}, \Phi_n$) were manually adjusted in order to fit the data.

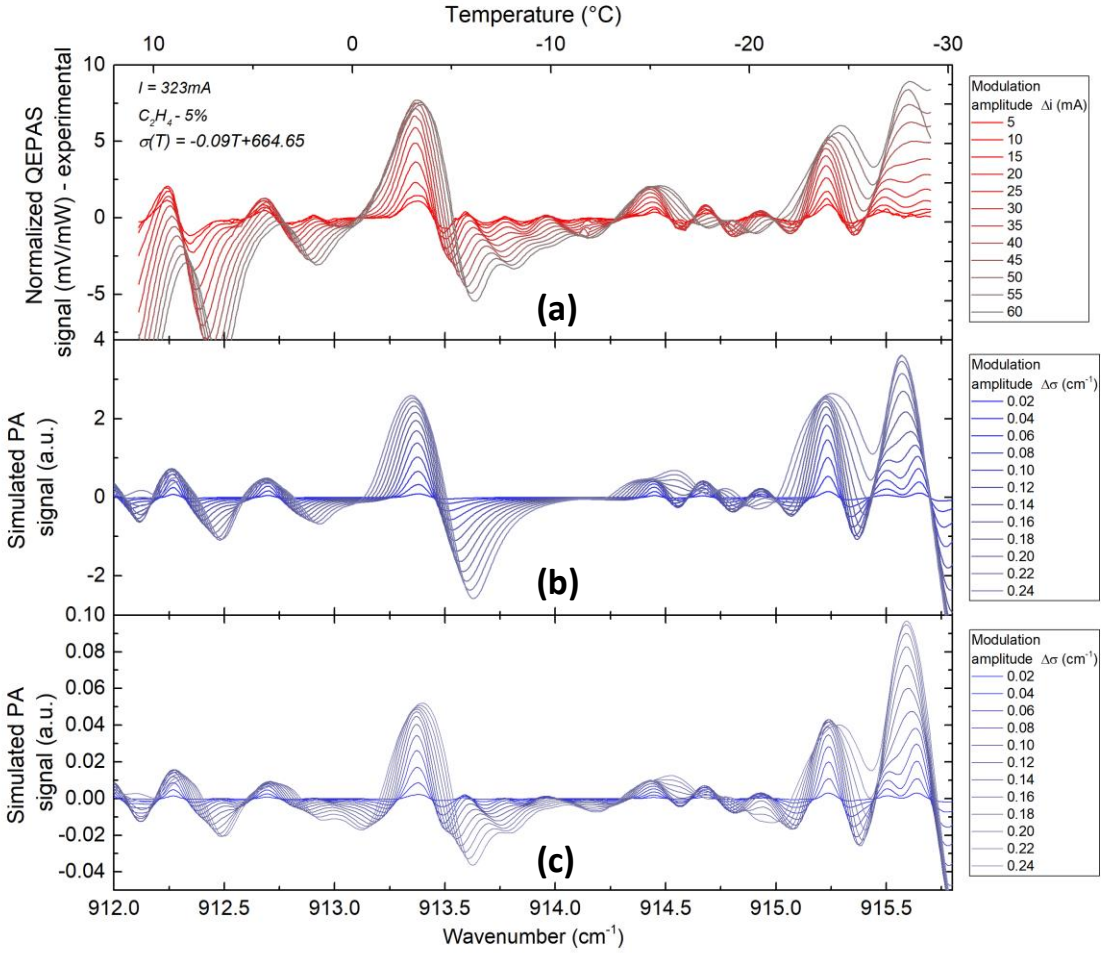

Figure 2.37: (a) QEPAS signal recorded while varying the temperature from -30 to 10°C. The signal is normalized by the instantaneous laser power. Simulated photoacoustic signal using synthetic peaks (b) or Hitran lines (c). The modulation parameters are ($\Psi = 0, p_{\Omega} = 0cm, p_{\omega} = -2cm, \phi_2 = 0$).

The experimental data, i.e. the QEPAS signal normalized by the power, are compared to the simulated photoacoustic signals (Figure 2.37). The simulations are close to the experimental signal. The simulation using Hitran lines is more accurate than the one from synthetic peaks, though it is more complex to compute, as discussed in the previous paragraph. The simulation of the PA signal is a useful tool to find the optimum laser current and modulation amplitude. Further refinements are necessary, notably to implement a fitting algorithm to accurately fit the data (on-going work).

2.3.3.4. Linearity and limit of detection

The linearity of the sensor was evaluated by monitoring the 1*f* QEPAS signal for different ethylene concentrations. The cell was successively filled with a calibrated gas concentration and flushed with N_2 between each steps to check the recovery of the zero signal. The results are

presented on Figure 2.38. The signal rises quickly, in a few seconds. The rise time is attributed to the gas mixer response time. Similarly, the signal overshoot at the onset might be due to the inaccuracy of the gas mixer when starting the new mixture or to the variation of the gas matrix affecting the QTF response. After 30 seconds, the signal reaches a steady state level that can be measured and plotted as a function of the ethylene concentration setpoint (Figure 2.38(b)). The curve is fitted to show the very good linearity of the sensor.

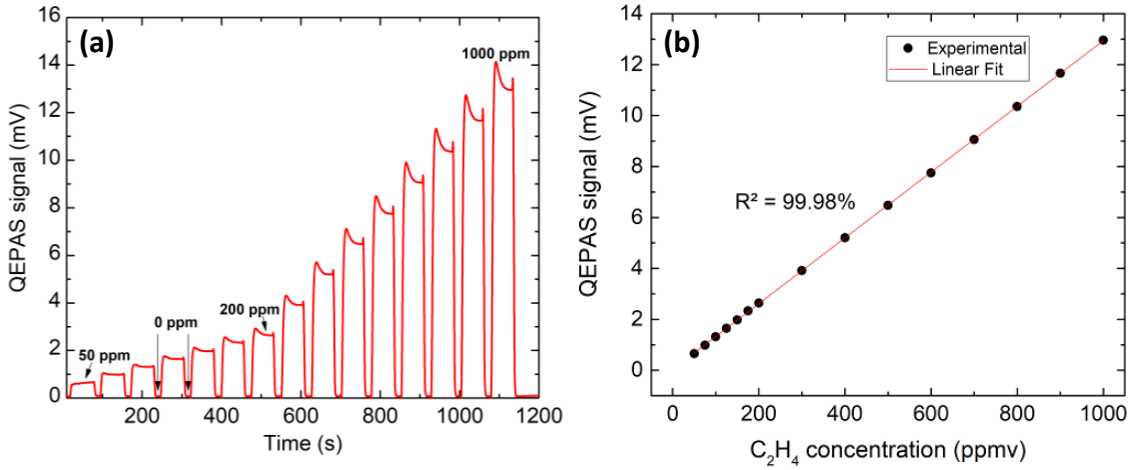

Figure 2.38: (a) 1*f* QEPAS signal during a gas step cycle, with concentration ranging from 50 to 1000ppmv. The ethylene mixture of known concentration is injected during 60s and the cell is flushed with pure N_2 for 15s. (b) The QEPAS signal versus injected ethylene concentration can also be represented. A linear fit is applied to show the linearity of the response. The integration time is set to 0.1s, giving an absolute error of 1.5 ppm.

Eventually, the sensor performances were tested in terms of limit of detection as a function of the integration time. 200 ppm of ethylene mixed with pure nitrogen were introduced into the gas cell. The signal was recorded for 30 minutes and the Allan-Werle deviation was calculated (Figure 2.39), as explained in section 1.3.5. The deviation exhibits a similar behavior for both 1*f* and 2*f* modes, with a $-t^{-1/2}$ slope indicating dominant white noise. Long-term drift appears after 60s. The limit of detection is of 60 ppb in the 1*f* mode, giving a NNEA of 4.8×10^{-8} W·cm^{-1}·Hz$^{-0.5}$.

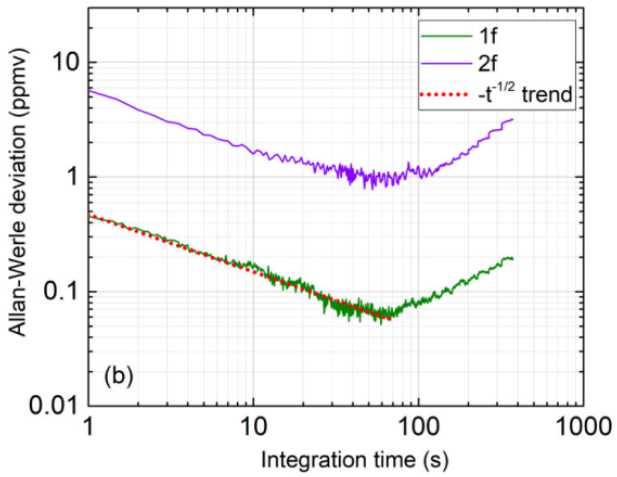

Figure 2.39: Allan-Werle deviation calculated from a 30 minutes acquisition for the 1*f* and 2*f* mode. The C_2H_4 concentration was 200ppm. The sensor was stable for 60s. The integration time is set to 100ms.

2.3.4. Verification of the results

The experiment involves a good management of the equipment and the automation through the Labview program, that has been increasingly improved and ruggedized during its PhD. We decided to carry out the same experiment, two years after the original one, in order to verify the consistency of the measurements. In particular, we were questioning the limit of detection. Indeed, on Figure 2.39, there is one order of magnitude between the 1*f* and the 2*f* signal, whereas on Figure 2.37 there is approximately a factor 2. This observation motivated us to remake the measurements.

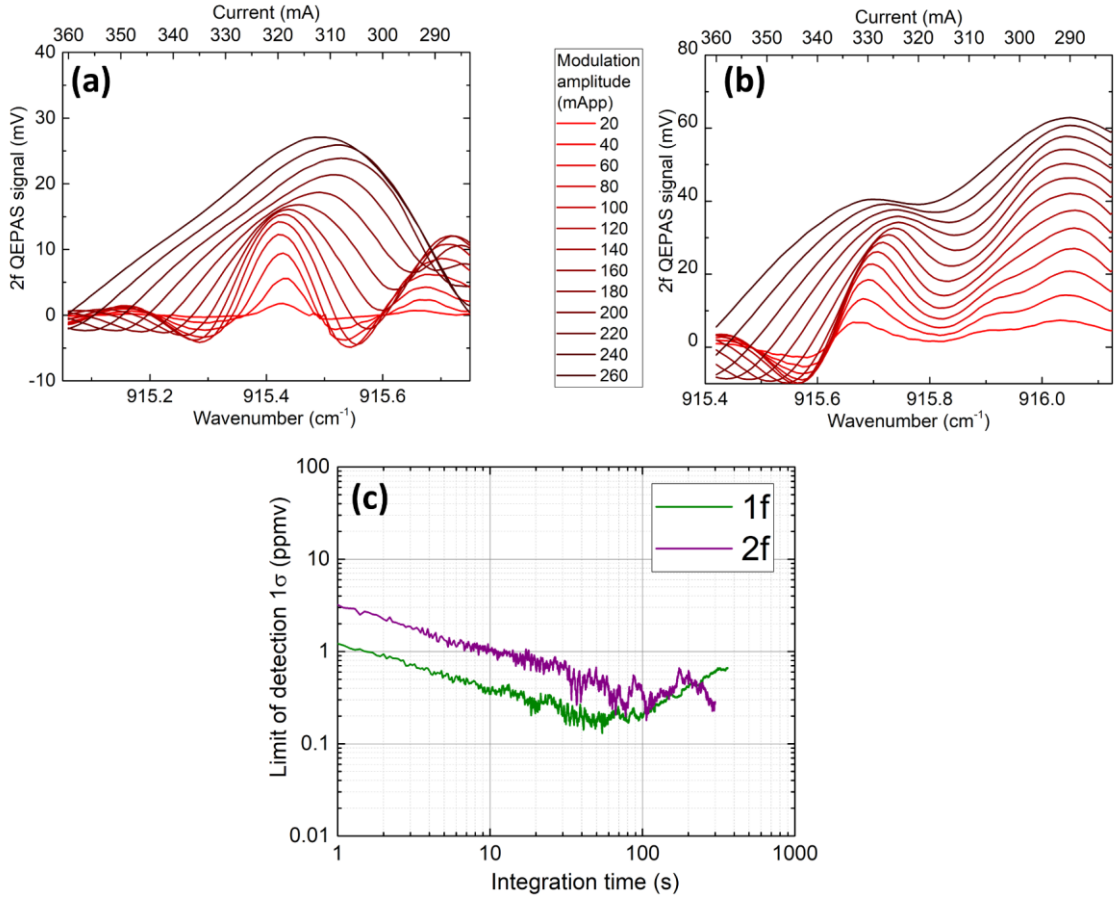

Figure 2.40: QEPAS signal measured as a function of the wavenumber, for the 2*f* (a) and 1*f* mode (b), for different modulation amplitudes. Allan-Werle for the 1*f* and 2*f* mode (c).

The experimental conditions were all set similar to the original experiment. The results are presented on Figure 2.40, which can be compared to Figure 2.35 and Figure 2.39. The new results are in very good agreement the original experiment. The QEPAS signal versus the laser current is very similar to the one obtained originally with minor variations that might be attributed to the temperature regulation system. The ratio of the maxima of the 1*f* to the 2*f* signal is around 2, as obtained before (Figure 2.35). The limits of detection are of 180 and 400 ppbv (50s), for the 1*f* and 2*f* mode, resp. It corresponds to about a factor 2 increase between the 1*f* and the 2*f*, which is in good agreement the ratio of the maximum of the 1*f* signal to the maximum of the 2*f* signal(Figure 2.35). The factor 10 obtained Figure 2.39 can be attributed to the laser setpoint that was not optimum for the 2*f* signal.

A global conclusion can be drawn from this second experiment. As the laser power and wavelength have a direct impact onto the output QEPAS signal, the stabilization of the laser requires a well-engineered system. For our lab experiments, a fair solution to obtain comparable results is to perform a complete calibration of the sensors, for instance here through a multiple current sweeps at different modulation amplitudes (Figure 2.35). It enables the optimization of the laser setpoint prior to measuring the sensor's limit of detection.

2.4. CO detection at 4.7μm

The carbon monoxide (CO) exhibits absorption lines in the mid-IR around 2.3μm and 4.7μm (Figure 2.1). Following the procedure described in section 2.1, at 2.3μm ($\alpha=4.10^{-7}cm^{-1}\cdot ppm^{-1}$ at $\sigma=4294.63cm^{-1}$), for a laser power of 5mW, the LOD of a QEPAS sensor can be estimated to be around 500ppbv for a 100s integration time. It is a factor 5 above MULTIPAS specifications (<100ppbv in 100s for CO). The CO absorption lines around 4.7um are about 2 orders of magnitude stronger than the lines at 2.3μm. Moreover, high-power QCLs can reach up to 100mW, about one order of magnitude stronger than a 2.3μm laser diode. In total, the sensor's SNR might be improved by 3 orders of magnitude. However, as we saw with the implementation of the 11μm QCL, longer wavelengths are optically constraining, and might affect the sensitivity of the setup. In this section, we characterize a 4.7μm QCL and implement it in a CO QEPAS sensor. Then, we employ the sensor for a medical application: breath analysis.

2.4.1. Characterization of the quantum cascade laser (mirSense)

The QCL was provided by mirSense in the frame of the MULTIPAS project. It was designed to emit around 4.7μm where CO lines are strong and interferent free. The laser was delivered mounted on a COS (Chip-On Submount). The package was realized at the IES using a homemade temperature regulated module, similar to the one for C_2H_4. Two additional parts were fabricated, by means of 3D printing, for holding the COS and to ensure electrical and thermal contacts (Figure 2.41). The module was sealed in order to avoid condensation when operated below the dew point. A 1mm-thick 3°-tilted antireflective-coated ZnSe window was placed as close as possible to the laser, thus allowing to use a short focal length to collect efficiently the highly divergent laser beam. Having the lens independent from the laser module is convenient for the alignment of the sensor.

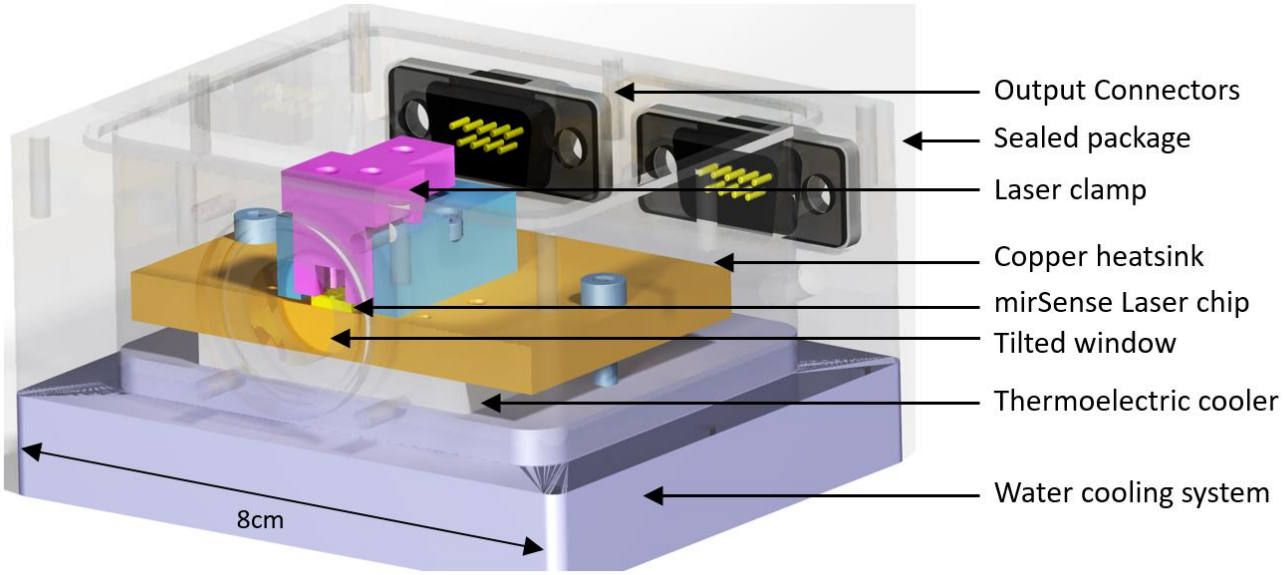

Figure 2.41: CAD image of the homemade laser module and the 3D printed parts holding the COS.

The laser was characterized electrically and spectrally (Figure 2.42). The threshold current is around 470 mA and the maximum power reaches 150mW. The laser temperature was set to 20°C and the spectra was measured using a Fourier Transform Infrared Spectrometer. The current tuning rate equals to -0.0125 cm^{-1}/mA. The targeted CO line is located at 2103.28 cm^{-1}, corresponding to a current of 630 mA (Figure 2.42(b)). Since the CO peak has a Lorentzian profile, the optimum modulation can be directly deduced using the WMS theory. The peak linewidth (HWHM) is of 0.058 cm^{-1}, leading to an optimum modulation amplitude of 18.5 mA for the second harmonic (2*f*).

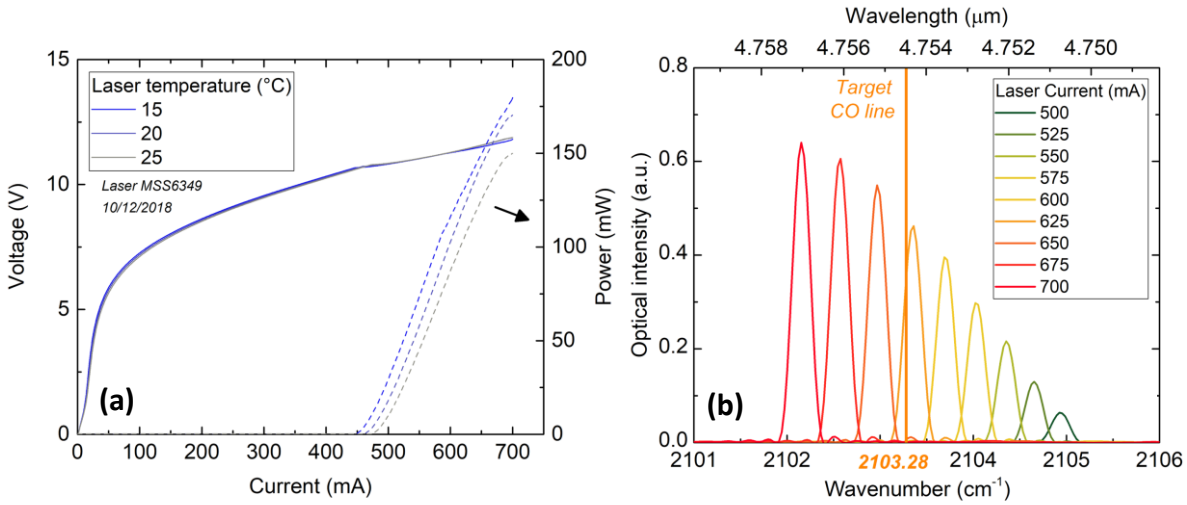

Figure 2.42: (a) LIV curves (b) Emission spectra for different currents at a laser temperature of 20°C.

As described in section 2.3.1.1, the laser beam diameter is important to dimension the microresonator radius R_{mR}. In order to estimate the laser emission waist, the far field spatial profile was measured. We used a simple setup by placing a long rail perpendicularly to the optical axis at a distance of 15 or 25 cm. A 4mm diameter InSb photodiode (J10D-M204-R04M-60, Teledyne Judson), enclosed in a cryostat and cooled with liquid nitrogen, was mounted onto

a carriage and put onto the rail. The signal from the photodiode was amplified and recorded using a Labview program. The photodiode was translated perpendicularly to the laser and the signal was recorded every 1mm. The experiment was realized twice, to obtain the far field for the slow and the fast axis.

The results are presented on Figure 2.43. The FWHMs were extracted from the curve (dotted line), giving a full divergence angle of 32° and 50° for the slow and fast axis, resp. It is important to note that the beam shape is far from a perfect Gaussian beam. It should be considered if optical simulations are undertaken. Two separate peaks are visible, probably due to multiple transverse spatial modes of the laser coexisting.

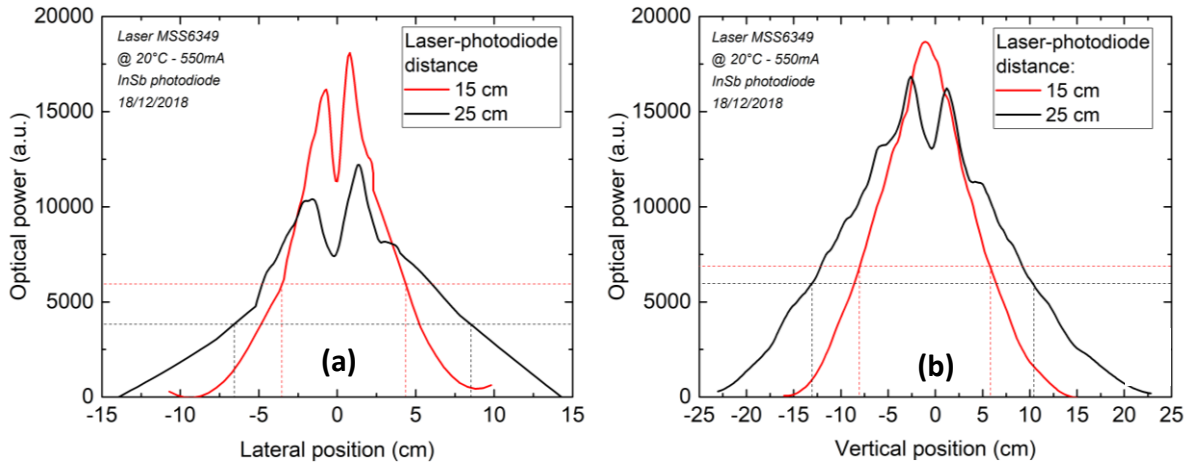

Figure 2.43: Far field profile along the slow (a) and the fast (b) axis.

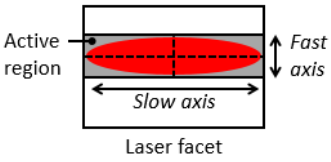

2.4.2. Experimental setup

The setup (Figure 2.44) is a replica of the C_2H_4 gas sensor (Figure 2.31) with slight modifications. The mR dimensions were adjusted: the mR radius R_{mR} was narrowed to 0.7mm as the laser beam diameter was smaller. The laser beam diameter at the entrance was estimated to be of 200µm compared to 520µm for the C_2H_4 gas sensor (Figure 2.30). The length L_{mR} was adjusted to 6.1mm. A new QEPAS cell was designed for electronic integration. The transimpedance amplifier is located closer to the QTF to avoid noise pickup. The QTF was mounted on a XY translation in order to finely adjust its position relatively to the mR, as measured in section 2.2.6. The cell was properly sealed with standard O-rings to prevent slow gas leakage and allow vacuum operation. SMA connectors were used for the amplifier output and a sub-d connector for the power supply, humidity and temperature sensor.

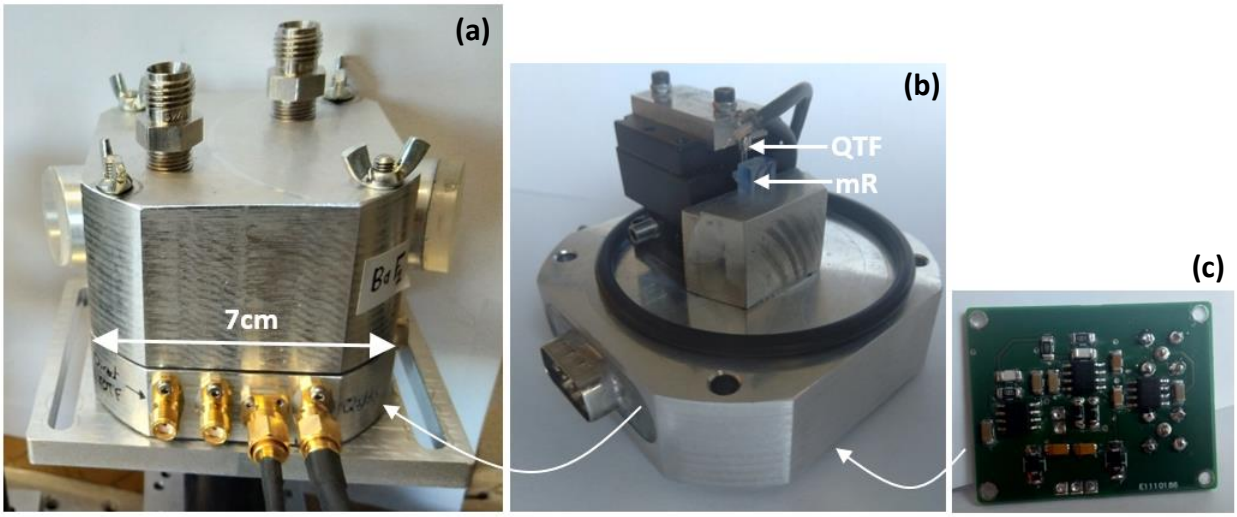

Figure 2.44: Picture of the new cell design open (a) and closed (b). The transimpedance amplifier with reduced footprint (c) is integrated in the bottom part of the cell.

2.4.3. An implementation for breath analysis

The CO QEPAS sensor was employed for human breath analysis [34]. It has a strong potential to be a fast and non-invasive technique for early stage medical diagnosis. The carbon monoxide is a biomarker, i.e. a measurable indicator of the biological state of the patient, that can be employed for the detection and diagnosis of pathologies. CO is naturally present in human body, but its concentration can fluctuate, notably during an exposure to air pollution and tobacco smoking [35]. The molecule has a high affinity with red blood cells, thus forming carboxyhemoglobin (HbCO). HbCO concentration can be estimated from the CO fraction in the exhaled air. Breath analysis is therefore an attractive technique for the measurement of HbCO. However, various parameters can affect the diagnosis performances such as the sampling type, the duration, the breath hold time [36]. The sampling type can be the total volume of exhaled air or only the alveolar volume. The alveolar volume is obtained by keeping the last part of the exhaled volume. In this volume, the molecular concentration may vary due to a change in the CO diffusion through the lung tissues.

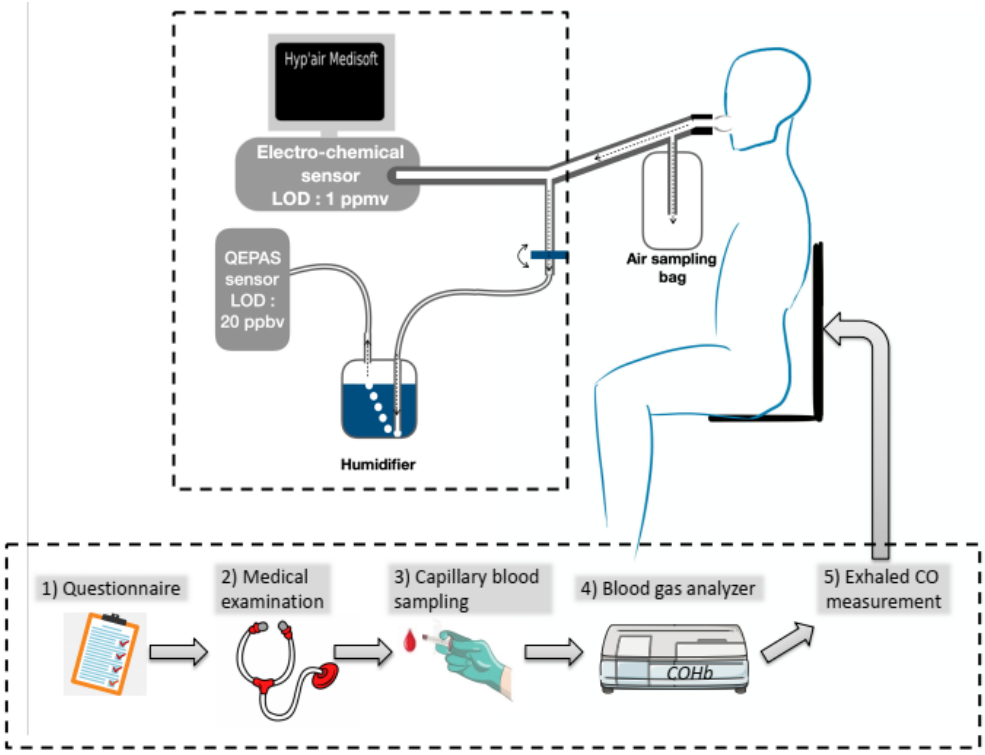

Figure 2.45: Protocol for the clinical evaluation consisting in a questionnaire, a medical examination, the HbCO blood test and finally the CO breath analysis. The same operator realized all the tests to improve the repeatability.

The QEPAS sensor was employed for a clinical evaluation in the department of clinical physiology, at Montpellier University Hospital in August 2019. The measurements were conducted by Nicolas Maurin during his training period. The variability, reliability and clinical validity of the CO-QEPAS sensor were studied on 20 healthy subjects (3 smokers, 1 male - 17 non-smokers, 8 males). The response of the sensor was compared to 2 reference instruments: a blood HbCO test and a commercial exhaled CO analyzer (HypAir, Medisoft, LOD=1ppmv). The protocol of the experiment is described on Figure 2.45. During the exhaled CO measurement, 4 types of measurement were conducted, based on the international standardization for the CO transfer measurements:

(1) After breathing normally, the subject was asked to fully expire, to take a full deep breath, then hold its air 10 s, and expire slowly (around 2 L/min). The air was conducted toward an air sampling bag (900 mL) and toward the humidifier to the QEPAS sensor cell. The gas contained in the bag was analyzed by the Hypair system.

(2) Similar to step 1, but after 10 s of breath-hold, the first 900 mL of the expired air were first extracted and not analyzed, so that the measured air sample was only from alveolar part.

(3) Similar to step 1, but the subject was asked to hold its breath for 2 s instead of 10.

(4) Similar to step 1.

The 4 measurements allow to observe the variability of the response for different breath-hold time and sampling type (total lung volume or alveolar only). Each measurement was repeated twice giving a total of 8 measurements per patient.

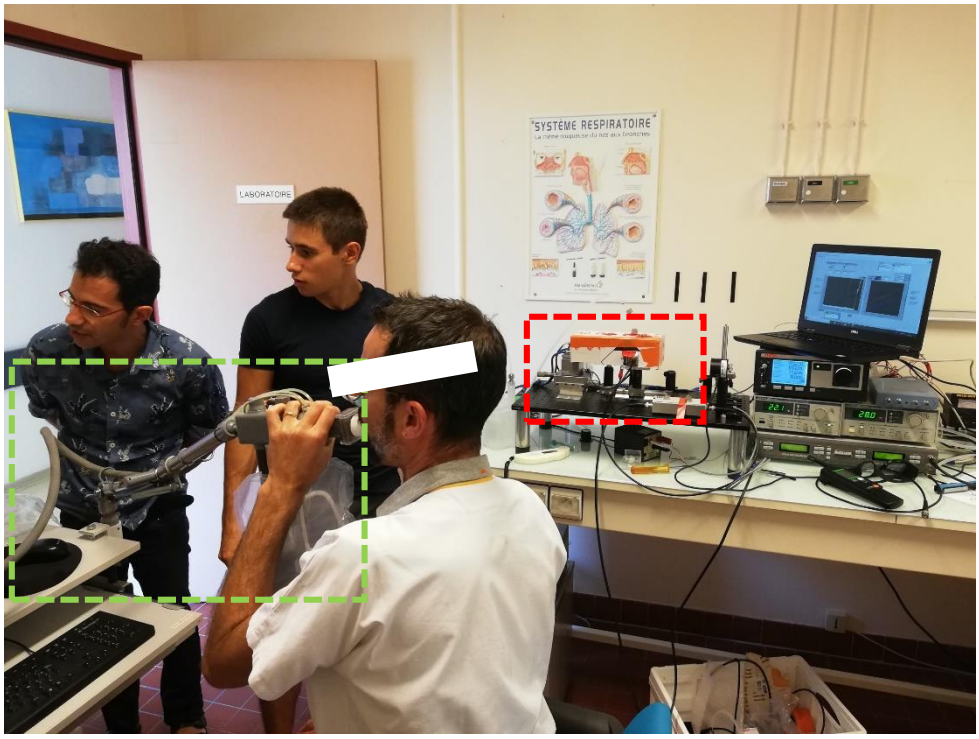

Figure 2.46: Measuring the exhaled CO during the clinical evaluation at the hospital, using the reference sensor from MEDISOFT (green square) and the QEPAS sensor (red square). A patient (right) is breathing out in the sensor while Nicolas Maurin (middle) and Fares Gouzi (far left) control the measurement.

2.4.3.1. Effect of the sample humidity

An important parameter in breath analysis is the humidity of the sample. Indeed, the water vapor concentration is known to affect the relaxation pathways and therefore the efficiency of the photoacoustic generation. It was well described that H_2O promotes the CO molecular relaxation [37]. Consequently, a factor 3 of signal increases is observed between a 30%RH and 85%RH (Figure 2.47).

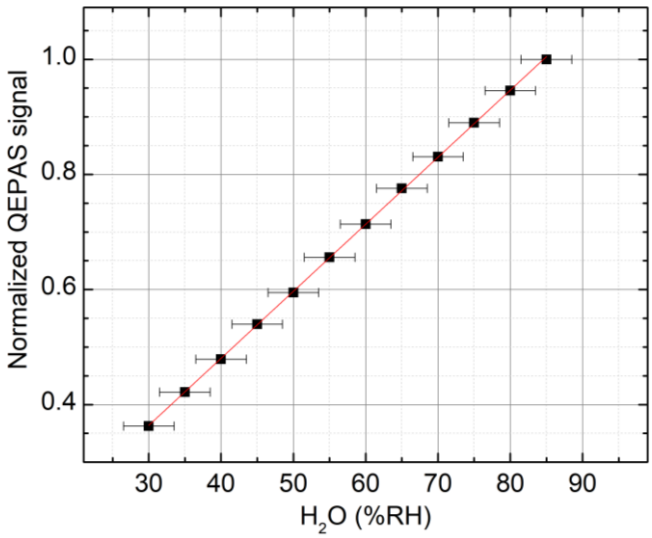

Figure 2.47: Effect of the humidity onto the amplitude of the QEPAS signal. The CO concentration is of 200ppmv, diluted in N_2.

In order to stabilize the humidity content of the gas sample, the sample was passed through a humidifier before introduction into the QEPAS sensor. The humidifier is a simple gas bubbling bath and regulates the humidity around 85%RH. Additionally, the humidifier helps stabilizing the temperature and the gas flow. The latter is also important in QEPAS, because high flow and turbulences can result in additional noise.

2.4.3.2. Calibration of the sensor

Sampling bags of CO/N_2 calibrated mixtures were used for calibrating the QEPAS sensor. The mixture was introduced into the QEPAS sensor after passing through the humidifier. The QEPAS signal was recorded until it stabilized (Figure 2.48(a)). The signal amplitude was measured for a few different concentrations. The points were linearly fitted in order to obtain the calibration curve (Figure 2.48(b)).

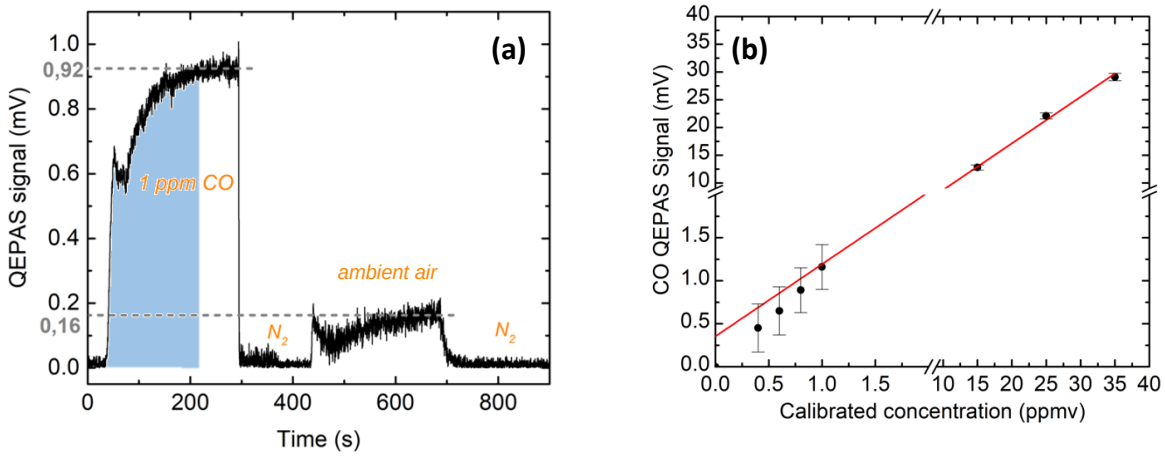

Figure 2.48: (a) Response of the QEPAS signal for a 1 ppmv concentration humidified CO compared with pure N_2 and ambient air. The response time is around 200s (blue area). (b) QEPAS signal for different mixture concentration (round dots). The calibration curve is obtained by applying a linear fit (red line).

The laser modulation frequency was also adjusted during the calibration. Indeed, the QTF resonance is sensitive to the humidity and will vary during the injection. The slow increase of the QEPAS signal (blue area on (Figure 2.48(a)) which lasted at about 200s, is probably due to the slow adsorption of water molecules onto the QTF surface, which leads to a shift of the QTF resonant frequency. For the experiment, the laser modulation frequency was set to meet the QTF resonance in the presence of the humidified mixture, thus maximizing the QEPAS signal. The slow QEPAS response did not prevent the experiment but a faster response would be appreciated, in particular to measure the CO profile as a function of the expired volume. In order to tackle the issue of the QTF resonance drift, we developed a new method called Resonance-Tracking QEPAS. The topic is covered in Chapter 3.

2.4.3.3. Limit of detection

After the calibration, the sensor signal was recorded with a calibrated concentration of humidified CO (350ppbv) diluted in N_2. The Allan-Werle deviation was calculated and is shown on Figure 2.49. The signal reaches an optimum integration time at 85s with a minimum LOD of 2ppbv, giving a NNEA of $2 \cdot 10^{-7} W \cdot cm^{-1} \cdot Hz^{-1/2}$. The moderate value of the NNEA can be attributed to the high laser power.

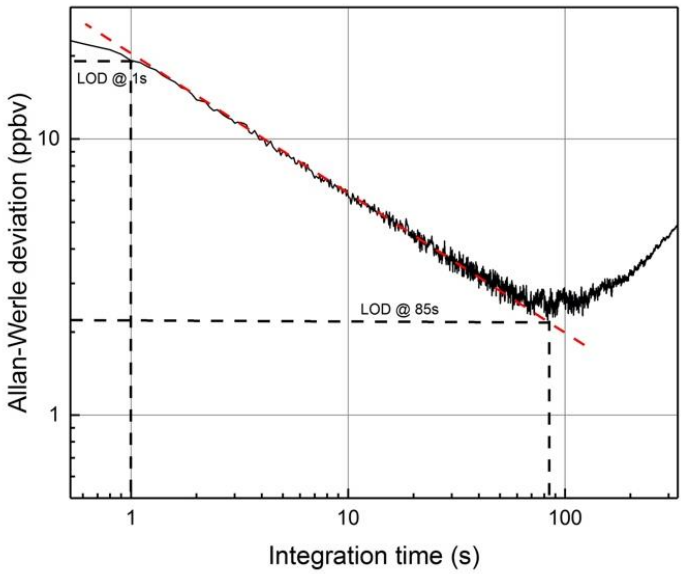

Figure 2.49: Allan-Werle deviation obtained for the CO sensor. The CO concentration was set to 350 ppbv and the time constant of the lock-in amplifier was of 100 ms.

2.4.3.4. Summary of the results

A complete collection of the results is available in the article [34]. Raw data of the QEPAS record is shown Figure 2.50. It corresponds to the 4 different tests, each repeated twice. The cell is flushed with nitrogen between each measurement and the QEPAS signal drops to the zero baseline. As we saw on (Figure 2.48(a)), the QEPAS response time is rather slow. However, the signal does stabilize and the CO concentration can be extrapolated. The total experiment takes more than an hour, limiting the number of patient tested per day. Modification of the protocol and improvement of the QEPAS response will reduce the testing time.

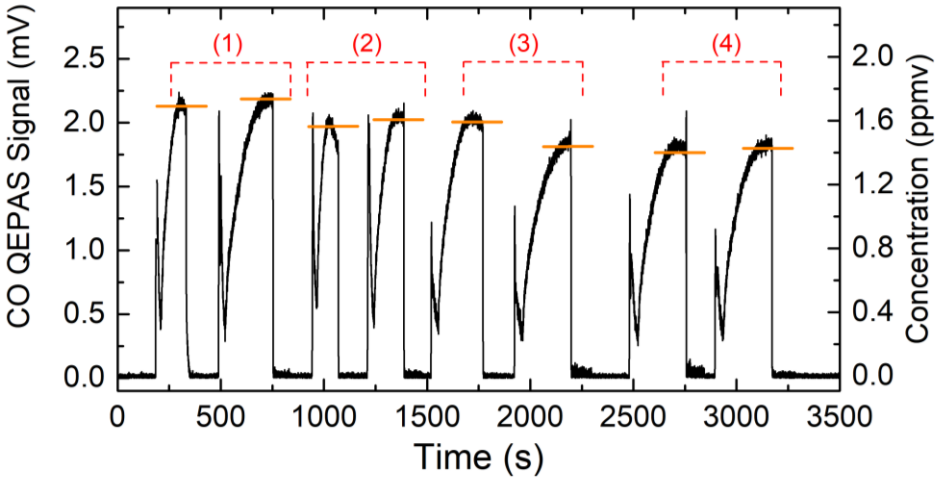

Figure 2.50: Chronogram of the 8 successive acquisitions realized on each tested subject with the QEPAS sensor. The measured values correspond to the mean top values (orange lines).

The comparison of the results from the CO QEPAS sensor and the HbCO blood test are presented on Figure 2.51. The measured values from the QEPAS sensor are consistent, with a

moderate dispersion for the different test conditions. They are in good agreement with the HbCO reference method. Some of the values for the HbCO are missing due to a failure of the test (blood coagulation). Among the 19 patients, the 3 regular smokers are clearly identified, as their exhaled CO concentration is above the smoker threshold of 10 ppmv.

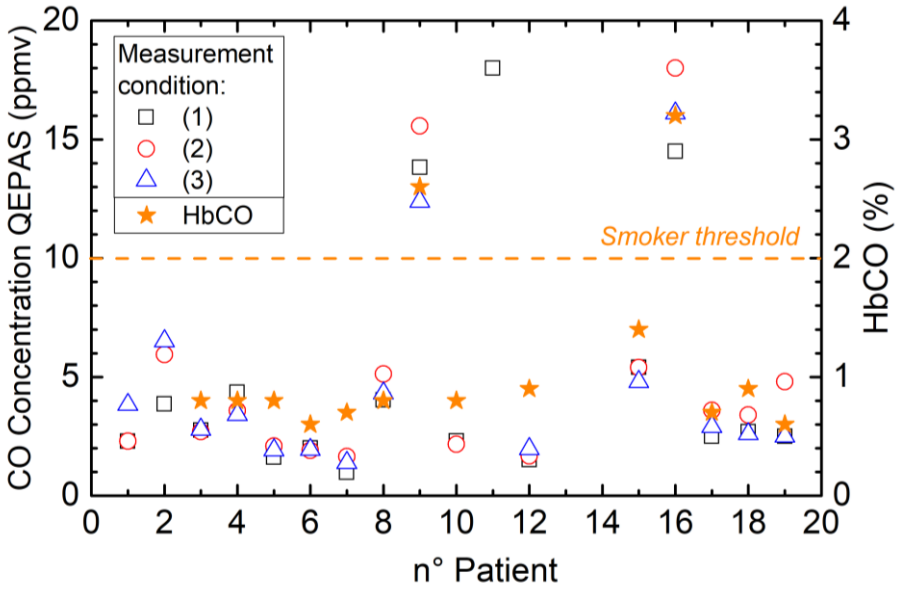

Figure 2.51: Summary of the results for the clinical study, comparing the response of the CO QEPAS sensor (left axis) and the HbCO blood test (stars, right axis).

2.4.4. Comparison with the literature

Laser optical spectroscopy has already been employed for measuring carbon monoxide in exhaled breath, including techniques such as WMS [1], ICOS (Integrated Cavity Output Spectroscopy) [2], OF-CEAS (Optical Feedback Cavity Enhanced Spectroscopy) [3] and CALOS (Cavity Leak Out Spectroscopy) [4]. It is worth comparing our CO QEPAS with the literature in terms of sensor performances, mostly based on the LOD and the response time, and in terms of the clinical protocol and results.

An early study (2006) from Murtz et al reported a CO sensor with very low limit of detection of 0.09 ppbv based the CALOS technique (1s integration time) [4]. Interestingly, the limit of detection increased to 0.5ppbv with exhaled CO compared to the calibrated CO mixture, illustrating well the complexity of breath analysis. Similar performances were obtained with OF CEAS, showing a LOD of 1ppbv in 0.3s [3]. OF-CEAS presents the advantage of being calibration free compared to other techniques based on optical cavities (CEAS, ICOS). A remarkable achievement is the design of a V-shaped optical cavity which allowed to obtain a very low cell volume (18cm^3). Consequently, the response time of the sensor (for a 1/e variation) was estimated to be of 0.3s for a flow rate of 8 cm^3/s. Even though fairly acceptable LODs could be obtained at much shorter integration times, the response time would still be limited by the gas cell volume. The fast sensor response allowed the authors to measure the real-time response of the carbon monoxide in patient breath, which brought additional information about the CO equilibrium and diffusion in the lungs.

Another study was conducted by Pakmanesh et al on both ICOS and WMS techniques [2]. They obtained similar limit of detection for both techniques, of around 7 ppbv (1s integration time). They were able to obtain fast response times by using a compact gas cell (35cm^3 volume) and moderate gas flow (ranging from 15 to 125 cm^3/s). Adjusting the flow rate is important from a technical point view as well as a medical one. Indeed, it is related to the diffusion of CO into the alveoli. Ghorbani et al studied thoroughly the effect of the flow rate and the breath holding time [1]. They found a slight increase in the exhaled CO concentration with an increased breath holding time and a decreased flow rate. Those results tend to show that the 'blood CO is not in equilibrium with the lungs and the CO is constantly diffusing into the alveolar air'.

In terms of performances, the CO QEPAS sensor we presented has a LOD very close to previous studies, in the ppbv range. Oppositely to sensors based on optical cavity, the QEPAS technique presents a simple and affordable optical setup, as already discussed in Chapter 1. In terms of response time, the QEPAS cell volume can be less than 10 cm^3. However, in our case, the limiting factor was the length of the tubing due to the use of the bubbler and the coupling with the medical sensor. Further developments will be focused on reducing the hydraulic volume in order to minimize the response time and to better observe the effects of the flow rate and the breath holding time. Nonetheless, we were able to observe significant effects (p-value < 0.05) of the breath holding time in good agreement with the expected CO diffusion dynamics. Compared to previous study, we presented a complete clinical study including the comparison of our CO sensor with a reference medical sensor.

2.4.5. Conclusion

In conclusion, we demonstrated a good agreement of the QEPAS sensor versus the reference method, therefore it appears to be very appropriate for the measurement of CO in exhaled breath. It was also shown that the CO QEPAS has a better clinical performance than a standard electrochemical analyzer. Further clinical analyses are already scheduled for CO, NO and C_3H_6O. The implementation of the QEPAS sensor to a real application was a good challenge, notably due to the high humidity of the gas sample. The QEPAS sensor proved to be very sensitive, though its response time was slow. It is mostly explained by the effect of the humidity onto the QTF resonance. This latter issue is very important and will be discussed in the next chapter.

2.5. Conclusion

In this chapter, we first conducted a study to assess the performances of the QEPAS sensor for different molecular species as defined in the requirements of the MULTIPAS project. We estimated that the limits of detection are fairly reachable for some species (CO, NH_3 and CH_4) with a moderate laser power, while for others (NO, NO_2 and SO_2), the required laser power is close to the actual laser performances.

Then, we presented an optimization of the acoustic microresonator. We developed an experimental setup to characterize the acoustic response of the microresonator based on a MEMS microphone and a laser dedicated to H_2O absorption. We used this useful tool to gather experimental data on a set of microresonators. We compared the results to a theoretical model and improved the goodness of the fit by adding correction factors. We also fabricated new designs of microresonators by 3D printing, notably we adjusted the shape of the slit and obtained a better acoustic coupling with the QTF. To go even further using the 3D printing technique, we developed a design with a double microresonator and a double optical pass, which lead to an increased sensitivity of the QEPAS sensor.

The study of the off-beam spectrophone allowed used to adapt the microresonator for large beam diameters and in particular for long-wavelength lasers. We used a 11µm QCL, fabricated at the IES, for the detection of ethylene. We designed a simple optical setup to prevent interferences while maintaining good performances of the spectrophone. We also studied the modulation scheme. Using the theory of wavelength modulation, we were able to simulate the photoacoustic signal by considering the composite absorption profile and we obtained results very close to the experimental signal. Finally, we were able to detect ethylene with a limit of detection of about 0.1 ppmv in one minute, which corresponds to state of the art results with the QEPAS technique for ethylene detection.

After this successful demonstration, we implemented a 4.7µm QCL for the detection of carbon monoxide, a target specie of the MULTIPAS project. We characterized the laser emission and optical profile and optimized the modulation scheme, allowing us to obtain very good limit of detection of 2 ppbv in 85s. Then, we employed it for a biomedical application, breath analysis, and conducted a clinical evaluation at the hospital. The QEPAS sensor showed a very good correlation with the reference instruments and so, has a potential for making a sensitive gas sensor for breath analysis.

2.6. References

1. Sanchez, N.P.; Dong, L.; Ye, W.; Li, C.; Zheng, C.; Nancy, P.; Gluszek, A.K.; Hudzikowski, A.J.; Griffin, R.J.; Tittel, F.K. Mid-infrared dual-gas sensor for simultaneous detection of methane and ethane using a single continuous-wave interband cascade laser detection of methane and ethane using a laser. *Opt. Express* **2016**, *24*, 16973–16985.
2. Holthoff, E.; Bender, J.; Pellegrino, P.; Fisher, A. Quantum cascade laser-based photoacoustic spectroscopy for trace vapor detection and molecular discrimination. *Sensors* **2010**, *10*, 1986–2002.
3. Du, Z.; Wan, J.; Li, J.; Luo, G.; Gao, H.; Ma, Y. Detection of atmospheric methyl mercaptan using wavelength modulation spectroscopy with multicomponent spectral fitting. *Sensors* **2017**, *17*, 379.
4. Gas Sample Dryers – Perma Pure Available online: https://www.permapure.com/scientific-emissions/products/gas-sample-dryers/.
5. Patimisco, P.; Sampaolo, A.; Dong, L.; Tittel, F.K.; Spagnolo, V. Recent advances in quartz enhanced photoacoustic sensing. *Appl. Phys. Rev.* **2018**, *5*.
6. Patimisco, P.; Scamarcio, G.; Tittel, F.K.; Spagnolo, V. Quartz-enhanced photoacoustic spectroscopy: A review. *Sensors* **2014**, *14*, 6165–6206.
7. Dong, L.; Spagnolo, V.; Lewicki, R.; Tittel, F.K. Ppb-level detection of nitric oxide using an external cavity quantum cascade laser based QEPAS sensor. *Opt. Express* **2011**, *19*, 24037.
8. Lewicki, R.; Kosterev, A.A.; Thomazy, D.M.; Risby, T.H.; Solga, S.; Schwartz, T.B.; Tittel, F.K. Real time ammonia detection in exhaled human breath using a distributed feedback quantum cascade laser based sensor. **2011**, *7945*, 79450K.
9. Yi, H.; Liu, K.; Chen, W.; Tan, T.; Wang, L.; Gao, X. Application of a broadband blue laser diode to trace NO_2 detection using off-beam quartz-enhanced photoacoustic spectroscopy. *Opt. Lett.* **2011**, *36*, 481.
10. Waclawek, J.P.; Lewicki, R.; Jahjah, R.; Ma, Y.F.; Chrysostom, E.T.H.; Lendl, B.; Tittel, F.K. A sensitive CW DFB quantum cascade laser based QEPAS sensor for detection of SO2. In Proceedings of the 2012 Conference on Lasers and Electro-Optics (CLEO); IEEE, Ed.; 2012; pp. 1–2.
11. Wang, Z.; Li, Z.; Ren, W. Quartz-enhanced photoacoustic detection of ethylene using a 10.5 μm quantum cascade laser. *Opt. Express* **2016**, *24*, 4143–4154.
12. Yi, H.; Chen, W.; Guo, X.; Sun, S.; Liu, K.; Tan, T.; Zhang, W.; Gao, X. An acoustic model for microresonator in on-beam quartz-enhanced photoacoustic spectroscopy. *Appl. Phys. B* **2012**, *108*, 361–367.
13. Serebryakov, D. V; Morozov, I. V; Kosterev, A.A.; Letokhov, V.S. Laser microphotoacoustic sensor of ammonia traces in the atmosphere. *Quantum Electron.* **2010**, *40*, 167–172.
14. Rück, T.; Bierl, R.; Matysik, F.M. NO2trace gas monitoring in air using off-beam quartz enhanced photoacoustic spectroscopy (QEPAS) and interference studies towards CO2, H2O and acoustic noise. *Sensors Actuators, B Chem.* **2018**, *255*, 2462–2471.
15. G.R.A.S G.R.A.S. Free-field Standard Microphone Available online: https://www.gras.dk/products/product/143-46be.
16. Batango – open source Bat Detector Dodotronic Available online: https://www.dodotronic.com/batango-open-source-bat-detector/?v=11aedd0e4327.
17. Ultrasound SPL meter by Godfried-Willem Raes Available online: https://logosfoundation.org/elektron/US_SPL_Meter/US_SPL_Meter.html.
18. Ngo, T.D.; Kashani, A.; Imbalzano, G.; Nguyen, K.T.Q.; Hui, D. Additive manufacturing (3D printing): A review of materials, methods, applications and challenges. *Compos. Part B Eng.* **2018**, *143*, 172–196.
19. Wang, X.; Jiang, M.; Zhou, Z.; Gou, J.; Hui, D. 3D printing of polymer matrix composites: A review and prospective. *Compos. Part B Eng.* **2017**, *110*, 442–458.
20. Dilase 3D HR MultiFAB Available online: https://www.laas.fr/projects/MultiFAB/dilase-3d-hr.

21. High resolution 3D printer Available online: https://www.kloe-france.com/en/laser-lithography/photolithography-systems/direct-laser-writing/3d-printer.
22. Parc machines en fabrication additive - Centre Pro3D Available online: https://centre-pro3d.fr/la-plateforme/equipement/.
23. Kinsler, L.E.; Frey, A.R.; Coppens, A.B.; Sanders, J. V. *Fundamentals of acoustics*; Wiley-VCH, Ed.; 1999; ISBN ISBN 0-471-84789-5.
24. Strutt, J.W.; Rayleigh, B. *The theory of sound*; 1945;
25. Mast, T.D. Simplified expansions for radiation from a baffled circular piston. *J. Acoust. Soc. Am.* **2005**, 3457–3464.
26. Kolbrek, B. Horn Theory: An Introduction, Part 1. *Audio Xpress* **2008**, *1*.
27. CRESILAS Available online: https://cresilas.fr/stereolithographie/.
28. Petra, N.; Zweck, J.; Kosterev, A.A.; Minkoff, S.E.; Thomazy, D. Theoretical analysis of a quartz-enhanced photoacoustic spectroscopy sensor. *Appl. Phys. B Lasers Opt.* **2009**, *94*, 673–680.
29. Hu, L.; Zheng, C.; Zheng, J.; Wang, Y.; Tittel, F.K. Quartz tuning fork embedded off-beam quartz-enhanced photoacoustic spectroscopy. *Opt. Lett.* **2019**, *44*, 2562.
30. Hu, L.; Zheng, C.; Zhang, M.; Yao, D.; Zheng, J.; Zhang, Y.; Wang, Y.; Tittel, F.K. Quartz-enhanced photoacoustic spectroscopic methane sensor system using a quartz tuning fork-embedded, double-pass and off-beam configuration. *Photoacoustics* **2020**, 100174.
31. Loghmari, Z.; Bahriz, M.; Thomas, D.D.; Meguekam, A.; Van, H.N.; Teissier, R.; Baranov, A.N. Room temperature continuous wave operation of InAs/AlSb-based quantum cascade laser at λ ∼11 µm. *Electron. Lett.* **2018**, *54*, 1045–1047.
32. Li, Z.; Shi, C.; Ren, W. Mid-infrared multimode fiber-coupled quantum cascade laser for off-beam quartz-enhanced photoacoustic detection. *Opt. Lett.* **2016**, *41*, 4095–4098.
33. Miklós, A.; Hess, P.; Bozóki, Z. Application of acoustic resonators in photoacoustic trace gas analysis and metrology. *Rev. Sci. Instrum.* **2001**, *72*, 1937–1955.
34. Maurin, N.; Rousseau, R.; Trzpil, W.; Aoust, G.; Hayot, M.; Mercier, J.; Bahriz, M.; Gouzi, F.; Vicet, A. First clinical evaluation of a quartz enhanced photo-acoustic CO sensor for human breath analysis. *Sensors Actuators, B Chem.* **2020**, 128247.
35. Veronesi, A.; Pecoraro, V.; Zauli, S.; Ottone, M.; Leonardi, G.; Lauriola, P.; Trenti, T. Use of carboxyhemoglobin as a biomarker of environmental CO exposure: critical evaluation of the literature. *Environ. Sci. Pollut. Res.* **2017**, *24*, 25798–25809.
36. Ghorbani, R.; M. Schmidt, F. Real-time breath gas analysis of CO and CO2 using an EC-QCL. *Appl. Phys. B* **2017**, *123*, 144.
37. Ma, Y.; Lewicki, R.; Razeghi, M.; Tittel, F.K. QEPAS based ppb-level detection of CO and N 2 O using a high power CW DFB-QCL. **2013**, *21*, 1008–1019.
38. Pakmanesh, N.; Cristescu, S.M.; Ghorbanzadeh, A.; Harren, F.J.M.; Mandon, J. Quantum cascade laser-based sensors for the detection of exhaled carbon monoxide. *Appl. Phys. B Lasers Opt.* **2016**, *122*, 10.
39. Ventrillard-Courtillot, I.; Gonthiez, T.; Clerici, C.; Romanini, D. Multispecies breath analysis faster than a single respiratory cycle by optical-feedback cavity-enhanced absorption spectroscopy. *J. Biomed. Opt.* **2009**, *14*.
40. Mürtz, M.; Halmer, D.; Horstjann, M.; Thelen, S.; Hering, P. Ultra sensitive trace gas detection for biomedical applications. *Spectrochim. Acta - Part A Mol. Biomol. Spectrosc.* **2006**, *63*, 963–969.

Chapter 3

QTF resonance tracking

3.1. Introduction

A QEPAS gas sensor can be employed in diverse applications, for instance in air pollution monitoring, engine exhaust measurements, breath analysis and biogas production. Depending on the application, the environmental conditions and the composition of the sample can greatly vary. In air pollution monitoring, the target species are present as traces (ppbv to ppmv), the gas density is supposedly stable, but the temperature and the humidity are prone to variations. In breath analysis, the humidity quickly increases from the start to the end of the exhalation. In biogas generation, the products of the microbial reactor are mostly methane and carbon dioxide, in various ratios, which translates in changes of the gas sample density.

The resonance of the QTF (Quartz Tuning Fork) in the vacuum is related to its physical properties features (geometry, density, Young's modulus…) and present long-term stability. However, when it is employed as a transducer in QEPAS, the QTF is immersed in the gas containing the target species. The QTF resonance can be considerably affected by the environmental conditions (temperature, pressure, humidity, gas density…), leading to a drift of the QEPAS signal if the operating frequency is fixed. A fast characterization of the QTF resonance is therefore required to correct the sensor's response.

In the first section, we present a literature review and a theoretical study of the techniques to measure the QTF resonance with 2 different approaches: based on the frequency response and based on the transient response. Next, we describe our setup based on the heterodyne measurement of the transient response and validate the accuracy of the technique by monitoring the influence of the temperature and the humidity onto the QTF resonance. Then, we implement our new technique, the Resonance Tracking (RT) QEPAS, in a gas experiment as a proof of concept. Finally, we develop a damping circuit in order to optimize the time spent for characterizing the QTF.

3.1.1. Architecture of the Resonance Tracking QEPAS

Optimal gas sensing is obtained when the QTF is resonantly excited, i.e. the frequency of the acoustic wave equals to the instantaneous frequency of the QTF. In laboratory experiments, the QTF is characterized prior to the QEPAS measurement. The QTF resonance is generally constant during the experiments because there are no significant changes in gas density, temperature and humidity. In a real environment, the QTF resonance is hardly predictable.

Different approaches are possible to prevent the QEPAS signal drift. The Beat Frequency (BF) QEPAS was presented to address this issue by simultaneous measurement of the gas concentration and the QTF parameters (the resonant frequency f_0 and the quality factor Q) [1]. However, the measurement accuracy of the QTF parameters depends on the acoustic wave amplitude and thus the gas concentration. Therefore, the QTF characterization is not possible when working close to the limit of detection. This is the first limitation. The second one comes from the reduced acoustic energy transmitted to the QTF and the broader lock-in amplifier bandwidth making BF QEPAS less sensitive than QEPAS. In BF QEPAS, the system stability is increased at the expense of the sensitivity. In order to overcome these limitations, we decided to investigate a similar technique but based on electrical excitation. In fact, if the QTF is characterized in a very short time, it can be done regularly with little impact on the QEPAS limit of detection.

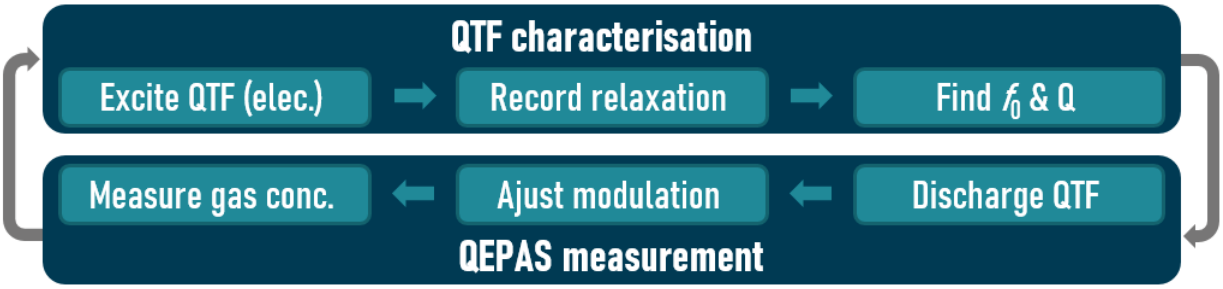

Figure 3.1 : Block representation of the RT-QEPAS.

The proposed architecture of RT QEPAS is shown on Figure 3.1. It is based on two stages. First, the QTF is characterized. After a quick electrical excitation, the QTF relaxation is recorded and the QTF parameters are calculated. Second, when the QTF is discharged, the laser modulation is adjusted to meet the QTF resonance and the gas concentration is measured by means of conventional QEPAS. The QTF characterization and the QEPAS measurement form the measurement cycle. The cycle time can be written as the sum of the time of the individual blocks :

$$t_{cycle} = t_{exc} + t_{relax} + t_{discharge} + t_{charge} + t_{QEPAS} \quad (3.1)$$

In order to achieve a high sensitivity, the ratio t_{QEPAS}/t_{cycle} should be maximized. Therefore, the QTF characterization time should be minimized. Before optimizing the cycle, the accuracy of the QTF characterization has to be determined.

3.1.2. Estimating the required accuracy on f0 & Q

The objective here is to set a criterion on the required accuracy for measuring the QTF parameters. Most of the industrial gas sensors have an accuracy of a few percent of the displayed value. Therefore, we estimated that a 1% relative error on the QEPAS signal was acceptable. In the following, we determine the required measurement accuracy, for both f_0 and Q, to fulfill this 1% error criterion.

$$\frac{\Delta S}{S(f_0)} < 0.01 \quad (3.2)$$

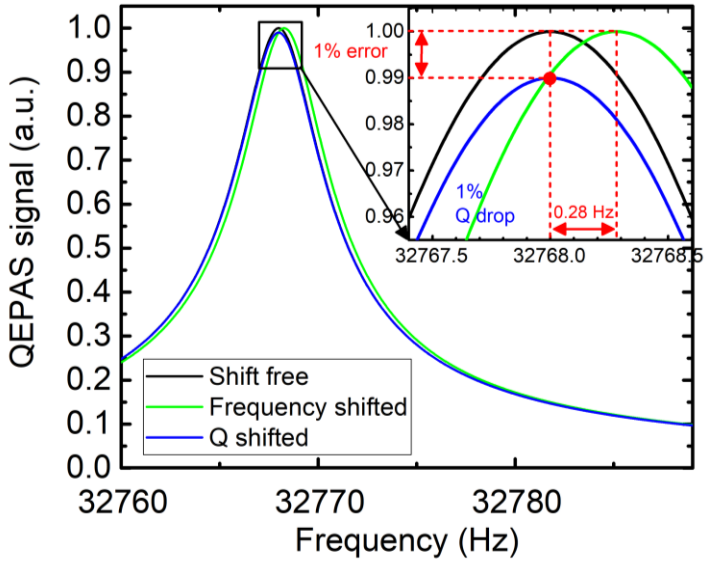

Figure 3.2 : The frequency response of the shift-free QEPAS signal (black) is represented. It is a Lorentzian curve centered at 32768Hz, having a quality factor of 8000. The QEPAS signal reaches a maximum value at $f = f_0$. The frequency response is also shown for a frequency shift of 0.28Hz (green) and Q shift of 80 (blue). The two curves intersect (red dot) at $f = f_0$, corresponding to a 1% QEPAS signal error as calculated.

The frequency response of the squared QEPAS signal can be described as a Lorentzian profile (Figure 3.2 black):

$$S^2(f,Q) = C\frac{Q^2}{1+\left(\frac{2Q(f-f_0)}{f_0}\right)^2} \tag{3.3}$$

where C is a constant. This 1% amplitude error can be converted in an error on the measured frequency Δf_0:
Isolating f in (3.3):

$$f(S) = \pm\frac{f_0}{2Q}\sqrt{\frac{CQ^2}{S^2}-1}+f_0 \tag{3.4}$$

Using (3.4), and noting that $S^2(f_0) = C\cdot Q^2$, one can find the frequency error :

$$\Delta f_0 = |f_0 - f(S-\Delta S)| = \frac{f_0}{2Q}\sqrt{\frac{1}{\left(1-\frac{S(f_0)}{\Delta S}\right)^2}-1}$$
$$\Delta f_0 = \frac{32\ 10^3}{2\cdot 8000}\sqrt{\frac{1}{(1-0.01)^2}-1} = 0.28\ Hz \tag{3.5}$$

It corresponds to the green curve on Figure 3.2. This amplitude error can be converted in an error on the quality factor as well. At $f = f_0$, the QEPAS signal has a linear relationship with Q, thus the error is quickly obtained:

$$\frac{\Delta Q}{Q} = \frac{\Delta S}{S(f_0)} \quad \rightarrow \Delta Q = 0.01Q = 80 \tag{3.6}$$

It is represented by the blue curve on Figure 3.2. From those calculations, it can be concluded that a frequency shift of 0.28 Hz or a Q shift of 80 lead to a 1% relative error on the QEPAS signal. Our objective is thus to find a technique to stay below these values while keeping the measurement time below 1s.

3.2. Characterizing the QTF parameters

As a common issue in signal processing, there is a compromise to find between the measurement time and the measurement accuracy [2]. Indeed, the measurement of a physical quantity in a system is made through multiple stages at which can occur the addition of noises. The signal carrying the information will be degraded by the noises. This effect is quantified by the signal to noise ratio (SNR). The higher the SNR, the greater the accuracy. Strategies like filtering and signal averaging can be employed to get higher SNRs, though the system's response time will increase as well. Depending on the requirements of measurement time and accuracy, different measurement techniques can be explored. They can be divided into two main categories: frequency-domain and time-domain. We will review those techniques[10], estimate their performances and select one that can meet the requirements for the QTF characterization.

3.2.1. From the frequency response

The QTF response was described in section 1.3.1.2. It can be modeled by the so-called Butterworth-Van Dyke model which corresponds to a series RLC circuit with a parallel capacitance C_0. R, L and C are the electrical equivalent parameters of the QTF motional parameters: γ, M and K. The two sets are linked by the piezo electric coefficient which can be related to the QTF geometry, the quartz piezoelectric and stiffness properties [3].

The knowledge of the electrical parameters can thus allow the direct deduction of the motional parameters, and vice-versa. The piezoelectric feature of the resonator is convenient because it allows a complete electrical characterization (no need for complex optical setup [4]). R represents the losses of the system, L the potential energy and C the kinetic energy. C_0 accounts for the parasitic capacitance due to metal electrodes and cables.

The most common technique to obtain the QTF frequency response is to excite it at a given frequency and to measure the output amplitude of the oscillation. The setup is simple, only requiring a sinewave generator and an oscilloscope. It is thoroughly described in the next section. The frequency response of the QTF can be obtained with many other techniques. Spectrum analyzers and impedance meters are useful laboratory instruments. A spectrum analyzer is specifically dedicated to characterize a signal in the frequency domain [5]. An impedance meter evaluates both the resistive and the reactive response to give the complex impedance of any electrical component. Both instruments are accurate and can be employed for

[10] Similar issues are encountered with microwave resonators and MEMS, sharing some common feature with the QTF. Relevant citations from those fields will appear regularly along this chapter.

the QTF characterization [6], but they are cumbersome and expensive. Apart of hardware based techniques, a frequency study can be software based. It is often realized using a Fast Fourier Transform (FFT). This technique was reported for characterizing the QTF [7]. A noise voltage source, made with a reverse biased zener diode, allows a broadband excitation of the QTF. The time-domain response of the QTF is recorded by a DAQ card and then the FFT is computed. In order to obtain a good accuracy i.e. a good FFT resolution, the recording time is long (0.2Hz resolution would require 1/0.2=5 seconds). Indeed, the Fourier transform is the inverse image of the time domain, the very sharp QTF response corresponds to a very long time response. Narrow frequency responses are hard candidates for the FFT tool. We focus on a simple and affordable setup to realize a frequency sweep, based on a lock-in amplifier, that is already implemented in the QEPAS setup. We compare the measurement accuracy of different signal processing methods for obtaining the QTF parameters.

3.2.1.1. Obtaining the QTF parameters

The QTF is excited by applying a frequency-swept sinusoid, and the output amplitude and phase are measured at the output of the lock-in amplifier (LIA) (Figure 3.3(a)). Both the amplitude and phase can be employed to measure the quality factor (Figure 3.3(b)). The Q factor can be extracted from the slope of the phase signal around the resonant frequency. For the high Q factor of the QTF, the phase signal is very steep. Thus the accuracy of the measurement is better with the magnitude signal than with the phase signal. Only the output magnitude is considered after, from which both QTF parameters are obtained. The results of the frequency sweep is a set of data points equally spaced in frequency (Figure 3.3(b)). Various parameters can be adjusted in the experiments:

- t_{step} : the timestep is the time spent for measuring one point at a given frequency
- f_{span} : the frequency span is the interval of frequencies covered during the sweep
- f_{step} : the frequency resolution correspond to the frequency difference between two measurement points

The goal is to optimize those parameters to minimize the measurement time, i.e. the time to complete one full frequency sweep, while keeping Δf_0 and ΔQ within the target accuracy. In the following paragraph, the measurement time is estimated based on a literature review. The results are reformulated and compared.

Reducing the measurement time with a given frequency span means having fewer data points or equivalently increasing the timestep. The QTF response time τ is related to the Q factor ($\tau=Q/(\pi f_0)\approx$100ms for $Q=10^4$). It takes about 3τ to reach the steady state, that sets the minimum value for the timestep (t_{step}>300ms). The frequency span should be adapted to experimental deviations of the peak. f_0 can vary up to a few Hz in variable environments (1-5Hz based on our experiments, see section 3.4), thus f_{span} set to 10Hz ensures to keep track of f_0. f_{span}, is a fixed parameter and f_{step} is a variable parameter that can be adjusted in order to meet the target accuracies. Eventually, the time required for a frequency sweep can be obtained : $t_{step} \times f_{span}/f_{res}$

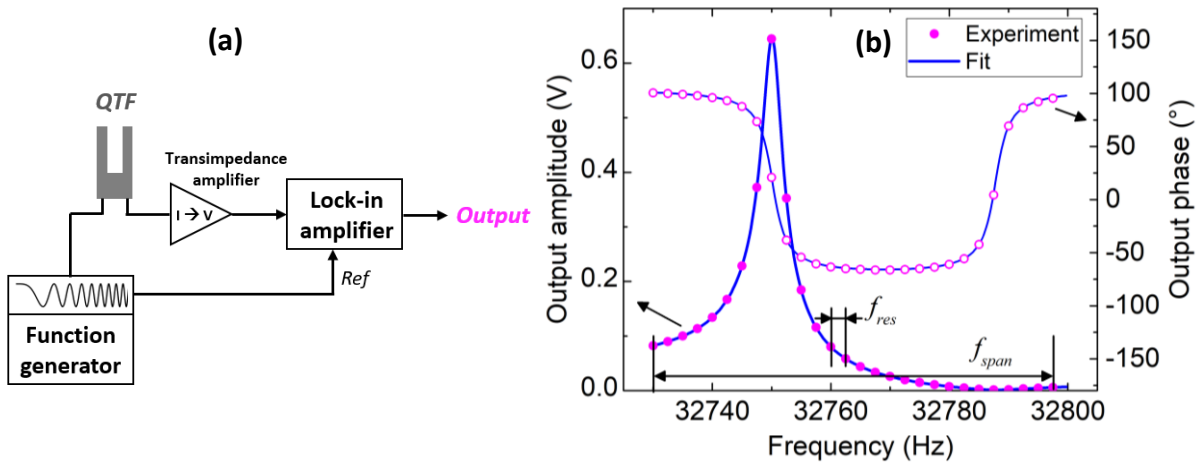

Figure 3.3 : (a) Our frequency sweep setup is based on a function generator for exciting the QTF, a transimpedance amplifier and a lock-in amplifier. (b) The frequency response of the QTF is represented in terms of magnitude and phase (solid line), and can be fitted using the QTF electrical model (dotted line).

Several techniques can be employed to calculate the QTF parameters [8]. The less computing intensive method consists in taking the frequency corresponding to the maximum amplitude for f_0, and finding the bandwidth (at -3dB) to then obtain Q. It is often called the *3dB technique*. However, since the frequency response is discretized, the accuracy will rapidly drop with the number of data points. Also, this technique is only appropriate for a Lorentzian response curve whereas the QTF response is a distorted lorentzian due to the presence of the electrode capacitance C_0. Instead of a single symmetrical peak, the frequency response is composed of a main resonance peak and an anti-resonance peak located just after (Figure 3.3(b)). In this case, the QTF parameters can be found using the Marshall and Brigham technique [9,10].

Another technique is the *non linear (NL) fitting technique*. The data points are fitted by a theoretical model, either the lorentzian curve, either the Butterworth Von Dyke model (see section 1.3.1.2), using the least squares method algorithm. This technique is proven to be more accurate since the information in all the data points is exploited instead of just 3 points in the *3dB technique*. Also, since the QTF response is a narrow peak, providing initial guessed parameters is essential in order to ensure the convergence of the algorithm. This technique is widespread in the literature for the characterization of resonant systems. However, the measurement accuracy can greatly differ, notably depending on the resonator's Q factor, the SNR and the frequency resolution. For the case of the QTF, the Q factor is very high (10^4-10^5) and the SNR (during electrical characterization) is high as well (10^3-10^4).

Gyure et al. proposed an analytical expression of the errors for the *NL fitting technique* [11]. The QTF response can be approximated by a lorentzian L, centered in f_0, of FWHM Δf and of amplitude C :

$$L(f) = \frac{C}{1+\left(\frac{2Q(f-f_0)}{f_0}\right)^2}, \tag{3.7}$$

The Lorentzian is fitted to the data using the least square method. Making the assumption that the frequency span is very large compared to the QTF FWHM (Δf), the relative fitting errors are expressed as in [12]:

$$\frac{\Delta f_0}{\Delta f} = \sqrt{\frac{2}{\pi}}\frac{\sigma}{C}\sqrt{\frac{1}{\Delta f}\cdot f_{step}} \tag{3.8}$$

$$\frac{\Delta Q}{\mathrm{Q}} = 2\sqrt{\frac{2}{\pi}}\frac{\sigma}{C}\sqrt{\frac{1}{\Delta f}\cdot f_{step}} \tag{3.9}$$

with Δf_0 and ΔQ the errors on f_0 and Q, resp, and σ the standard deviation of the residual after the Lorentzian fit of the experimental data.

The authors purposely introduced the relative error as $\Delta f_0/\Delta f$ instead of $\Delta f_0/f_0$ so that the figure of merit will be constant if Q varies. As presented, the relative error on f_0 and Q only differ by a factor 2. Considering the SNR as the ratio of the maximum of the Lorentzian C to the standard deviation σ, the absolute errors can be written as:

$$\Delta f_0 = \sqrt{\frac{2}{\pi}}\frac{1}{SNR}\sqrt{\Delta f\cdot f_{step}} \tag{3.10}$$

$$\Delta Q = 2Q\sqrt{\frac{2}{\pi}}\frac{1}{SNR}\sqrt{\frac{1}{\Delta f}f_{step}} \tag{3.11}$$

It is clear that the errors both depend on f_{step} and the SNR for a given resonator. We compared those analytical expressions with another study from Inoue et al. [13]. The authors do not offer analytical expressions but the simulation results, from which we were able to make the comparison.

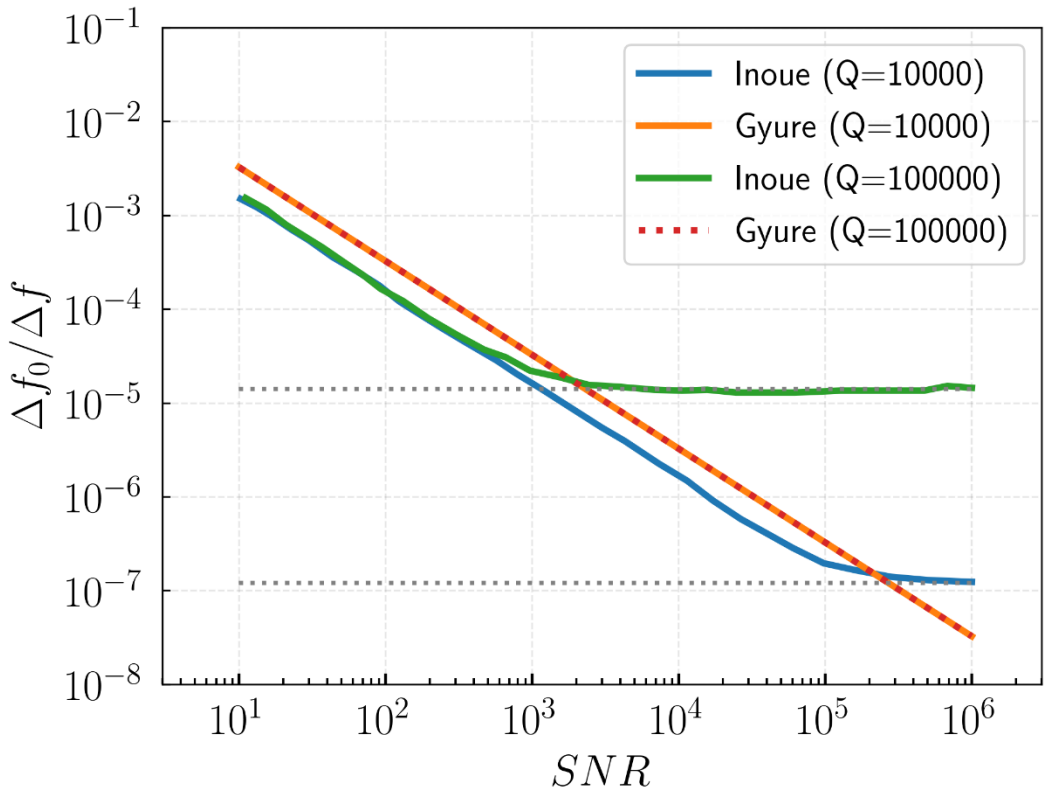

Figure 3.4: Error on the resonant frequency with the NL fit as a function of the SNR, using the data from Inoue et al [13] and the equation from Gyure (equation (3.8)) [12].The simulation parameters correspond to Inoue's article [13] : $f_0 = 10^9$Hz, N = 1201, $f_{span} = \Delta f$, $f_{step} = f_{span} / N$.

The results from Inoue et al. and Gyure et al. , presented on Figure 3.4, are in good agreement: the error decreases with the SNR and is constant for a varying quality factor. However, Inoue et al. obtained that for high values of the Q factor the errors become constant for high SNR ratios (grey dotted lines). This "saturation" behavior is related to the algorithm of the *NL fitting method*, which could be considered inefficient in such conditions of high Q and high SNR. Under those conditions, algorithms using the complex response of the resonator can be employed [13]. For the QTF at standard conditions of pressure ($Q \approx 10^4$), the saturation occurs when the SNR equals 10^5. Such SNRs can be reached for high values of excitation amplitude. However, in our case the SNR is estimated to be around 10^3-10^4. , therefore the NL fit is not in the saturation regime.

For a QTF with f_0=32000Hz, Q=8000, f_{step}=1Hz and SNR=10^3, it gives $\Delta f_0 = 2mHz$ and $\Delta Q = 3$. Those results seems very optimistic and are valid only under the assumption of $f_{span} \geq \Delta f$. As we set the condition $f_{span} \geq 10Hz$, the measurement time has a minimum value of 3s ($10\tau_{step}$). It gives us a first estimation of the measurement time. About the scope of the model, the validity of the equations can be questioned in the case of very high quality factors ($Q>10^4$).

This first estimation is supported with the experimental results mentioned in [7]. For a 10s record time and about 2^{18} data points (i.e. f_{step}=0.6Hz), it gives a relative error of 0.065Hz for f_0 (good enough) and 470 for Q (poor). The measurement time cannot be used for comparison because it is a FFT based technique, but the measurement accuracy can be because it employs

a similar *NL fitting method*. The experimental Δf_0 is greater than the theoretical estimation by an order of magnitude for a very similar f_{step}, giving credit that the theory was optimistic.

Another important issue is raised in this article: the parasitic capacitance (C_0 in Fig) can strongly affect the accuracy of the measurement. It can be tackled in two manners: modification of the fitted model or current compensation. The theoretical errors are given for a Lorentzian, as described by (3.7) whereas the BVD, including C_0, is a more realistic model. The fit can thus be realized with the BVD model, though it would add complexity. The other solution is to compensate the current from C_0. A current of the same amplitude and π phase shifted can be used to annihilate the current from C_0. A gain of about two orders in accuracy can be obtained in the case of a 99% compensation of the capacitance compared to no compensation [7]. The issue was tackled by adding a bridge circuit in scanning probe microscopes [14,15].

We have seen different methods in order to obtain the frequency response of the QTF. However, due to its sharp response, the QTF response time is long. Thus, the frequency sweep method takes at least a few seconds. The alternative is to measure the QTF parameters from the transient response.

3.2.2. From the transient response

3.2.2.1. Modelling the QTF response

The QTF is a harmonic oscillator whose equation of motion can be written with the electrical equivalent parameters RLC, giving the following ordinary differential equation (ODE):

$$\ddot{I} + \frac{\omega_0}{Q}\dot{I} + {\omega_0}^2 I = S \tag{3.12}$$

with I the QTF current in the RLC branch, $\omega_0^2 = 1/LC$, $Q = (1/R)\sqrt{(L/C)}$ and S a source term. The effect of the parasitic capacitance can be neglected when the QTF is at resonance, its contribution to the total current is small compared to the current in the RLC branch.

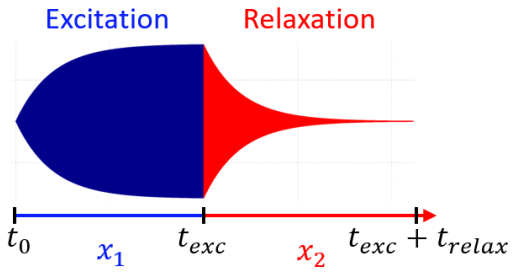

Figure 3.5: Simulation of the QTF transient current response during a step of excitation and relaxation.

After having described the solution in the frequency domain, we focus on the transient response. This technique is well-known, notably in the characterization of MEMS [4]. The QTF behavior is simulated in a two steps experiment (Figure 3.5): Excitation (1) and Relaxation (2). At t_0, the QTF is at rest, giving the initial boundary conditions : $I_1(t_0) = 0$ and $\dot{I}_1\ (t_0) = 0$. During (1), some energy is provided to the QTF in the form of a sine wave at a frequency f_{exc}. The QTF is operated in a forced regime thus a source term is added on the right hand side of

the ODE ($S = \mathrm{A}\cos(2\pi f_{exc}t)$). Then, during (2) the QTF freely oscillates (S=0). The continuity is ensured between (1) and (2) : $I_1(t_{exc}) = I_2(t_{exc})$ and $\dot{I}_1\ (t_{exc}) = \dot{I}_2\ (t_{exc})$. The simulation is performed on Python 3 using the standard scientific libraries Numpy, Scipy and Matplotlib. Typical results are presented on Figure 3.6 for two different excitation frequencies. At the top is represented the QTF oscillation amplitude, and at the bottom the instantaneous oscillation frequency (obtained by counting the number of periods in subsets of 100µs duration).

When the excitation corresponds to the QTF resonance (Figure 3.6(a)), the signal envelope rises exponentially, and the frequency is constant. When the excitation is 20Hz off the resonance (Figure 3.6(b)), a signal beating appears during excitation and the steady state signal amplitude is smaller. The frequency varies accordingly to the signal beating and eventually stabilizes at f=f_{exc}. When the excitation is disabled, the resonator brutally returns back to its natural motion, corresponding to its resonant frequency f_0. This piece of information is crucial for us because it means that **the QTF characterization can be started immediately after the excitation is stopped**.

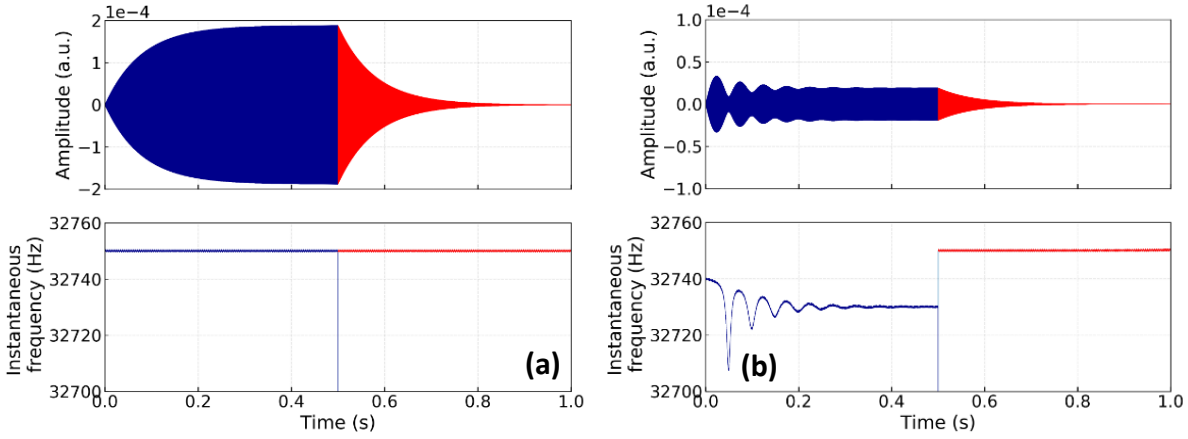

Figure 3.6 : QTF oscillation amplitude (top) and instantaneous frequency (bottom) for two different excitation frequencies : f_{exc} = f_0 (a) and f_{exc} = f_0-20Hz (b) (f_0=32750Hz, Q=8000, t_{exc}=t_{relax}=500ms).

Whatever the excitation frequency, the steady state is reached after about 3 times the QTF response time τ. The optimization of the excitation frequency will be discussed in section 3.3.1.2.

3.2.2.2. Excitation signal for the BF technique

When the QTF is operated at resonance, as it is the case in a usual QEPAS experiment, the amplitude of the signal grows exponentially after the excitation onset. The signal envelope growth is monotonic. The longer is the charge time, the larger the oscillation amplitude. Going away from the resonance, we could expect the signal to decrease progressively. This is true when considering the signal amplitude after charge is complete (at t_{exc}). However, the shape of the signal is not a simple exponentially growing sine wave. Instead, the mismatch between the excitation frequency and the QTF resonant frequency give rise to interferences. It can be understood qualitatively. Consider at t_0, the excitation brutally starts, and the QTF feels it as a pulse and starts oscillating at his own frequency f_0. But because of the frequency mismatch, the excitation drifts away from the QTF oscillation. A moment later, that is a period of the BF

signal $T_{BF} = 1/(|f_0 - f_{\text{exc}}|)$, the excitation reaches a minimum while the QTF oscillation is at maximum creating a minimum in the signal envelope. The interferences amplitude is slowly damped as the QTF is forced to oscillate at f_{exc}.

The QTF output signal during excitation can be approximated by a BF signal, plus an offset. The QTF parameters could be obtained during excitation, however it is practically inconvenient. Indeed, the excitation source is enabled during excitation, and could be responsible of cross talks to the amplifier output due to electromagnetic radiations.

It is convenient to measure the QTF parameters during the relaxation. The excitation can be optimized to be as short as possible while maximizing the amplitude of the QTF oscillations. During the excitation, the interferences are periodical (Figure 3.6(b)) and the first maximum is reached after half a period $T_{BF}/2$. Since we are not supposed to know exactly f_0, the optimal excitation time cannot be calculated. But it can be approximated well enough to obtain a decent relaxation signal and thus a good accuracy on the measured QTF parameters. Figure 3.7 illustrates of the envelope of the QTF signal with an optimized excitation time $t_{exc} = T_{BF}/2$ for different values of $|f_0 - f_{\text{exc}}|$.

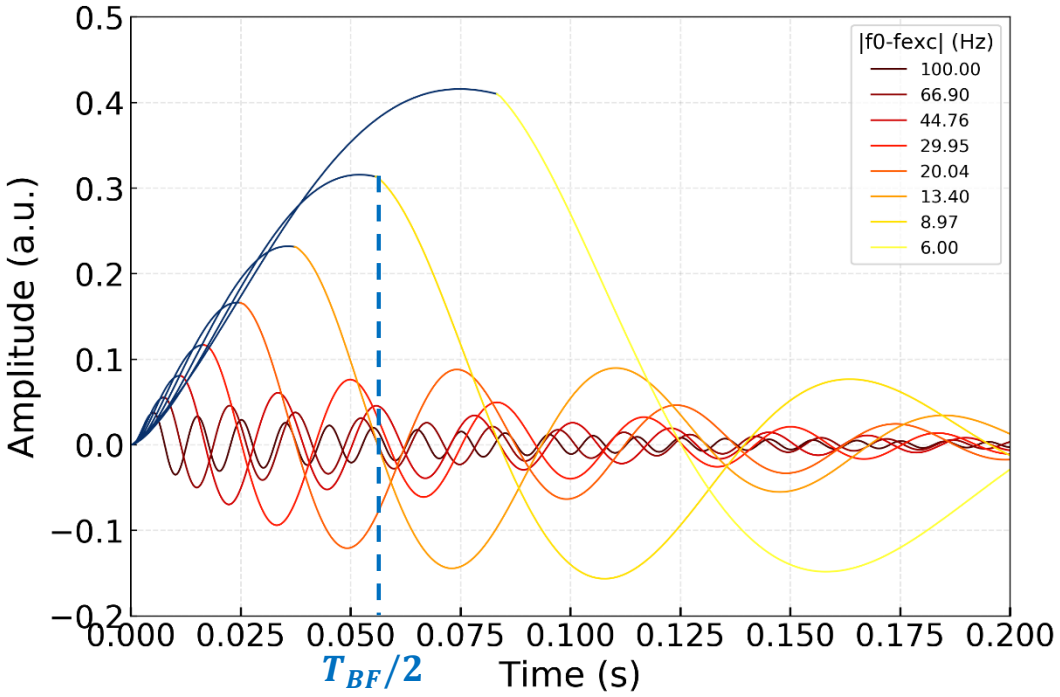

Figure 3.7 : Evolution of the amplitude of the QTF oscillation enveloppe in time for different excitation frequencies. The excitation time is equal to $T_{BF}/2 = (|f_0 - f_{\text{exc}}|)/2$.

3.2.2.3. Direct measurement of the QTF parameters

The goal is to find the QTF parameters. It could be possible to obtain them both from the excitation and the relaxation signal. Using the relaxation signal is relevant since there is a straightforward access to f_0 and Q through the measurement of the signal period and the decay rate of the envelope, resp. The relaxation signal can be described as:

$$V_{out}(t) = \hat{V}_{out} \sin[2\pi f_0 (t - t_{exc})]\, exp\left[-\frac{\pi f_0}{Q}(t - t_{exc})\right],\ (t > t_{exc}), \qquad (3.13)$$

$\hat{V}_{out}$ is the steady-state output voltage amplitude after excitation.

A key point for the simulation is to choose an appropriate timestep. A 32kHz sine wave gives a period of about 30µs. Thus the timestep was chosen to be 1µs, giving 30 points per oscillation. (Other simulations were conducted on Pspice. Similarly, timesteps above 1 µs lead to inconsistent results). Consequently, the time array was constituted by half a million data points.

The measurement of f_0 can be realized by counting the number of periods for a given time. The longer the measurement time – i.e the more averaging over the periods of the signal – the more accurate the measurement. Actually, the accuracy Δf_0 depends on two parameters : the sampling frequency f_s and the measurement time.

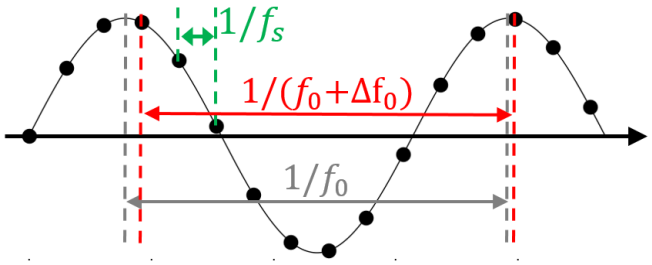

Figure 3.8 : A sinewave of frequency f_0 is sampled at a frequency f_s. The measured frequency by taking the difference between the locations of the two maxima is $1/(f_0+\Delta f_0)$.

We present a simple model here to assess the minimum sampling frequency to reach the required Δf_0. A sine wave of frequency f_0 is discretized at a frequency f_s (Figure 3.8). Only the effect of discretization is observed and the effect of quantization is neglected (true for most today's ADCs with 12 or 16 bits). If the period $1/f_0$ is measured by taking the difference of the two maxima of the discrete data, the error on the period can be first approximated as equals to the sampling period, on average.

$$\Delta T = \frac{1}{f_s} \tag{3.14}$$

Then the error in frequency can be expressed as:

$$\Delta f_0 = \frac{{f_0}^2}{f_s} \tag{3.15}$$

The error on the resonant frequency is thus proportional to the square of the frequency. For a 32kHz signal and a target accuracy of 0.2Hz, it gives a minimum sampling frequency of **5GHz**. To reduce this great value, the counting can be averaged over n periods, gaining a factor n. For a 100ms measurement, the minimum sampling frequency shrinks to about **1MHz**, which is a fast but reachable data acquisition time [16]. Counting in the MHz range can be realized both analogically using a counter or numerically.

The value of the Q factor is contained in the signal envelope. As before, it can be measured both analogically and digitally. This function is called an envelope detector. For high Q factors, envelope detection is easy since the typical decay time is very long compared to the oscillation period, thus the signal averaging can be adjusted very roughly. The typical electronic circuit for envelope detection is made of a capacitor and diode. However, any offset in the input signal or caused by the electronic circuit itself will lead to erroneous values. This issue can be improved by using more complex circuits based on operational amplifier [17,18], even though

they also show a remaining offset. With the latter, the relative error on Q can be estimated around 2-5%. Digitally, there could also be some offsets during amplification stages between the QTF and the ADC. However, offsets can be compensated after digitization, thus the Q value can be obtained with a great accuracy.

3.2.2.4. Measurement of the QTF parameters in a heterodyne configuration

Although the QTF parameters can be obtained from the transient response, a high sampling frequency is needed to fulfill the required accuracy. This issue can be overcome by employing a heterodyne configuration. This technique is very well known in the field of time and frequency for the analysis of highly stable clock oscillators [19]. It consists in mixing the signal from an unknown oscillator with a reference signal, whose frequency is considered perfectly stable, in order to obtain a "beating". The Beat Frequency signal (BF) contains all the information about the frequency stability of the unknown oscillator, but at a lower frequency, where it can be processed with greater accuracy. From a mathematical point of view, the multiplication of two sine functions, of frequency f_0 and f_{ref}, generates two sines components at $|f_0 - f_{ref}|$ and at $f_0 + f_{ref}$.. Then, a low pass filter is applied to keep only the frequency difference. Since f_0 and f_{ref} values are close, the beat signal will have a low frequency.

In our case, the signal was extracted using a lock in amplifier (LIA). It is convenient because the LIA is also employed for the detection of the photoacoustic signal by harmonic detection. The LIA realizes the demodulation of the output signal by the reference signal of frequency f_{ref}, giving rise to a beating at a frequency $f_0 - f_{ref}$. In order to avoid the LIA low-pass filtering, the bandwidth is selected to be broader than the beat frequency (BF), thus the time constant is typically taken to be around 1ms. This signal is provided by a function generator. Using equation (3.13), the BF signal can be expressed as :

$$V_{BF}(t) = \hat{V}_{out} \sin\left[2\pi|f_0 - f_{ref}|(t - t_{exc})\right] exp\left[-\frac{\pi f_0}{Q}(t - t_{exc})\right], \quad (t > t_{exc}), \tag{3.16}$$

The BF signal envelope is similar to the transient response one, only the frequency of the oscillation has changed, as shown on Figure 3.9. Hence, the Q factor is measured with the same accuracy, whereas the accuracy on f_0 is strongly improved. Using equation (3.15) for a BF signal at a frequency of 20Hz and a moderate 50kHz sampling frequency, the theoretical relative error equals to 8mHz, that is an order of magnitude below the target accuracy.

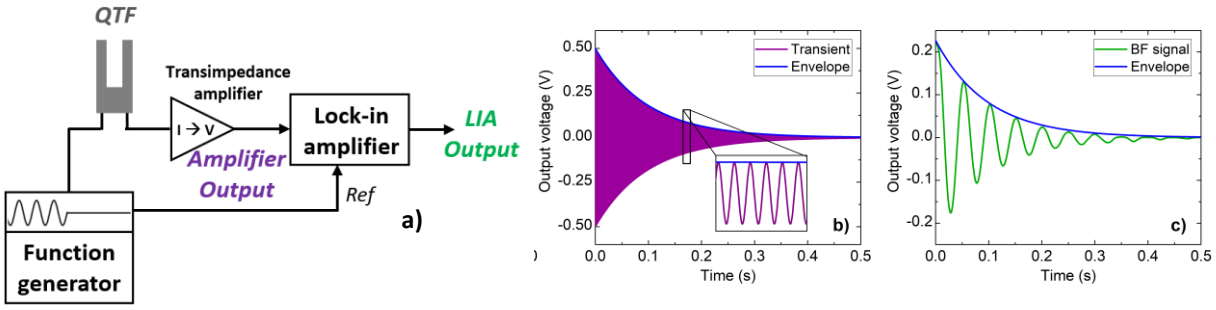

Figure 3.9 : The BF characterization setup is made of a function generator as the excitation source, a QTF, a TA and a LIA to realize the heterodyne detection. Typical signals observed at the amplifier output (b) and the LIA output (c), at a frequency of f_0 and Δf, resp.

We used the BF technique in order to convert the 32 kHz in a low frequency signal in order to obtain higher accuracy on the frequency measurement while reducing the required sampling rate compared to the direct transient measurement.

Apart of the frequency response and the transient response, another technique consists in placing the QTF in an oscillator circuit to measure its resonant frequency.

3.2.3. Measurement of the QTF parameters in an oscillator circuit

An oscillator is a closed loop system made of two elements: an amplifier and a selective filter. The frequency of the oscillator is determined by the central frequency of the passband filter (f_0 for the QTFs). At start, the energy in the system is only the electronic noise. This noise propagates in the circuit, restricted in frequency by the narrow bandwidth of the filter and amplified by the amplifier. The non-filtered signal increases progressively. The oscillator will reach a steady-state if the circuit gain equals to 1. Therefore, the amplifier gain is designed to be non linear, decreasing for high signal amplitudes (for instance due to the saturation of the amplifier). The critical point in the design of the electronics is to obtain a stable system.

From an automation point of view, the amplifier and the selective filter are represented as A and B transfer functions, resp. The transfer function of the oscillator equals to:

$$H = \frac{V_{out}}{V_{in}} = \frac{A}{1 - AB} \tag{3.17}$$

The oscillator is stable if it fulfills the Barkhausen criterion AB=1, or in terms of gain and phase, |AB|=1 and φ(AB)=0°. For instance, an inverting gate can be used as an amplifier, leading to an 180° phase shift. Two capacitors C_1 and C_2 are thus added to reach a total phase shift of 360°. This circuit is a typical Pierce oscillator (Figure 3.10(a)). Many other circuits ensure the same function [20]. The initial function of those oscillators is to output a frequency stable signal, to be used as an electronic clock. However, when the QTF is used as a transducer, such as in scanning probe microscopy, the circuit can become more complex (Figure 3.10(b)). First, when the QTF is in air, the frequency response is broader and smaller, making the current contribution of the parasitic capacitance less negligible. Parasitic compensation is often implemented in the oscillator circuit [21]. Second, as the quality factor is affected by the surrounding environment, an adjustment of the gain is needed to place the oscillator in a stable regime [22,23]. Third, the QTF oscillation amplitude in an oscillator is very high compared to typical values with the photoacoustic excitation. This set point is chosen to obtain a good SNR in an oscillator, but prevents sensitive detection in photoacoustics. A modified oscillator circuit was designed to achieve lower electrical excitation [24]. QTF drivers specially dedicated for AFM are commercially available [25].

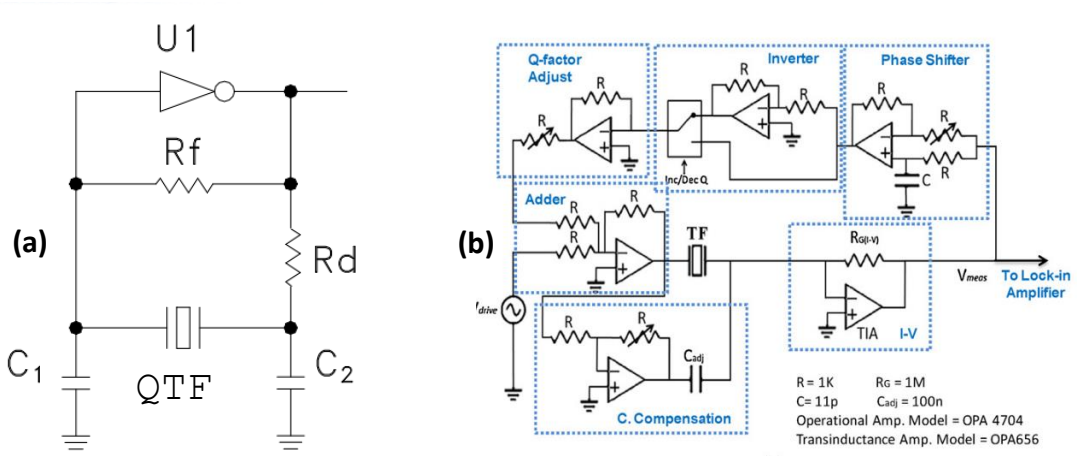

Figure 3.10 : (a) Typical Clapp oscillator with an inverter gate and two capacitors to adjust the phase shift [24]. (b) QTF oscillator dedicated to scanning probe microscopy, including parasitic compensation and Q factor adjustment [21].

The stability of an oscillator depends on the intrinsic stability of the quartz crystal, as well as the stability of the electronic circuit. The frequency shift of the oscillator Δf_{osc} is written as [26]:

$$\frac{\Delta f_{osc}}{f_{osc}} = \frac{\Delta f_0}{f_0} + \frac{1}{2Q}\left(1 + \left(\frac{2fQ}{f_0}\right)^2\right)^{\frac{1}{2}} d\phi(f) \qquad (3.18)$$

With f_{osc} the frequency of the oscillator and dϕ the variation of the feedback loop phase. This phase shift is due to the environmental sensitivity of the components, mostly to temperature variations. The high Q factor of the QTF minimizes the effect of the phase shift. The stability of the oscillator is expressed as the relative shift of the oscillator in ppm (part per millon). For a basic crystal oscillator (XO), the medium term frequency shift of the oscillator is around tens of ppm. The residual variations are mostly due to temperature, that is why some oscillators are Temperature-Compensated (TCXO) or Oven-Controlled (OCXO), reaching frequency shift of 1ppm down to 10^{-2} ppm. Those performances are far above the requirements for a QEPAS sensor. Once the circuit is oscillating steadily, the amplifier output frequency corresponds to the QTF instantaneous frequency, that can be measured directly (section 3.2.2.3), with a measurement accuracy given by (3.15), or in an heterodyne configuration (section 3.2.2.4). The amplifier output signal can also be employed directly in a controlled system. There is no direct measurement of the Q value, because the QTF is kept at resonance by the oscillator circuit. In clock oscillators, as the QTF is vacuum sealed, the Q value is highly stable and does not need to be calibrated. In scanning probe microscopy, the QTF is often calibrated using the frequency sweep method.

In conclusion, the oscillator is a closed-loop system with the ability to drive the QTF at resonance. The circuit is more complex when the QTF is employed as a sensitive transducer with a surrounding environment. The measurement of f_0 is fast and accurate though the quality factor cannot be measured and is often calculated beforehand.

3.2.4. Comparison of the techniques

Various methods can be employed in order to obtain the QTF parameters. The accuracy of the measurement can greatly vary depending on the experimental conditions, in particular

depending on the measurement time. Some relevant data from the literature is summarized in Table 3-1. Characterizations are often made in the frequency domain because the measurement is simple and the accuracy is good. However, the measurement time is long, in the order of 10s. Similar performances are obtained with FFT based methods. On the other hand, recording the transient response of the QTF takes less than a second. Q is easily measured from the envelope. The direct measurement of f_0 requires high speed data acquisition, in the MHz range. Although technically feasible it remains more complex than the heterodyne method, based on a simple benchtop lock-in amplifier, which offers a great accuracy on the measurement of f_0 at an affordable sampling frequency.

Characterization method	**f_0 error (Hz)**	**Q error**	**Measurement time (s)**	**Reference**
Frequency response (Theoretical)	0.002	3	10	[13]
Frequency response (from FFT)	0.065	470	10	[7]
Frequency response	6.6	/	/	[27]
Transient analysis	26	590	/	
Transient analysis (analogical)	/	160	1	[17,18]
Oscillator circuit	0.001 (Theoretical)	/	0.1	[28]
Oscillator circuit	0.01	/	1	[29]
	0.001	/	10	

Table 3-1: Summary of the measurement accuracy on f_0 and Q with different characterization techniques.

3.3. Experimental setup

The different methods for characterizing the QTF were theoretically compared, either in the frequency or the time domain. The Beat Frequency (BF) technique was estimated to be the only one able to offer less than 1% measurement error on the QTF parameters in less than 1s, as we were targeting. The BF technique appears to offer the best compromise in terms of measurement time and measurement error. We present here the implementation of the BF technique, the practical issues and the solutions to accurately measure the QTF parameters from the transient signal. We test the validity of the setup by monitoring the QTF response in variable environments (humidity, temperature). Finally, we integrate the QTF characterization in the QEPAS sensor to ensure real time correction of the QTF resonance, accordingly to the presented architecture.

3.3.1. Global design

The first setup was designed to offer the possibility to study 2 QTFs simultaneously. Indeed, since 2 QTFs are almost identical, it was interesting to study the simultaneous evolution the resonant frequencies of 2 different QTFs located nearby and to observe the correlation of the relative variations of the resonances of the 2 QTFs. If the correlation is high, the resonance of one QTF could be measured and used to correct the drift of the second QTF ; the second QTF being used for photoacoustic detection.

The second setup was a refined version of the BF setup (designed for a single QTF characterization). Both prototypes were a functional implementation of Figure 3.9. The essential modifications are described in the following paragraph, notably changing the LIA and refining the fitting algorithm. Measurements on the influence of temperature (Section 3.4.1) were obtained with the first prototype while other results were obtained with the second prototype.

The BF setup is represented on Figure 3.11. First an excitation signal, a simple sine wave; is generated. The excitation has to be switched off in order to start the QTF relaxation. Practically, it can be done internally with a function generator, either by turning off the channel, either by setting its amplitude to 0. In both cases, the function generator uses a relay to turn off the channel or to change the amplitude range. Since this operation will be repeated numerously (every seconds), and that relays only have thousands of cycles estimated lifetime, we decided to employ an external relay (Hongfa HDF31). The switching could have been realized by other means, such as with: reed relays, solid state relays, multiplexers, analog switches. However, due the very low currents generated by the QTFs (down to pA), an electromechanical relay was preferred to avoid any leakage current. This topic will be discussed again in section 3.6.8.

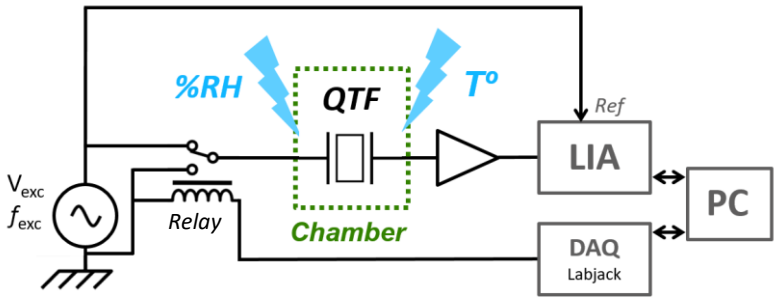

Figure 3.11 : Setup for the BF measurement. The QTF is enclosed in a temperature and humidity regulated chamber. The relay, controlled by the analog output of a DAQ card (Labjack T7), is used to switch between the excitation source and the ground. The QTF current is amplified and then demodulated by a lock-in amplifier. A labview program on a laptop synchronizes the instruments to obtain the BF signal, from which are extracted the QTF parameters in real time.

Apart of the relay, the circuit resembles to the conventional QEPAS circuit with a transimpedance amplifier followed by a lock-in amplifier (EG&G 7260). In the first setup, a Labjack T7 DAQ card was employed both for driving the relay coil and for recording the BF signal during about 500s with a sampling rate of 50kHz. The relay, the QTFs and the transimpedance amplifiers were integrated on a stripboard circuit (Figure 3.17(a)). The main issue we encountered was the electromagnetic radiation from the excitation source. Indeed, the QTF has a high impedance, thus to generate a few nA an excitation voltage of a few mV is

needed. Even though the connections between the board and the instruments were made through shielded BNC cables, parasitic signals were visible in the relaxation signal (Figure 3.12(a)). Additional shielding on the circuit board was necessary obtain a proper signal (Figure 3.12(b)). In the second setup, the data acquisition and the relay command were operated by the LIA (MFLI – Zurich Instruments). The use of a single instrument allowed more accurate timing control and noise reduction.

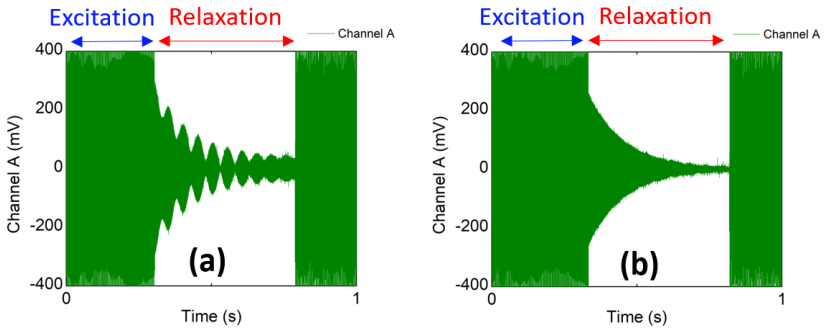

Figure 3.12 : Issue with the first prototype. The relaxation signal after the amplifier catches an additional frequency component due to the radiation of the excitation source (a). With proper shielding, the relaxation signal corresponds to the expected exponentially decaying sine wave (b).

In many scientific experiments, the LIA is used to reduce the noise of the system by working in a narrow frequency band in the kHz range, thus avoiding the 1/f noise. The bandwidth of the LIA (BW_{LIA}) can be adjusted by changing the time constant. The longer the time constant, the narrower the bandwidth. However, in the BF technique, the QTF oscillation does not match exactly the reference LIA oscillator. If the bandwidth is too narrow, the BF signal will be attenuated by the low pass filter. Equivalently said with the criterion : $|f_0 - f_{ref}| < BW_{LIA}$. For our setup, the QTF was generally operated 20Hz off resonance, the time constant and the filter slope of the lock-in amplifier were respectively 1ms and 18dB/oct, giving a filter bandwidth (at -3dB) of 80Hz.

3.3.1.1. Fitting algorithm

After digitizing the BF signal, a Labview program collects the data. Two different methods were tested to calculate the QTF parameters: one based on a peak finding function and the other based on a non linear fit. With the first technique ('Find peaks'), a built-in Labview function was used to obtain the coordinates of the positive peaks. The average of the differences between the locations of two consecutive peaks gives the period of the BF signal. The frequency of the BF signal is summed with f_{exc} to obtain f_0. Then, the peak maxima are fitted with an exponential decay to obtain the measured Q value.

The second technique consists in directly fitting the data with the theoretical model (equation (3.16)) using a non linear (NL) fitting algorithm (such as the well-known Levenberg–Marquardt). The theoretical model along with guessed parameters is passed to the algorithm. If the signal is well described by the model, the result is very accurate. The guessed parameters are essential to ensure the convergence of the algorithm, which can be difficult to control. This is the main downside of the NL fit. Also, the computation time is long for large sets of data, though it can be reduced by downsampling the data (also called decimating). In comparison with the find peaks method, the NL fit is more accurate but less robust.

The two methods, find peaks and NL fit, were tested with a synthetic signal from a function generator (Tektronix AFG 1062). An exponential decay, of time constant 100ms and of period 1s, and a 32kHz sinewave were generated on channels 1 and 2, resp. Then, channel 2 was amplitude modulated with channel 1. The output of channel 1 gave an exponentially decaying sine wave similar to the QTF relaxation with supposedly better repeatability. For both algorithms, the measured QTF parameters were recorded for 5 minutes (Figure 3.13). It is clear that the NL fit outstands the find peaks technique, for measuring f_0. However, for measuring Q, the signals from both algorithms appear highly correlated, shown by a Pearson correlation coefficient (R=0.9928) very close to 1. The algorithms have very different architectures and their results should not be correlated. This is a good indication to state that the measurement error on Q (ΔQ) is not related to the accuracy of the algorithm but to the stability of the synthetic signal. No conclusion about ΔQ can be drawn from this experiment.

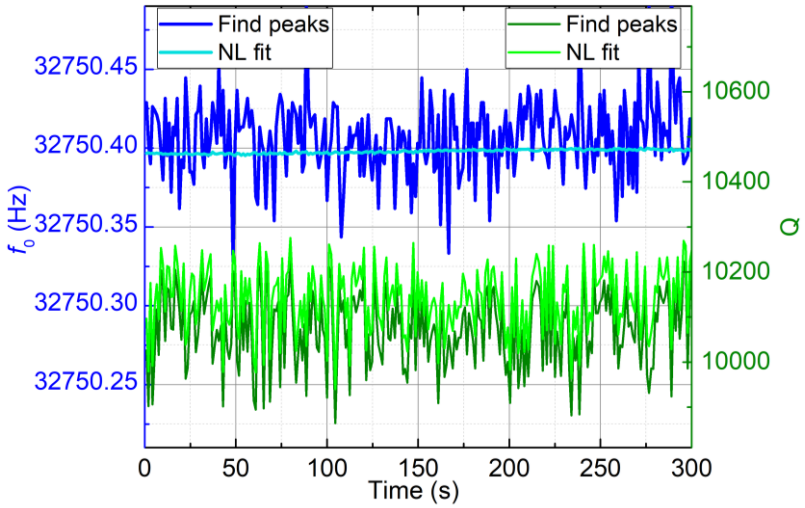

Figure 3.13: Measured resonant frequency and quality factor from the synthetic BF signal with the two different algorithms: find peaks and NL fit.

An oscillator with a more stable Q was required to test the algorithms and the acquisition. We avoided using the QTF as a reference in the first place because its response can vary with temperature. But if the temperature is controlled, the frequency should be highly stable, thus leading to very low Δf_0 and ΔQ. This setup is known as an Oven-Controlled Crystal Oscillator (OCXO). A QTF was stabilized at T=20°C (see Section 3.4.1), and the QTF parameters were extracted (Figure 3.14). The accuracy on f_0 is better for the NL fit than for the find peaks by an order of magnitude. ΔQ decreased by about a factor 20 compared to the Figure 3.14(a), confirming that in the previous experiment, the errors were not related with the algorithm but to the poor stability of the synthetic signal.

Also, it should be mentioned that the theoretical limit accuracy of the algorithms could be calculated through numerical simulations, by generating a perfect BF signal with a controlled amount of noise. We preferred to test the whole system, thus checking not only the accuracy but also the robustness of the fit method with a true signal.

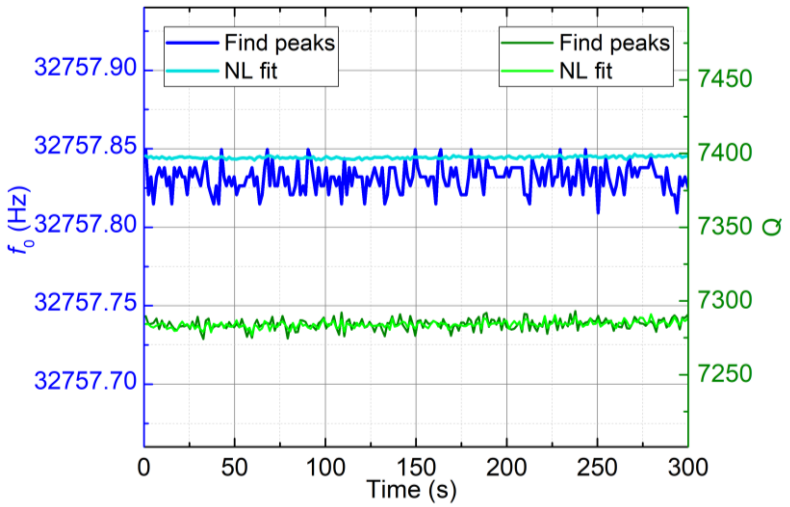

Figure 3.14 : Evolution of the QTF parameters for the two algorithms, find peaks and NL fit. The temperature of the QTF is regulated at 20°C (V_{exc}=0.1V_{pp}, f_{exc}=32730Hz).

Originally, the BF signal was sampled at a frequency of 50kHz, thus obtaining around 10000 points. It was necessary to obtain a good accuracy with the find peaks algorithm. Nonetheless, the NL fit should not be as sensitive to the number of data points. We verified it experimentally by measuring the error on the QTF parameters as a function of the number of data points. After changing the number of data points, the sampling rate of the BF signal was adjusted to keep a sample length of 0.5s. The QTF parameters were recorded for 60s using both algorithms. Then, the errors were deduced by taking the standard deviations of the data sets (Figure 3.15). The errors for the find peak algorithm highly depend on the number of data points whereas they are almost constant for the NL fit. Even for a 100 data points, that is only 10 points per period for a frequency 20Hz, the accuracy is very good. We obtain an accuracy well below the initial requirements : $\Delta f_0 = 2mHz \ll 0.2$ and $\Delta Q = 2 \ll 80$. This is mostly explained by the high SNR of the BF signal.

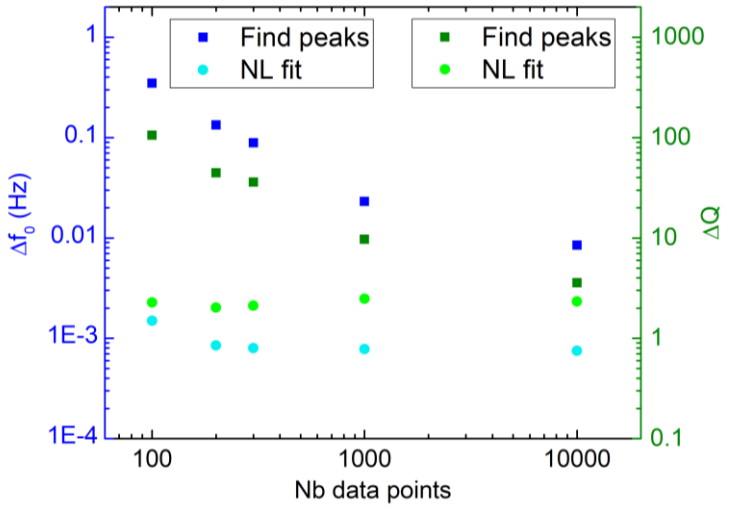

Figure 3.15 : Error on the QTF parameters as a function of the number of the data points of the digitized BF signal (V_{exc}=0.1V_{pp}, $|f_0 - f_{exc}|$=28Hz).

The two methods for extracting the QTF parameters are suitable for measuring the QTF parameters, with an even enhanced accuracy for the NL fit method. The computation time is negligible in the case of the find peaks methods and can be optimized by reducing the number of data points in the case of the NL fit.

3.3.1.2. Optimizing the excitation signal

The purpose of the BF characterization setup is to output the QTF parameters. Those parameters are sensed by first exciting the QTF with a sine wave. An ideal setup would be excitation independent, i.e. would give an identical output whatever the shape of the excitation. In a real system, systematic and random errors can occur. In order to verify the righteousness of our system, the effect of the frequency and amplitude of the excitation sine wave onto the measured parameters was observed (Figure 3.16). For each data points, the QTF parameters were recorded for 60s, at a rate of 1Hz, using the find peaks method. The mean value and the standard deviation were then calculated. The acceptable error f_0 and Q are represented by shaded areas. The measurement is almost unaffected by the excitation frequency (Figure 3.16(a)), except when f_{exc} is close to f_0, because the processing algorithm was not thought for slowly varying signals. When $|f_0-f_{exc}|$ is in the range [5, 50] Hz, the accuracy is very high and has a flat response. This flat response over the frequency shows how robust the measurement is. It will be unaffected by a sudden shift of the QTF response.

The effect of the excitation amplitude (Figure 3.16(b)) was studied on a wide range, from 3mV to 0.3V. For low amplitudes, the large error bars illustrate the random error due to a poor SNR. When the amplitude increases, the error decreases and the mean values quickly converges. The target errors are met for an excitation voltage superior than 0.02V.

This study quantifies the errors of our characterization setup. For high values of V_{exc}, the measurement accuracy is way over the target.

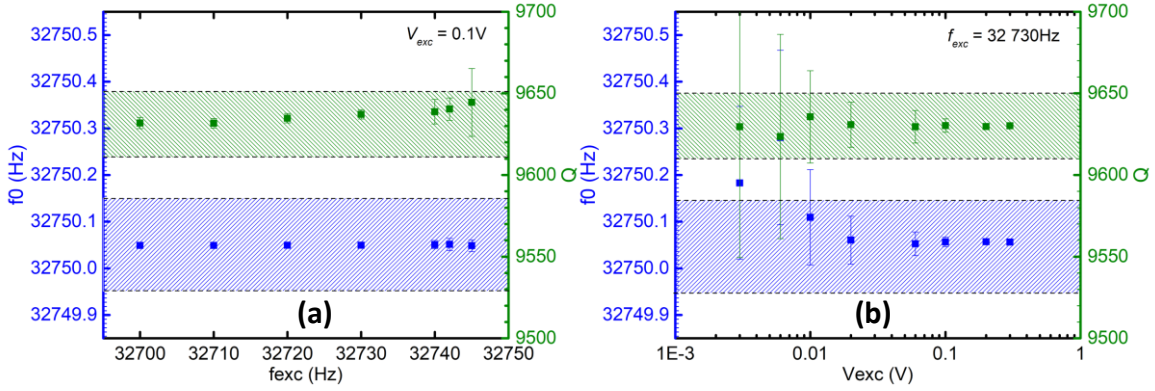

Figure 3.16 : Measured QTF parameters as a function of the excitation frequency (a) and the excitation amplitude (b). The hatched areas correspond to the target accuracy and the error bars to the standard deviation. The excitation time t_{exc} is set to 200ms to ensure the QTF is at steady state before the onset of the relaxation.

3.4. Influence of environmental parameters

The accuracy of the QTF characterization setup was measured to be within the target range, both for f_0 and Q. The next step was to test the QTF in real conditions. Most of field sensors do not monitor only one information, such as the gas concentration, but often integrate temperature and humidity probes. The data about those environmental parameters can be displayed in real-time, later used for further data analysis and correlations, and also the sensor itself might apply a temperature/humidity compensation onto the output signal.

In our case, the influence of the temperature and humidity on the QTF had mostly two purposes. First, the variation of the resonant frequency as a function of temperature is specified by QTF manufacturers. It appeared to as being a straightforward mean of comparing our technique to a certified reference. The temperature response was thus an intermediate experiment in order to validate the accuracy and reliability of our QTF characterization setup. Second, the humidity is likely to vary in certain applications such as breath analysis. Very few articles on this topic exist to our knowledge. One article, presenting a humidity sensor based on coated QTFs [28], contains some data about the evolution of f_0 as a function of the humidity, though no value are reported for Q since it is an oscillator based measurement. A complete characterization of the QTF with the humidity varied from 30 to 90% is first reported using our setup.

3.4.1. Temperature

Concerning the study of temperature and humidity, the two parameters were studied with different setups. The QTF temperature behavior was observed using a homemade temperature regulated system. A commercial PID temperature controller was driving a thermoelectric cooler at a given temperature (Figure 3.17(a)). In the first setup, the QTF was enclosed in a metal box which was regulated in temperature. Even though the whole box was thermalized, the stabilization of f_0 was long (Figure 3.17(b)), about 5min, indicating a slow and unstable thermal response. As a matter of improvement, the QTF metal cap was directly connected to the cold plate of the thermoelectric cooler in the second setup. In this way, the air gap between the QTF and the temperature controlled cap was small, ensuring high thermal conductivity, and thus fast response time (about 20 seconds). Originally manufactured under vacuum, the QTF cap was punctured (but not removed) to obtain atmospheric pressure when needed. The QTF was connected to the electronic board with coaxial cables to obtain the continuity of the shielding from the excitation source to the transimpedance amplifier.

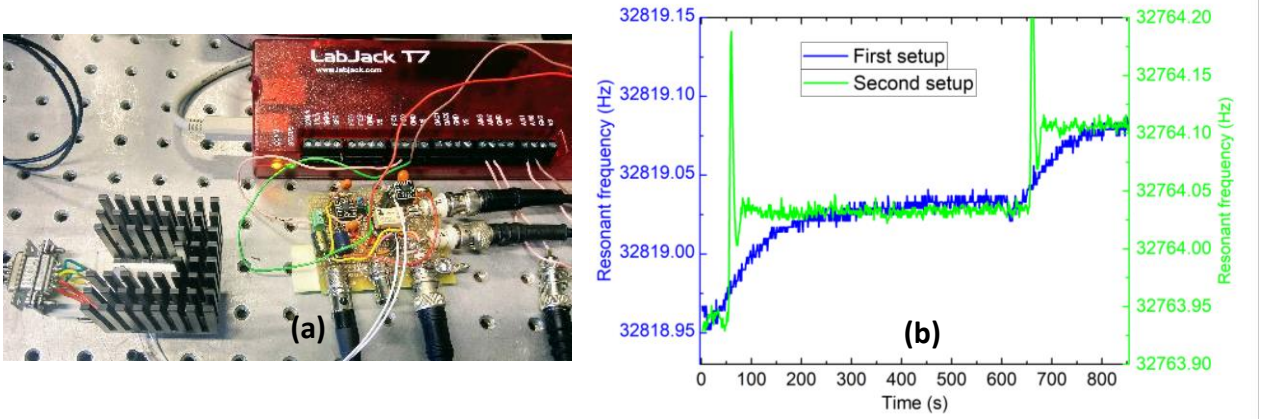

Figure 3.17 : (a) Picture of the characterization setup including the temperature regulated box containing the QTF (left), the electronic board (bottom right) and the data acquisition card (top right). (b) QTF resonant frequency response to a temperature step of 2.5°C. In the first setup, the transient response is slow due to poor thermal diffusion (blue curve), whereas it takes only a few seconds in the second setup (green curve).

A temperature ramp, ranging from 10 to 60°C, with 2.5°C steps, was applied to the QTF, while recording the resonant frequency. Two different QTFs were tested, one at atmospheric pressure and one vacuum capped. As described previously, the setup was engineered in order to ensure good thermal conductivity. The average value of every step was calculated and plotted as a function of the temperature (Figure 3.18(a)). The curves show a smooth and almost perfect parabolic response. This corresponds very well to the description in the QTF specification sheet (Figure 3.18(b)).

Theoretical models have also been used to derive the parabola [30,31]. It was shown in section 1.3.1.1 that f_0 can be calculated with the QTF geometry, the quartz density and Young's modulus. Those physical parameters are all temperature-dependent to a certain extent, that can be described by using Taylor expansions with given temperature coefficient. They can be rearranged to obtain the expression of the frequency as a second order polynomial:

$$f(T) = f(T_0)\left\{1 + \alpha(T - T_0) + \frac{1}{2}\beta(T - T_0)^2 + o(T^3)\right\} \qquad (3.19)$$

with α and β, the first and second order temperature coefficient, resp. Since quartz is a crystalline material, the physical properties depends on the crystal orientation. The temperature coefficients can greatly vary depending on the quartz angle cut. For an as-manufactured QTF, the angle cut is advisedly chosen to minimize the temperature sensitivity of the oscillator at room temperature. Therefore, the vertex of parabola is theoretically at 25°C, very close to the experiment at 22.5°C (f_0 = 32764.20Hz) for the vacuum QTF. By opening the QTF case, the pressure increases and thus the fluid density increases causing a vertex to shift up to 30°C (f_0 = 32757.75Hz). The effect of the density has already been studied [32]. In both cases, the temperature coefficient β (second order coefficient) is of 0.052ppm/(°C)², very close to the 0.04ppm/(°C)² given in the specification sheet.

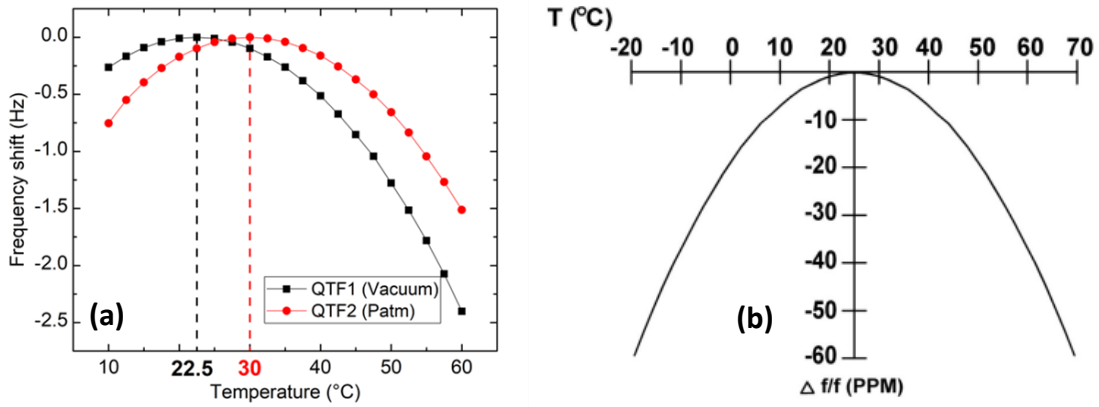

Figure 3.18 : (a) Resonant frequency of a vacuum capped (black) and an open QTF (red) as a function of temperature. (b) Frequency shift as a function of the temperature as given by the datasheet of the NC38LF QTF.

3.4.2. Humidity

The study on the QTF response to temperature gave us confidence on the relevancy of our setup. The next step was to observe the response to humidity, for which there does not exist very accurate study in the literature, and which had already been disruptive in our experiments when sensing high humidity gas samples.

As we demonstrated, good results can be obtained with a proper homemade temperature regulation system. However, building a humidity chamber is not as obvious. A simple well-known solution is to employ saturated salt solutions in order to obtain a stable humidity [33]. The level of humidity can be varied by changing the type of salt. The saturated bath is placed in a sealed container. Some minutes to hours are required for the humidity to stabilize, making the simple system unpractical for quick characterization.

For an accurate regulation of the humidity, we preferred to use a laboratory humidity chamber (ESPEC SH-242[11]). The QTF was located in the middle of the chamber, close to the temperature and humidity probes (Figure 3.19). It was connected through coaxial cables longer than usual (specifically from the QTF to the transimpedance), though the accuracy of the measurement was not altered. The same characterization using the frequency sweep would have yielded to poor accuracy of the measured QTF parameters because of the additional cable capacitance. It is a good illustration of the strength of the BF analysis versus the frequency sweep.

[11] We acknowledge Brice Sorli for his support on the experiment with the humidity chamber.

Figure 3.19: Picture of the setup with, on the left, the humidity chamber (ESPEC SH-242) with the QTF inside and the BF characterization setup on the right.

The humidity was varied from 30 to 90% RH with 10%RH step, followed by two steps at 50 and 30%RH (Figure 3.20(a)). The chamber response is in the range of a few minutes, thus each humidity step was hold for 30 minutes. The temperature was kept constant during a whole experiment. In Figure 3.20, the QTF response is shown for two temperatures : 20 and 40°C. The temperature was constant throughout the experiment except a small increase for the 90%RH step, which should lead to a minor shift compared to the humidity-related shift. The QTF parameters follow the same trend: they decrease with increasing humidity. The evolution of f_0 is very similar at both temperatures. It shows a shift of about 2 Hz from 30 to 80%RH, and almost 1Hz from 80 to 90%RH. The humidity response of Q depends considerably on the temperature : a variation of 315±20 at 20°C and 624±20 at 40°C. The variation of Q practically doubled from 20 to 40°C. Since the experiment at 40°C was conducted after the one at 20°C, it might also be questionable if the QTF response could have been degraded by the exposure to humidity. It could be verified by repeating the experiment.

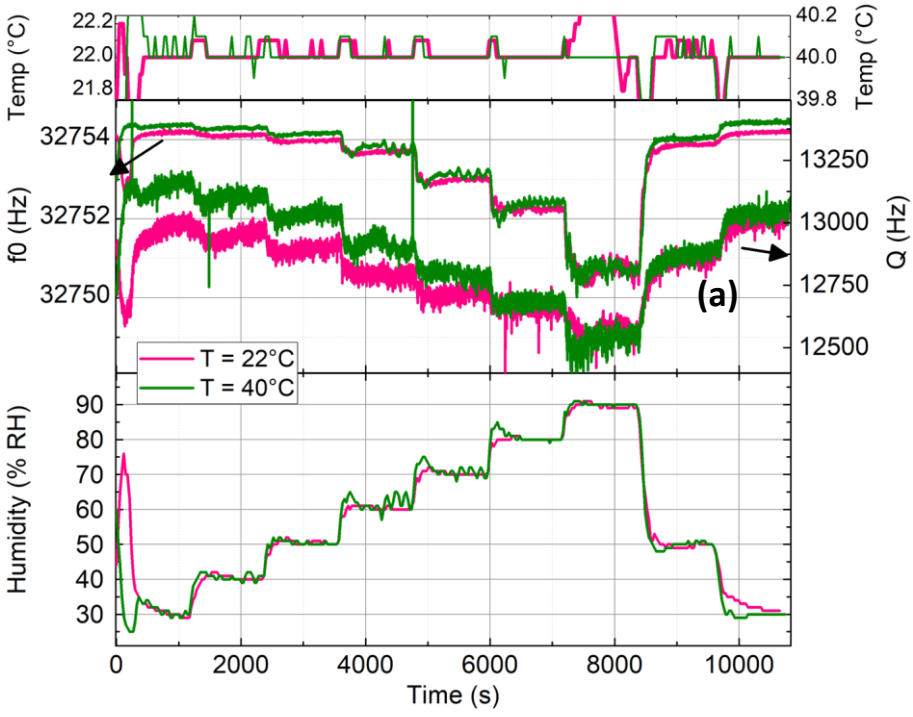

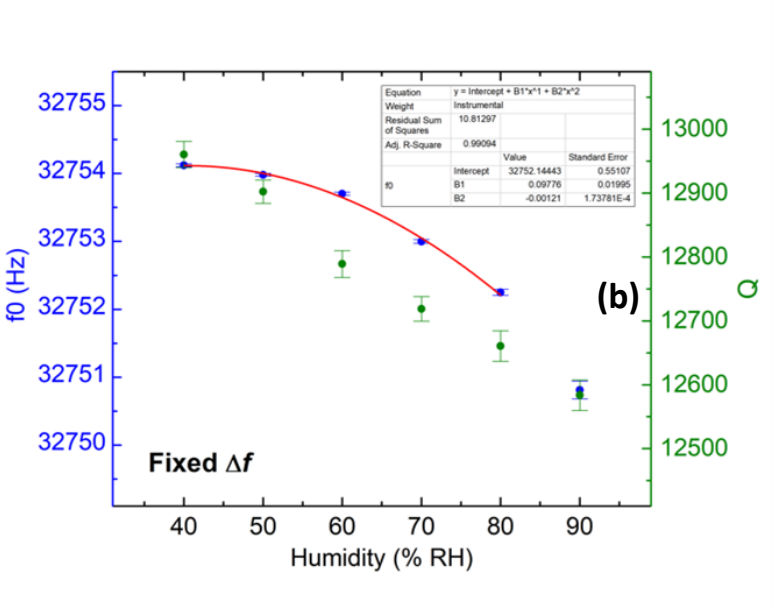

Figure 3.20 : (a) Evolution of the QTF parameters f_0 and Q while varying the humidity, for two different temperatures 20 and 40°C. The humidity cycle is made of 10%RH steps : 7 ascending steps (30 to 90%RH) and 2 descending steps (50 and 30%RH). (b) Results of the experiment at T=20°C presented with the mean value and the standard deviation.

The humidity response can also be presented with the mean value and the standard deviation for each value of humidity (Figure 3.20(b)). The resonance frequency shows quadratic behavior whereas Q evolves linearly.

We have studied of the influence of the temperature and the humidity. The QTF response to temperature corresponds to the manufacturer specifications. A shift of the parabola vertex is observed when releasing the QTF to ambient pressure. The QTF response to humidity was accurately measured from 30 to 90%RH, providing typical figures of the humidity related shift in a real sensor. Those results enhance the importance to take into account the temperature and humidity in a sensor employing a QTF as a sensitive transducer. We have proposed a setup based on BF technique to quantify the variations of these parameters. The curves can be used to determine the gas sensor error for a given temperature and humidity range. They can also be used as calibrated curves in order to make a temperature/humidity compensated sensors and thus improve the sensor performances. Another option is to employ the BF technique for real time resonance tracking as it is presented in the next section.

3.5. Simultaneous gas sensing and QTF Resonance Tracking (RT-QEPAS)

After having successfully implemented the BF analysis for measuring the QTF parameters and its variations with temperature and humidity, the next step was to add it to the gas sensor to continuously monitor the changes. A post-processing approach would be to use the results of the BF measurement to normalize the output signal. Another approach would be to add a feedback loop to ensure the resonant operation of the QTF and thus to maximize the output signal. Here, we present this last method, we called it Resonance Tracking (RT) QEPAS.

The RT-QEPAS architecture is based on the sequential QTF characterization and gas measurement, as presented on Figure 3.1, and implemented in the setup on Figure 3.21. The synchronization of the two stages is crucial and is realized by a rigorous sequence involving two switches, S1 and S2, either hardware or software controlled. S1 is a three-p

ort switch connecting the QTF terminal either to the sinewave source for the excitation (A), to the damping circuit (B) (discussed later in 3.6) or to the ground for QEPAS sensing (C). S2 is used to select the LIA demodulation frequency, either to f_{exc} (U) for the characterization or to f_0 (W) for QEPAS. For our setup, S2 is activated internally in the LIA (MFLI, Zurich Instruments) while S1 is based on a low noise analog switch. The analog switch prevents the QTF re-excitation during the characterization-to-QEPAS transition, it will be further discussed in 3.6.

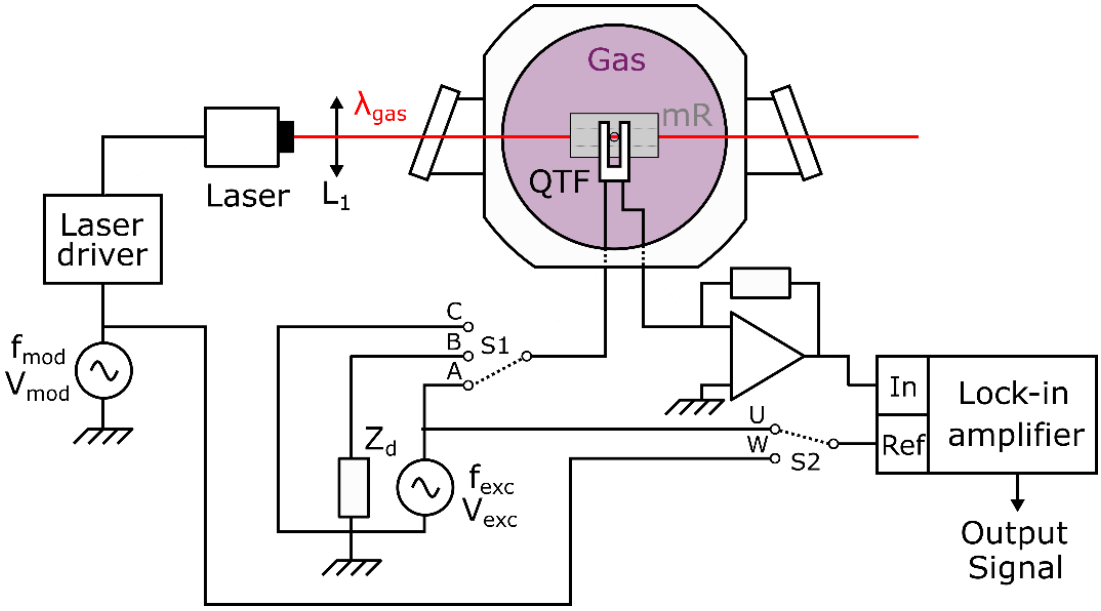

Figure 3.21 : Setup for the RT QEPAS.

Summarizing the sequence:

1. Excite the QTF (S1=A, S2=U)
2. Record BF relaxation signal (S1=C, S2=U)
3. Find f_0 &Q
4. Let the QTF discharge (S1=C) or force is to discharge (S1=B)

5. Adjust the modulation frequency (S2=W)
6. Measure the gas concentration with QEPAS

The sequence is constituted with the main actions to ensure the resonant operation of the QTF and thus limit QEPAS signal drift. The sequence can be extended to improve the system stability (e.g. adjusting f_{exc}), the system accuracy (e.g. adjusting V_{exc} or V_{mod}). Those improvements depend on the sensor's applications.

The first implementation was tested for the detection of methane at 4294.55 cm^{-1} (2328.53 nm) with a DFB laser (NORCADA). The laser is operated at 20 °C and 143.4 mA. The current is wavelength-modulated with a sine wave at 32.7 kHz and covering 0.8 cm^{-1}.

The humidity affects the sensor through two main mechanisms: modification of the relaxation time and modification of the QTF resonance. We have seen in section 3.4.2 the impact of humidity on the QTF parameters. Due to the long relaxation time of methane, the photoacoustic effect in the 30kHz frequency range is not very effective. H_2O promotes non-radiative relaxation and increase the efficiency of the photoacoustic effect. It is thus relevant trying to increase the water content of the sample. A simple way of humidifying a gas is to use a bubbling bath. The gas passes through the water and the humidity increases. The humidity level depends essentially on the flux and the bath temperature.

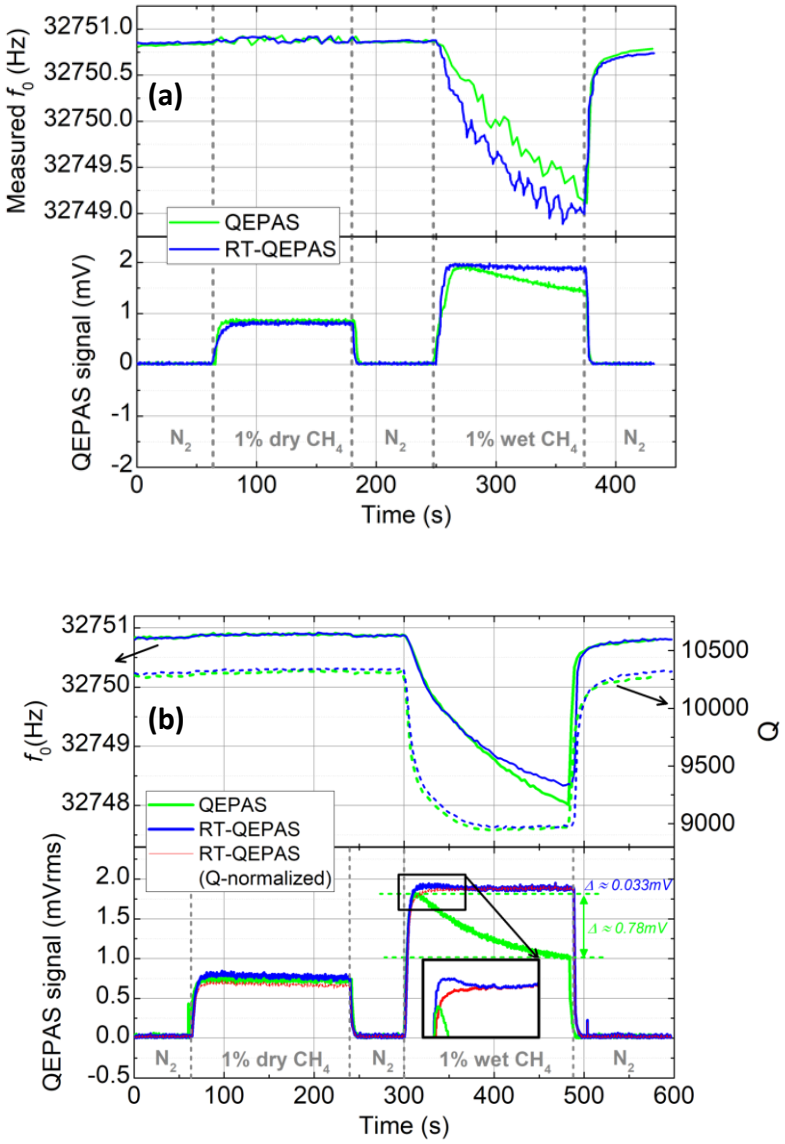

Figure 3.22 : Evolution of the resonant frequency (top, continuous line), the quality factor (top, dotted line) and response of the gas sensor (bottom) to an injection of 1% dry CH_4 and 1% wet CH_4, with the QEPAS (green) and the RT-QEPAS technique. The laser modulation is kept on in (a) during the QTF characterization while it is off in (b). In RT-QEPAS, the QTF instantaneous frequency f_0 is used as a feedback for the laser modulation frequency (blue), and then normalized by the Q factor (red). The RT-QEPAS sensor is thus more robust to environment changes than the conventional QEPAS sensor. The gas cell is flushed with pure nitrogen between the two injections.

In this experiment, we observe the response of the sensor to a gas cycle including a step of 1% dry CH_4 followed by a step of 1% wet CH_4. The gas cycle is repeated twice, first with standard QEPAS, and second with RT-QEPAS (Figure 3.22). The QTF parameters are recorded in both cases but used for real time correction of the laser modulation frequency only in RT-QEPAS. In both cases, the injection of dry CH_4 leads to the same QEPAS signal. However, during the wet CH_4 step, the QEPAS signal (green curve) exhibits a strong decrease whereas the RT-QEPAS one (blue curve) remains practically constant. The QEPAS signal drift creates a measurement artifact, which can be chiefly explained by the frequency shift of the QTF. The shift of about 3Hz implies in the case of QEPAS, a 44% relative change in amplitude. During

the first experiment (Figure 3.22(a)), we remarked that the measurement of the QTF parameters was noisier. The noise is only visible during methane injection, thus inferring the acoustic generation as the disturbance and discarding our first assumption that the acoustic generation is negligible compared to the electrical excitation in our system. However, this assumption would remain true for trace gas sensing at low concentration. The experiment was repeated (Figure 3.22(a)) with the modulation frequency turned off during the QTF characterization. The noise measurement of the QTF parameters was strongly improved, as the accuracy of the RT-QEPAS. The relative deviation is less than 2% during the humidity step. Then the signal can be normalized by Q (red curve), leading to less than a 1% signal shift, which is a significant reduction of the error caused by the frequency shift of the QTF. This normalization further improves the shape of the signal, and corrects the overshoot of the RT-QEPAS signal (as shown in the inset). The normalized signal response follows an exponential growth. Interestingly, Figure 3.22(b) also provides some information about the kinetics of the QTF parameters. The shift rate is higher for the Q factor than for f_0, meaning they are partially independent. It seems to indicate that multiple physical effects are acting on the QTF upon a humidity change and opens up new questions to study about the QTF behavior.

Summarizing the previous results of this chapter, that can also be found in our article [34], we first focused on the QTF characterization, in the frequency and time domain. We concluded that the BF technique gives the best compromise between time and accuracy. We optimized the accuracy as a function of the excitation amplitude and frequency. In order to study the QTF behavior and check our setup, we observed the QTF response to temperature and humidity. After this, we estimated that the QTF characterization was ready to be implemented with gas sensing. We demonstrated the ability of RT QEPAS to correct the signal drift due to a varying environment. RT QEPAS makes the sensor more robust by spending about one second for each QTF characterization. It might be well within the requirements for an industrial sensor in terms of response time. Still, we questioned ourselves if there was a way to make it faster.

3.6. The damping circuit

3.6.1. Calculation of the free decay time

The QTF has a large dynamic range and its energy level after electrical excitation can be orders of magnitude higher than after the photoacoustic excitation. Since our purpose is to alternate the QEPAS measurement and the QTF characterization, the dead time between the two measurements must be quantified in order to minimize the characterization time. Let us calculate the decay time after an initial electrical excitation.

Using (3.13), the signal envelope can be written as :

$$Env(V_{out}(t)) = \hat{V}_{out} exp\left[-\frac{\pi f_0}{Q}(t - t_{exc})\right],\ (t > t_{exc}), \tag{3.20}$$

The initial signal amplitude is $\hat{V}_{out}$ at t_{exc} and decreases exponentially (Figure 3.23). The QTF energy is considered negligible below the threshold voltage V_{th}, reached at a time t_{relax} :

$$t_{relax} - t_{exc} = \tau\ ln\left(\frac{V_{out}}{V_{th}}\right) \tag{3.21}$$

Considering the typical QEPAS experiment for the detection of methane at 2.3µm as described in section 3.5, the limit of detection of 10ppmv corresponds to a LIA voltage of about 2µV, which can be used as a threshold voltage. For V_{th}=2µV, V_{exc}=0.1V, $\hat{V}_{out} = 0.6V$, we obtain :

$$t_{relax} - t_{exc} \approx 12\tau \tag{3.22}$$

The relaxation time takes 12τ, that is around 1s for Q=8000.

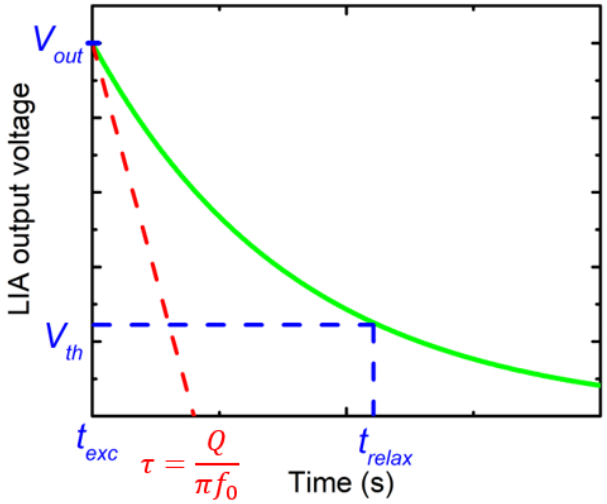

Figure 3.23 : Illustration of the signal envelope of the relaxation signal. At the end of the excitation ($t=t_{exc}$), the amplitude equals to V_{out}. It takes a time t_{relax}-t_{exc} for the envelope to reach the threshold voltage V_{th}.

3.6.2. Loading the QTF with a resonant impedance

The QTF is a mechanical harmonic oscillator. The moving parts can be represented as a simple mass-spring system; the losses are accounted by adding a damper. Now, if another damper is added in series, specifically of a higher value, the total losses of the system would necessarily decrease, having the *desired damping effect*. Due to its piezoelectric feature, the QTF motional behavior is equivalently represented by a series RLC circuit. However, the

charge collection on the quartz material with the electrodes create a parallel capacitance C_0. If the QTF is loaded with a resistance R_d ("an electrical damper"), it becomes in parallel with C_0. The energy stored in the motional RLC, instead of being absorbed by R_d, prefers to go through the resistance free C_0. As a simple damping resistor cannot interact with the QTF; the use of a more complex damping impedance has to be considered.

Let us try a metaphor. Two people, Laurent (L) and Cerruti (C), are playing a tennis match, throwing back and forth the ball. As they get tired, they shoot the ball slower and slower until the ball stops moving. If the two people do not get tired easily, the pace will decrease slowly. Now, if we add weigths (R_d) to the player's ankles, tiredness (R) will be increased. However, a friend Cechero (C_0) comes to watch Laurent and Cerruti playing and lifts the weights. Laurent and Cerruti can play with the same endurance thanks to Cechero. Then, another friends Lancelaud (Ld) arrives. They start a four player match with Laurent and Cerruti. Since Cechero carries the weights, his shots are slower, affecting the match pace. Cechero alone does not affect the match pace, but he does if Lancelaud is playing as well. Through this metaphor, we wish to illustrate that a single resistor cannot interact with the oscillating QTF. Another oscillatory system is required to enable interaction and thus a damping effect.

The observation of C_0 is decoupled from the motional RLC. By simply adding an inductance L_d, a parallel LC circuit is formed. Its resonance frequency $f_d=1/(2\pi L_d C_0)$ should match with f_0 to favor the energy transfer. For the QTF, it results in an excessively large inductance L_d of 2H. To lower L_d, we increased C_0 by adding another capacitor C_d in parallel (the damping capacitor). This new circuit shows a resonance at $f_d=1/(2\pi L_d(C_0+C_d))$. We named the term (C_d+C_0) the effective damping capacitance. The next step is to add losses to the damping circuit through a resistance R_d, in series with L_d. The value of R_d has a minimum due to the real coil intrinsic resistance. The final shape of the damping circuit is a R_dL_d–(C_0+C_d) (Figure 3.24) parallel impedance with a resonance $f_d=f_0$. The values of C_d and R_d will be further adjusted to maximize the QTF energy decay rate in section (3.6.5).

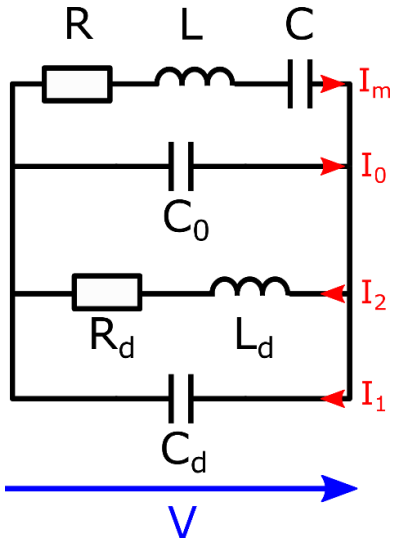

Figure 3.24: Electrical equivalent circuit of the QTF, that is a RLC in parallel with C_0, connected to the damping circuit, formed by a R_dL_d branch in parallel with the capacitance C_d and C_0.

3.6.3. SPICE electronics simulations

In order to optimize the damping circuit, some electrical simulations were carried out with the software OrCAD based on the SPICE simulator [35] (Simulation Program with Integrated Circuit Emphasis). SPICE was developed for testing integrated circuits before industrial production. SPICE aimed to replace breadboard circuit testing which can be inaccurate at a transistor level due to parasitic contribution of the board and the wiring. It allows the simulation of the time-domain and frequency-domain response of analog and digital circuits. The OrCAD library contains a wide range of components. Each one has a graphical representation that corresponds to a SPICE model. The components are inserted on a schematic and wired. The simulation typically starts by a DC analysis to calculate the operating point of each component.

Then, for AC analysis, nonlinear components such as transistors are simplified using a small signal linear model.

The schematic of the simulated circuit is shown on Figure 3.25. It includes the damping circuit, a sinewave voltage source, an electro-mechanical relay, the QTF equivalent model and the TA. The effect of the damping circuit is best observed using a transient simulation. First, the circuit is excited by the excitation source during 10ms. Then, the relay switches and the damping circuit starts interacting with the QTF. The results of the simulation contain the current and voltage at each node. The effect of the damping circuit is well described by displaying the QTF energy ($Li^2(t)+Cu^2(t)$) or the output of the amplifier. The latter is more relevant because it is the one practically measurable.

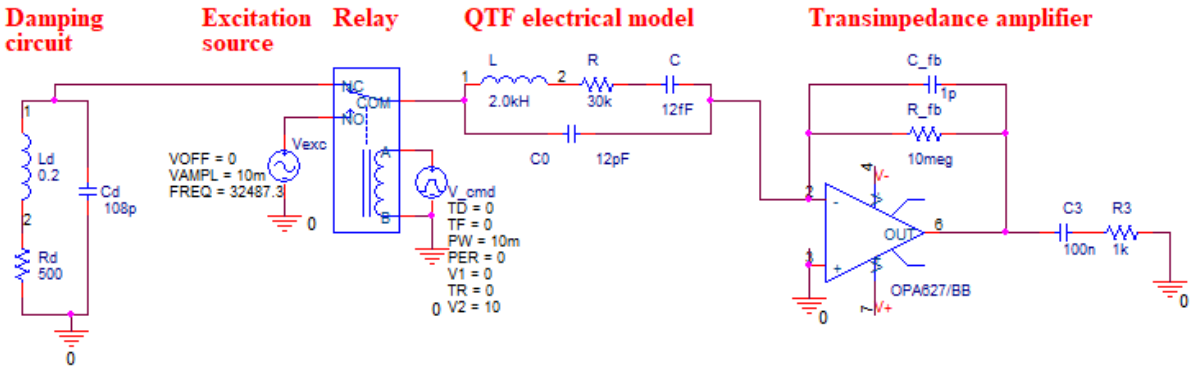

Figure 3.25 : Schematic of the electronics circuit on OrCAD Capture including the damping circuit, the excitation source, the switching relay, the QTF and the transimpedance amplifier.

In order to simulate the QTF response properly, timing must be considered. Similarly to a finite element analysis where the object under study is spatially discretized, forming a mesh, the circuit time response in SPICE is discretized temporally. The discrete timesteps must be small enough compared to the rate of change of the circuit, for instance much lower than the QTF oscillation period. Due to the high Q value, the QTF time constant is very long compared to its oscillation period ($\tau \cdot f_0 \approx 10\ 000$). During the simulation the energy transfer is approximated point by point. An inaccuracy in the calculated voltage will lead to a variation of the apparent f_0.

Taking 30 points per QTF period would give a time step of 1us. We simulated the QTF damped response with different timesteps around 1us (Figure 3.1). The response is highly affected by the simulation timestep, most particularly the signal offset after the transient regime (t > 30ms). The solution converges for timesteps higher than 500ns and the amplifier output voltage corresponds to the experimental value (1 to 10µV). Therefore, we selected a timesteps of 200ns for the simulations (section 3.6.5).

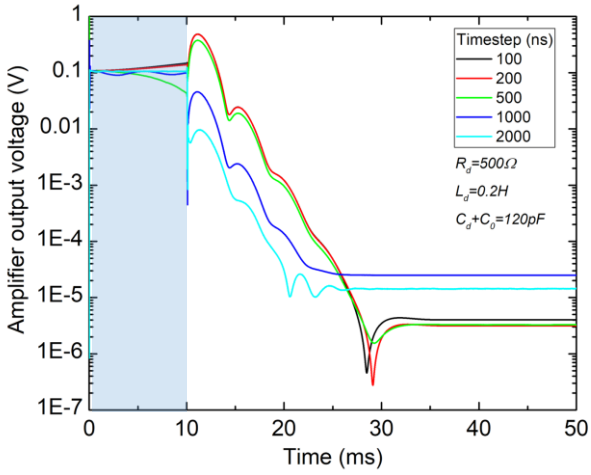

Figure 3.26 : Damped QTF relaxation for different PSPICE simulation timesteps. At t_{exc}=10ms, the electrical excitation is stopped and the QTF is connected to the damping circuit.

3.6.4. Measurement of the transfer function of the damping circuit

After the first attempts of coupling the damping circuits with the QTF, we realized that matching the resonance of the 2 components was not trivial. We thus decided to develop a setup to obtain the frequency response of the damping circuit. Different circuits based on a lock-in amplifier (MFLI, Zurich Instruments) were tested (Figure 3.27).

The circuit 1 is a simple voltage divider. In this case the circuit is excited with a given voltage (1mV$_{rms}$) and the current is measured through a load resistance (10kΩ). The damping circuit works as a stop band filter (blue curve on Figure 3.27(d)). However, the damping circuit is connected in parallel with the QTF, therefore the admittance is to be considered instead of the impedance.

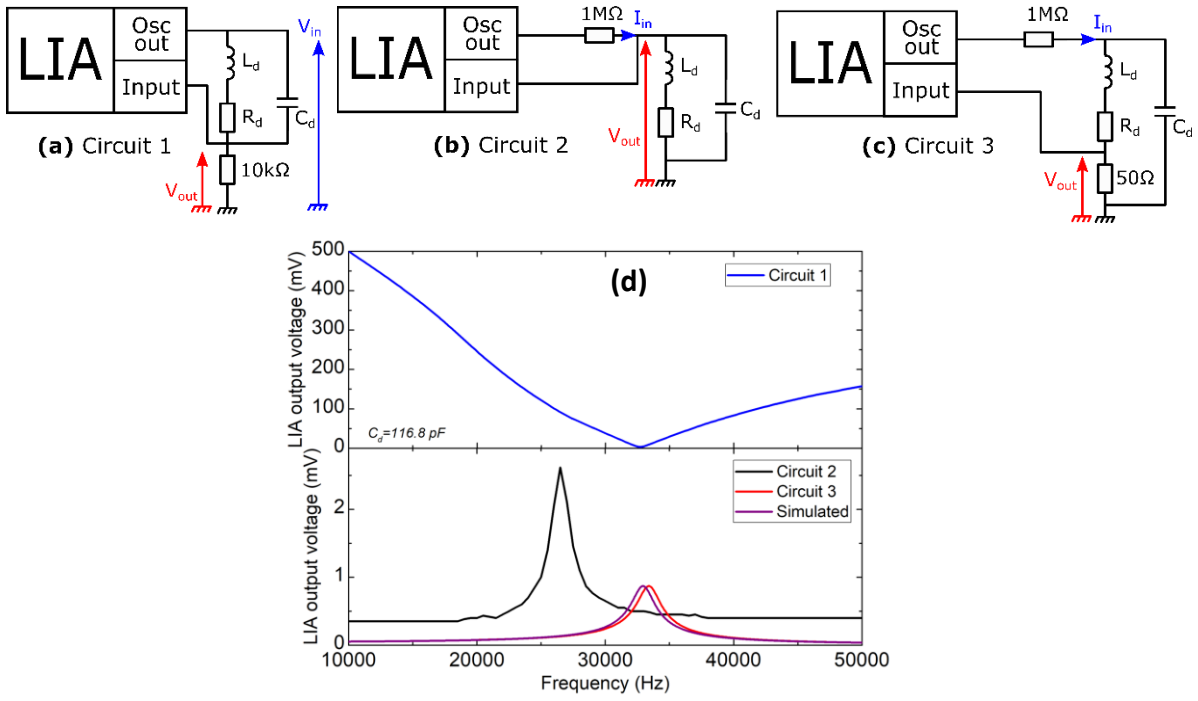

Figure 3.27 : Different circuits employed for the characterization of the damping circuit, based on a voltage divider (a) or a constant current source (b-c). (d) The response of the three circuits (a), (b) and (c) are shown as the blue, black and red curves, resp. The values of the components are: Rd=1kΩ, Ld=0.2H (Cd+C0)=116.8pF. The PSPICE simulated response is also shown (purple).

In the circuit 2, a 1MΩ resistor is added to make a constant current source and the voltage is measured at the damping circuit outputs. The admittance corresponds well to a pass-band filter, but the peak was shifted in frequency (black curve). It was explained by the BNC cable equivalent capacitance of about 30pF that was not negligible compared to the damping capacitance. This issue was circumvented by inserting a 50Ω resistance in the RL branch. Since all impedances were proportional to the current in the branch, reading the current through the 50Ω gave us a direct access to the voltage. The circuit behavior was unaffected by the 50Ω resistor that was low compared to the damping resistor. Alternatively, the issue could have been solved by using a well-calibrated oscilloscope test probe.

Eventually, with the circuit 3, we obtained a peak (red curve) matching well with the QTF resonance and corresponding to the response simulated on PSPICE (purple curve). Above all, this step of characterizing the lone damping circuit helped us to identify the critical part of the circuit: the damping capacitor. Indeed since the circuit is parallel to the QTF, any component between the two elements can add parasitic capacitances and thereby shifting the damping circuit resonance. A mindful design of a PCB can considerably minimize this risk.

3.6.5. Optimizing the damping resistor and capacitor

In this section, we focus on the maximization of the QTF decay rate. The damping circuit is a parallel R_dL_d–(C_0+C_d) circuit with a fixed value of 0.2H for the inductor. Therefore, the optimization is done by adjusting the values of the resistor and the capacitor.

On Figure 3.28, the results for both the simulation and the experiment are compared. The QTF is excited electrically during about 10ms (blue area). Then, the electrical excitation is stopped and the QTF is connected to the damping circuit.

As expected, the fastest decay is obtained when the QTF and the damping circuit are resonantly matched, corresponding to C_d+C_0=120pF theoretically (Figure 3.28(a)) and obtained when C_d=108pF experimentally (Figure 3.28(b)) (C_0 is not mentioned as it is difficult to measure it with an accuracy that is good enough). Small variations of less than 1 pico farad greatly affect the damping effect, confirming the importance of eliminating any parasitic capacitance, as discussed in section 3.6.4. Illustrating the troubles we encountered, we first used variable capacitor in order to tune C_d. Upon touching the variable capacitor adjustment screw with a screwdriver, a parallel capacitance was added to the system, shifting the resonance, and thus hindering the damping effect. In terms of damping resistance, at low values, an interference pattern can be observed (Figure 3.28(c)). The optimum decay time is simulated for a resistance around 500Ω, which happened to correspond to the intrinsic resistance of the damping inductor. Higher R_d value leads to less damping, as observed experimentally.

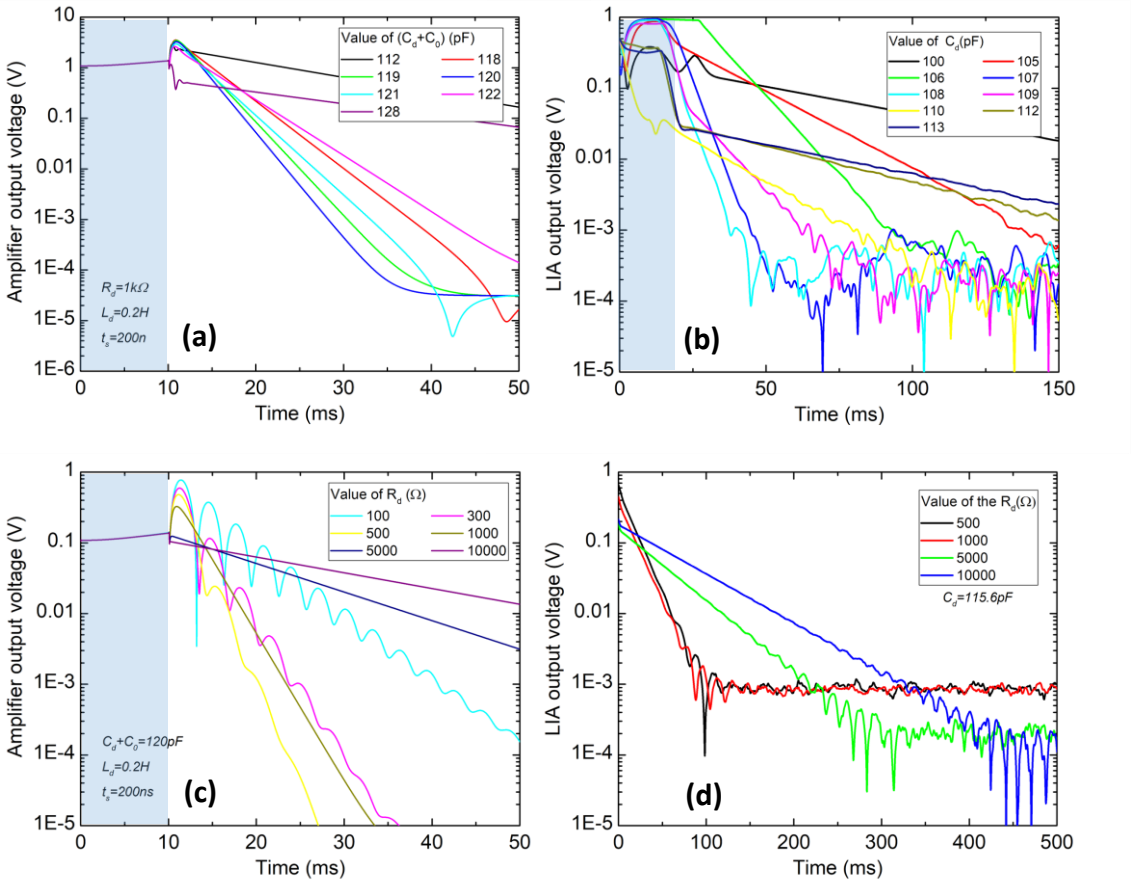

Figure 3.28 : Simulated (left) and experimental (right) QTF response with the damping circuit while varying the damping capacitance (a-b) (with Rd=500Ω) and the effective damping resistance (c-d) (with C_d+C_0=120pF). The electrical excitation occurs during about 10ms as represented by the blue area. Then, the electrical excitation is stopped and the QTF is connected to the damping circuit.

As we focus on the damping effect, it is more convenient to represent the same results in terms of decay time (Figure 3.29). The 1-decade decay time τ_d is the inverse of the slope on a logarithmic scale, and represents the time spent for a 1-decade signal drop. It follows a parabolic behavior as a function of the damping capacitance with an optimum value $\tau_{d,opt}$ .corresponding to the minimum value of the parabola. The position of the parabola vertex is similar for the experiment and the simulation. However, the experiment is more sensitive to the effective damping capacitance than the simulation, that made us question our simulation parameters and the true behavior of the components. In order to assess the validity of our simulations, we developed an analytical model of the damping circuit.

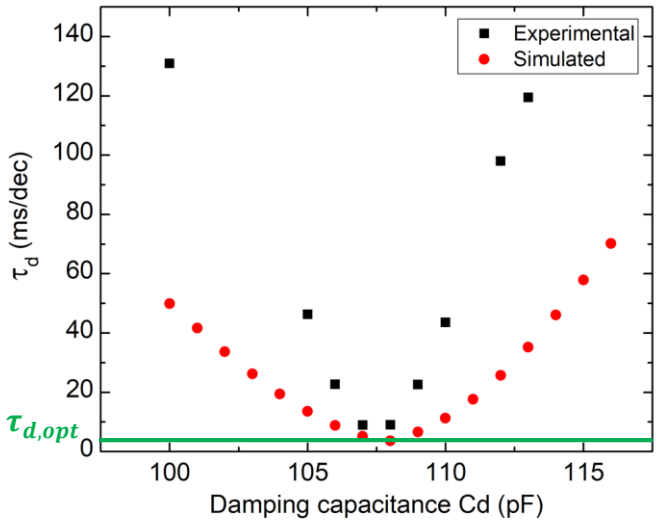

Figure 3.29 : 1-decade decay time as a function of the damping capacitance, for the PSPICE simulation (red dots) and the experiment (black square). Compared to Figure 3.28, the values of the damping circuit for the simulation are adjusted to match the experimental resonance. $\tau_{d,\,opt}$ represents the minimum damping time.

3.6.6. Passive vibration damping

The analytical study we present here focuses on the optimization of the damping circuit. It is based on a similar work [36] in which a piezo patch is mechanically bonded to a cantilever to reduce his movement through passive electrical damping.

The QTF is represented by the BVD equivalent model (Figure 3.30), with a motional branch RLC and the electrodes capacitance C_0. The damping circuit is a parallel R_dL_d–C_d circuit.

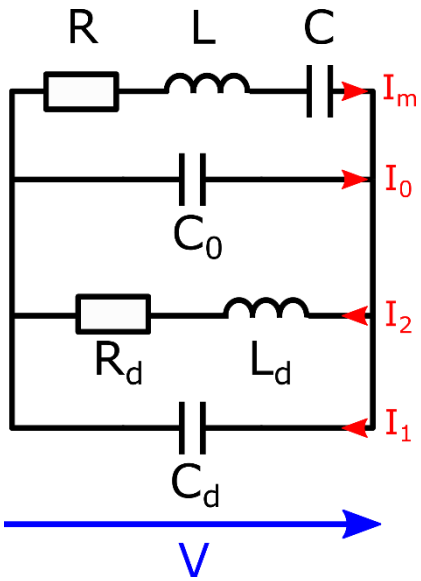

Figure 3.30: Schematic of the QTF and the damping circuit.

First, writing Kirchhoff's voltage law for the QTF motional branch and the R_dL_d branch:

$$L\ddot{q}_m + R\dot{q}_m + \frac{1}{C}q_m + V = 0 \tag{3.23}$$

$$L_d\ddot{q}_2 + R_d\dot{q}_2 - V = 0 \tag{3.24}$$

As a convention, the derivative of the charge is considered to have the same sign as the current:

$$\dot{q}_\iota = I_i \tag{3.25}$$

The charge stored in the QTF is the sum of the contributions from the RLC and the C_0 branch:

$$q = q_m + q_0 = q_m - C_0V \tag{3.26}$$

And similarly for the damping circuit:

$$q = q_1 + q_2 = C_dV + q_2 \tag{3.27}$$

Using (3.26) and (3.27), the voltage can be obtained as a function of q_m and q_2 :

$$V = \frac{q_m - q_2}{C_0 + C_d} \tag{3.28}$$

Making the variable change $\alpha=C_d/C_0$ in (3.23) and (3.24), and using (3.28), we obtain a system of coupled differential equations:

$$L\ddot{q}_m + R\dot{q}_m + \left(\frac{1}{C} + \frac{1}{C_0(1+\alpha)}\right)q_m + \frac{1}{C_0(1+\alpha)}q_2 = 0 \tag{3.29}$$

$$L_d\ddot{q}_2 + R_d\dot{q}_2 + \frac{1}{C_0(1+\alpha)}q_2 - \frac{1}{C_0(1+\alpha)}q_m = 0 \tag{3.30}$$

Normalizing the system and making a variable change on the time $T = t\omega_m$ (so that $f(T) = f(t)$, $\dot{f}(T) = \dot{f}(t)/\omega_m$ and $\ddot{\dot{f}}(T) = \ddot{f}(t)/\omega_m^2$) :

$$\ddot{Q}_m + 2\nu\dot{Q}_m + (1+\kappa^2)Q_m + \kappa\omega_rQ_2 = 0 \tag{3.31}$$

$$\ddot{Q}_2 + 2\rho\omega_r\dot{Q}_2 + \omega_r^2Q_2 - \kappa\omega_rQ_m = 0 \tag{3.32}$$

with:

$$Q_m = q_m\sqrt{L} \quad Q_2 = q_2\sqrt{L_d} \quad T = t\omega_m$$

$$\nu = \frac{1}{2}R\sqrt{\frac{C}{L}} \quad \omega_m = \frac{1}{\sqrt{LC}} \quad \rho = \frac{1}{2}R_d\sqrt{\frac{C_0(1+\alpha)}{L_d}} \quad \omega_d = \frac{1}{\sqrt{L_dC_0(1+\alpha)}}$$

$$\kappa = \sqrt{\frac{C}{C_0(1+\alpha)}} \quad \omega_r = \frac{\omega_d}{\omega_m}$$

Where T, Q_m and Q_2 represents the dimensionless t, q_m and q_2. ν is the QTF mechanical dissipation, ω_m the angular resonant frequency of the QTF, ρ the electrical dissipation of the damping circuit, ω_d the angular resonant frequency of the damping circuit, κ is the piezoelectric coupling coefficient, and ω_r is the ratio of the electrical (damping) resonance to the mechanical resonance.

Then the solution of the fourth order system can be written as:

$$Q_m = \sum_{i=1}^{4} C_i \exp(\Lambda_i T) \tag{3.33}$$

with Λ_i the complex roots of the characteristic equation of the system of differential equations and C_i are polynomials of the variable T which depend on the initial conditions.

Then the system is optimized using the pole placement technique, the procedure is explained in [36]. Briefly, the solution (3.33) is inserted in (3.31) and (3.32). The characteristic equation of the system is calculated with the determinant of the coefficient matrix. Then the fourth-order polynomial is factorized. This factorization is valid for certain values of κ and ν. These assumptions are always valid for our system where the Q factor of the QTF is large compared to the Q factor of the damping circuit, and also the QTF capacitance is low compared to the electrode capacitance ($C << C_0$). The roots of the factorized characteristic equation gives the values $\omega_{r,opt}$ and ρ_{opt} which maximize the decay rate :

$$\omega_{r,opt} = 1 + \kappa^2 + \kappa\nu\sqrt{1+\kappa^2} \tag{3.34}$$

$$\rho_{opt} = \frac{\kappa}{1+\kappa^2} + \frac{1}{1+\kappa^2}\nu \tag{3.35}$$

$$\Lambda_{opt} = \frac{\kappa}{2}\sqrt{1+\kappa^2} + \left(1 + \frac{\kappa^2}{2}\right)\nu \tag{3.36}$$

For the QTF, it is reasonable to make the assumption that $1 \gg \kappa \gg \nu$, the previous equations can be simplified :

$$\omega_{r,opt} = 1 \tag{3.37}$$

$$\rho_{opt} = \kappa \tag{3.38}$$

$$\Lambda_{opt} = \frac{\kappa}{2} \tag{3.39}$$

Eventually, the optimized values of the damping resistance and inductance can be obtained using (3.37) and (3.38):

$$R_{d,opt} = 2\kappa\sqrt{\frac{L}{C_0(1+\alpha)}} \tag{3.40}$$

$$L_{d,opt} = L\kappa^2 \tag{3.41}$$

From (3.39), the optimum 1-decade decay time can be expressed :

$$\tau_{d,opt} = \frac{2\ln(10)}{\kappa\omega_m} = \frac{2\ln(10)}{\omega_m}\sqrt{\frac{C_0(1+\alpha)}{C}} \tag{3.42}$$

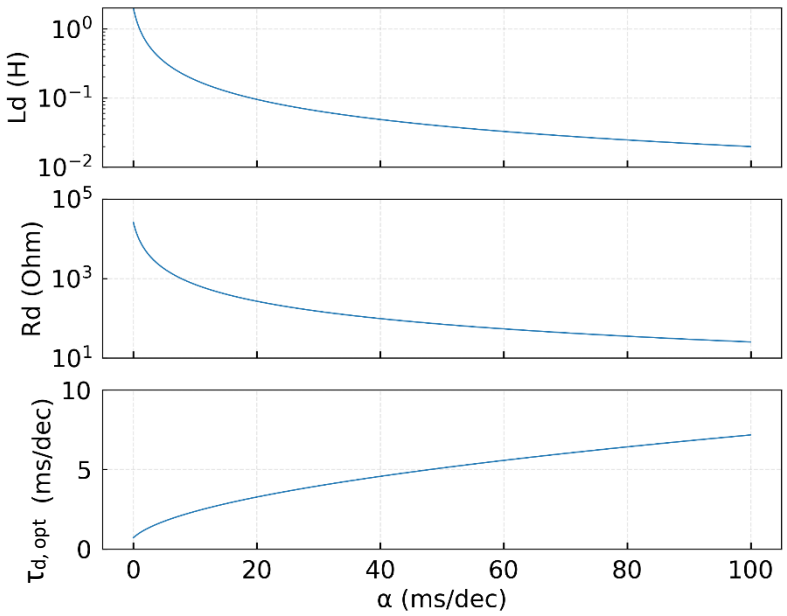

Figure 3.31 : Evolution of the optimum damping inductance, resistance and 1-decade decay time as a function of α. (R=30kΩ, L=2kH, C=12fF, C_0=12pF)

The optimum parameters are plotted on Figure 3.31 as a function of α. R_d and L_d are decreasing with α while the decay time increases. The decrease of L_d with increasing of α (equivalently C_d), is necessary to ensure the resonant condition of the damping circuit ($\omega_e=\omega_m$). The variation of R_d can be understood in terms of losses. A damping circuit with low losses will not quickly absorb the charges from the QTF, while a damping circuit with high losses will not interact with the QTF efficiently as the charges will bypass the RL through the parallel capacitance. Therefore, R_d has an optimum value, which appears to be inversely proportional to the damping capacitance. Oppositely, the decay time is proportional to the square root of alpha. For a typical setup with the QTF for which α = 9, the decay time equals to 2.3ms/dec, only about three times longer than the optimum value when α = 0. Those results are in very good agreement with the simulation, from which a decay time of 3.4ms/dec was obtained.

The analytical study is comparable to the simulation in terms of optimal values. However, the study does not give any information concerning the decay time for non-optimal value. Indeed, since the damping circuit is resonantly pulling the energy out of the QTF, the variation of the damping capacitance or inductance would lead to a shift of the damping resonance and a longer decay time. In this regard, the PSPICE simulation provides complementary information to the analytical study.

3.6.7. Adjusting the QTF electrical parameters

The effect of the damping circuit was simulated based on the values of the QTF electrical equivalent model, the Butterworth Von Dyke model (Figure 3.24). However, after observing the discrepancy between the experiment and the simulation about the effect of the damping

capacitance (Figure 3.29), the values of the BVD model, obtained from the fit of the frequency response, were questionable.

The frequency response of the QTF was measured as described in section 3.2.1.1 (Figure 3.3) and can be expressed as the product of the input excitation voltage V_{exc}, the QTF admittance Y_{QTF} (=1/Z_{QTF}) and the gain of the transimpedance amplifier G_{TA}:

$$V_{amp}(\omega) = V_{exc}(\omega)\, Y_{QTF}(\omega)\, G_{TA}(\omega) \tag{3.43}$$

The measured response can be fitted by the nonlinear function V_{amp}. Direct non linear fitting of a narrow frequency response is difficult. To ensure the convergence of the fit, the fitting procedure was made of two steps: a 'rough' fit and a 'fine' fit. The rough fit starts by finding the resonant frequency f_0 and the quality factor Q, by finding the maximum and the FWHM of the response, resp. It allows to deduce the value of L and C. Only R, C_0 and G_{TA} are fed as variables to the fitting algorithm, which facilitates its convergence. The results of the rough fit are then fed as initial parameters for the fine fit. The fine fit uses the function from (3.43) with a set of 5 unknown parameters of (R, L, C, C_0, G_{TA}) to fit the experimental data with greater accuracy than the rough fit.

We remarked that the initial value of gain G_{TA} provided to the rough fit had a serious impact on the output fitted parameters (Figure 3.32). For different initial values of the gain (left column), different sets of fitted parameters were obtained, even though all the sets provide a good fit of the data, as indicated by the values of the deduced parameters.

Initial gain	Fitted parameters					Deduced parameters	
	R (Ω)	L (H)	C (F)	C0 (F)	gain	f0 (Hz)	Q
1.00E+06	30.65E+03	1.90E+03	12.41E-15	7.27E-12	9.08E+06	32758.05	12770
5.00E+06	6.85E+03	424.84E+00	55.56E-15	32.55E-12	2.03E+06	32758.05	12770
1.00E+07	8.50E+03	527.24E+00	44.77E-15	26.23E-12	2.52E+06	32758.05	12770
5.00E+07	16.64E+03	1.03E+03	22.86E-15	13.39E-12	4.93E+06	32758.05	12770
1.00E+08	29.03E+03	1.80E+03	13.10E-15	7.68E-12	8.60E+06	32758.05	12770
5.00E+08	75.51E+03	4.69E+03	5.04E-15	2.95E-12	2.24E+07	32758.05	12770
1.00E+09	92.75E+03	5.75E+03	4.10E-15	2.40E-12	2.75E+07	32758.05	12770
5.00E+09	204.57E+03	12.69E+03	1.86E-15	1.09E-12	6.06E+07	32758.05	12770

Figure 3.32: Fitted parameters obtained with a different value of the initial gain. f_0 and Q are deduced from the fitted parameters. The initial value of the gain does not ensure the validity of the parameters as the fitted value of the gain is generally an order below the initial gain.

One solution would be to improve the fitting algorithm to better match the initial gain. Another solution is to select the fit that matches the known value of the TA gain. In our case, we know the value of the gain ($G_{TA} = 3 \cdot 10^7$ at 32kHz) and we can deduce the value of the BVD model (red square).

With the new set of QTF parameters (model B), we re optimized the damping circuit (Figure 3.33). Compared to the original model (model A), the value of the parasitic capacitance C_0 decreased by a factor 6.

The value of the damping inductance L_d and the resonant frequency ω_m are fixed, thus the value of C_d is the same in both models. C_d stays at the same value, but C_0 decreases, which results in an increase of the capacitance ratio $\alpha = C_d / C_0$ by a factor 6 for the model B compared to A ($\alpha_B/\alpha_A \approx 6$). Consequently, the optimum damping resistance is approximately divided by 2, and the optimum decay time is approximately doubled.

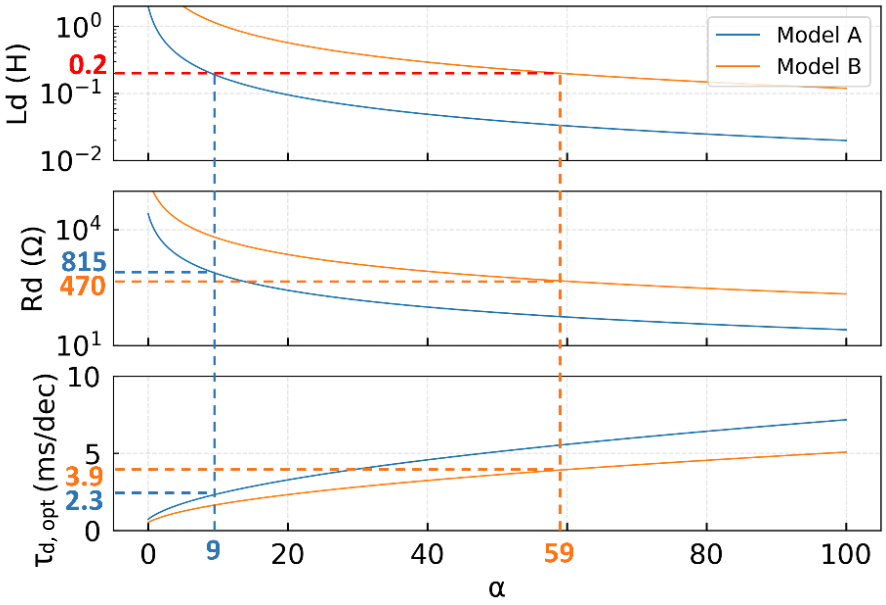

Figure 3.33: Evolution of the optimum damping inductance, resistance and 1-decade decay time as a function of α for the model A (R=30kΩ, L=2kH, C=12fF, C_0=12pF) and the model B (R=100kΩ, L=6kH, C=4fF, C_0=2pF)

The change in the parasitic capacitance C_0 has an effect on the optimum damping time $\tau_{d,opt}$, but more importantly onto the evolution of the decay time τ_d (Figure 3.34).

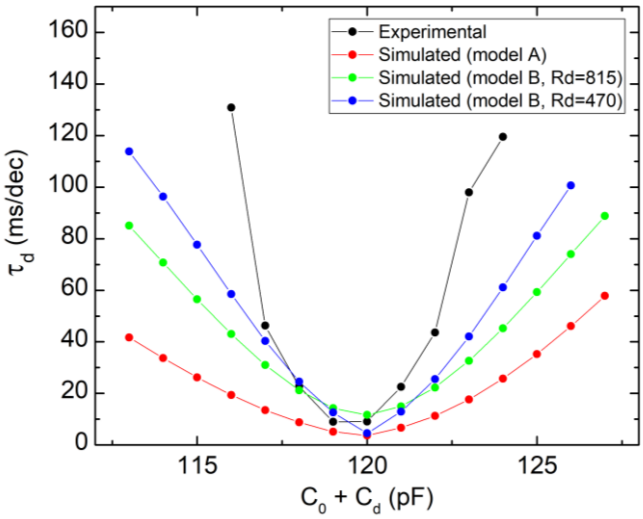

Figure 3.34 : Evolution of decay time as a function of the effective damping capacitance, comparing the experiment with the different simulations.

The lower the C_0, the higher the α, the more sensitive the system to the variation of the damping capacitance C_d. The corrected QTF parameters (model B) yields a curve (blue) that fits better the experimental results (black) than the original model A (red). In the model B, the value of C_0 is 4pF, which is very low, and could still have some contribution from the characterization setup. Even though the cable length between the damping circuit and the QTF was minimized, the circuit might have contributed to the measured parasitic capacitance.

Therefore, the practical value of α was probably higher than 60, which might explain why the experimental data change faster than the curve for the model B.

The only solution to decrease the α is to change the value of the damping inductance. Nonetheless, the value of L_d was discussed earlier and purposely chosen to be 0.2H to have acceptable physical dimensions. We can conclude that we are very close to the theoretical limitations of the damping circuit.

3.6.8. Switching devices

So far, we have focused on the effect of the damping circuit onto the QTF and demonstrated that it can considerably decrease the QTF relaxation time. The next step was to include the damping circuit into the architecture of the RT-QEPAS (step 4 on Figure 3.21). In the first RT-QEPAS experiments, we employed an electromechanical relay as a switching device to alternate between the QTF excitation and relaxation. The electromechanical relay was chosen at first because it was simple to implement and it ensured a minimal crosstalk between the excitation source and the QTF. Indeed, the relay is a switch whose contacts are mechanically separated, ensuring the circuit is physically open, oppositely for instance to a transistor which can suffer from leakage currents. Although the electromechanical relay has no leakage current, it causes a parasitic current pulse upon switching, that results in an unwanted QTF re excitation. The parasitic current pulse is barely observable while monitoring the QTF free relaxation but it is not the case with the damped relaxation. After the QTF is discharged, the damping circuit needs to be disconnected from the QTF without re exciting it, which was not feasible using the relay.

We present here an attempt to lower the switching parasitic excitation by replacing the mechanical action of the relay with a purely electrical switching, either based on an analog switch, or based on a MOSFET device.

The switching device has to fulfill one main requirement, that is to have a low crosstalk level between the excitation source and the QTF. We first employed an analog switch (ADG736) that was selected to have a low ON resistance ($R_{ON}\approx 2.5\Omega$), a low OFF leakage current (10pA) and a low channel-to-channel crosstalk (-82dB). During the first experiments on a test board, we observed the damping effect but we were limited by the electromagnetic radiation and could not assess the crosstalk of the analog switch. To overcome this, we fabricated a PCB (Figure 3.35) and mounted the damping circuit along with an analog switch and a reed relay. SMA connectors were used to connect the QTF and the excitation source. The damping circuit was made of 2 inductors (0.1H), a resistor (1kΩ) and variable capacitors. Variable capacitors were used to adjust the resonance of the damping circuit, in particular because the analog switch and the coaxial cable bring additional parallel capacitances that sums up with the capacitance of the damping circuit and create a shift of its resonance.

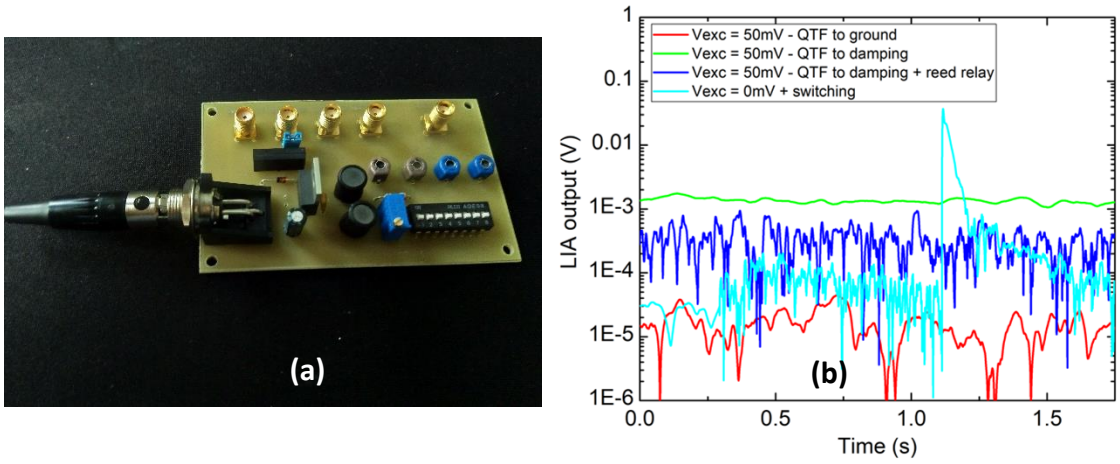

Figure 3.35: (a) Picture of the printed circuit board hosting the damping circuit and the analog switch. (b) Lock-in amplifier signal obtained for different configurations of the damping circuit.

In order to evaluate the crosstalk of the circuit, the damping circuit was tested in different conditions (Figure 3.35(a)) and we observed the voltage level at the output of the lock-in amplifier. First, the excitation source was set to 50 mV and the QTF was connected to the ground, a noise level of about 10^{-4}-10^{-5}V was obtained (red curve on Figure 3.35(a)), corresponding to the thermal noise of the QTF. Then the QTF was connected to the damping circuit, leading to a voltage level of 10^{-3}V (green curve), indicating crosstalk from the excitation source. Further experiments would be needed to indicate if the crosstalk is due to the PCB or due to the analog switch, for instance by desoldering the analog switch. Finally, the excitation voltage was set to 0 mV and the analog switch was turned on (light blue curve). A parasitic current pulse of about 30mV was observed. It allowed us to attribute the re excitation of the QTF observed during some of the previous RT QEPAS experiments to the switching of the analog switch.

The analog switch is a device made of passive components, mostly transistors. In order to tailor the behavior of our switching device and obtain a 'silent' switching, we developed another circuit based on a MOSFET.

Compared to the analog switch that has multiple inputs and outputs, the MOSFET can only be used as a two-port switch. It cannot completely replace the analog switch, but can be employed where the analog switch failed to its purposes, that is to disconnect 'silently' the damping circuit. To this end, we placed the transistor placed inside the RL branch of the damping circuit (Figure 3.36(a)), thus obtaining a voltage-controlled damping resistor. The selected transistor is a p-channel enhancement MOSFET (ZVP2106A) meaning the current is allowed to pass from the drain to the source, when the gate voltage is strictly negative ($V_{GS}<0$). If the gate voltage V_{GS} is positive, the drain-source resistance (R_{DS}) is high, so the damping circuit is inactive. Oppositely, if V_{GS} is negative, R_{DS} is very small compared to the damping resistor R_d, so the damping circuit is active.

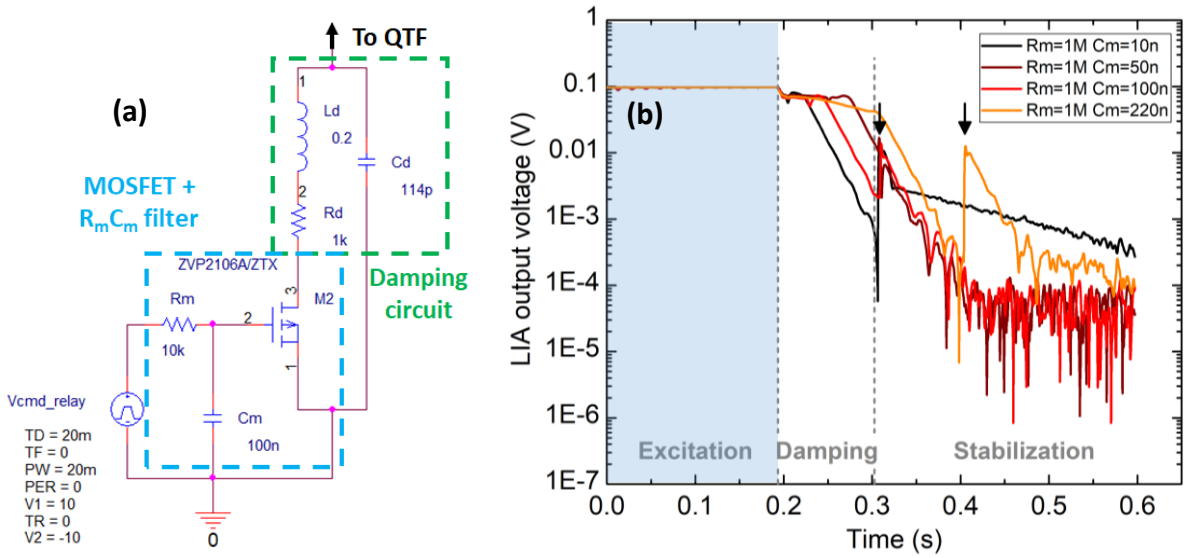

Figure 3.36: (a) PSPICE schematic of the of the damping circuit and the MOSFET inserted in the RL branch. The MOSFET gate is driven by a voltage source connected to a low pass RC filter. (b) Observing the QTF response to damping for different values of the filter capacitance C_m. The damping is enabled just after the end of the excitation by applying a negative voltage to the MOSFET gate. The arrows indicate the moment the MOSFET was turned off, that is 100ms after the onset of the damping, except for the orange curve, for which the MOSFET was triggered lately due to the high value of C_m.

The damping circuit is driven by the voltage at the MOSFET gate (V_{GS}). When the MOSFET is polarized, charges accumulate inside the gate. The charges might leak into the source upon changing the polarization. In order to smooth this parasitic effect and avoid QTF re excitation, a low pass R_mC_m filter was added before the MOSFET gate. The resistance R_m is chosen to be 1MΩ to have a low gate current. To adjust the triggering delay of the MOSFET, different capacitance values C_m were tested and the response of the QTF with the damping circuit was observed (Figure 3.36(b)).

The QTF is first excited, then discharged by the damping circuit and finally the damping circuit is disabled and the QTF is let free for stabilization. When C_m is low (black), the RC filter constant is small, so is the smoothing effect of the low pass filter, causing the QTF to be re excited by the fast pulse, as indicated by the slowly decaying slope driven by the QTF free relaxation. When C_m is high (orange), the RC filter constant is large, and the pulse is delayed. When C_m is ideally chosen (brown and red), the pulse does not provoke the QTF re excitation and allows to maintain the desired damping effect. It can be seen that the signal has reached the noise floor (10^{-4}-10^{-5}V), about 200ms after the onset of the damping.

3.6.9. Demonstration of the effective damping of the QTF

We have just presented a circuit based on a MOSFET as a switching device in order to minimize the QTF switching time after the damping, while preventing the QTF re excitation. Next, we integrate the damping circuit into the RT QEPAS experiment as a proof of concept.

Since the purpose of this proof of concept is to reach the smallest QTF characterization time, we modified the Labview program, suppressing the acquisition of the BF signal and the post processing actions. Consequently, the timing was not software limited. The data

acquisition was directly done through the interface of the lock-in amplifier (Zurich Instruments LabOne using the data acquisition module).

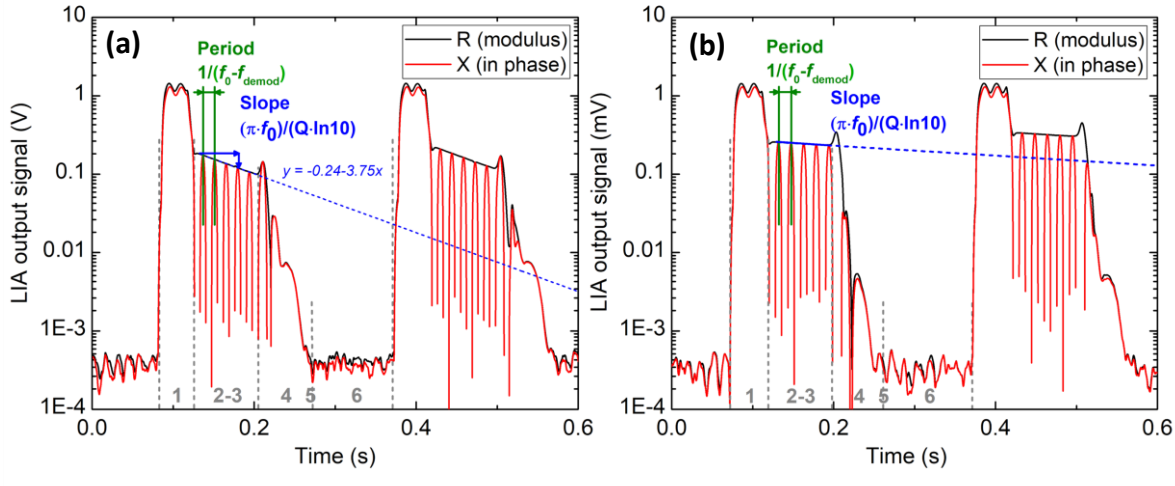

RT-QEPAS sequence:	
1. Excite the QTF	4. Force the QTF discharge
2. Record BF relaxation signal	5. Adjust the modulation frequency
3. Find f_0 &Q	6. Measure the gas concentration
	QEPAS (here the laser is off) **(c)**

Figure 3.37 : Monitoring the lock-in amplifier signal during a complete RT-QEPAS cycles with 2 QTFs having Q factors of 12000 (a) and 71000 (b). The amplitude and in-phase component are represented in black and red, resp. The RT-QEPAS sequence is made of 6 steps as listed in (c). The QTF parameters can be obtained from step 3. The QTF free relaxation exponential decay is indicated by the blue dotted line.

The results are presented on Figure 3.37. 2 QTFs with different quality factors were tested during a complete RT-QEPAS sequence as described on Figure 3.37(c). The sequence was successfully achieved in 200ms.

It must be noted that the excitation time was limited by the relay switching time which took about 50ms instead of a few ms required to excite the QTF. The BF signal was recorded for 70ms and could probably be even shorter. It was used to deduce the QTF parameters, as represented on the graph: f_0 the inverse of the period of the LIA in-phase signal (green) and Q related to the slope of the LIA signal amplitude (blue). The slope can be extrapolated to image the free relaxation of the QTF (blue dotted line), which is very slowly decaying compared to the damped relaxation (step 5) taking only about 70ms. The measured QTF resonant frequency is then used to adjust the laser modulation frequency, and the QEPAS can be started right after. The photoacoustic could not be tested as the laser had not been implemented in the setup. The time spent for the QEPAS measurement (step 6) can be adjusted depending on the application and should be as long as possible to increase the integration time, and therefore decrease the limit of detection. In this experiment, the step 6 is made short (100ms) to demonstrate that the QTF is well at rest after the damping and that the QTF characterization can be re started. 2 complete cycles are represented, showing very good repeatability and a similar damping time for the 2 different Q values.

In summary, we presented here the first proof of concept involving the complete sequence of the RT QEPAS architecture. Notably, we were able to achieve the full QTF characterization in a very short time (about 200ms), which will allow to have a longer integration time for the QEPAS measurement and therefore a lower limit of detection.

3.7. Conclusion

The QTF is a key element in a QEPAS gas sensor. It allows to detect very low concentration of gases, but its resonance can be affected by the variability of the environment. In this chapter, we described the development of a setup for real time characterization of the QTF resonance. We analyzed thoroughly the different techniques for measuring the QTF parameters. The sharp frequency response of the QTF makes it difficult to obtain a good accuracy on both the resonant frequency and the quality factor.

After comparison of the techniques, we concluded that the Beat Frequency measurement, based on an electrical excitation, offers a good compromise between the measurement time and the measurement accuracy. The BF technique has considerable advantages: simultaneous measurement of f_0 and Q, constant excitation amplitude and use of QEPAS conventional benchtop instruments. We developed an experimental setup, optimized it and verified its performances by observing the influence of the temperature and the humidity onto the QTF resonance. Then, we implemented the QTF characterization in a feedback loop in order to ensure the resonance tracking of the QTF. We presented a proof of concept of the Resonance Tracking-QEPAS with the detection of CH_4, and showed a consistent reduction of the signal drift.

The main limitation of the QTF characterization based on the transient response stems from the long QTF response time. We overcome this limitation by designing a damping circuit, that quickly absorbs the QTF energy and drastically reduces the discharge time. We optimized the circuit based on electronics simulations and tested it experimentally. It allowed us to improve the QTF discharge time from about 1s to less than 100ms using the damping circuit. Eventually, we successfully implemented the damping circuit in the RT-QEPAS architecture as a proof of concept and a motivation to continue the topic. Future work will concern the operation of RT-QEPAS in combination with the photoacoustic detection and the evaluation of its performances in various environmental conditions. Also, as the damping circuit best performs close to the QTF, it would be interesting to realize its integration onto the QEPAS electronic board.

3.8. References

1. Wu, H.; Dong, L.; Zheng, H.; Yu, Y.; Ma, W.; Zhang, L.; Yin, W.; Xiao, L.; Jia, S.; Tittel, F.K. Beat frequency quartz-enhanced photoacoustic spectroscopy for fast and calibration-free continuous trace-gas monitoring. *Nat. Commun.* **2017**, *8*, 1–8.
2. International Organization for Standardization, I. 5725-1:1994 Accuracy (trueness and precision) of measurement methods and results — Part 1: General principles and definitions.
3. Aoust, G. Developpements de sources infrarouges et de resonateurs en quartz pour la spectroscopie photoacoustique, Paris-Saclay, 2016.
4. Bosseboeuf, A.; Mathias, H. Experimental Techniques for Damping Characterization of Micro and Nanostructures. In *Advances In Multiphysics Simulation And Experimental Testing Of MEMS*; 2008; pp. 183–233.
5. Peterson, B. Keysight Technologies Spectrum Analysis Basics. **2013**.
6. Matsiev, L.F. Application of flexural mechanical resonators to simultaneous measurements of liquid density and viscosity. *Proc. IEEE Ultrason. Symp.* **1999**, *1*, 457–460.
7. Scandurra, G.; Cannata, G.; Giusi, G.; Ciofi, C. A simple and effective testbench for quartz tuning fork characterization and sensing applications. In Proceedings of the 2015 IEEE International Instrumentation and Measurement Technology Conference (I2MTC) Proceedings; IEEE, Ed.; 2015; pp. 1871–1876.
8. Petersan, P.J.; Anlage, S.M. Measurement of resonant frequency and quality factor of microwave resonators: Comparison of methods. *J. Appl. Phys.* **1998**, *84*, 3392–3402.
9. Marshall, W.J.; Brigham, G.A. Determining equivalent circuit parameters for low figure of merit transducers. *Acoust. Res. Lett. Online* **2004**, *5*, 106–110.
10. Manzaneque, T.; Hernando, J.; Rodríguez-Aragón, L.; Ababneh, A.; Seidel, H.; Schmid, U.; Sánchez-Rojas, J.L. Analysis of the quality factor of AlN-actuated micro-resonators in air and liquid. *Microsyst. Technol.* **2010**, *16*, 837–845.
11. Gyüre, B.; Márkus, B.G.; Bernáth, B.; Murányi, F.; Simon, F. A time domain based method for the accurate measurement of Q-factor and resonance frequency of microwave resonators. *Rev. Sci. Instrum.* **2015**, *86*, 094702.
12. Gyure-Garami, B.; Sagi, O.; Markus, B.G.; Simon, F. Supplementary Material for : A highly accurate measurement of resonator Q -factor and resonance frequency. *Rev. Sci. Instrum.* **2018**, *89*, 113903.
13. Inoue, R.; Miwa, K.; Kitano, H.; Maeda, A.; Odate, Y.; Tanabe, E. Highly accurate and real-time determination of resonant characteristics: Complex linear regression of the transmission coefficient. *IEEE Trans. Microw. Theory Tech.* **2004**, *52*, 2163–2168.
14. Grober, R.D.; Acimovic, J.; Schuck, J.; Hessman, D.; Kindlemann, P.J.; Hespanha, J.; Morse, A.S. Fundamental limits to force detection using quartz tuning forks. *Rev. Sci. Instrum.* **2000**, *71*, 2776–2780.
15. Smit, R.H.M.; Grande, R.; Lasanta, B.; Riquelme, J.J.; Rubio-Bollinger, G.; Agraït, N. A low temperature scanning tunneling microscope for electronic and force spectroscopy. *Rev. Sci. Instrum.* **2007**, *78*.
16. Toledo, J.; Manzaneque, T.; Hernando-García, J.; Vázquez, J.; Ababneh, A.; Seidel, H.; Lapuerta, M.; Sánchez-Rojas, J.L. Application of quartz tuning forks and extensional microresonators for viscosity and density measurements in oil/fuel mixtures. *Microsyst. Technol.* **2014**, *20*, 945–953.
17. Zhang, M.; Llaser, N.; Rodes, F. High-precision time-domain measurement of quality factor. *IEEE Trans. Instrum. Meas.* **2012**, *61*, 842–844.
18. Zhang, M.; Llaser, N.; Mathias, H. Improvement of the architecture for MEMS resonator quality factor measurement. *Proc. 15th IEEE Int. Conf. Electron. Circuits Syst. ICECS 2008* **2008**, 255–258.
19. Riley, W.J. *Handbook of Frequency Stability Analysis*; National Institute of Standards and Technology: Washington, US, 2008; ISBN 3019753058.
20. Eichelbaum, F.; Borngräber, R.; Schröder, J.; Lucklum, R.; Hauptmann, P. Interface circuits for

quartz-crystal-microbalance sensors. *Rev. Sci. Instrum.* **1999**, *70*, 2537–2545.
21. González, L.; Otero, J.; Cabezas, G.; Puig-vidal, M. Physical Electronic driver with amplitude and quality factor control to adjust the response of quartz tuning fork sensors in atomic force microscopy applications. *Sensors Actuators A. Phys.* **2012**, *184*, 112–118.
22. Jahng, J.; Lee, M.; Noh, H.; Seo, Y.; Jhe, W. Active Q control in tuning-fork-based atomic force microscopy. *Appl. Phys. Lett.* **2007**, *91*.
23. Ctistis, G.; Frater, E.H.; Huisman, S.R.; Korterik, J.P.; Herek, J.L.; Vos, W.L.; Pinkse, P.W.H. Controlling the quality factor of a tuning-fork resonance between 9 and 300 K for scanning-probe microscopy. *J. Phys. D. Appl. Phys.* **2011**, *44*.
24. Mordmüller, M.; Köhring, M.; Schade, W.; Willer, U. An electrically and optically cooperated QEPAS device for highly integrated gas sensors. *Appl. Phys. B* **2015**, *119*, 111–118.
25. NanoAndMore GMBH "Tuning Fork Sensor Controller" Available online: www.nanoandmore.com/pdf/manual-nam-controller-website.pdf.
26. Walls, F.; Gagnepain, J. Environmental Sensitivities of Quartz Oscillators. *IEEE Trans. Ultrason. Ferroelectr. Freq. Control* **1992**, *39*, 241–249.
27. Toledo, J.; Manzaneque, T.; Hernando-García, J.; Vazquez, J.; Ababneh, A.; Seidel, H.; Lapuerta, M.; Sanchez-Rojas, J.L. Application of quartz tuning forks and extensional microresonators for viscosity and density measurements in oil / fuel mixtures. *Microsyst Technol* **2014**, *20*, 945–953.
28. Carullo, A.; Vallan, A.; Afify, A.S.; Tulliani, J.-M. Development of a fast humidity sensor based on quartz tuning fork. In Proceedings of the 2016 IEEE International Instrumentation and Measurement Technology Conference Proceedings; IEEE, 2016.
29. Zhang, J.; O'Shea, S. Tuning forks as micromechanical mass sensitive sensors for bio- or liquid detection. *Sensors Actuators, B Chem.* **2003**, *94*, 65–72.
30. Nakamura, Y.; Miyashita, S. Frequency-Temperature Characteristics of Quartz Crystal Flexure Bars and Quartz Crystal Tuning Forks. *IEEE Trans. Sonics Ultrason.* **1979**, *26*, 369–376.
31. Bechmann, R.; Ballato, A.D.; Lukaszek, T.J. Higher-Order Temperature Coefficients of the Elastic Stiffnesses and Compliances of Alpha-Quartz. *Proc. IRE* **1962**, *50*, 1812–1822.
32. Matsiev, L.F. Application of Flexural Mechanical Resonators to Simultaneous Measurements of Liquid Density and Viscosity. In Proceedings of the 1999 IEEE Ultrasonics symposium; IEEE, 1999; pp. 457–460.
33. Rockland, L.B. Saturated Salt Solutions for Static Control of Relative Humidity between 5° and 40° C. *Anal. Chem.* **1960**, *32*, 1375–1376.
34. Rousseau, R.; Maurin, N.; Trzpil, W.; Bahriz, M.; Vicet, A. Quartz tuning fork resonance tracking and application in quartz enhanced photoacoustics spectroscopy. *Sensors* **2019**, *19*, 5565.
35. Nagel, L.W.; Pederson, D.O. SPICE (Simulation Program with Integrated Circuit Emphasis) 1973.
36. Caruso, G. A critical analysis of electric shunt circuits employed in piezoelectric passive vibration damping. *Smart Mater. Struct.* **2001**, *10*, 1059–1068.

Conclusion

A gas sensor needs to respond to different criteria such as sensitivity, selectivity, compactness and affordability. Independently from the technology employed in the sensor, those criteria are hard to combine and it often results in a compromise of low-cost but low sensitivity and selectivity, or high sensitivity and selectivity but high cost. These compromises limit the development and the spreading of gas sensors. Among the existing sensing techniques, photoacoustic spectroscopy based on laser absorption is very promising to achieve low-cost, miniaturized, highly sensitive and selective gas sensors. In particular, QEPAS has already been used in many different configurations and successfully employed for the detection of many species. However, the path to obtain a functional product for field application is to continue. In this sense, this PhD offered its own contribution in the optimization of the QEPAS sensor by discussing the limitations, by adopting a different perspective to provide solutions and by developing new experimental setups.

The Chapter 1 describes the theoretical notions that are essential for the understanding and the development of a QEPAS sensor, and more generally for a sensor based on laser spectroscopy. We started by presenting the absorption spectroscopy and the motivation for using mid-infrared lasers, and in particular quantum cascade lasers which exhibit excellent properties for making optical gas sensors. Then, we developed the concept of wavelength modulation spectroscopy and described the complex theoretical signals. We presented the photoacoustic spectroscopy which allows to achieve small footprints while preserving the sensitivity and the selectivity of laser-based sensors. Finally, we thoroughly described the QEPAS technique, with a specific focus on the piezoelectric transducer and the various existing configurations of the sensor.

In the Chapter 2, we discussed the selection of the laser wavelength, which is the first step of the sensor design. Using molecular spectra, we identified the most suitable locations which combine high absorption of the specie and low absorption of the other interfering species. This pre-study allowed us to estimate the feasibility of the sensor, which showed that the limit of detection is reachable for most of the species of interest.

We also presented a thorough study of the off-beam spectrophone; first considering the fabrication and the characterization of the microresonator alone and then its coupling with the QTF. In order to verify the consistency of the theoretical models, we developed a setup to characterize the acoustic response of the microresonator. It is based on a laser targeting a water absorption line and a MEMS microphone, which makes the setup easy to use and allows quick characterization. We took advantage of the setup to characterize the microresonators with various profiles and compared their performances. In particular, we fabricated the resonators by 3D printing and demonstrated the possibility to improve the coupling with the QTF. We also presented a new and more complex microresonator design with two resonators and two optical passes. In summary, using 3D printing and acoustic characterization, we presented a technique for rapid optimization of the microresonator.

The study of the off-beam spectrophone allowed us to adapt the microresonator for large beam diameters and in particular for long-wavelength lasers. We used a 11μm QCL for the detection of ethylene with an important optimization on the modulation scheme. Using the theory of wavelength modulation, we were able to simulate the modulated signal by considering the composite absorption profile and we obtained results very close to the experimental signal. The Python script developed for the simulation can easily be re-employed and would be particularly interesting for broad absorption spectra, for instance occurring in high pressure conditions.

After this successful demonstration, we also implemented a 4.7μm QCL for the detection of carbon monoxide and employed it for a biomedical application. We conducted a clinical evaluation on CO breath analysis at the hospital. The QEPAS sensor showed a very good correlation with the reference instruments and even better limit of detection. Upon discussion with the scientists in physiology, we identified that measuring in real time was crucial in breath analysis, and that QEPAS had the potential to meet this need. The future project has already been planned and will focus on real time measurement and the detection of multiple species.

The Chapter 3 is dedicated to the development of a new QEPAS technique. Compared to conventional photoacoustic spectroscopy, QEPAS is based on a highly resonant transducer which provides an enhanced noise immunity but an increased sensitivity to the environment, that can, depending on the operating condition of the sensor, give rise to the drift of the sensor response. The topic is rarely discussed in the literature as the QEPAS prototypes are tested in controlled environments. In the last chapter, we tackled this technical issue. We studied the different QTF characterization techniques, presented their limitations and quantified their performances. We selected the technique that offers the best compromise between the measurement time and the measurement accuracy. We validated the accuracy of the technique by characterizing the QTF response to the temperature and the humidity. We presented a new architecture which allows to continuously correct the resonance and therefore correct the sensor drift. Eventually, we developed a damping circuit to reduce the measurement time and therefore provide a fast correction. Inspired from the field of vibration damping, the damping circuit is a totally new approach in the field of QEPAS, but it could be exploited more generally for the characterization of highly resonant system, such as MEMS resonators.

The QEPAS technique is very promising for the realization of the next generation of gas sensors as it combines the key properties of sensitivity, selectivity and compactness. Physically, QEPAS is very unique as it involves multiple physical processes, and therefore a multitude of parameters can be optimized. A myriad of sensor configurations was presented in the literature, but there is still an important work to select the appropriate technological solutions depending on the specific application. For instance, QEPAS sensors could be compared with existing industrial sensors in order to identify their weaknesses and their strengths. Combining QEPAS with other technologies is also an interesting opportunity. New fabrication techniques such as 3D printing can be keys to provide new designs with simple fabrication processes. QEPAS has already been employed along with gas chromatography or placed in an optical cavity for sensitivity enhancement, but solutions for making QEPAS more performant and more relevant as a product are far from exhausted and they are worth being studied more extensively.

QEPAS sensors have not been very often employed outside of laboratories (see Chapter 3 of this manuscript) and there is a gap in the literature about the effect of a variable environment,

and even less to harsh environments that can be required for industrial applications. Although such conditions might affect the sensor, many strategies can be engineered to render the sensor robust and therefore viable for field applications.

Publications

Journal articles

Roman Rousseau, Zeineb Loghmari, Michaël Bahriz, Kaim Chamassi, Roland Teissier, et al.. Off-beam QEPAS sensor using an 11-µm DFB-QCL with an optimized acoustic resonator. *Optics Express*, Optical Society of America, 2019, 27 (5), pp.7435. ⟨10.1364/OE.27.007435⟩. ⟨hal-02067231⟩

Roman Rousseau, Nicolas Maurin, Wioletta Trzpil, Michaël Bahriz, Aurore Vicet. Quartz Tuning Fork Resonance Tracking and application in Quartz Enhanced Photoacoustics Spectroscopy. *Sensors*, MDPI, 2019, 19 (24), pp.5565. ⟨10.3390/s19245565⟩. ⟨hal-02441936⟩

Nicolas Maurin, Roman Rousseau, Wioletta Trzpil, Guillaume Aoust, Maurice Hayot, et al.. First clinical evaluation of a quartz enhanced photo-acoustic CO sensor for human breath analysis. *Sensors and Actuators B: Chemical*, Elsevier, 2020, pp.128247. ⟨10.1016/j.snb.2020.128247⟩. ⟨hal-02616215⟩

Kaim Chamassi, Wioletta Trzpil, Richard Arinero, Roman Rousseau, Aurore Vicet, et al.. Capacitive silicon micro-electromechanical resonator for enhanced photoacoustic spectroscopy. *Applied Physics Letters*, American Institute of Physics, 2019, 115 (8), pp.081106. ⟨10.1063/1.5098140⟩. ⟨hal-02441779⟩

Patents

Aurore Vicet, Roman Rousseau, Erwan Terrier, Mathias Digneton. Détecteur à cellules modulaires de mesure opto-acoustique exaltée par résonateur à quartz. France, Patent n° : 18 71734. 2018.

Conferences

Roman Rousseau, Wioletta Trzpil, Nicolas Maurin, Aurore Vicet, Michael Bahriz. Real time resonance tracking of a Quartz Tuning Fork and its application for Quartz Enhanced Photoacoustics Spectroscopy. *SPIE Photonics Europe*, 2020, Strasbourg, France. (Accepted oral presentation)

Roman Rousseau, Zeineb Loghmari, Michaël Bahriz, Kaim Chamassi, Guillaume Aoust, and Aurore Vicet. C2H4 and CO photoacoustic gas sensors with quantum cascade lasers. *JNRDM 2019 – Journées Nationales du Réseau Doctoral en Micro-nanoélectronique*, 2019, Montpellier, France. (Poster)

Roman Rousseau, Zeineb Loghmari, Michaël Bahriz, Kaim Chamassi, Aurore Vicet. QEPAS sensors for high sensitivity monitoring. Ethylene and air quality applications. *FLAIR 2018 - Field laser Applications in Industry and Research*, 2018, Assisi, Italy. (Poster)

Roman Rousseau, Zeineb Loghmari, Michaël Bahriz, Kaim Chamassi, Aurore Vicet. Laser photoacoustic spectroscopy for high sensive ethylene monitoring at 11 µm. *JNMO 2018*, 2018, Cap Esterel, France. (Poster)

A.Vicet, M. Bahriz, K. Chamassi, R. Rousseau, Z. Loghmari and D. Oussalah , Photoacoustic spectroscopy with resonant devices : from QEPAS to Silicon Resonant Detection. *PIERS 2018*, 2018, Toyama, Japan (Invited oral presentation)

K. Chamassi, A. Vicet, R. Rousseau, D. Oussalah and M. Bahriz New silicon micro-electromechanical resonator for enhanced photoacoustic spectroscopy applications *PIERS 2018*, 2018, Toyama, Japan (Oral presentation)

New optomechanical microresonator for photo-acoustic gas detection, Paper 11354-47, Wioletta Trzpil, Roman Rousseau, Nicolas Maurin, Aurore Vicet, Michael Bahriz, *SPIE Photonics Europe*, 2020.

Kaïm Chamassi, Wioletta Trzpil, Roman Rousseau, Aurore Vicet and Michael Bahriz - Methane detection based on photoacoustic spectroscopy with a new silicon micro-electromechanical *resonator FLAIR 2018 - Field Laser Applications in Industry and Research, 201*8, Assisi, Italy. (Poster)

Appendix A

QTF Lorentzian response

In this document, we provide the steps to express the QTF admittance as a Lorentzian function.

The QTF is represented by the Butterworth-Von Dyke (BVD) equivalent model, with a motional branch RLC and the electrodes capacitance C_0 (Figure A.1).

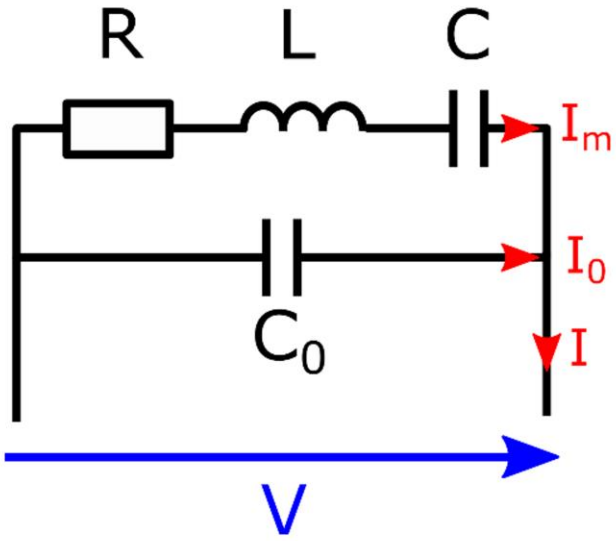

Figure A.1: Schematic of the QTF electrical equivalent circuit.

The first assumption is to neglect the parasitic capacitance, C_0. The admittance can be written as:

$$Y(\omega) = \frac{1}{1 + jL\omega + \frac{1}{jC\omega}} \tag{A.1}$$

Then, multiplying by $1/jL\omega$:

$$Y(\omega) = \frac{1/jL\omega}{1 - \frac{1}{LC\omega^2} - j\frac{R}{L\omega}} \tag{A.2}$$

Using the definition of the resonant frequency $\omega_0 = 1/\sqrt{LC}$ and the quality factor $Q = (1/R)\sqrt{L/C}$:

$$Y(\omega) = \frac{1/jL\omega}{1 - (\frac{\omega_0}{\omega})^2 - j\frac{\omega_0}{\omega Q}} \tag{A.3}$$

Then taking the square of the admittance modulus:

$$|Y(\omega)|^2 = \frac{(1/L\omega)^2}{\left[(1-(\frac{\omega_0}{\omega})^2\right]^2 + (\frac{\omega_0}{\omega Q})^2} \tag{A.4}$$

The left term of the denominator can be developed, and simplified using the assumption that $\omega = \omega_0$:

$$\left[1-\big(\frac{\omega_0}{\omega}\big)^2\right]^2 = \left[\big(1+\frac{\omega_0}{\omega}\big)\big(1-\frac{\omega_0}{\omega}\big)\right]^2 \approx \left[2\big(1-\frac{\omega_0}{\omega}\big)\right]^2 \tag{A.5}$$

Inserting A.5 in A.7 and dividing by $\big(\frac{\omega_0}{\omega}\big)^2$:

$$|Y(\omega)|^2 = \frac{(1/L\omega_0)^2}{\left[2\big(\frac{\omega}{\omega_0}-1\big)\right]^2 + (\frac{1}{Q})^2} \tag{A.6}$$

Multiplying by Q and finally re writing the equation:

$$|Y(\omega)|^2 = \frac{(1/L\omega_0)^2 Q^2}{\left[\frac{2Q(\omega-\omega_0)}{\omega_0}\right]^2 + 1} = \frac{1}{R^2}\frac{1}{1+\left[\frac{2Q(\omega-\omega_0)}{\omega_0}\right]^2} \tag{A.7}$$

Hence, we obtain that the square of the admittance modulus follows a Lorentzian function of central frequency ω_0, of full width at half maximum Q/ω_0 and of maximum $1/R^2$.

Appendix B

Optimum length for the off-beam microresonator

The purpose of this appendix is to detail the calculations on the optimum length of the off-beam microresonator. First, we calculate the acoustic impedance and resonance frequency of a cylindrical pipe. Then, we account for the effect of the slit and we derive the equation as presented by H.Yi in his article[1].

B.1 Resonance in a pipe

The pressure inside the tube can be considered as a one dimensionnal wave travelling back and forth along the tube axis x :

$$P(x,t) = A\exp(i(\omega t - kx)) + B\exp(i(\omega t + kx)) \tag{B.1}$$

with ω the angular frequency, k the wave vector, A and B some constants. Knowing the expression for the fluid particle velocity :

$$u(x,t) = -\frac{1}{\rho}\int \delta\frac{\partial P(x,t)}{\partial x}dt = -\frac{1}{\rho v}\big[A\exp(i(\omega t - kx)) - B\exp(i(\omega t + kx))\big]$$

with ρ the density of the fluid and v the speed of sound. The acoustic impedance is defined as the ratio of the pressure $P(x,t)$ to the product of fluid velocity $u(x,t)$ and the cross section area S :

$$Z(x) = \frac{P(x,t)}{Su(x,t)} = \frac{\rho v}{S}\frac{A\exp(-ikx) + B\exp(ikx)}{A\exp(-ikx) - B\exp(ikx)} \tag{B.2}$$

Now, expressing the impedance at the boundaries of the tube :

$$Z_0 = Z(0) = \frac{\rho v}{S}\frac{A+B}{A-B}$$

Isolating A and B :

$$\frac{A}{B} = -\frac{\frac{\rho v}{S} + Z_0}{\frac{\rho v}{S} - Z_0}$$

[1] Yi, H.; Liu, K.; Sun, S.; Zhang, W.; Gao, X. Theoretical analysis of off beam quartz-enhanced photoacoustic spectroscopy sensor. *Opt. Commun.* **2012**, *285*, 5306–5312.

Substituting the fraction in $Z(x)$:

$$\begin{aligned}
Z(x) &= \frac{\rho v}{S}\frac{\frac{A}{B}\exp(-ikx)+\exp(ikx)}{\frac{A}{B}\exp(-ikx)-\exp(ikx)} \\
Z(x) &= \frac{\rho v}{S}\frac{-\frac{\frac{\rho v}{S}+Z_0}{\frac{\rho v}{S}-Z_0}\exp(-ikx)+\exp(ikx)}{-\frac{\frac{\rho v}{S}+Z_0}{\frac{\rho v}{S}-Z_0}\exp(-ikx)-\exp(ikx)} \\
Z(x) &= \frac{\rho v}{S}\frac{(\frac{\rho v}{S}+Z_0)\exp(-ikx)-(\frac{\rho v}{S}-Z_0)\exp(ikx)}{(\frac{\rho v}{S}+Z_0)\exp(-ikx)+(\frac{\rho v}{S}-Z_0)\exp(ikx)} \\
Z(x) &= \frac{\rho v}{S}\frac{Z_0(\exp(-ikx)+\exp(ikx))+\frac{\rho v}{S}(\exp(-ikx)-\exp(ikx))}{Z_0(\exp(-ikx)-\exp(ikx))+\frac{\rho v}{S}(\exp(-ikx)+\exp(ikx))} \\
Z(x) &= \frac{\rho v}{S}\frac{Z_0+\frac{i\rho v}{S}\frac{(\exp(-ikx)-\exp(ikx))}{i(\exp(-ikx)+\exp(ikx))}}{iZ_0\frac{(\exp(-ikx)-\exp(ikx))}{i(\exp(-ikx)+\exp(ikx))}+\frac{\rho v}{S}} \\
Z(x) &= \frac{Z_0-\frac{i\rho v}{S}\tan(kx)}{\frac{SZ_0}{i\rho v}\tan(kx)+1}
\end{aligned}$$

Eventually obtaining :

$$Z(x) = \frac{\rho v}{S}\frac{Z_0-\frac{i\rho v}{S}\tan(kx)}{\frac{SZ_0}{i\rho v}\tan(kx)+1} \tag{B.3}$$

This expression is similar to the one found in the litterature [2]. The resonance and the antiresonance of the pipe correspond to condition of the reactance equals to 0. For an open-open tube at resonance, the pressure at $x = 0$ and $x = L$ equal to zero, thus $Z(0) = Z(L) = 0$.

$$Z(L) = -\frac{i\rho v}{S}\tan(kL) => \tan(kL) = 0 \tag{B.4}$$

The resonance condition on the wavevector is given as : $k = \frac{n\pi}{L}$.

For our purpose, the standing wave is aimed to be extracted from the tube by an aperture located in the middle of the pipe. The antinode must be located at this specific position. This can be expressed as a second condition on the resonance : $Z(L/2) \to \infty$.

$$\begin{aligned}
Z(L/2) \to \infty \Rightarrow \tan(kL/2) &= 0 \\
\tan(\frac{n\pi}{2}) &= 0 \\
n = m+1, m \subset \mathbb{N}&
\end{aligned}$$

Only the harmonics with an odd number n have an antinode in the middle of the pipe, as for instance on Figure B.1 the 1st and 3rd harmonics.

[2] Kinsler, L.E.; Frey, A.R.; Coppens, A.B.; Sanders, J. V. *Fundamentals of acoustics*; Wiley-VCH, Ed.; 1999; ISBN 0-471-84789-5.

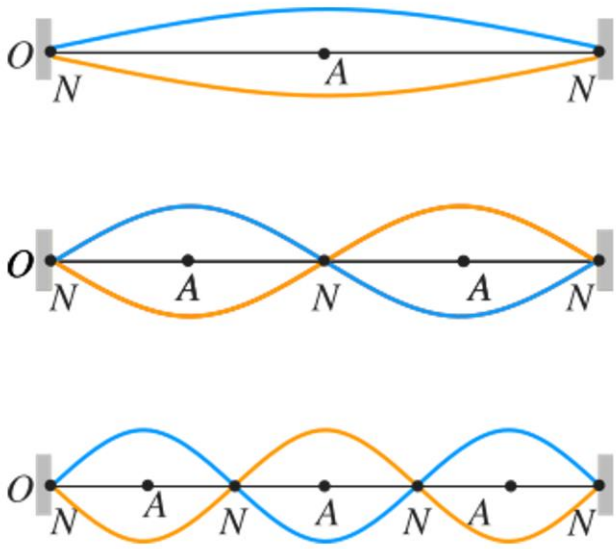

Figure B.1: Pressure standing wave for the first three harmonics

B.2 H. Yi original model

In H.Yi model, a slit is added to the previously studied cylindrical resonator. The slit is a circle of radius r_0, located in the middle of the tube (Figure B.2).

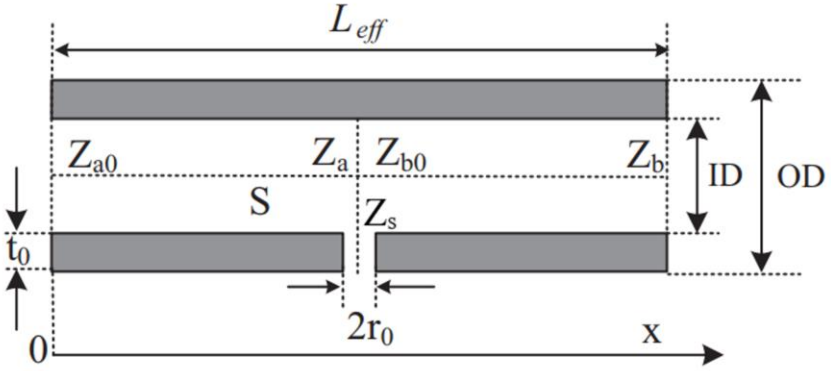

Figure B.2: Cross section view of the mR[3]

The behavior of the tube is affected by this slit of impedance Z_s.
Starting from :

$$Z(x) = \frac{Z_{a0} - \frac{i\rho v}{S}\tan(kx)}{\frac{SZ_{a0}}{i\rho v}\tan(kx) + 1} \tag{B.5}$$

The equation is valid on one half of the resonator $0 \leq x < a$ and can be used to obtained $Z(a)$ from $Z(0)$. Similarly, $Z(b0)$ can be written as a function of $Z(b)$. Linking the impedances with the slit impedance using the continuity equation :

$$\frac{1}{Z_a} = \frac{1}{Z_s} + \frac{1}{Z_{b0}} \tag{B.6}$$

[3]Yi, H.; Liu, K.; Sun, S.; Zhang, W.; Gao, X. Theoretical analysis of off beam quartz-enhanced photoacoustic spectroscopy sensor. *Opt. Commun.* **2012**, *285*, 5306–5312.

$$
\begin{aligned}
Z(a) &= \frac{Z_0 - \frac{i\rho v}{S}\tan(kL_{eff}/2)}{\frac{SZ_0}{i\rho v}\tan(kL_{eff}/2)+1} \\
Z(b) &= \frac{Z_{b0} - \frac{i\rho v}{S}\tan(kL_{eff}/2)}{\frac{SZ_{b0}}{i\rho v}\tan(kL_{eff}/2)+1}
\end{aligned}
$$

Z_s is the impedance of the slit and be written as [4]:

$$Z_s = -\frac{i\rho v k}{\sigma_s} \tag{B.7}$$

σ_s is the acoustic conductivity of the slit and is expressed as :

$$\sigma_s = -\frac{s_s}{t_{eff}} \tag{B.8}$$

with s_s and t_{eff}, the surface area and the effective thickness of the slit, resp.
As before, the resonance is found by nulling the input and output acoustic impedance or equivalently : $Z_{a0} = Z_b = 0$.

$$
\begin{aligned}
Z(a) &= \frac{Z_{a0} - \frac{i\rho v}{S}\tan(kL_{eff}/2)}{\frac{SZ_{a0}}{i\rho v}\tan(kL_{eff}/2)+1} = -\frac{i\rho v}{S}\tan(kL_{eff}/2) \\
Z(b) &= \frac{Z_{b0} - \frac{i\rho v}{S}\tan(kL_{eff}/2)}{\frac{SZ_{b0}}{i\rho v}\tan(kL_{eff}/2)+1} = 0 \;\Rightarrow Z_{b0} = \frac{i\rho v}{S}\tan(kL_{eff}/2)
\end{aligned}
$$

Leading directly to :

$$\frac{1}{Z_s} = \frac{1}{Z_a} - \frac{1}{Z_{b0}} = -\frac{2S}{i\rho v}\cot(kL_{eff}/2) \tag{B.9}$$

Using B.8 and B.9 :

$$tan(kL_{eff}/2) = -\frac{2SZ_s}{i\rho v} = -\frac{2kS}{\sigma_s}$$

Making the plausible assumption that $\pi < kL_{eff}/2 < 3\pi$ i.e $\lambda/4 < L_{eff} < 3\lambda/4$:

$$\frac{kL_{eff}}{2} = \pi - \arctan\left[\frac{2kS}{\sigma_s}\right]$$

Therefore, obtaining a expression for the effective length :

$$L_{eff} = \frac{v}{f_0}\Big[1 - \frac{1}{\pi}\arctan(\frac{4\pi S}{\sigma_s}\frac{f_0}{v})\Big] \tag{B.10}$$

And finally applying the open-end correction to obtain H.Yi's equation :

$$L_{mR} = L_{eff} - 1.2R$$

$$\boldsymbol{L_{mR} = \frac{v}{f_0}\Big[1 - \frac{1}{\pi}\arctan(\frac{4\pi S}{\sigma_s}\frac{f_0}{v})\Big] - 1.2R} \tag{B.11}$$

[4] E.G. Richardson, Technical aspects of sound: sonic range and airborne sound, Elsevier Pub. Co., Amsterdam; New York, 1957, pp. 12, 487